GEOPHYSICAL TESTING OF ROCK AND ITS RELATIONSHIPS TO PHYSICAL PROPERTIES

FINAL REPORT

Sponsored by the Florida Department of Transportation Research Center
Contract Number BDK-75-977-01

Dr. Dennis R. Hiltunen, P.E.
Principal Investigator

Dr. Nick Hudyma, P.E.
University of North Florida
Faculty Co-Investigator

Dr. Khiem T. Tran and Ariel I. Sarno
Graduate Student Researchers

DEPARTMENT OF CIVIL & COASTAL ENGINEERING
UNIVERSITY OF FLORIDA

February 2011

DISCLAIMER

The opinions, findings, and conclusions expressed in this publication are those of the authors and not necessarily those of the State of Florida Department of Transportation or the U.S. Department of Transportation.

Prepared in cooperation with the State of Florida Department of Transportation and the U.S. Department of Transportation.

METRIC CONVERSION TABLE

SYMBOL (US)		MULTIPLY BY	TO FIND	SYMBOL (SI)
		LENGTH		
in	inches	25.4	millimeters	**mm**
ft	feet	0.305	meters	**m**
yd	yards	0.914	meters	**m**
mi	miles	1.61	kilometers	**km**
		AREA		
in^2	squareinches	645.2	square millimeters	**mm^2**
ft^2	squarefeet	0.093	square meters	**m^2**
yd^2	square yard	0.836	square meters	**m^2**
ac	acres	0.405	hectares	**ha**
mi^2	square miles	2.59	square kilometers	**km^2**
		VOLUME		
fl oz	fluid ounces	29.57	milliliters	**mL**
gal	gallons	3.785	liters	**L**
ft^3	cubic feet	0.028	cubic meters	**m^3**
yd^3	cubic yards	0.765	cubic meters	**m^3**
		MASS		
oz	ounces	28.35	grams	**g**
lb	pounds	0.454	kilograms	**kg**
T	short tons (2000 lb)	0.907	megagrams (or "metric ton")	**Mg (or "t")**
		TEMPERATURE (exact degrees)		
°F	Fahrenheit	5 (F-32)/9 or (F-32)/1.8	Celsius	**°C**
		FORCE and PRESSURE or STRESS		
lbf	poundforce	4.45	newtons	**N**
lbf/in^2	poundforce per square inch	6.89	kilopascals	**kPa**

SYMBOL (SI)		MULTIPLY BY	TO FIND	SYMBOL (US)
		LENGTH		
mm	millimeters	0.039	inches	**in**
m	meters	3.28	feet	**ft**
m	meters	1.09	yards	**yd**
km	kilometers	0.621	miles	**mi**
		AREA		
mm^2	square millimeters	0.0016	square inches	**in^2**
m^2	square meters	10.764	square feet	**ft^2**
m^2	square meters	1.195	square yards	**yd^2**
ha	hectares	2.47	acres	**ac**
km^2	square kilometers	0.386	square miles	**mi^2**
		VOLUME		
mL	milliliters	0.034	fluid ounces	**fl oz**
L	liters	0.264	gallons	**gal**
m^3	cubic meters	35.314	cubic feet	**ft^3**
m^3	cubic meters	1.307	cubic yards	**yd^3**
		MASS		
g	grams	0.035	ounces	**oz**
kg	kilograms	2.202	pounds	**lb**
Mg (or "t")	megagrams (or "metric ton")	1.103	short tons (2000 lb)	**T**
		TEMPERATURE (exact degrees)		
°C	Celsius	1.8C+32	Fahrenheit	**°F**
		FORCE and PRESSURE or STRESS		
N	newtons	0.225	poundforce	**lbf**
kPa	kilopascals	0.145	poundforce per square inch	**lbf/in^2**

1. Report No.	2. Government Accession No.	3. Recipient's Catalog No.
4. Title and Subtitle Geophysical Testing of Rock and Its Relationships to Physical Properties		5. Report Date February 2011
		6. Performing Organization Code
7. Author(s) Khiem T. Tran, Dennis R. Hiltunen, Ariel I. Sarno, and Nick Hudyma		8. Performing Organization Report No.
9. Performing Organization Name and Address Department of Civil and Coastal Engineering University of Florida 365 Weil Hall, P.O. Box 116580 Gainesville, FL 32611-6580		10. Work Unit No. (TRAIS) 11. Contract or Grant No. BDK-75-977-01
12. Sponsoring Agency Name and Address Florida Department of Transportation 605 Suwannee Street, MS 30 Tallahassee, FL 32399		13. Type of Report and Period Covered Final Report May 2008-February 2011 14. Sponsoring Agency Code

15. Supplementary Notes

16. Abstract

Testing techniques were designed to characterize spatial variability in geotechnical engineering physical parameters of rock formations. Standard methods using seismic waves, which are routinely used for shallow subsurface investigation, have limitations in characterizing challenging profiles at depth that include low-velocity layers and embedded cavities. This research focuses on overcoming these limitations by developing two new methods using both sensitive data and a global inversion scheme. The first method inverts combined surface and borehole travel times for a wave velocity profile. The technique is based on an extremely fast method to compute first-arrival times through the velocity models. The capability of this inversion technique is tested with both synthetic and real experimental data sets. The inversion results show that this technique successfully maps 2-D velocity profiles with high variation. The inverted wave velocities from real data appear to be consistent with cone penetration test (CPT), geotechnical borings, and standard penetration test (SPT) results. The second method inverts full waveforms for a wave velocity profile. The strength of this approach is the ability to generate all possible wave types and, thus, to simulate and accurately model complex seismic wave fields that are then compared with observed data to deduce complex subsurface properties. The capability of this inversion technique is also tested with both synthetic and real experimental data sets. The inversion results from synthetic data show the ability of detecting reverse models that are hardly detected by traditional inversion methods that use only the dispersion property of Rayleigh waves. The inversion results from the real data are generally consistent with crosshole, SPT N-value, and material log results. Employed for site characterization of deep foundation design, the techniques can provide credible information for material at the socket and partially detect anomalies near the socket. Lastly, based upon a laboratory testing program conducted on rock cores, it does appear that relationships between geophysical measurements and geotechnical engineering design parameters are credible, though significant scatter does exist in the data. It could be postulated that geophysical measurements should be capable of indentifying large zones of poor quality rock, and the results can provide characterization of spatial variability in geotechnical engineering physical parameters useful in the design of deep foundations.

17. Key Word	18. Distribution Statement
Drilled shafts, finite difference, full waveform, global optimization, rock sockets, seismic waves, simulated annealing	No Restrictions

19. Security Classif. (of this report)	20. Security Classif. (of this page)	21. No. of Pages	22. Price
Unclassified	Unclassified	190 Pages	

EXECUTIVE SUMMARY

The primary objective of the research is to continue incorporation of appropriate geophysical testing techniques into site characterization activities of the Florida Department of Transportation (FDOT). More specifically, testing techniques were designed to characterize spatial variability in geotechnical engineering physical parameters of rock formations useful in the design of deep foundations. Standard methods using seismic waves, which are routinely used for shallow subsurface investigation in engineering, have limitations in characterizing challenging profiles at depth that include low-velocity layers and embedded cavities. The limitations are often due to insensitivity of data used for inversion, and pitfalls of local inversion schemes employed in these methods. This research focuses on overcoming these limitations by developing two new methods using both sensitive data and a global inversion scheme, simulated annealing.

The first method is an inversion technique to invert combined surface and borehole travel times for a wave velocity profile. The technique is based on an extremely fast method to compute first-arrival times through the velocity models. The core of the simulated annealing, the Metropolis sampler, is applied in cascade with respect to shots to significantly reduce computer time. The capability of this inversion technique was tested with both synthetic and real experimental surface data sets. The inversion results show that this technique successfully maps 2-D velocity profiles with high variation. The inverted wave velocities from real data appear to be consistent with cone penetration test (CPT), geotechnical borings, and standard penetration test (SPT) results.

The second method is a technique to invert full waveforms for a wave velocity profile. The strength of this approach is the ability to generate all possible wave types (body waves and surface waves, etc.) and thus to simulate and accurately model complex seismic wave fields that

are then compared with observed data to deduce complex subsurface properties. The capability of this inversion technique was also tested with both synthetic and real experimental data sets. The inversion results from synthetic data show the ability of detecting reverse models that are hardly detected by traditional inversion methods that use only the dispersion property of Rayleigh waves. The inversion results from the real data are generally consistent with crosshole, SPT N-value, and material log results.

Lastly, a laboratory testing program was conducted on rock cores that assess the relationships between geophysical measurement results to geotechnical engineering design parameters. Based upon these results, it does appear that relationships between geophysical measurements and geotechnical engineering design parameters are credible, though significant scatter does exist in the data. In could be postulated that geophysical measurements should be capable of identifying large zones of poor quality rock. Employed for site characterization of deep foundation design, the techniques can provide credible information of material at the socket and partially detect anomalies near the socket. The inversion results can provide characterization of spatial variability in geotechnical engineering physical parameters of subsurface formations useful in the design of deep foundations.

TABLE OF CONTENTS

INTRODUCTION 9

1.1 Problem Statement 9
1.2 Objectives 14
1.3 Scope 15
1.4 Organization of Report 17

SITE CHARACTERIZATION METHODS USING SEISMIC WAVES 19

2.1 Seismic Waves 19
2.2 Site Characterization Methods Using Seismic Waves 21
2.2.1 Goals of Seismic Wave Methods 21
2.2.2 Borehole Methods 21
2.2.3 Surface Methods 21
2.3 Overview of the Surface Methods 27
2.3.1 Methods Using Surface Travel Times 27
2.3.2 Methods Using Surface Wave Dispersion 29
2.4 Limitations of the Standard Methods Using Seismic Waves 30
2.4.1 Limitations due to Insensitivity of Data 31
2.4.2 Limitations due to Local Inversion Techniques 31
2.5 Suggested Improvements 32
2.5.1 Improvements by Using Sensitive Data 32
2.5.2 Improvements by Employing Global Inversion Techniques 33

INVERSION OF FIRST-ARRIVAL TIMES USING SIMULATED ANNEALING 34

3.1 Introduction 34
3.2 Methodology 36
3.2.1 Forward Modeling 36
3.2.2 Optimization Method 37
3.3 Applications 39
3.3.1 Applications on Synthetic Data 39
3.3.2 Applications on Real Test Data 43
3.4 Chapter Summary 55

INVERSION OF COMBINED BOREHOLE AND SURFACE TRAVEL TIMES 57

4.1 Introduction 57
4.2 Inversion of Synthetic Data 57
4.2.1 Synthetic Model 1 57
4.2.2 Synthetic Model 2 62
4.2.3 Synthetic Model 3 64
4.3 Inversion of Real Test Data 67
4.3.1 Newberry Test Site 67
4.3.2 Ft. McCoy Test Site 74

4.3.3 Dunedin Test Site 78
4.4 Chapter Summary 87

INVERSION OF FULL WAVEFORMS USING SIMULATED ANNEALING 89

5.1 Introduction 89
5.2 Methodology 90
5.2.1 Forward Modeling 90
5.2.2 Optimization Method 94
5.3 Applications 97
5.3.1 Applications on Synthetic Data 97
5.3.2 Applications on Real Test Data 121
5.4 Chapter Summary 134

GEOTECHNICAL ENGINEERING PARAMETER RELATIONSHIPS 135

6.1 Literature Review 135
6.1.1 Weathering of Limestone 135
6.1.2 Classification of Weathering 136
6.1.3 The Effect of Weathering on Geotechnical Properties 138
6.2 Laboratory Testing 140
6.2.1 Limestone Specimens 141
6.2.2 Specimens 142
6.2.3 Weathering Classification 142
6.2.4 Unit Weight Measurements 151
6.2.5 Dynamic Testing 152
6.2.6 Static Testing 155
6.3 Results 157
6.3.1 Coefficient of Determination Measurements 157
6.3.2 Introduction to the Developed Relationships 158
6.3.3 Unit Weight and Weathering 159
6.3.4 Comparison of Static Elastic Modulus and Unconfined Compressive Strength 161
6.3.5 Static Properties and Unit Weight 162
6.3.6 Dynamic and Physical Properties 165
6.3.7 Dynamic and Static Properties 168
6.4 Chapter Summary 177

CLOSURE 179

7.1 Summary of Findings 179
7.1.1 Inversion Technique Using Travel Times 179
7.1.2 Inversion Technique Using Full Waveforms 180
7.1.3 Rock Parameter Relationships 181
7.2 Conclusions 182
7.3 Recommendations 183

LIST OF REFERENCES 187

CHAPTER 1
INTRODUCTION

1.1 Problem Statement

A blue-ribbon panel of experts has authored a report published in 2006 by the National Research Council (NRC) of the National Academy of Sciences (NAS) entitled "Geological and Geotechnical Engineering in the New Millennium: Opportunities for Research and Technology Innovation." In this report the panel indicates that "Perhaps the most significant contribution geoengineering can make to construction efficiency is through improved site characterization, as unanticipated site conditions still represent the most common and most significant cause of problems and disputes that occur during construction."

It is understood that personnel of the Florida Department of Transportation (FDOT) might concur with the assessment of the NRC panel. The problem is particularly acute in karst geologic settings like those in Florida where subsurface conditions are often highly variable. For deep foundations, the problem is further exaggerated by increased use in Florida of single, large-diameter, non-redundant drilled shafts as foundation elements. Reliance on traditional subsurface characterization methods that invasively probe and sample a very small volume of material frequently results in problems and inefficiencies.

For example, such techniques often produce poor assessment of the spatial variation in subsurface conditions. This can lead to use of very conservative design parameters and produce expensive design solutions. Even worse, poor assessment of spatial variation can also result in failure to identify a significant anomaly, which can lead to substructure failure.

An additional concern with traditional techniques is that they are often unreliable in characterizing the engineering parameters of soft rock such as Florida limestone. For example, the standard penetration test (SPT) can fracture soft rock during driving, producing results that

are too low, and design parameters that are too conservative or construction claims for differing site conditions.

The NRC report concludes that "Faster, more rapid, more cost-effective, more accurate, and less invasive techniques for characterizing the subsurface is [sic] perhaps the most important need in geoengineering, irrespective of the specific problem to be solved." They further suggest that "New, efficient geophysical sensing devices coupled with versatile modeling and inversion software that can run on personal computers facilitate the application of geophysical techniques and permit the real-time visualization of subsurface conditions. These developments offer the promise of a shift in the balance between traditional invasive exploration techniques and geophysical methods."

For example, the elastic wave fields measured via seismic wave propagation techniques carry substantial information about characteristics of media they propagate in, and these techniques use this information to derive the properties of media. There are many techniques that are routinely used for shallow subsurface investigation, such as techniques using wave velocity dispersion, including spectral analysis of surface waves (SASW) (Nazarian, 1984), multi-channel analysis of surface waves (MASW) (Park et al., 1999), refraction microtremor (ReMi) (Louie, 2001), and passive-source frequency-wavenumber (f-k), and techniques using travel times, including conventional seismic refraction and seismic refraction tomography (SRT). However, these standard techniques utilized in current engineering evaluations have limitations in dealing with challenging profiles, which include anomalies such as low-velocity zones and cavities. The limitations of these methods are generally caused by: 1) insensitivity of data used for inversion, and 2) shortcomings of local inversion techniques often employed in these methods.

Regarding the insensitivity of data, standard techniques usually use only a limited portion of information carried by elastic wave fields, such as travel times or wave velocity dispersion. Synthetic tests in this research indicate that surface travel times are not very sensitive to the anomalies. Thus, the anomalies are not well detected if using only surface travel times. For the techniques using wave velocity dispersion, O'Neill (2003) found that a low-velocity layer (LVL) of a few meters thickness buried at depth of a few meters cannot be inverted with confidence, due to loss of sensitivity with depth. In addition, the dispersion property is insensitive to lateral variation, thus techniques using wave velocity dispersion are only for 1-D problems and cannot be applied in regions with high lateral variation.

Regarding the shortcomings of local inversion techniques, geotechnical inversion problems are typically highly non-linear, non-unique, and influenced by inherent noise in measured data. Results from any local inversion technique heavily depend on the initial model and a priori information. In order to obtain a good inversion result, these local techniques require both a reasonable initial model and a priori information that are not always available. In addition, there is no guarantee that the model corresponding to the smallest error (best fitting) is closest to the true model because of the noise and non-uniqueness of inverted solutions. Any of many thousand models that have a similar degree of fitting can be the inversion result. The issue here is how to decide which model is the best, and the uncertainty associated with that model.

This research focuses on overcoming the aforementioned limitations by developing new methods using both sensitive data and global inversion schemes. Firstly, data sensitive to anomalies, such as borehole data, will be utilized to improve resolution of travel time inversion results. By using borehole data, it is possible to increase the depth of investigation, to reduce the uncertainty associated with the inversion result, and to improve resolution of inverted profiles.

Secondly, full waveform data will be utilized to solve 2-D reverse problems when borehole data is not available. The reason to use the full waveform data instead of the wave velocity dispersion, is that it is more sensitive to the anomalies. Lastly, global optimization schemes based on simulated annealing will be employed in both travel time and full waveform inversions. These global techniques do not depend on the initial model, and become important in regions where no a priori information about subsurface profiles is available.

In practice, the design of an efficient foundation system depends on appropriate characterization of the supporting soil and rock, and determining the proper geotechnical parameters for design. In the case of drilled shafts in rock, the unconfined compressive strength and elastic modulus of a rock specimen is insufficient for proper design because of scale effect; strength and deformability of rock masses are only a portion of those determined in laboratory specimens because of the presence of discontinuities within the rock mass. The rock mass supporting the drilled shaft foundation must be sufficiently characterized to determine the capacity and potential failure modes within the discontinuous rock mass.

Rock masses are characterized through the use of rock mass classification systems. Most rock mass classification systems were developed to aid in the design of underground openings or support systems for underground openings. However, four rock mass classification systems (rock quality designation (RQD), rock mass rating (RMR), Q-system, and Geological Strength Index) are used in correlation with parameters applicable to the design of foundations in rock masses. These systems use a combination of drilling data, mapping data, geologic descriptions of discontinuities, and water inflow data to quantify the classification of a rock mass.

The use of rock mass classification systems has been highly successful within jointed (discontinuous) rock masses because the classification systems rely on mapping and descriptions

of the joint sets present within the rock mass. However, the karstic limestone in Florida does not readily fit into a model that can be assessed using traditional rock mass classification systems because the discontinuous nature of the limestone is derived from weathering and not joint systems. The near-surface karstic limestone in Florida has a poorly developed to non-existent joint system. The strength and stiffness of the limestone is controlled by the degree of weathering within the rock mass from weathering events throughout geologic history, and on-going weathering. The degree of weathering is highly variable with respect to both depth and lateral extent within the rock mass. The presence of cavities within the limestone also adds to the difficulties in classifying the rock mass. This extreme spatial variability and lack of a developed joint system makes the use of the traditional rock mass classification systems ineffective.

The research will assess the potential to quantify geotechnical parameters associated with the design of drilled shafts in rock from geophysical measurements. The non-joint discontinuous nature of the karstic limestone cannot be quantified using only core data. The only viable approach to both quantify spatial variability, and quantify the geotechnical parameters required for the design of drilled shaft foundations in rock, is geophysics. Geophysical measurements can potentially be made from both surface and downhole measurements as proposed. In addition, geotechnical engineering physical properties used in the design of shafts can also be developed via laboratory and field test methods conducted on the same materials characterized via geophysics. These methods can include unconfined compression strength, split tensile strength, cone penetration test results, rock shear tests results, and other physical properties and indices. This initial study will use laboratory tests on rock cores collected for a previous FDOT research

study to assess whether reliable correlations can be established to relate geophysical measurement results to important physical properties.

1.2 Objectives

The primary objective of the research is to continue the incorporation of appropriate geophysical testing techniques into site characterization activities of FDOT. More specifically, testing techniques were designed to characterize spatial variability in geotechnical engineering physical parameters of rock formations useful in the design of deep foundations. This will be particularly useful in implementing the new load and resistance factor design (LRFD) design methodology that can explicitly account for spatial variability in design parameters. The primary focus was to develop inversion techniques that can well characterize challenging profiles with requirement of a little or no a priori information, and can also evaluate the uncertainties associated with the inverted profiles. In addition, a laboratory testing program was conducted to investigate the feasibility of relating geophysical measurements to appropriate geotechnical design parameters.

It is expected that geophysical techniques can improve the accuracy and reliability of engineering parameters determined for design of deep foundations, and will increase the volume of material actually evaluated in a subsurface investigation. It is anticipated that improved characterization would lower uncertainty and risk, and reduce overall cost of subsurface construction. More specific objectives of this research include the following:

- Develop a global inversion technique to invert travel times for a velocity structure. The technique is independent of initial model, and can be applied in regions where no a priori information is available.
- Determine the uncertainty associated with the inverted profile from travel times. This uncertainty represents the influence of noise in measured data and non-uniqueness of inversion solutions.

- Incorporate borehole data into a travel time inversion to improve the resolution of the inverted profile and reduce the associated uncertainty.
- Develop another global inversion technique using full waveforms. This technique is primarily used when borehole data is not available, particularly for cases of reverse velocity structures.
- Conduct laboratory tests on rock cores available from the Newberry test site to assess whether reliable correlations can be established to relate geophysical measurement results to important geotechnical properties and parameters.

1.3 Scope

Geophysical sensing involves using techniques deployed from the ground surface or a borehole to define soil and rock profiles, and to determine physical, chemical, or biological properties of earth materials. Most geophysical methods are based on detecting a physical property contrast in space or time. The target must have sufficient size or contrast to be detectable by the geophysical sensor, and there is an inherent tradeoff between resolution and target depth. Although geophysical measurements are often conducted at a boundary, they can be processed using inversion techniques to deduce the field of a parameter away from the boundary.

There is a wide range of geophysical testing methodologies available for application, and based upon several physical principles. The broad categories of methodologies include seismic wave propagation, electromagnetic wave propagation, electricity, magnetics, and gravity. Each class of methods produces measurements that are sensitive to particular physical properties of the material under investigation. For example, seismic waves are primarily dependent on the elastic modulus and mass density of a material, while electromagnetic waves are primarily governed by the dielectric constant.

While the broad categories of methodologies have been established for some time, specific applications are continually under development and improvement as sensing, data acquisition,

computing, and other technologies evolve. A thorough review of both established and emerging geophysical methods was conducted to determine and recommend specific technologies for characterizing rock formations in Florida. Emphasis was placed on techniques for assessing two-dimensional (2-D) and three-dimensional (3-D) spatial variation of rock formations at depth and within a zone of material that will eventually contain a drilled shaft foundation. In addition, it is important that geophysical parameters can be related to geotechnical engineering physical parameters useful in the design of drilled shaft foundations. While the overall objective is a challenging geophysical imaging problem to solve, two potential strategies employing seismic waves were investigated.

As part of the investigation, nondestructive tests including refraction test, full waveform test and/or invasive tests including cone penetration test (CPT), geotechnical borings, standard penetration test (SPT), and crosshole test were conducted at four test sites:

- A National Geotechnical Experiment Site (NGES) at Texas A&M University (TAMU).
- A Florida Department of Transportation (FDOT) stormwater runoff retention basin in Alachua County off of state road 26, Newberry, Florida.
- A test site near Ft. McCoy, Florida.
- A test site in Dunedin, Florida.

Two inversion techniques that use travel times and full waveforms have been developed and intensively tested on synthetic models before being applied to real test data. For the technique using travel times, it was first tested on many synthetic models that were previously tested on three commercial refraction tomography codes by Sheehan et al. (2005) to verify its capability, and then applied to several real data sets. The inverted profiles from nondestructive data were compared to CPT, SPT, and geotechnical borings results to appraise its feasibility for geotechnical engineering applications.

Similarly, the technique using full waveforms was first tested on challenging 1-D and 2-D synthetic models, that include low- and high-velocity layers, to verify its capability of dealing with reverse profiles, and then applied to real test data. The inverted results from the real test data were also compared to SPT, crosshole test, and refraction test results for partially appraising the accuracy of those inverted results.

Finally, a laboratory testing program was conducted on rock cores obtained from the Newberry test site that assesses the relationships between geophysical measurement results such as P-wave velocity and dynamic elastic modulus to geotechnical engineering design parameters, including unconfined compression strength and static elastic modulus.

1.4 Organization of Report

An overview of the report is as follows. Chapter two provides an overview of site characterization methods using seismic waves, limitations of these standard methods, and suggested improvements.

Chapter three presents a global inversion technique to invert travel times using simulated annealing. The technique is described in detail, including forward modeling, optimization method, and its applications to synthetic and real test data sets. In this chapter, only travel times measured on the surface are used for inversion, and inverted results are compared to invasive test results to appraise the capability of the inversion technique.

Chapter four demonstrates the coupling of so-called downhole and refraction tomography techniques, which use combined borehole and surface travel times. Comparisons of inversion results utilizing the combined data against results developed using just the surface data are presented to both quantitatively and qualitatively appraise the benefit when adding data from a borehole. The focus here is to detect voids in rock that may be filled by air, water or soil.

Chapter five presents another inversion technique to invert full waveforms using simulated annealing. This technique is also described in detail, including forward modeling, optimization method, and its applications to synthetic and real test data sets. The primary applications of this technique are for reverse profiles when the borehole data is not available.

Chapter six presents the geotechnical engineering parameter relationships developed from the laboratory test results on rock cores obtained from the Newberry test site.

Finally, based upon the information presented in Chapters two through six, a summary of the study, a listing of the findings and conclusions, and recommendations for site characterization in Florida is presented in Chapter seven.

CHAPTER 2
SITE CHARACTERIZATION METHODS USING SEISMIC WAVES

2.1 Seismic Waves

A wave is a perturbation that travels in a medium and carries energy (Doyle, 1995). Waves that propagate in a medium can be divided into two categories: body waves and surface waves, whose particle motions are presented in Figure 2-1. Body waves that propagate in the interior of a medium include longitudinal waves (P-wave) and shear waves (S-wave). P-waves generate compression or dilatational particle motions parallel to the direction of propagation, and S-waves generate particle motions perpendicular to the direction of propagation. Unlike body waves, surface waves only propagate in a shallow zone near a free surface. They are essentially of two different kinds: Love waves and Rayleigh waves. Love waves only exist when a medium consists of a soft, superficial zone over a stiffer zone, and the particle motions associated with them are transversal with respect to the direction of propagation. Rayleigh waves always exist near a free surface, and their particle motions consist of vertical and horizontal components that are 90^0 out of phase, and thus the particle motion path is an ellipse.

Many techniques for soil characterization at very small strain levels are based on measurement of particle motions associated to wave propagation. This is made possible because of strong links between wave propagation characteristics and mechanical properties of the medium that is to be characterized. These links are between wave velocities and elastic moduli:

$$G \equiv \mu = \rho V_S^{\,2} \tag{2-1}$$

$$\lambda = \rho(V_P^{\,2} - 2V_S^{\,2}) \tag{2-2}$$

$$E = \frac{\mu(3\lambda + 2\mu)}{\lambda + \mu} \tag{2-3}$$

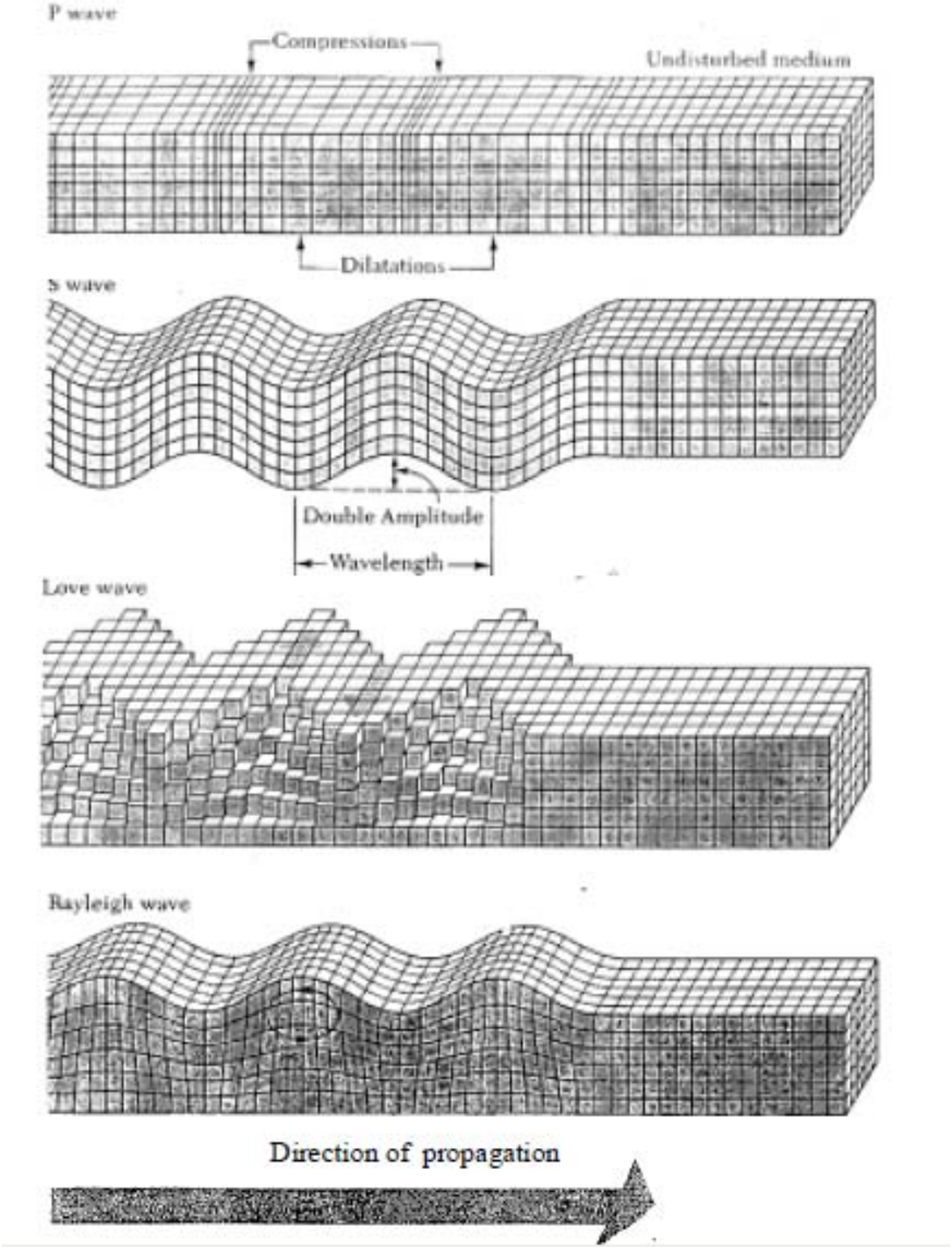

Figure 2-1. Particle motions associated with body waves and surface waves (from Bolt, 1976)

where V_P and V_S are P-wave and S-wave velocities, μ and λ are Lame's parameters, G and E are shear and Young's moduli, and ρ is mass density.

2.2 Site Characterization Methods Using Seismic Waves

2.2.1 Goals of Seismic Wave Methods

The primary goal of site characterization methods using seismic waves is to determine the elastic modulus of subsurface materials. The modulus is used either directly in design of engineering structures, or as an indication to delineate anomalies such as voids and low-velocity zones embedded in the subsurface profile.

2.2.2 Borehole Methods

Borehole methods include seismic downhole and crosshole methods (Figure 2-2). Downhole tests can be performed in a single borehole. In the downhole test, an impulsive source is located on the surface, and a single receiver that can move, or a string of receivers are fixed to the walls of the borehole to measure the wave fields from the source. A plot of travel time versus depth is generated, and the slope of the travel time curve represents the wave velocity at depth for a 1-D soil profile.

Crosshole tests use two (or three) boreholes. A source and one (or two) receiver are located at the same depth in the boreholes, and the wave velocity of the material between the boreholes at that depth is measured. By testing at various depths, a 1-D velocity profile is obtained.

The borehole methods can be used to obtain credible 1-D velocity profiles. However, these methods are not as popular as surface methods because of the requirement of boreholes, and due to the need for more complicated equipment for making the measurements.

2.2.3 Surface Methods

Surface methods are attractive because the measurements on the surface are relatively easy, and the measured signals carry important information about the mechanical properties of

a)

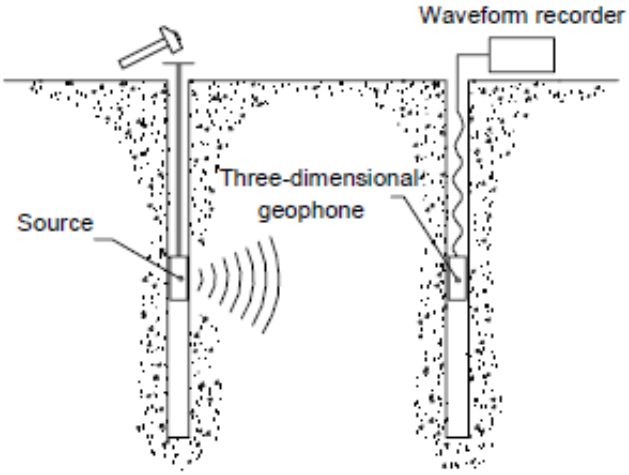

b)

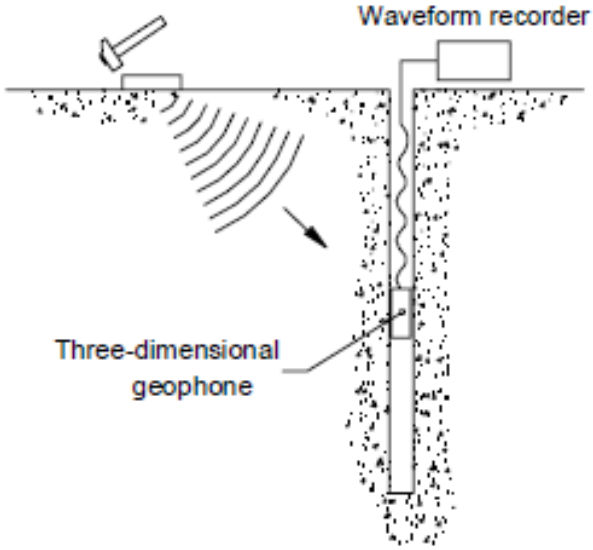

Figure 2-2. Borehole methods: a) crosshole test and b) downhole test (from Foti, 2000)

the medium. These methods have been intensively developed and routinely used for geotechnical site characterization in the last few decades. They are roughly categorized into two groups: methods using travel times, and methods using wave velocity dispersion.

2.2.3.1 Methods using surface travel times

Methods using surface travel times are often referred to as seismic refraction methods, including conventional methods and seismic refraction tomography (SRT). The seismic refraction methods consist of measuring data at a test site, picking travel times from the measured data, and doing inversion to invert the travel times for a subsurface wave velocity profile. Figure 2-3 presents a test setup, picked travel times, and inverted velocity tomogram of a typical seismic refraction tomography.

A measurement is conducted at known points along the surface to obtain a seismic wave field generated by an energy source. The energy source is usually a small explosive charge or accelerated weight drop, such as a sledgehammer. Energy that propagates out from the source either travels directly through the upper layer, known as a direct arrival, or travels down to and laterally along a lower high-velocity layer, known as a refracted arrival. This energy is detected on the surface using receivers arranged in a linear array, and travel times are derived by manually picking the first-arrival signals. The travel times are then used in an inversion to generate a velocity profile of the subsurface along the length of the refraction profile, relying upon the assumption that the velocity of the subsurface material increases with depth.

During inversion, while the conventional methods divide the model into continuous layers of constant velocity, SRT divides the model into a large number of smaller constant velocity grid cells or nodes. The model is adjusted during each iteration in an attempt to match the calculated

a)

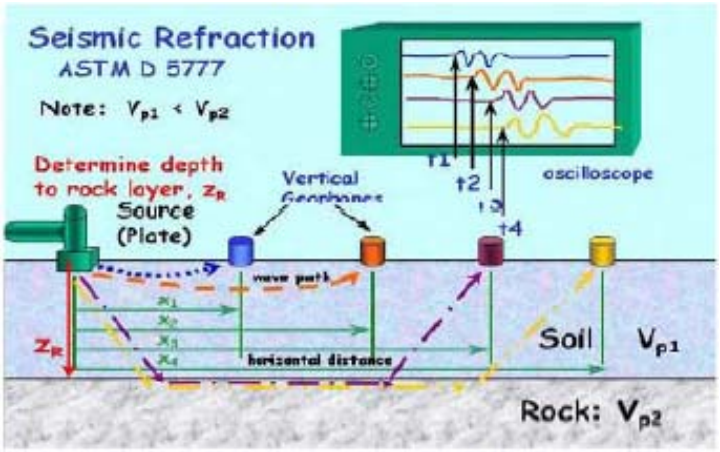

b)

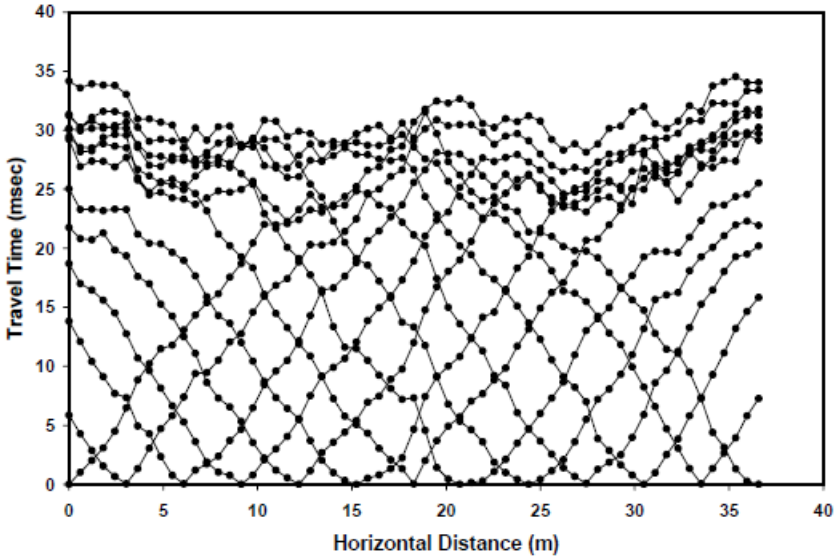

c)

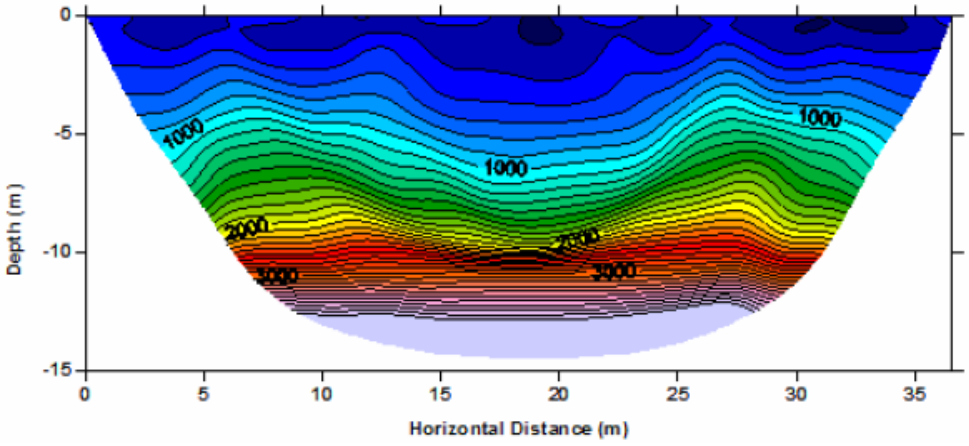

Figure 2-3. Seismic refraction tomography: a) test setup, b) travel times, and c) inverted velocity tomogram

travel times with the measured as closely as possible. This is repeated until a pre-defined stop criterion is achieved, and the inverted profile is then derived.

2.2.3.2 Methods using surface wave dispersion

Two popular methods using the dispersion property of measured wave fields are spectral analysis of surface waves (SASW) (Nazarian, 1984), and multi-channel analysis of surface waves (MASW) (Park et al., 1999). They both consist of three steps: measuring data from a test site, processing the measured data to obtain a dispersion curve, and inverting the dispersion curve for a subsurface shear wave velocity profile. Figure 2-4 presents a test setup, a typical dispersion curve, and an inverted velocity profile of SASW. For MASW, multiple receivers are used instead of two; dispersion data and inverted velocity profiles are similar to those of SASW.

For the first step, a wave field from an active source is measured by two receivers (SASW) or multiple receivers (MASW). The receivers are located far enough from the source to obtain dominant components of Rayleigh waves in the measured wave field. For the second step, a cross power spectrum analysis (SASW), or a multi-channel data processing method (MASW), is applied to the measured wave field to obtain the dispersion property. The measured wave field is here decomposed into components of different frequencies, and the phase velocity of each component is calculated to establish a dispersion curve that is used as experimental data for an inversion in the last step.

Inversion of the dispersion curve is a process for determining a shear wave velocity profile from the frequency-phase velocity relationship. This process consists of evaluation of a theoretical dispersion curve for an assumed profile, and comparison with the experimental dispersion curve. When the theoretical and the experimental dispersion curves match, the assumed profile is the desired solution. The assumed profile is typically composed of horizontal layers that are homogeneous, isotropic, and the shear velocity in each layer is constant.

a)

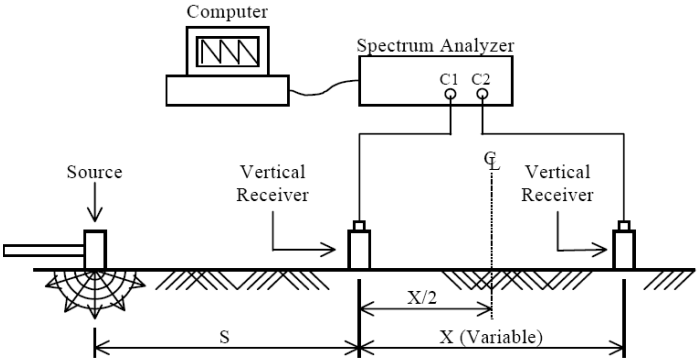

b)

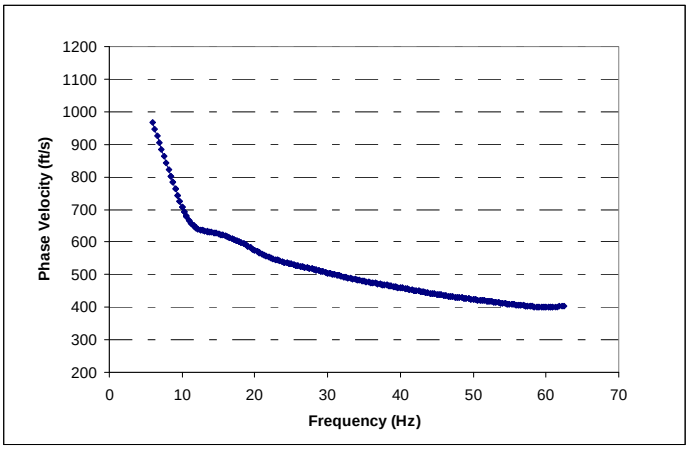

c)

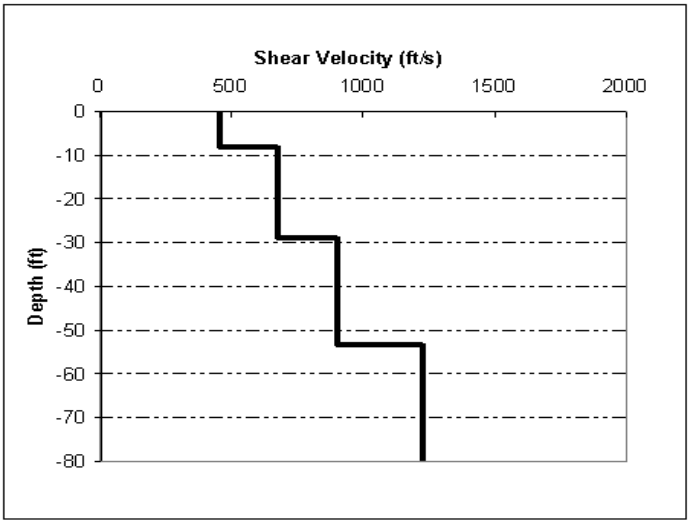

Figure 2-4. SASW: a) test setup, b) dispersion data, and c) inverted velocity profile

The theoretical dispersion curve calculation is often based on the matrix formulation of wave propagation in layered media given by Thomson (1950).

Besides methods using the dispersion property of active wave fields, there are also methods using the dispersion property of passive wave fields. These include the refraction microtremor method (ReMi) (Louie, 2001), and the passive-source frequency-wavenumber (f-k) method. Passive methods also require three steps as those in active methods. First, a wave field that is generated via ambient vibrations is measured by a linear receiver array (ReMi), or a two-dimensional receiver array (f-k). Second, a signal processing method, which is a slowness-frequency transformation (ReMi), or frequency-wavenumber transformation (f-k), is applied to the measured signal to obtain an experimental dispersion curve. Lastly, an inversion technique, which is exactly the same as that of active methods, is used to invert the experimental dispersion curve for a subsurface shear wave velocity profile.

2.3 Overview of the Surface Methods

2.3.1 Methods Using Surface Travel Times

Conventional refraction methods are useful for a simple profile consisting of a few constant velocity layers with linear interfaces (Sheehan et al., 2005). In this case of sharp contrasts in velocity at the interfaces, the conventional method is more suitable than SRT for two reasons. First, SRT will always model a sharp contrast in velocity with a gradient in velocity. Second, SRT requires that more shots and receivers be used than conventional techniques. This increase in field data collected significantly increases the amount of time necessary to perform the field testing. The time required to process this data, i.e., make first- arrival picks, and the time required for inversion is also significantly increased.

Seismic refraction tomography is able to resolve velocity gradients and lateral velocity changes within the subsurface with greater ability than conventional methods. As such, SRT

may be applied in settings where conventional refraction methods fail, such as areas of compaction, karst, and zone faults (Zhang and Toksoz, 1998).

Carpenter et al. (2003) used SRT programs on sites known to be karstic in Illinois and Kentucky to determine their accuracy by comparing with known subsurface geology from outcrops, borehole logs, other geophysical methods, and synthetic travel time data. The tomograms seemed to indicate consistency with known geology and borehole information. However, the authors mention problems with artifacts appearing, such as pinnacles or cutters in the lower third of the model when too many velocity elements are used. These artifacts may be due to the insensitivity of the surface measured travel times to the deep and small velocity elements. These small elements can be assigned any velocity without changing the surface travel times, thus the artifacts are created as a product of inversion.

Sheehan et al. (2005) investigated the ability of SRT programs for karst terrains that frequently contain sinkholes, irregular and gradational bedrock interfaces, and voids in rocks that may be filled by air, water or soil. They found that SRT performs well in many situations where conventional methods fail, e.g., where vertical and lateral gradients compose a significant component of the velocity structure. However, SRT fails to detect embedded cavities. The surface travel times are not sensitive to the embedded cavities, and these cavities are hardly detected by surface-based SRT methods.

Hiltunen and Cramer (2008) used SRT to characterize the subsurface at Pennsylvania bridge sites in mantled karst terrain. Refraction profiles generated by the commercial software SeisImager were compared with pile tip elevations at driving refusal and drilling data. They found that SRT appears to be able to characterize the soil/rock interface. However, in one example, there exists a zone where pile tip elevations are much deeper than the soil/rock

interface depth from SRT. This discrepancy is due to the presence of a low-velocity zone, which SRT fails to detect by just using the surface measurements. The failure to detect the low-velocity zone can be explained as follows. The inversion technique of SeisImager is a deterministic method that depends on an initial model, which has velocity increasing with depth. During the inversion, travel times and ray paths of each assumed model are calculated, and only cells containing ray paths are updated. It is likely that no ray paths go through the area where the low-velocity zone supposes to be, and thus this area is not frequently updated, and has the velocity similar to that of the initial model.

2.3.2 Methods Using Surface Wave Dispersion

For active surface wave methods, SASW and MASW have become very popular in recent years for shallow nondestructive testing of both layered natural (soil and rock) and artificial (pavement and concrete) structures. They typically perform well on normal profiles that have velocity increasing with depth. However, for reverse profiles consisting of both high-velocity and low-velocity layers, these methods need to be used with particular care.

O'Neill (2003) intensively investigated inversion using surface wave dispersion of multiple modes on a variety of models. He found that the most difficult parameters to accurately interpret with surface wave dispersion are layers below a high-velocity layer (HVL), and a deep (a few meters) buried low-velocity layer (LVL) with a thickness of a few meters cannot be inverted with confidence. He also found that for a case of real data from a well characterized test site, a 5 m thick stiff silt-sand layer at 20 m depth, in a mostly soft, clay background cannot be interpreted with any surface wave dispersion method, due to loss of sensitivity with depth. The main reason behind these limitations is that the surface wave dispersion is not very sensitive to thin (relatively to depth) embedded LVL or HVL.

Jin et al. (2009) studied the role of forward model in surface-wave inversion to delineate a HVL of 1.5-m thickness, 2-m depth, and 1500 m/s shear velocity (V_s). They found that the HVL can be detected by an inversion technique consisting of simulated annealing, followed by a linearized inversion, using only the fundamental mode. However, even though using simulated annealing to search over a large parameter space at the beginning of inversion, it still requires relatively strict constraints for the HVL, such as thickness, 0 to 2 m; depth, 1 to 5 m; V_s, 1000 to 2000 m/s. This means thet strictly a priori information about the HVL is needed to delineate it, and the technique would fail if the a priori information is not available.

For passive surface wave methods, ReMi and f-k methods have been routinely used recently for deep shear wave velocity profiles. The most important advantage of testing methods using passive energy is the ability to obtain deep depths of investigation with very little field effort. Rayleigh waves from passive seismic arrivals are relatively pure plane waves at low frequencies, allow determining V_s profiles down to large depths.

Li (2008) applied ReMi and f-k methods on real data sets measured from eleven test sites distributed over a distance of about 180 km in the upper Mississippi Embayment in the central United States to obtain V_s profiles down to depths of several hundred meters. The V_s profiles are compared to those from SASW and MASW, which used a newly developed low-frequency vibrator to generate wave fields at very low frequencies down to 1 Hz. He found that the active surface wave methods are more reliable than passive wave methods for deep V_s profiling.

2.4 Limitations of the Standard Methods Using Seismic Waves

As reviewed in section 2.3, the limitations of the standard methods using seismic waves are generally caused by insensitivity of data used for inversion, and the shortcomings of local inversion techniques.

2.4.1 Limitations due to Insensitivity of Data

The standard seismic wave methods use either surface travel times or surface wave dispersion to interpret subsurface velocity structures. The travel time from a shot to a receiver on the surface is measured from the fastest ray that starts from the shot, and travels through a medium to the receiver. This fastest ray tends to go through stiffer material (high velocity zones), and avoids softer material (low-velocity zones). Thus, the surface travel times are not sensitive to these low-velocity zones, and consequently these zones cannot be well characterized with only surface travel times.

Surface wave dispersion data is more sensitive to a low-velocity layer than surface travel times. However, the dispersion property is developed by taking account of the entire material within a depth of approximately one wavelength from the surface for each frequency, and is more sensitive to a shallow, stiff layer than to a deep, soft layer. When the depth of investigation increases, lower frequency or longer wavelength components are required, larger volumes of material are utilized to derive the dispersion property, and the dispersion data becomes insensitive to a deep and thin low-velocity layer. Hence, the low-velocity layer is hardly detected by using only the surface wave dispersion. In addition, the dispersion property is insensitive to lateral variation, thus techniques using wave dispersion are only for 1-D problems, and cannot be applied in regions with high lateral variation.

2.4.2 Limitations due to Local Inversion Techniques

The main goal of inversion is to find earth models that explain the seismic observations. The inversion involves finding an optimal value of a misfit function of several variables. The misfit function characterizes the differences between the observed data and synthetic data calculated by using an assumed earth model. The earth model is described by physical

parameters that characterize properties of soil/rock layers, such as compression and shear wave velocities, mass density, etc.

For many geotechnical applications, the misfit function is highly complicated, and its surface consists of multiple hills and valleys. Thus, such a function will have many maxima and minima; the minimum of all the minima is called the global minimum, and all other minima are called the local minima. Local inversion techniques, such as gradient descent methods, typically are able to find a minimum in the close neighborhood of the starting solution. They use the local properties of the misfit function (gradients) to calculate the update to the current position, and search in the downhill direction that only accepts a model having a smaller misfit value. Thus, these techniques can miss the global minimum if the starting solution is nearer to one of the local minima than the global minimum.

2.5 Suggested Improvements

2.5.1 Improvements by Using Sensitive Data

The capability of the seismic wave methods can be significantly improved by using more sensitive data for inversion. The target of this research was to develop techniques that can characterize anomalies such as low-velocity layers, and voids in rocks that may be filled by air, water, or soil. For this purpose, combined travel times measured both on the surface and in a borehole are utilized to obtain higher-resolution inverted profiles. In addition, full waveforms are employed to characterize reverse profiles when the borehole data is not available. The full waveform has been used by researchers for deep (> 1 km) subsurface investigation, in both time domain (Shipp and Singh, 2002; Sheen et al., 2006) and frequency domain investigations (Pratt, 1999). In all of these applications, body waves are dominant components in wave fields used for inversion. This research uses Rayleigh waves as dominant components in wave fields. Since Rayleigh waves are more sensitive to shear wave velocity, and less sensitive to Poisson's ratio or

mass density of a medium, they are useful for geotechnical applications where the shear wave velocity primarily controls properties of soil particles.

2.5.2 Improvements by Employing Global Inversion Techniques

The capability of the seismic wave methods are also improved by employing global inversion techniques. Although these techniques require much more computer time than local techniques, they are feasible for geotechnical engineering problems with the advent of fast computers.

Unlike local inversion techniques, global inversion techniques such as simulated annealing, genetic algorithm, and other importance sampling approaches attempt to find the global minimum of the misfit function by searching over a large parameter space. They have recently been applied in evaluation of various geophysical data sets (Sen and Stoffa, 1991, 1995; Pullammanappallil and Louie, 1994; Sharma and Kaikkonen, 1998). Most of the global inversion techniques are stochastic, and use more global information to update the current position, thus, they are more likely to converge to the global minimum. In this study, simulated annealing was employed for inversion problems in geotechnical engineering because it can be used in cases where the model-data relationship is highly nonlinear, and produces multimodal misfit functions (Sambridge and Mosegaard, 2000).

CHAPTER 3
INVERSION OF FIRST-ARRIVAL TIMES USING SIMULATED ANNEALING

3.1 Introduction

A geophysical means of characterizing the material to contain and surround a drilled shaft foundation could be conducted using a cross borehole tomography technique similar in concept to crosshole sonic logging (CSL) used to characterize drilled shafts. Here, data would be collected by "shooting" across pairs of boreholes at frequent intervals of depth, and then constructing a 3-D volumetric image of the zone of interest. As with CSL, a minimum of 3-4 boreholes would be required to develop an image. While this approach certainly has merit, it may be too costly in that multiple boreholes would be required.

In this and the following chapters, the coupling of so-called downhole and refraction tomography techniques is presented as an alternative geophysical method, which uses only one borehole. Here a string of sensors is placed both horizontally along the ground surface, and down a single borehole. The borehole sensors could be contained within another apparatus like a CPT or rock shear device. With the sensors so located, energy is created and propagated from the ground surface, and then detected via the sensor strings. The combined travel times are derived by picking first-arrival signals and then 2-D or 3-D velocity structure is obtained by inverting the measured data.

Refraction tomography using combined data can be utilized for site characterization of deep foundation design. It can provide important physical parameters of material at a rock socket that often carries a majority of load from deep foundations. The inversion results of the combined data enable characterization of spatial variability in geotechnical engineering physical parameters of subsurface formations useful in the design of deep foundations. This could be particularly useful in implementing the new LRFD design methodology that can explicitly

account for spatial variability in design parameters. The refraction tomography using the combined data will improve the accuracy and reliability of engineering parameters determined for design of deep foundations, and will increase the volume of material actually evaluated in a subsurface investigation. The improved characterization will lower uncertainty and risk, and reduce overall cost of subsurface construction.

To begin, this chapter presents a general inversion technique to invert first-arrival time collected from a ground surface array using simulated annealing. The scheme is based on an extremely fast finite-difference solution of the Eikonal equation to compute the first-arrival time through the velocity models by the multistencils fast marching method. The core of the simulated annealing, the Metropolis sampler, is applied in cascade with respect to shots to significantly reduce computer time. In addition, simulated annealing provides a suite of final models clustering around the global solution, and having comparable least-squared error, to allow determining uncertainties associated with inversion results.

The most important advantage of global inversion techniques is to avoid being trapped in local minima, and thus to allow final inversion results to be independent of the initial model. However, these global inversion techniques can require significant computer time, especially if the model contains a large number of model parameters. This disadvantage is reduced herein by using an extremely fast forwarding model solution, and by sampling in cascade with respect to shot position. First-arrival time inversions usually require many shots to obtain a high-resolution profile, and each shot needs a forwarding model solution. Meanwhile, global optimization methods sample over a large number of trial models, and only accept a small number of them. Using an acceptance rule in cascade, forward model solutions for only a few shots are often

required to reject the biased models. For the cases presented herein, a saving in computer time of 70% is achieved when utilizing the acceptance rule in cascade.

The technique is presented herein for surface-based synthetic data sets created from models that were previously tested on three commercial refraction tomography codes by Sheehan et al. (2005), and two experimental data sets from a well documented test site. The inversion results show that this technique successfully maps 2-D velocity profiles with high variation. The inverted wave velocity from the real data appears to be consistent with cone penetration test (CPT), geotechnical borings, and standard penetration test (SPT) results.

3.2 Methodology

3.2.1 Forward Modeling

Two main approaches that have been routinely used to calculate first-arrival times are the shortest path method (SPM), and the Eikonal equation solution. SPM originated in network theory (Dijkstra, 1959), and was applied by Nakanishi and Yamaguchi (1986) and Moser (1991) to seismic ray tracing. The main advantage of SPM is its simplicity, and capacity for simultaneous calculation of both the first-arrival time and the associated ray path, but it takes more time for calculation, and is not very efficient to use for the global optimization methods. The Eikonal equation shown below has been solved by many authors, including (Vidale, 1988; Van Trier and Symes, 1991; Nichols, 1996; Sethian, 1996, 1999; Kim, 1999; Chopp, 2001; Hassouna and Farag, 2007).

$$\left(\frac{\partial u}{\partial x}\right)^2 + \left(\frac{\partial u}{\partial z}\right)^2 = \frac{1}{V(x,z)^2} \tag{3.1}$$

In this equation, u=u(x,z) and V(x,z) are the arrival time and velocity at point (x,z), respectively. Among these methods, the fast marching method (FMM) is typically considered the fastest and most stable and consistent method for solution of the Eikonal equation. It was first presented by

Sethian (1996), and has been improved by other authors. In this study, the improved version of FMM by Hassouna and Farag (2007), the so called multistencils fast marching (MSFM), is utilized to compute first-arrival times for forward modeling. MSFM computes the solution at each point by solving the Eikonal equation along several stencils, and then picks the solution that satisfies the upwind condition.

3.2.2 Optimization Method

Simulated annealing (SA) was first proposed by Metropolis et al. (1953), and significantly improved by Kirkpatrick et al. (1983). SA is a probabilistic methodology for the global optimization problem, namely locating a good approximation to the global optimum of a given function in a large search space. The name and inspiration come from annealing in metallurgy, a technique involving heating and controlled cooling of a material to increase the size of its crystals and reduce their defects. The heat causes the atoms to become unstuck from their initial positions (a local minimum of the internal energy) and wander randomly through states of higher energy; the slow cooling gives them more chances of finding configurations with lower internal energy than the initial one. By analogy with this physical process, each step of the SA algorithm replaces the current solution by a random "nearby" solution, chosen with a probability that depends both on the difference between the corresponding function values and also on a global parameter T (called the temperature), that is gradually decreased during the process. The dependency is such that the current solution changes almost randomly when T is large, but increasingly "downhill" as T goes to zero. The allowance for "uphill" moves saves the method from becoming stuck at local optima. The analogy of simulated annealing has also been well described by Sen and Stoffa (1995) for problems in geophysics, and a brief description of the process used in this study is presented in the following:

1. Select an initial velocity model V, and then calculate the least-squared error E_i, for the *ith* shot, and average error E_{mean}, as:

$$E_i = \frac{1}{N}\sum_{k=1}^{N}\left[d_{k,i} - g_{k,i}(V)\right]^2 , \tag{3.2}$$

$$E_{mean} = \frac{1}{M}\sum_{i=1}^{M} E_i , \tag{3.3}$$

where $d_{k,i}$ and $g_{k,i}$ are the *kth* observed and computed travel times from the *ith* shot, respectively, N is the number of observation points, and M is the number of shots.

2. Following the idea of Pullammanappallil and Louie (1994), perturb the velocity model by randomly selecting a box within the medium, and randomly assign all of the cells within the box a new velocity between the minimum and maximum velocities chosen by the user. Next, to avoid unusual artifacts and high velocity gradients that would violate the assumption of an Eikonal equation solution, the model is smoothened. The smoothing is accomplished by adjusting the velocity of each cell in contact with and just outside the boundary of the box. The adjusted velocity for each of these perimeter cells is established by averaging the velocities of the four cells in contact with the four edges of the perimeter cell. Following the process described, a new model is now obtained.

3. Apply the acceptance rule in cascade with respect to shots for the new model. The travel times from one shot at a time are used to test the new model. For the *ith* shot, the least-squared error E_i corresponding to the new model is calculated as equation (2). The new model unconditionally passes the *ith* shot if its least-squared error is smaller than that from the previous model, and conditionally passes the *ith* shot if its least-squared error is bigger with the following probability:

$$p_i = \exp\left(-\frac{\Delta E_i}{T}\right), \tag{3.4}$$

where ΔE_i is the positive difference between the least-squared errors of the two models. If the new model passes the first shot, then it is tested for the second shot and so on. It is immediately rejected if failing at a certain shot, i.e., the new model is only accepted if it passes all of the shots.

4. Repeat steps 2 and 3 until a desired number of accepted models are completed, then reduce the temperature to the next level according to a schedule:

$$T(k) = \frac{T(k-1)}{2} , \tag{3.5}$$

where *T(k)* and *T(k-1)* are the temperatures at the *kth* level and the *(k-1)th* level.

The criterion for convergence requires that the relative difference between the maximum and minimum average errors E_{mean} from all accepted models at a particular temperature become very small (empirically say between 0.1% and 0.5%). If the criterion for convergence is not

satisfied, the temperature is reduced to the next level. At a sufficiently low temperature, the accepted models are in the vicinity of the global minimum and the optimization converges.

The selection of a correct initial temperature is very important. Selecting a high value leads to unnecessary computations, whereas starting from a low value can lead to a local solution. Based on the idea of Sharma and Kaikkonen (1998), and as implemented in this study, the initial temperature is taken to be the nearest lower power of ten to the least-squared error; for example, if the least-squared error is 50.59, then the initial value is 10. In this way, the initial temperature is usually higher than the critical temperature, and any bias created by the initial model will be destroyed.

The cooling schedule is another important parameter in the global optimization. Many schedules have been investigated for inversion problems up to 1500 cells, and it has been found that the number of accepted models at each temperature should be at least 10,000, and the temperature needs to reach a very low value to obtain the global solution. In the studied cases, the final temperature was about 10^{-3} to 10^{-4} when the initial temperature was 10. When the number of cells increases, the procedure needs a slower schedule, i.e., more accepted models at each temperature or a smaller change in temperature, and hence the time of computation increases to obtain a global solution. Thus, the cooling schedule must be selected with care.

3.3 Applications

3.3.1 Applications on Synthetic Data

Synthetic models refer to earth models whose velocity profile is assumed or known a priori. Using a known velocity structure, travel time data is calculated for an assumed test layout. This travel time data is then input to the inversion program as if it were data collected from a field test, and velocity structure is calculated from travel time data. Theoretically, the interpreted velocity profile should be the same as the model assumed at the start.

Synthetic model studies were conducted for at least two reasons. The first objective was to assess ability of the inversion technique to identify and delineate subsurface features that are routinely present in test sites. It was important to determine prior to actual field testing whether the system is sensitive to these features, otherwise there was no point in conducting an actual field test. Second, in conducting model studies in which the "answer" is known, an analysis protocol can be developed to systematically and consistently analyze travel time data to develop believable velocity tomograms. In order to be confident of results interpreted from actual field data, one has to develop confidence that the program and analysis procedures are reputable. Synthetic model studies help build this confidence since interpreted velocity profiles can be compared to the known starting profile.

The technique presented was intensively tested on many synthetic models, and three of them with high lateral variation are presented herein in Figures 3-1 to 3-3. These three synthetic models (1, 2, and 3) are models 3, 5, and 6 from Sheehan et al. (2005), respectively. They include a notch (model 1), a stair step (model 2), and broad epikarst (model 3). For all three models, 25 shots into 48 geophones were used to create synthetic first-arrival times. The geophone spacing was 1 m for models 1 and 2, and 2 m for model 3. For all models, all 25 shots were within the geophone spread, and the shot spacing was twice the geophone spacing. With this arrangement, the number of shots, the number of geophones, and the geophone spacing are the same as those used in Sheehan et al. (2005).

To run the inversion, the medium sizes were kept the same as the true models, and discretized with a grid size of 1 m for ease in picking the first-arrival times from the forward modeling. The velocity constraints were assigned by slightly increasing the maximum true value, and decreasing the minimum true value. Thus, the velocity was allowed to vary between 100 m/s

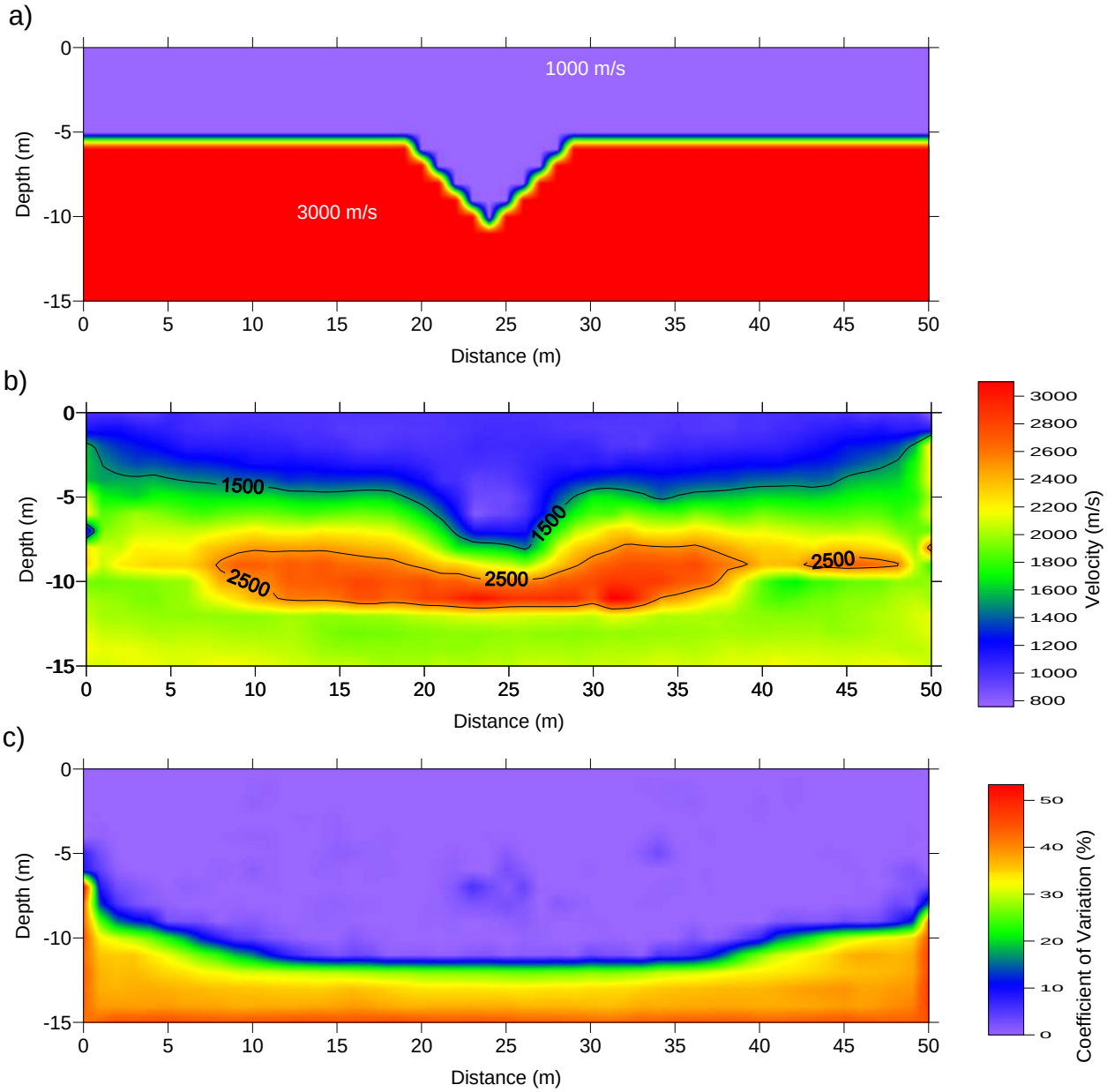

Figure 3-1. Synthetic model 1: a) true model, b) inverted model, and c) uncertainty associated with the inverted model

and 4000 m/s for models 1, and 2, and between 100 m/s and 5000 m/s for model 3. All initial models were specified with a constant velocity of 2000 m/s, which leads to an initial temperature of 10. Velocities of cells were then perturbed, models were updated, and temperature was reduced after each 10,000 accepted models until the criterion of convergence was satisfied. Because of the non-uniqueness of the inversion problem, and to further avoid unusual artifacts, in all three cases, 50,000 accepted models from the last five temperature levels, and that have least-squared errors within a few percent from the smallest error, are averaged to derive the final inverted model, and the associated uncertainty in the form of a coefficient of variation (COV).

First, consider the results for model 1 presented in Figure 3-1. A primary feature of refraction tomography is delineation of both vertical and horizontal changes in seismic wave velocity, e.g., detection of anomalies. Here it is observed that the inversion is able to reasonably characterize the presence, location, and general shape of the notch. However, it is also observed that the inverted model is not identical to the true model. Most notably, as discussed by Sheehan et al. (2005) and others, refraction tomography will always model a sharp contrast in velocity with a gradient in velocity (this is usually a result of some method of smoothing of the velocity model such as utilized herein). This reality largely accounts for the differences in the two models. In addition, refraction tomography is not able to characterize zones of material outside of the ray coverage. Here is where the uncertainty results (Figure 3-1c) are helpful. The uncertainty is low in zones with good ray coverage, such as zones near the surface, and high in zones with poor ray coverage, such as zones near the bottom corners of the medium. In zones of high uncertainty, the inversion routine simply reports the velocity as the average value from all values randomly and uniformly withdrawn between the minimum and maximum velocity constraints selected by the user. Otherwise, in the zones of low uncertainty, the inverted velocity

is independent of the constraints, and thus more reliable. From these results, it appears that the delineation between low and high uncertainty is reasonably established at a COV value of approximately 20%. Finally, the result from the presented technique seems better than that shown in Sheehan et al. (2005) for commercial codes GeoCT-II, SeisImager, and Rayfract because the results from these codes all show a high velocity artifact under the notch, and the notch is not well detected.

Second, the results for model 2 are presented in Figure 3-2. Similar to model 1, the anomaly (stair step) is reasonably recovered for both the location and general shape. The primary difference between the true and inverted models is again due to the gradient. The gradient is mostly inserted at the interface between layers, and the interface can be interpreted from areas of maximum gradient in the inverted model, such as the contour line of 2000 m/s shown in Figure 3-2b. In addition, the result from the presented technique seems better than that from GeoCT-II, and similar to those from SeisImager and Rayfract.

Last, the results for model 3 are presented in Figure 3-3. It is observed that the inverted model is an excellent recovery of the true model. Both velocities and interfaces between layers are very well inverted. The result from the presented technique is consistent with that obtained from all three commercial codes.

3.3.2 Applications on Real Test Data

The University of North Florida (UNF) and the University of Florida (UF) have developed a Florida Department of Transportation (FDOT) dry retention pond into a karstic limestone geophysical/ground proving test site in Alachua County, Florida. The site contains a number of survey lines and five PVC-cased boreholes extending to approximately 15 m.

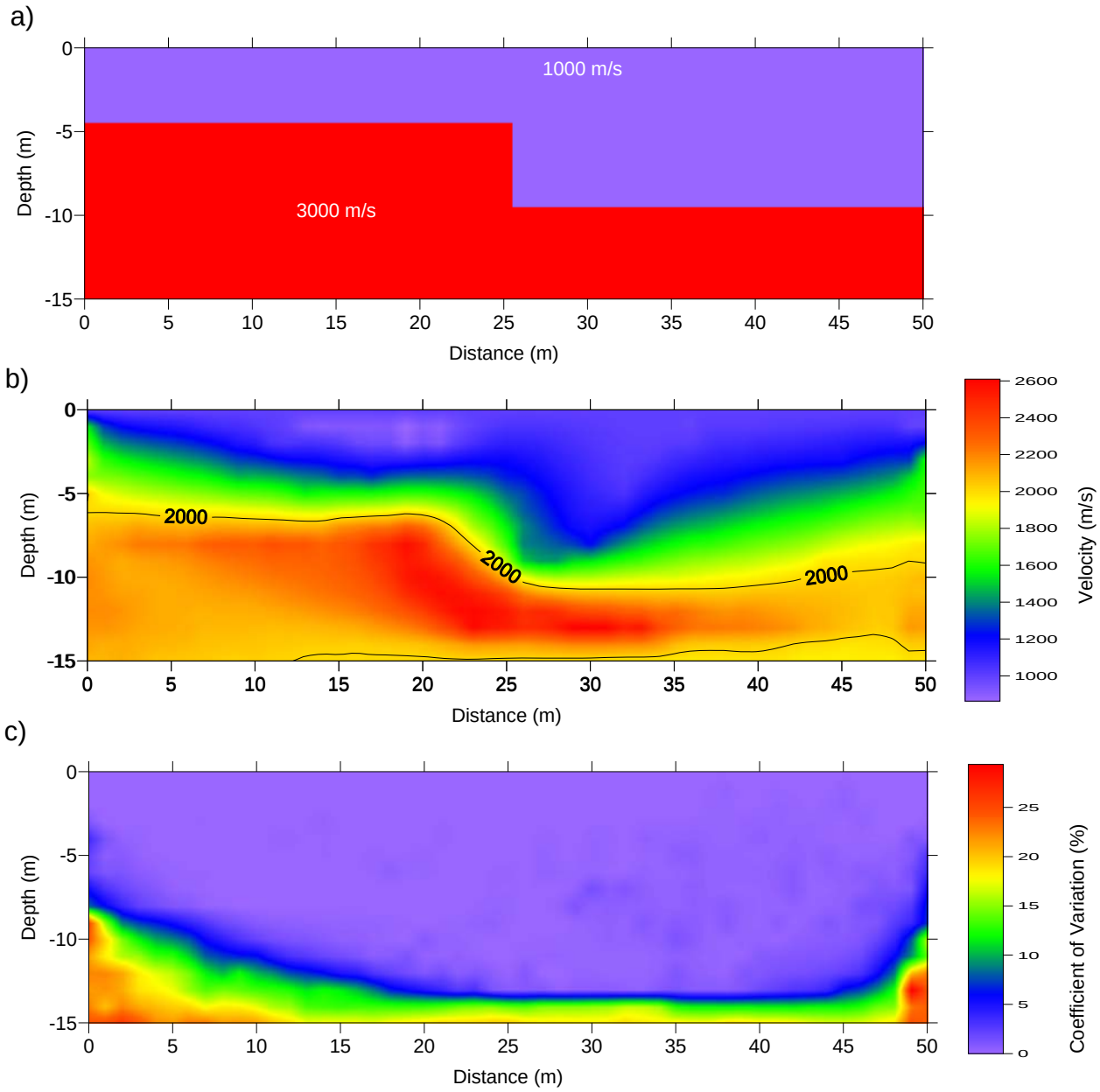

Figure 3-2. Synthetic model 2: a) true model, b) inverted model, and c) uncertainty associated with the inverted model

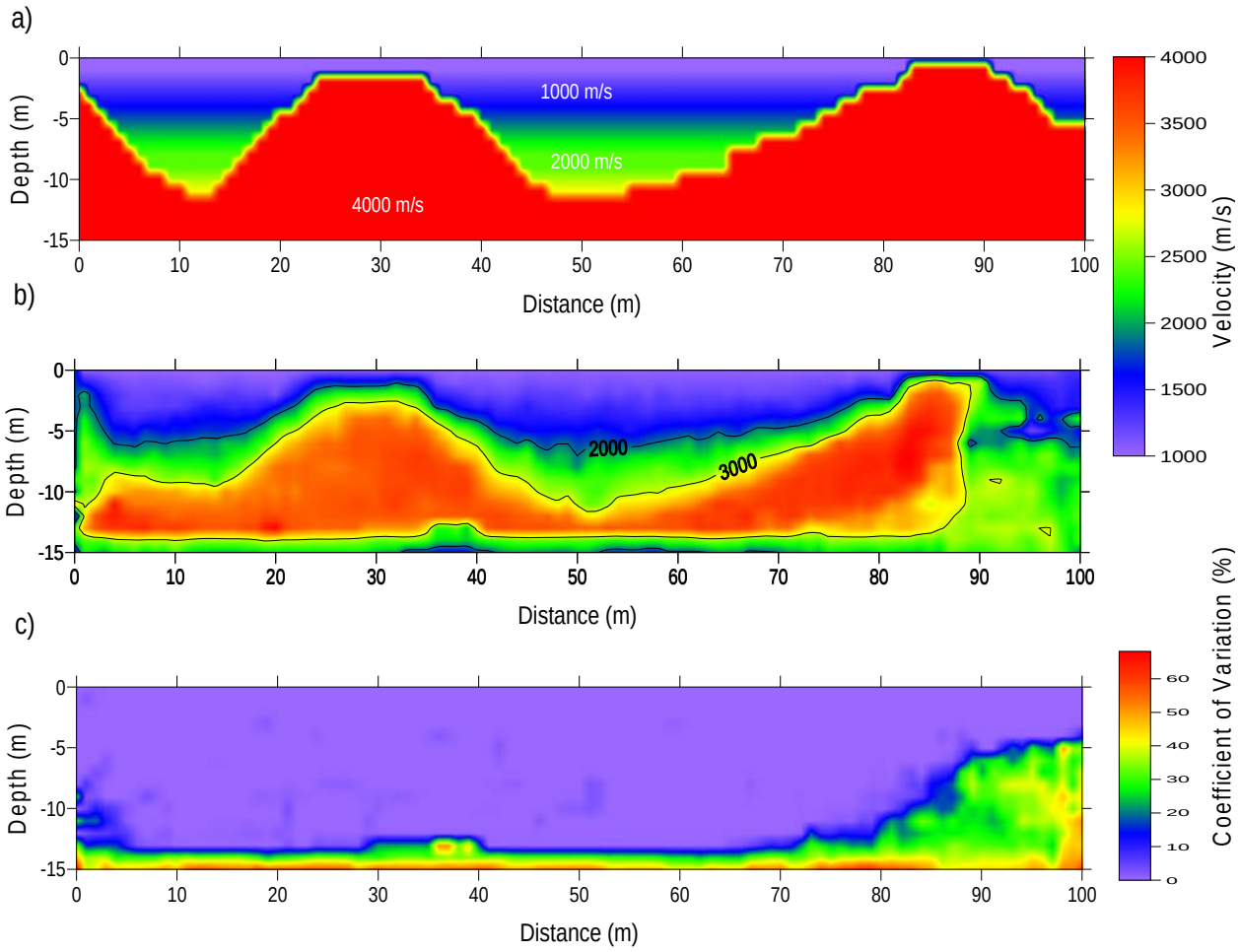

Figure 3-3. Synthetic model 3: a) true model, b) inverted model, and c) uncertainty associated with the inverted model

The geophysical/ground proving test site is located outside of Newberry, Florida on State Road 26 in Alachua County. The site is approximately 29 km from Gainesville, and approximately 150 km from Jacksonville. The test site is a dry retention pond, approximately 1.6 ha in size. The northern portion of the site has been susceptible to sinkhole formation, and a number of large sinkholes have formed and been repaired. However, the southern portion has been relatively free of sinkholes and is an ideal location for characterizing karst limestone sites. The southern portion of the test site was subdivided into 26 north-south survey lines equally spaced a distance of 3.0 m apart. The lines were labeled A through Z from west to east across

the site, and each line was 85.3 m long, with station 0 m located at the southern end of the site. Two 36.6-m long refraction tests were conducted end-to-end along lettered site lines A, F, K, P, U, and Z, and beginning at station 0. Thus, the 12 refraction tests covered six of the site lines from station 0 to 73.2 m.

Each 36.6-m long refraction test was conducted with 4.5 Hz vertical geophones spaced equally at 0.61 m, for a total of 61 measurements. Seismic energy was created by vertically striking a metal ground plate with an 89 N sledgehammer, thus producing compression wave (P-wave) first arrivals. Shot locations were spaced at 3.0-m intervals along the 36.6-m line and starting at 0 m, for a total of 13 shots. Since a 32-channel dynamic signal analyzer was used to collect time records, and each line required 61 measurements, each line was conducted in two stages. In stage one, 31 geophones were placed at 0.61-m intervals from station 0 m to station 18.3 m. In stage two, 31 geophones were placed at 0.61-m intervals from station 18.3 m to station 36.6 m. Since there was a designed overlap between the two stages at station 18.3 m, a total of 61 measurement locations were collected. For each stage, time records were collected at each of the 13 shot locations, and then the data were combined to produce a complete shot gather for the survey line from station 0 m to station 36.6 m. Data from gridline A is chosen to present herein because these data displayed the most variable condition along the line. The measured travel time is presented in Figures 3-4 and 3-5. Cone penetration tests (CPT), geotechnical borings, and standard penetration tests (SPT) were also conducted on gridline A for partially verifying the inverted P-wave tomograms.

To run the inversion, the velocity constraints and the medium depth need to be established. Even though the inversion technique does not require strict velocity constraints for convergence, required computer time can be reduced significantly if they are available. To save computer time,

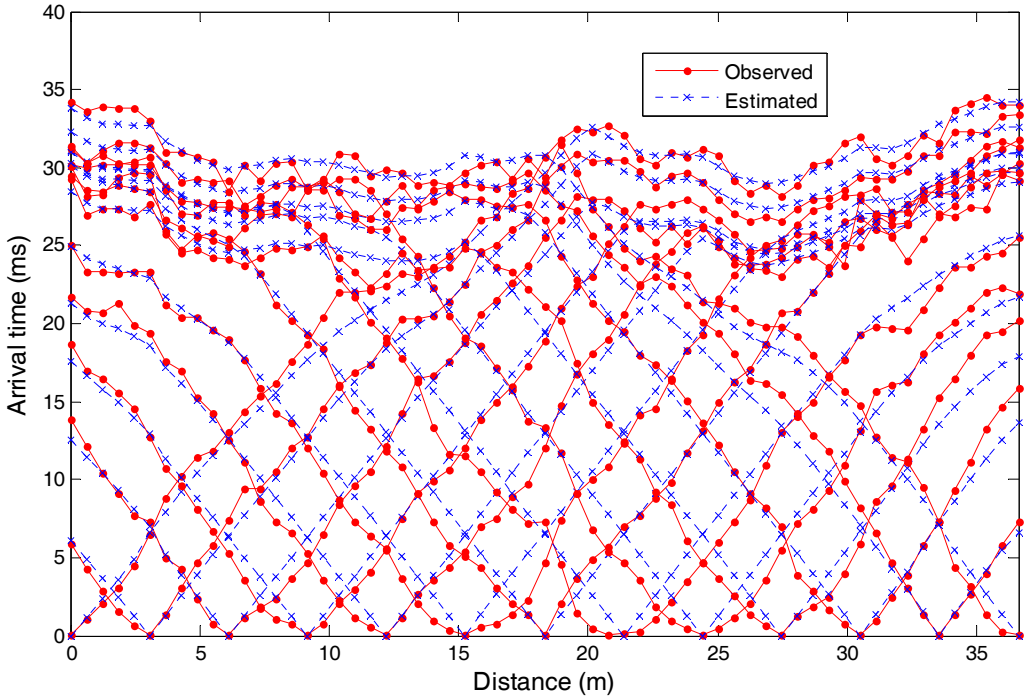

Figure 3-4. Comparison between the estimated and observed first-arrival time for the real data A_0-36.6

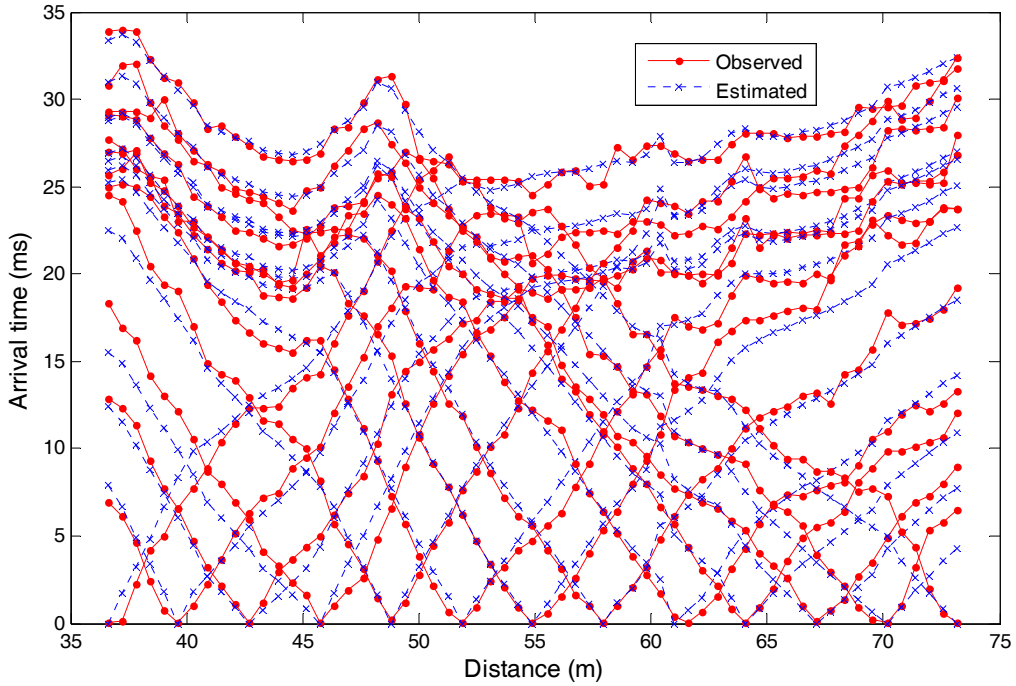

Figure 3-5. Comparison between the estimated and observed first-arrival time for the real data A_36.6-73.2

an estimate of the minimum and maximum layer velocities must be determined. For these estimates, results from a simple two-layer velocity profile determined via traditional refraction analysis procedures (Burger, 1992; Redpath, 1973) were employed. These simple velocity models were generated using travel time curves from only the two outside source locations (e.g.,0 and 36.6 m for data set A_0-36.6) of the refraction surveys. From the simple profile thus determined, the first layer velocity was used to determine the minimum velocity constraint, and the second layer velocity was used to determine the maximum velocity constraint. For both data sets presented herein, the minimum and maximum velocities were determined as 300 m/s and 3000 m/s, respectively.

It is very important to determine a reasonable medium depth to get credible inversion results. If one assigns a very large medium, new models will be easily accepted because models are highly perturbed at less sensitive zones, or zones outside of ray coverage, and the inversion may not well characterize the velocity structure. For cases without any a priori information, one can assign a large depth such as equal to the geophone spread, and run a trial inversion. This run with a large medium may not give a high resolution of velocity structure, but the uncertainty result will provide rational information about the depth of investigation. The delineation between low and high uncertainty zones can then be used to determine the depth of the medium for an improved inversion run. Alternatively, the depth of the medium can also be estimated from experience as 1/3 to 1/2 of the geophone spread. For both data sets presented herein, the depth of the medium was simply taken as 1/3 of the geophone spread.

In the inversion process, for convenience of calculating the first-arrival time in the forward modeling, the medium was discretized with a grid size equal to the geophone spacing of 0.61 m. The initial models were specified the same for both tests with a constant velocity of 1000 m/s,

and the initial average least-squared errors were 63.0082 ms^2 for data set A_0-36.6, and 30.1335 ms^2 for data set A_36.6-73.2, thus, the initial temperature was 10 for both. Velocities of cells were perturbed by randomly assigning values between the constraints, models were updated with the number of accepted models at each temperature level equal to 10,000, and the temperature was lowered until the criterion of convergence was reached at which the least-squared errors were 0.8652 ms^2 for data set A_0-36.6, and 0.8927 ms^2 for data set A_36.6-73. The criterion of convergence was not satisfied until the estimated first-arrival times from the final accepted model were very close to the observed travel times (shown in Figures 3-4 and 3-5). In order to reach the criterion of convergence, both inversion runs were required to test more than one million trial models, and each run took a few hours on a standard laptop computer.

Because of noise, subjective judgments in manually picking first-arrival times, and non-uniqueness of inverted solutions, there is no guarantee that the model corresponding to the smallest error is closest to the true model. Therefore, the inversion results should be derived from many accepted models clustering around the global minimum, and having similar errors, instead of from only one model that has the smallest error. As with the synthetic models, the last 50,000 accepted models were used to derive the final inversion results and the associated uncertainties.

Figures 3-6a and 3-7a present two-dimensional compression (P) wave refraction tomograms determined from test data collected along the surface. These tomograms indicate that the P-wave velocity at this site generally increases with depth, and that the specific pattern of increase depends on lateral location across the site. Figures 3-6b and 3-7b show the uncertainties associated with the inverted P-wave profiles. Again, the uncertainty is consistent with expectations: low uncertainty in zones with good ray coverage (near the surface), and high uncertainty in zones with poor ray coverage (near the bottom corners of the medium). With the

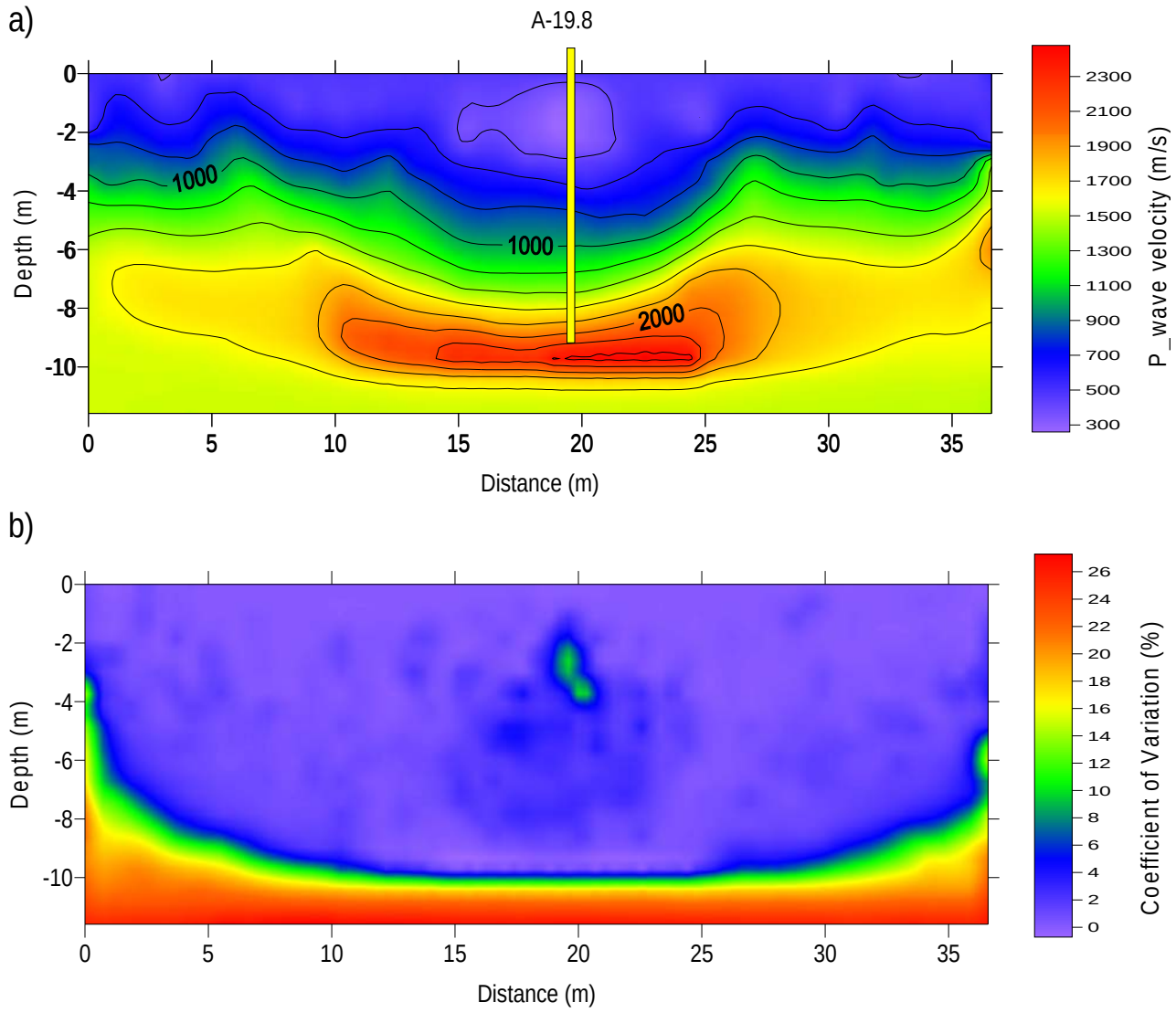

Figure 3-6. Inversion result for the real data A_0-36.6: a) inverted model, and b) uncertainty associated with the inverted model

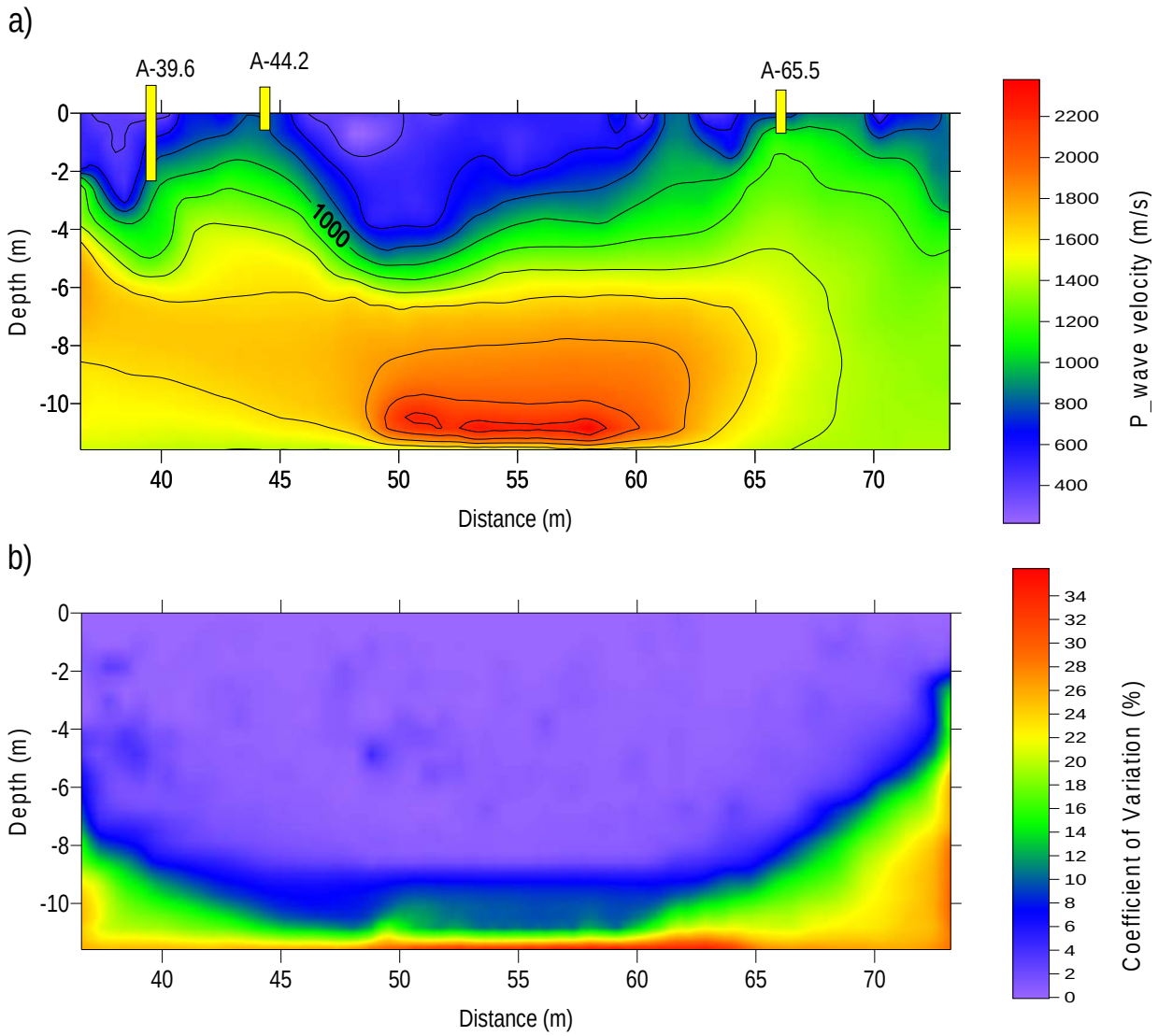

Figure 3-7. Inversion result for the real data A_36.6-73.2: a) inverted model, and b) uncertainty associated with the inverted model

confidence gained from running synthetic models, the depth of investigation is about 10 m at the middle of the model where the COV from the ground surface to that depth is less than 20%.

Following refraction data collection and analysis, invasive ground proving information was collected at the site to provide partial verification of the refraction test result interpretations, and these data are presented in the following paragraphs.

Cone Penetration Tests (CPT):

Ten CPT soundings were conducted at strategic locations across the site. Because line A displayed the most lateral variability along the line, four of the 10 soundings were conducted along line A. These four tests were located at the following horizontal stations: 19.8, 39.6, 44.2, and 65.5 m. The measured tip resistance results are shown in Figure 3-8, and the length of each test run is shown atop the tomograms in Figures 3-6a and 3-7a. These results are compared with the refraction tomograms from Figures 3-6a and 3-7a as follows:

- At station 19.8 m, the CPT tip resistance approached a large value of 30 MPa, and the test was terminated at a depth of about 9.2 m. Station 19.8 m is near the middle of a valley feature on the tomograms (Figure 3-6a), and the CPT tip terminates at a P-wave velocity of ±2000 m/s.

- The sounding at 39.6 m was terminated before the tip resistance approached a large value because the CPT rod system was bending seriously to the south as penetration was attempted. It is interesting to note on the tomograms (Figure 3-7a) that station 39.6 m is slightly to the left of a block/pinnacle feature, and bending of the CPT rod to the south at the site (to the left or lower station number on tomogram) is consistent with this block feature.

- At stations 44.2 and 65.5 m the tests were terminated at shallow depths less than 0.5 m because the CPT tip resistance approached a large value of 30 MPa. Stations 44.2 and 65.5 m are both located near the top of block/pinnacle features on the tomograms (Figure 3-7a). However, in contrast to station 19.8 m, the CPT tips terminated at P-wave velocities less than 1000 m/s at stations 44.2 and 65.5 m.

- It is reported that small, rock outcrops were visible near stations 62.5-64 m and 66.1-67.1 m, which are on both sides of the CPT sounding at 65.5 m.

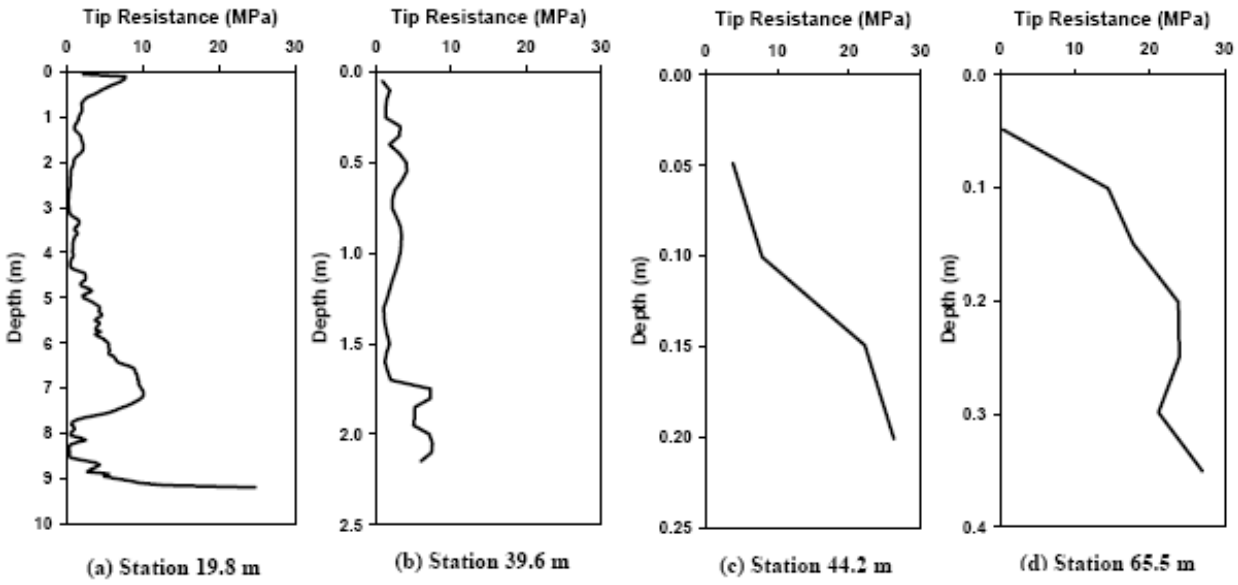

Figure 3-8. Cone penetration tip resistance, line A

Geotechnical Borings and Standard Penetration Tests (SPT):

Eight geotechnical borings and SPT soundings were conducted at strategic locations across the site. Similar to above, the refraction tomograms and CPT results were used to select these locations. All of the borings included drilling and recovery of rock cores through a minimum of 3 m of material, and in one core, through 11 m of material. The following information is provided:

- Three of the eight borings were located along line A at the following stations: 19.8, 35.6, and 65.5 m. These borings coincided with CPT tests at 19.8 and 65.5, while the boring at 35.6 m was slightly to the left of the CPT sounding at 39.6 m.

- At station 19.8 m, the boring was advanced through predominantly sand overburden soil having SPT N-values less than 10 to a depth of 9.0 m. Below 9.0 m, coring was conducted to a depth of 12.5 m, and the material was reported to be tan limestone with fossils throughout. The recovery of this material was 100% throughout, and the rock quality designation (RQD) was reported as 100, except for the first 0.5 m which was broken at the top (RQD approximately 85).

- At station 35.6 m, the boring was advanced through sandy clay and sand overburden soil having SPT N-values between 7 and 10 to a depth of 2.3 m. Below 2.3 m, coring was

conducted to a depth of 11.0 m, and the material was reported to be predominantly light tan to white limestone with fossils throughout.

- At station 65.5 m, the boring was advanced through sand overburden soil to a depth of only 0.3 m. Below 0.3 m, coring was conducted to a depth of 9.4 m, and the material was reported to be predominantly light tan to white limestone with fossils throughout. The recovery of this material varied between 80-100%, with approximately 60% of the run reported at the 100% recovery level. The boring notes report that several zones appeared to be weak and broken, and the RQDs varied widely between 30 and 100. Nearly half the run indicated an RQD between 60 and 80, a short distance (10%) at RQD of 100, and the remaining 40% reported a RQD between 30 and 60.

  These results are compared with the refraction tomograms from Figs. 6a and 7a, and the

CPT results from Figure 3-8 as follows:

- The CPT and boring information at stations 19.8 and 65.5 m appear to be in good agreement. At 19.8, CPT testing was terminated upon approaching a limiting large value at a depth of 9.2 m, while boring information reported the overburden soil/rock interface at a depth of 9.0 m. Similarly, at 65.5, CPT testing was terminated at a depth less than 0.5 m, while the top of rock was reported at 0.3 m.

- The undulating, valley/bowl to block/pinnacle features noted along the P-wave velocity tomograms appear to be the result of lateral variation in the overburden soil/rock interface along the length of the refraction line. At 19.8, a valley/bowl feature appears, and the top of rock is found at 9.0 m, while at 65.5, a block/pinnacle feature appears, and the top of rock is found at 0.3 m.

- While the undulating features in the velocity tomograms are generally indicative of the soil/rock interface, the top of rock does not appear along a constant contour of P-wave velocity. Within a valley (station 19.8), the top of rock is found at approximately 2000 m/s, while at the top of a block (station 65.5), the top of rock is found at a velocity of approximately 500 m/s. However, the rock under station 19.8 m was reported competent and intact, with 100% recovery and RQD of 100 throughout all but a short length at top of core run, while the rock under station 65.5 m was reported to be of lower quality. Velocity differences between these two materials should be expected.

- Finally, it is interesting to note that the CPT appears to penetrate a particulate, sand material of higher velocity (station 19.8) easier than it will a rock of lower velocity (station 65.5). A possible explanation is as follows. Velocity is related to the small-strain modulus of the material, while CPT tip resistance is related to bearing capacity or strength of the material. Even though the rock at station 65.5 has a relatively low velocity as measured through a large volume of material, the local strength beneath the cone tip is still large. A large, broken mass of this material under low confinement near the ground surface has low velocity. However, the local, broken pieces are still an intact, cemented material, and highly resistant to local CPT penetration. Alternatively, the particulate, sand material under large confinement at 9 m is considerably stiffer, yet will undergo local shear failure

under CPT penetration. Thus, these results reinforce the premise that good site characterization practice should include measurement of multiple parameters to fully understand expected behavior.

The results from the synthetic models have shown the capability of the presented technique in dealing with high lateral and vertical variation profiles. In the end, to gain acceptance and wide-spread application, it must be demonstrated that results from the technique compare well with ground truth information obtained from real test sites. Thus, it has been applied to a well-documented test site. In summary, it would appear that the invasive site characterization results provide excellent corroborating evidence for the refraction tomograms presented herein, and suggest that the refraction tomograms provide valuable information regarding subsurface characteristics.

3.4 Chapter Summary

A global optimization scheme based on simulated annealing is presented to obtain near-surface velocity profiles from travel times collected with a surface-based array. By using an extremely fast forwarding model solution and an acceptance rule in cascade to reduce the computer time to a few hours on a standard laptop, the technique is feasible for practical engineering inversion problems. Although the presented technique requires more computer time than the three mentioned commercial packages, the technique offers several advantages. First, the inversion technique does not depend on the initial model, and this becomes important in regions where a priori information about subsurface profiles is not available. Second, rather than just one final model, simulated annealing provides a suite of final models clustering around the global solution, and having comparable least-squared error. This provides an inversion result by averaging all of these accepted models to mitigate the influence of noise and the non-uniqueness of the inversion solutions. Last, the technique can determine the uncertainties associated with inverted results. In cases where the inversion results of subsurface formations are used for the

design of engineering structures such as foundations, the uncertainty can be particularly useful in implementing the new LRFD methodology that can explicitly account for spatial variability and uncertainty in design parameters.

CHAPTER 4
INVERSION OF COMBINED BOREHOLE AND SURFACE TRAVEL TIMES

4.1 Introduction

As previously described, the target of this research was to develop techniques that can characterize anomalies, such as low-velocity layers, and voids in rocks that may be filled by air, water, or soil. For this purpose, it was anticipated that combined travel times measured both on the surface and in a borehole be utilized to obtain higher-resolution inverted profiles. The addition of borehole data to surface data was expected to improve inversion results, thus the need to know the capability of the combined surface and borehole data was critical. To both qualitatively and quantitatively appraise the capability of the data, the global inversion scheme presented in chapter 3, and illustrated with data from surface arrays, was next used on many synthetic and real test data sets, with or without boreholes, to obtain both inverted profiles and associated quantitative uncertainties. A comparison of tomograms utilizing the combined borehole and surface data against tomograms developed using just the surface data, suggests that significant additional resolution of inverted profiles at depth are obtained with the addition of a borehole. The uncertainty estimates provide a quantitative assessment of the reliability of the interpreted profiles. It is also found that the quantitative uncertainties associated with the inverted profiles are significantly reduced when adding a borehole.

4.2 Inversion of Synthetic Data

4.2.1 Synthetic Model 1

Synthetic model 1 (Figure 4-1a) was designed to illustrate the benefit of using borehole data. It includes three layers increasing in velocity with depth, and a low-velocity zone buried in layers 2 and 3. Two sets of travel time data were created from this model. The first set was calculated with 51 surface receivers at 1-m spacing and 17 shots at 3-m spacing. The second set

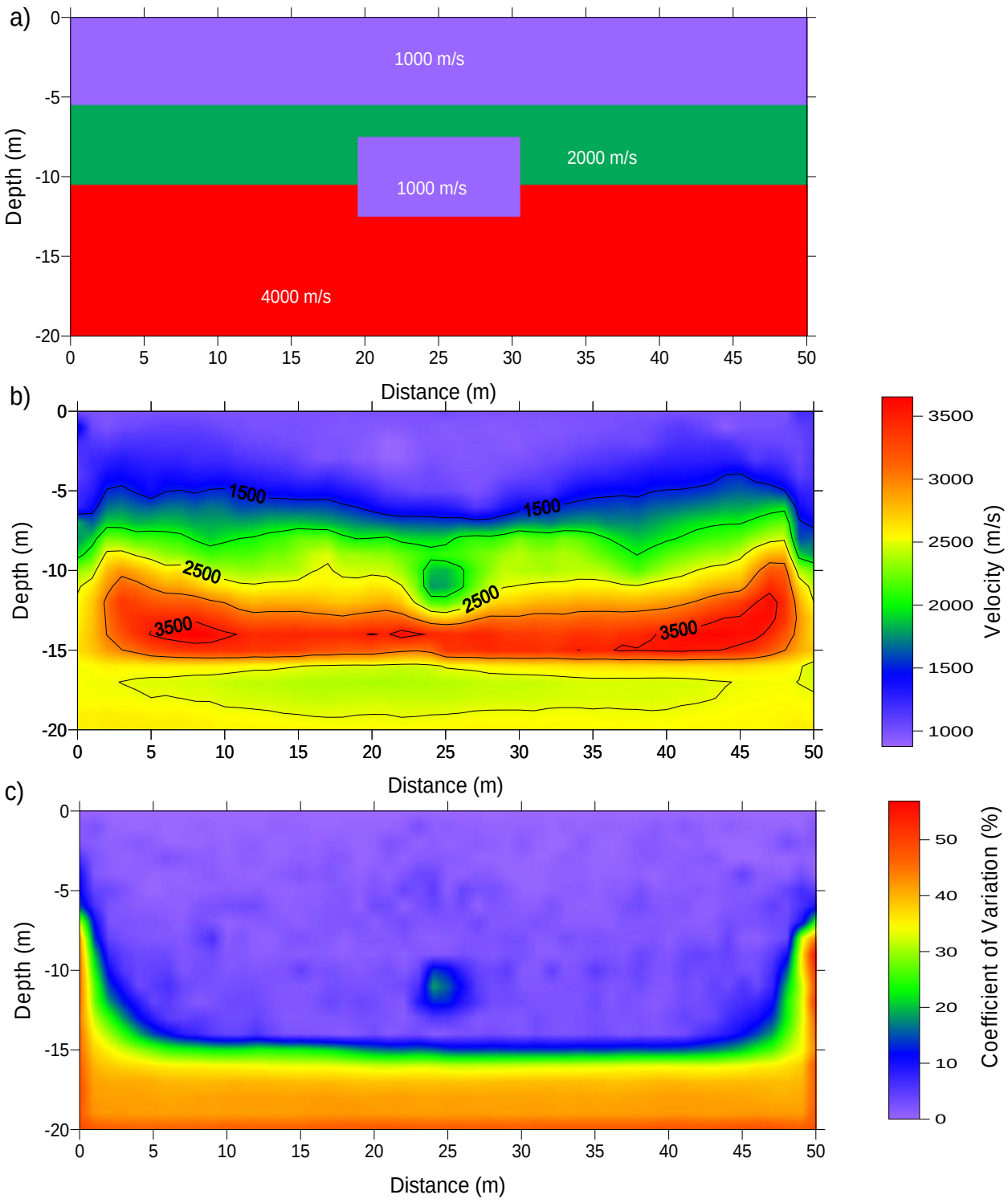

(Figure 4-1 is continued on the next page)

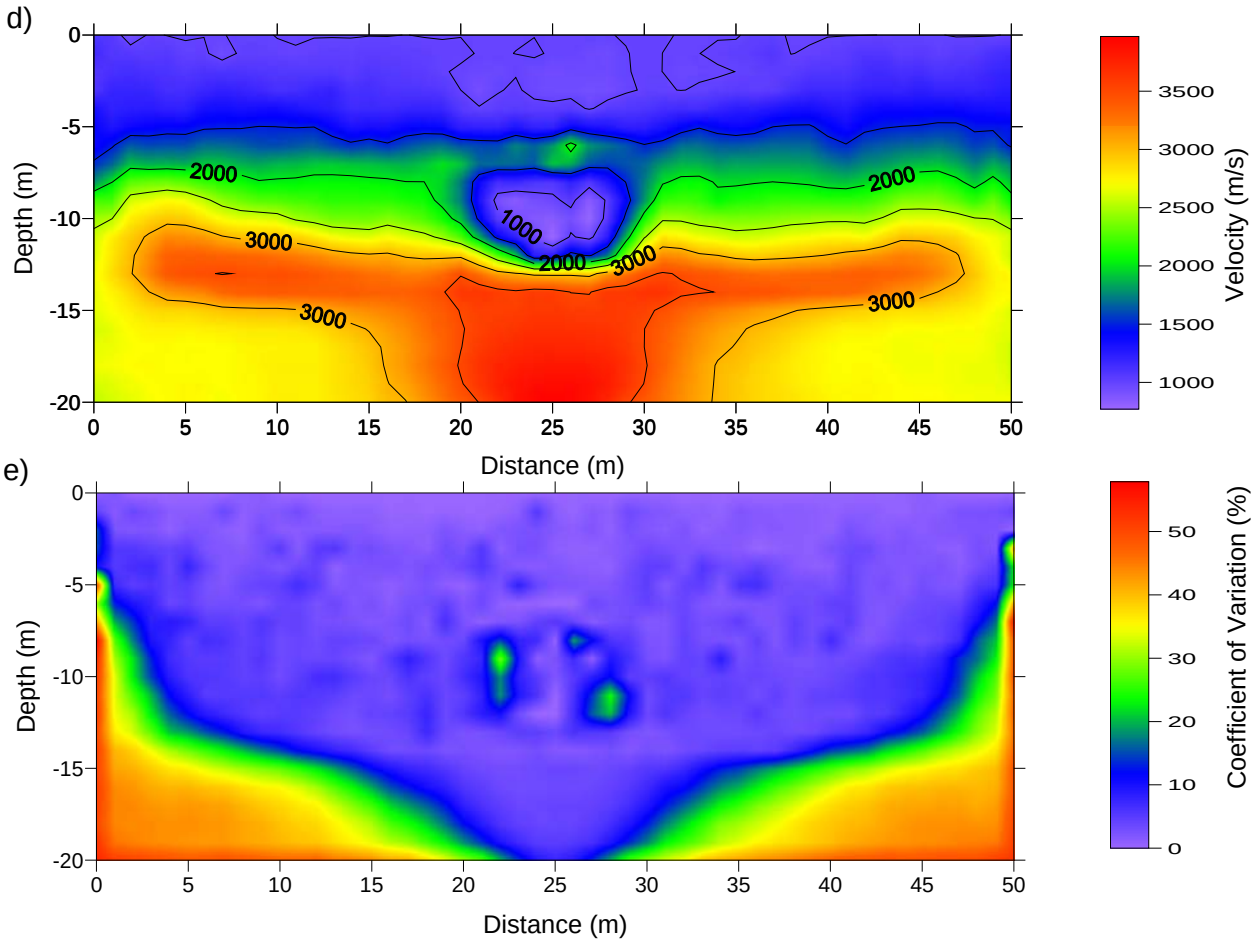

Figure 4-1. Synthetic model 1: a) true model, b) inverted model of the surface data, c) uncertainty associated with the inverted model in figure b, d) inverted model of the combined data, and e) uncertainty associated with the inverted model in figure d

was calculated with 51 surface receivers and 20 borehole receivers at 1-m spacing, and 16 shots at 3-m spacing. All the shots were on the surface and within the surface geophone spread (no shot at borehole location). The borehole was placed at the middle of the medium, and it runs through the low-velocity zone to the bottom of the medium. This travel time data was then used to invert the velocity structures.

To run the inversion, the medium sizes were kept the same as the true models, and discretized with a grid size of 1 m for ease in picking the first-arrival times from forward modeling. The velocity constraints were assigned by slightly increasing the maximum true value, and decreasing the minimum true value, and thus the velocity was allowed to vary between 100 m/s and 5000 m/s. The initial model was specified with a constant velocity of 2000 m/s, which leads to an initial temperature of 10. Velocities of cells were then perturbed, models were updated, and temperature was reduced after each 10,000 accepted models until the criterion of convergence was satisfied. Because of the non-uniqueness of the inversion problem, and to further avoid unusual artifacts, 50,000 accepted models from the last five temperature levels, and that have least-squared errors within a few percent from the smallest error, were used to derive the final inverted model and the associated uncertainty.

First, consider the inverted model (Figures 4-1b) using only surface travel time data. A primary feature of refraction tomography is delineation of both vertical and horizontal changes in seismic wave velocity, e.g., detection of anomalies. Here, it is observed that the inversion is able to reasonably characterize the presence and location of the low-velocity zone. However, it fails to recover the general shape and true velocity of 1000 m/s of the low-velocity zone. This is the typical limitation of refraction tomography using only surface data, because the technique can only model structures with velocity increasing with depth. In addition, refraction tomography is

not able to characterize zones of material outside of the ray coverage. Here is where the uncertainty results (Figures 4-1c) are helpful. The uncertainty is low in zones with good ray coverage, such as zones near the surface, and high in zones with poor ray coverage, such as zones near the bottom corners of the medium. In zones of high uncertainty, the inversion routine simply reports the velocity as the average value from all values randomly and uniformly withdrawn between the minimum and maximum velocity constraints selected by the user. Otherwise, in the zones of low uncertainty, the inverted velocity is independent of the constraints and more reliable. From these results, it appears that the delineation between low and high uncertainty is reasonably established at a COV value of approximately 20%.

Here the inversion fails to provide rational information of the velocity structure below the depth of investigation of 15 m. This can be explained as follows. The half-space (third layer) in this model has the highest velocity, thus the fastest rays that travel through the half-space can be detected on the surface if the geophone spread is large enough. However, these fastest rays only travel within a few meters at the top of the half-space, regardless of the length of the geophone spread. Therefore, the technique using only surface data fails to characterize the velocity structure below these few meters from the top of the half-space. In this case, the borehole data is necessary. The borehole location can be decided from the inversion results of the surface data (Figures 4-1b and 4-1c), which provide credible information of the location of the low-velocity zone. The borehole should be located at or near the low-velocity zone in order to well characterize this zone.

Second, consider the inverted model (Figure 4-1d) using combined borehole and surface data. It is observed that the presence, location, general shape, and true velocity of the low-velocity zone are well characterized. Velocity structure at depth near the borehole is well

recovered. However, even using the combined data, the inverted model is not the same as the true model. Most notably, as discussed by Sheehan et al. (2005) and others, refraction tomography will always model a sharp contrast in velocity with a gradient in velocity. This reality largely accounts for the differences in the two models. In addition, from the uncertainty (Figure 4-1e), the zone of investigation is again taken as the area having COV less than 20%.

Finally, a comparison of the tomogram (Figures 4-1d) utilizing the combined borehole and surface data, against the tomogram (Figures 4-1b) developed using just the surface data, suggests that significant additional resolution of inverted profiles at depth is obtained with the addition of a borehole. The borehole data help well characterize the low-velocity zone, and also help to increase the depth of investigation near the borehole. Similarly, by comparing the uncertainty results (Figure 4-1c against Figure 4-1e), the uncertainty is significantly reduced at depth for the case of using the borehole data.

4.2.2 Synthetic Model 2

Synthetic model 2 (Figure 4-2a) was designed to investigate whether a low-velocity zone can be characterized if the borehole does not run through this zone. It also includes three layers increasing in velocity with depth, and a low-velocity zone of 6 m by 6 m buried in layers 2 and 3. This model is 10 m deeper than model 1, and the low-velocity zone is placed nearby the borehole, which runs from the top to the bottom at the middle of the medium. Two sets of travel time data were created from this model using the same test layouts as model 1, except using 30 borehole receivers at 1-m spacing in this case.

As described for model 1 above, the inversion was conducted for both travel time data sets, and the results are as follows. For the surface data only, the inversion results (not shown here) cannot provide any information about the low-velocity zone. This can be explained that the low-velocity zone is buried at a significant depth compared to the surface geophone spread, and also

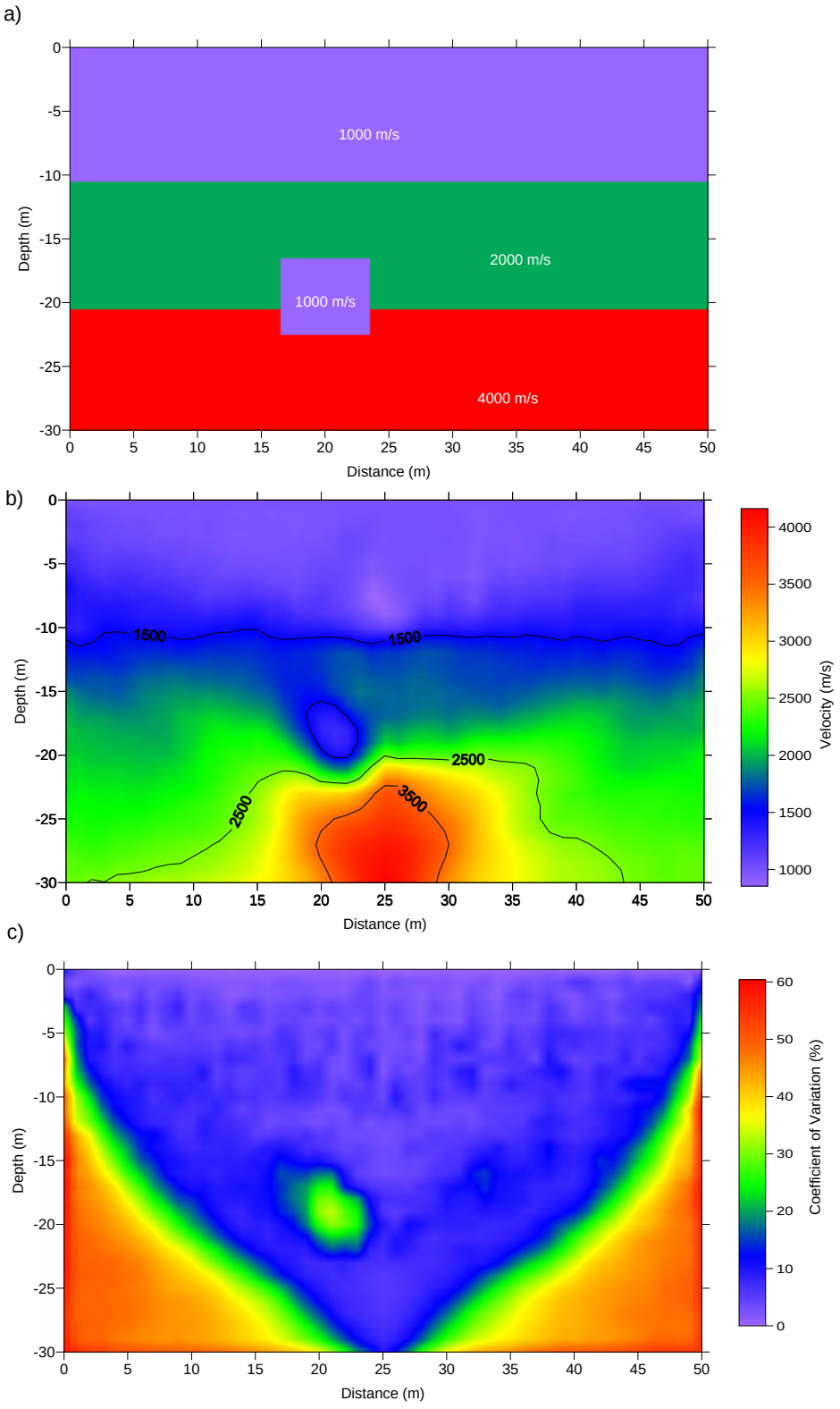

Figure 4-2. Synthetic model 2: a) true model, b) inverted model c) uncertainty associated with the inverted model

the surface refraction tomography can only model structures with velocity increasing with depth. For the combined data, the inverted model is presented in Figure 4-2b. It is observed that the velocity structure near the borehole from the top to the bottom of the model is reasonably characterized. Particularly, the low-velocity zone is successfully recovered even though the borehole does not run through this zone. However, the inverted model and the true model are again not the same. The primary difference between the two models is due to the gradient.

Figure 4-2c presents the uncertainty associated with the inverted model. Similar to that of model 1, the uncertainty is low in zones with good ray coverage, such as zones near the borehole, and high in zones with poor ray coverage, such as zones near the bottom corners of the medium. It is interesting to note that the location and general shape of low-velocity zone also can be recognized in the uncertainty image as a high uncertainty area inside a low uncertainty zone. It is understood that the fastest rays from shots to geophones tend to avoid the low-velocity zone if no geophones are placed in this zone. Therefore, the low-velocity zone has lower ray coverage than the adjacent high-velocity zones, and it is less defined and has higher uncertainty. The indication of a low-velocity zone in the uncertainty image significantly increases the credence of a real low-velocity zone instead of an artifact of the inversion.

4.2.3 Synthetic Model 3

Model 3 (Figure 4-3a) was designed to optimize test layouts in order to obtain a reasonable inverted profile near the borehole with the fewest possible number of shots. This model is similar to model 2, including 3 layers, and a buried low-velocity zone of 4 m by 4 m, and the borehole is placed at the middle from the top to the bottom of the medium. The focus here is to delineate the velocity structure at depth within 5 meters around the borehole, and it was expected the goal can be achieved by using only a few shots on the ground surface. To optimize the number of shots, three cases were tested using three sets of combined data created with the number of surface

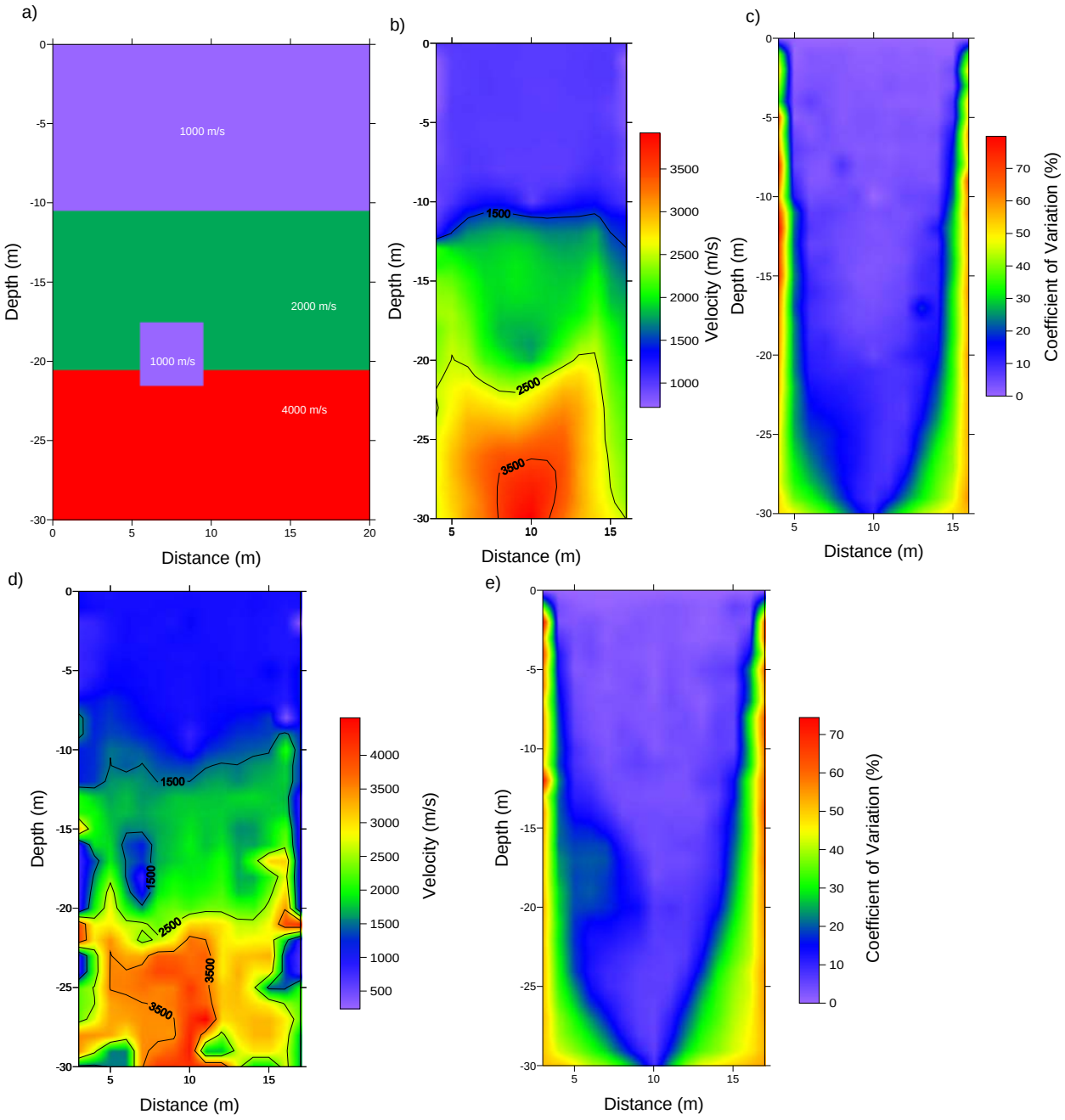

(Figure 4-3 is continued on the next page)

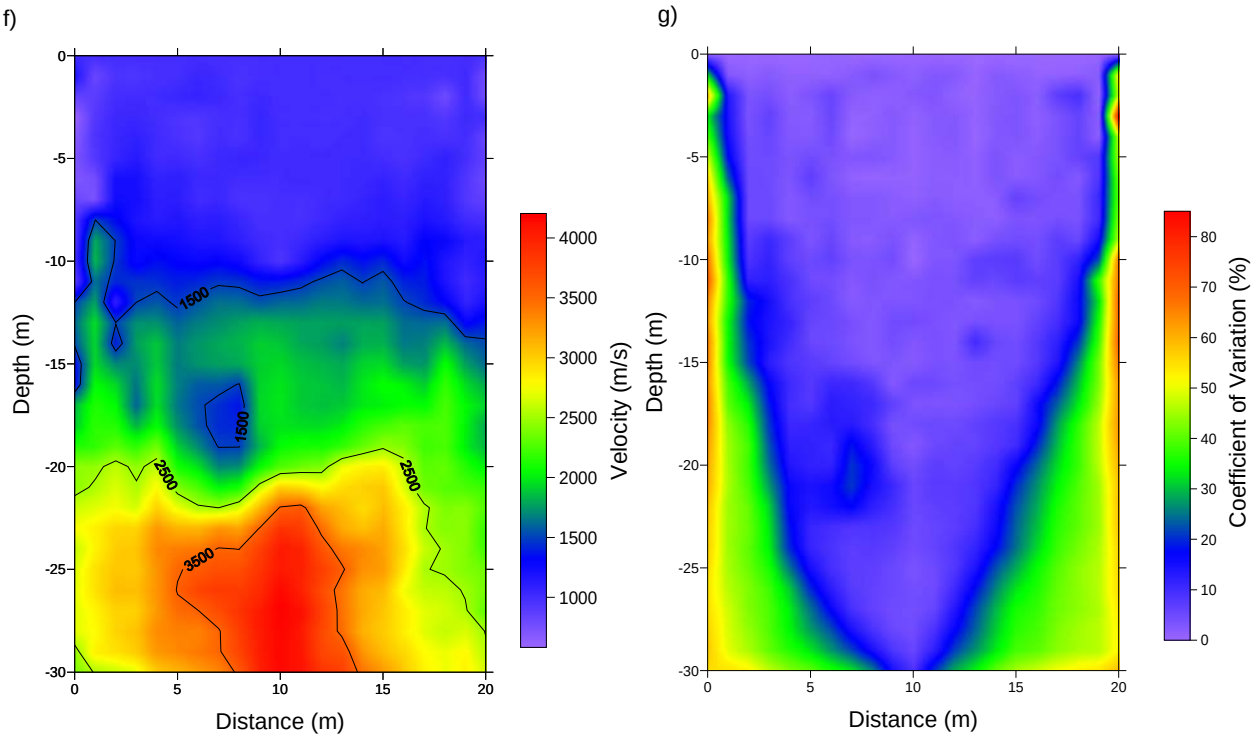

Figure 4-3. Synthetic model 3: a) true model, b and c) inverted model and uncertainty using 2 shots, d and e) inverted model and uncertainty using 4 shots, f and g) inverted model and uncertainty using 6 shots

shots as 2, 4, and 6. For the first case, 2 shots were placed 5 m on each side of the borehole. And for other cases, shots were placed at both sides every 3 m away from the borehole. Receivers were placed both on the surface within the shot spread, and in the borehole at 1-m spacing. The inversion results of the three cases are as follows.

First, the inversion results using 2 shots are presented in Figures 4-3b and 4-3c. Here the inversion characterizes the velocity of the three layers, but it fails to provide any information of the low-velocity zone. This may be explained that there are not enough rays through the low-velocity zone if using only one shot on each side of the borehole. Second, consider the inversion results using 4 shots (Figures 4-3d to 4-3e). It is observed that the velocity structure near the borehole is reasonably characterized. With respect to the low-velocity zone, the location and the true velocity are well inverted. However, its general shape is not fully recovered. Last, the inversion results using 6 shots are presented in Figures 4-3f and 4-3g. The velocity structure near the borehole is well characterized; especially the low-velocity zone is well recovered.

From the inversion results for the cases of model 3, it is possible to utilize just a few shot locations on the ground surface within a few meters around the borehole, surface geophones within this few meters, and a string of borehole geophones, to reliably assess the subsurface properties at depth near the borehole. This is a significant reduction in test effort in comparison to full surface arrays such as those used in models 1 and 2.

4.3 Inversion of Real Test Data

4.3.1 Newberry Test Site

The description of the Newberry test site was provided in section 3.3.2. For the case presented here, the test was conducted on line K to measure both surface and borehole data. The surface data were measured with vertical geophones equally spaced at every 1 m, for a total of 37 measurements. The borehole data were measured in a borehole installed at the 18-m station with

downhole geophones at 1-m spacing, for a total of 17 measurements. Seismic energy was generated by vertically striking a metal ground plate with a sledgehammer, thus producing compression wave (P-wave) first arrivals. Shot locations were placed at 3-m spacing along 36 m, and starting from 0 m, for a total of 13 shots.

First, consider the surface data only (Figure 4-4). To run the inversion, the velocity constraints and the medium depth were established. Similar to the surface data sets in chapter 3, the minimum and maximum velocities were determined as 300 m/s and 3000 m/s, respectively, and the depth of the medium was simply taken as 1/2 of the geophone spread.

Second, for the case of the combined surface and borehole data (Figure 4-5), the velocity constraints were assigned the same as those for the case of the surface data only. The depth of the medium was taken the same as the depth of the borehole, because it is expected that the measured data does not provide information of the structure below the tip of the borehole. In addition, because of the influence of a borehole casing, the data from the shot at the borehole location is excluded from the combined data. Thus, 12 shots were used in this case, instead of 13.

In the inversion process of the two cases, the medium was discretized with a grid size equal to the geophone spacing of 1 m. The initial model was selected with a constant velocity of 1000 m/s, velocities of cells were perturbed by randomly assigning values between the constraints, models were updated, and the temperature was reduced after every 10,000 accepted models until the criterion of convergence was reached. The criterion of convergence was not satisfied until the estimated first-arrival times from the final accepted model were very close to the observed travel times (shown in Figures 4-4 and 4-5).

Because of noise, subjective judgments in manually picking first-arrival times, and non-uniqueness of inverted solutions, there is no guarantee that the model corresponding to the

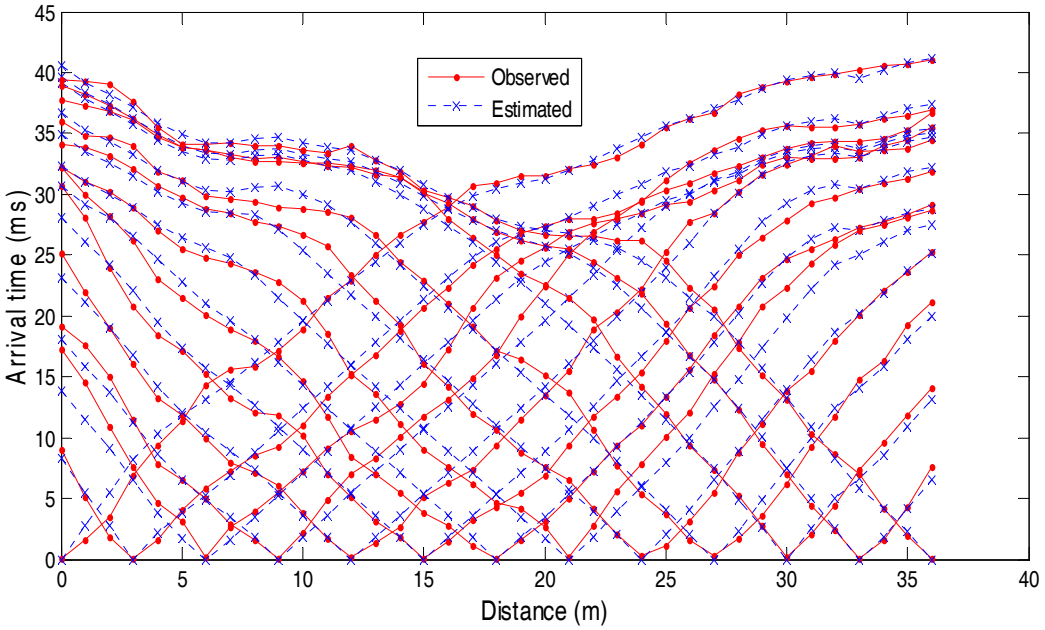

Figure 4-4. Comparison between the observed and estimated first-arrival times for Newberry surface data

a)

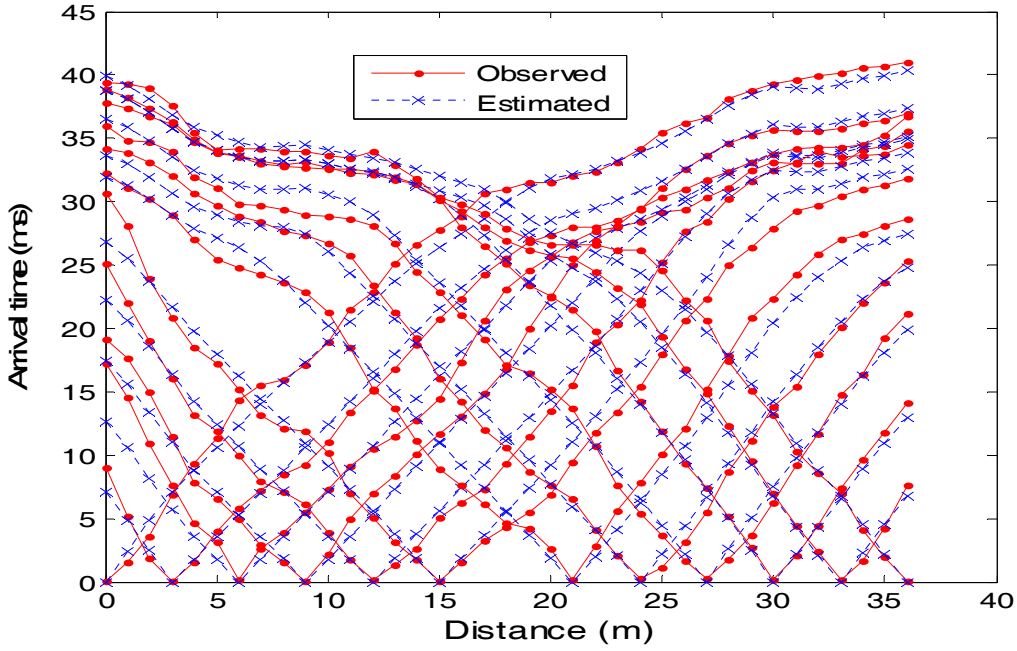

b)

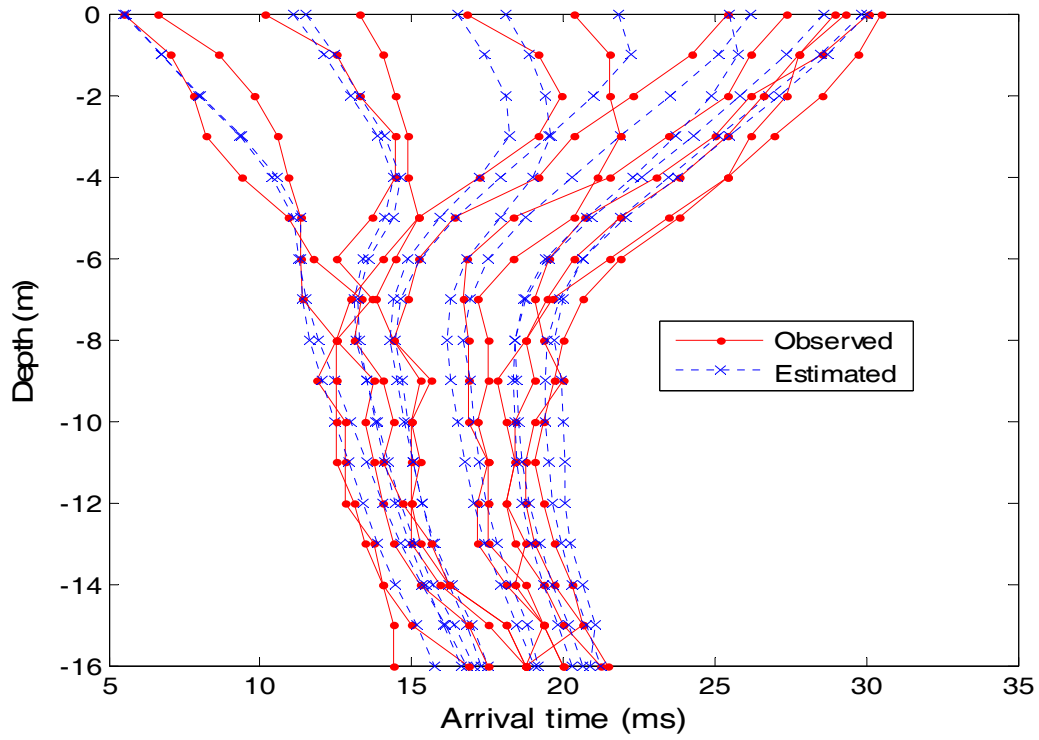

Figure 4-5. Comparison between the observed and estimated first-arrival times for Newberry combined data: a) surface data, and b) borehole data

smallest error is closest to the true model. Therefore, the inversion results should be derived from many accepted models clustering around the global minimum, and having similar errors, instead of from one model that has the smallest error. Similar to synthetic model cases, the last 50,000 accepted models were used to derive the inverted profiles and the associated uncertainties.

Figure 4-6a presents the 2-D compression (P) wave refraction tomogram determined from test data collected along the surface. This tomogram indicates that the P-wave velocity generally increases with depth within the investigation area. Figure 6b shows the uncertainty associated with the inverted P-wave profile. Again, the uncertainty is consistent with expectation: low uncertainty in zones with good ray coverage, and high uncertainty in zones with poor ray coverage. With the confidence gained from running synthetic models, the depth of investigation is about 10 m, where the COV from the ground surface to that depth is less than 20%.

Figure 4-7a presents the two-dimensional P-wave refraction tomogram determined from combined data collected both along the surface and down the borehole. It is observed that a slightly low-velocity zone is found near the tip of the borehole. The position of this zone is also shown as the high value area in the uncertainty image (Figure 4-7b). Also, based on the low uncertainty zone, the inverted velocity structure is credible near the borehole at depth.

Comparing the velocity profiles, Figure 4-6a against Figure 4-7a, the profiles are similar at shallow depth. This similarity is understandable, because the shallow structure is mainly determined by the surface data, which is the same in both inversion runs. At deeper depth, the profiles are very different because the profile from the combined data is determined from the test measurement, while the other is simply reported by inversion as an average of the minimum and maximum velocity constraints. Similarly, comparison of uncertainty results (Figure 4-6b against Figure 4-7b), indicates that the uncertainty is significantly reduced at depth for the case of

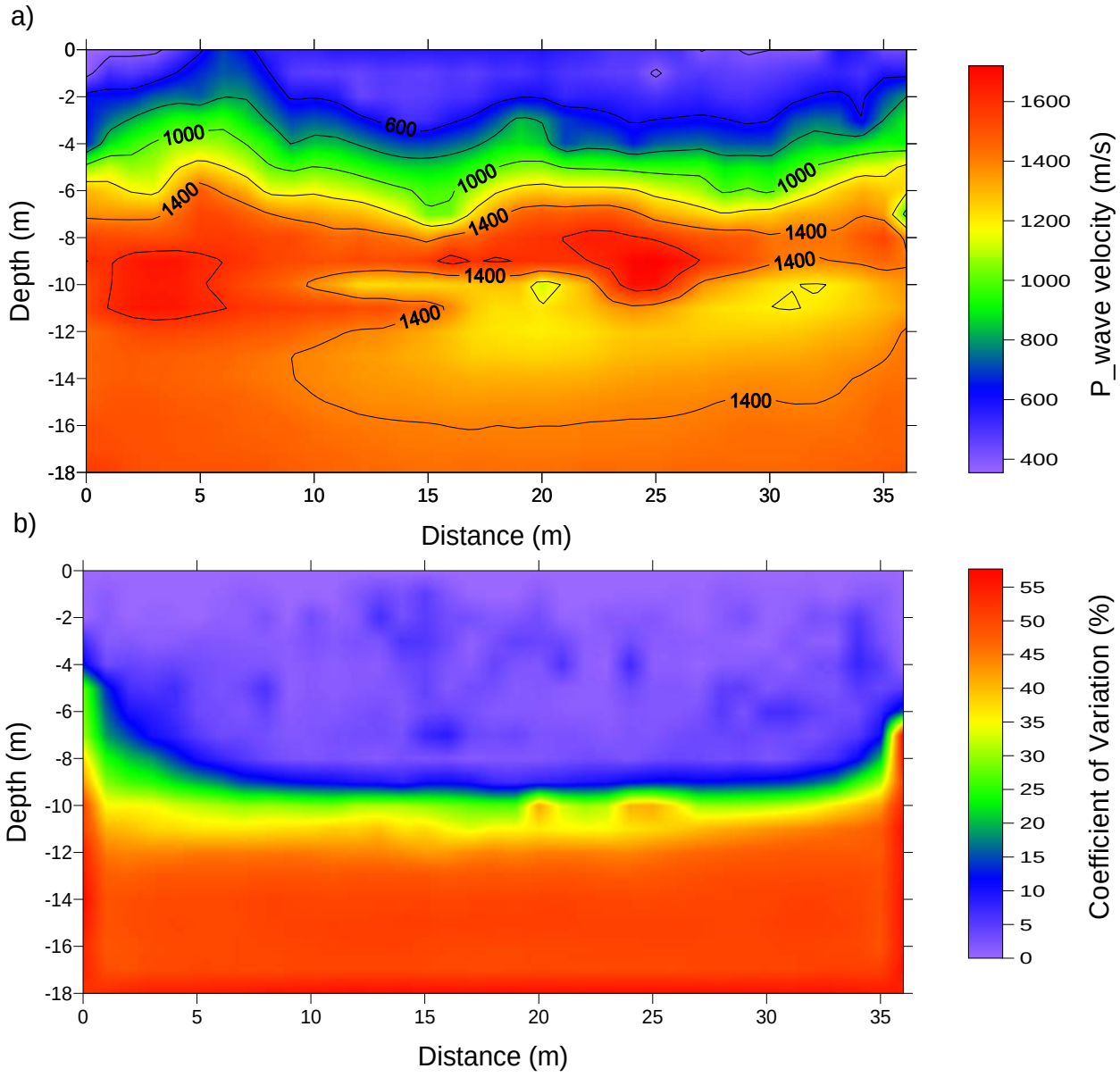

Figure 4-6. Newberry surface data: a) inverted model, and b) uncertainty

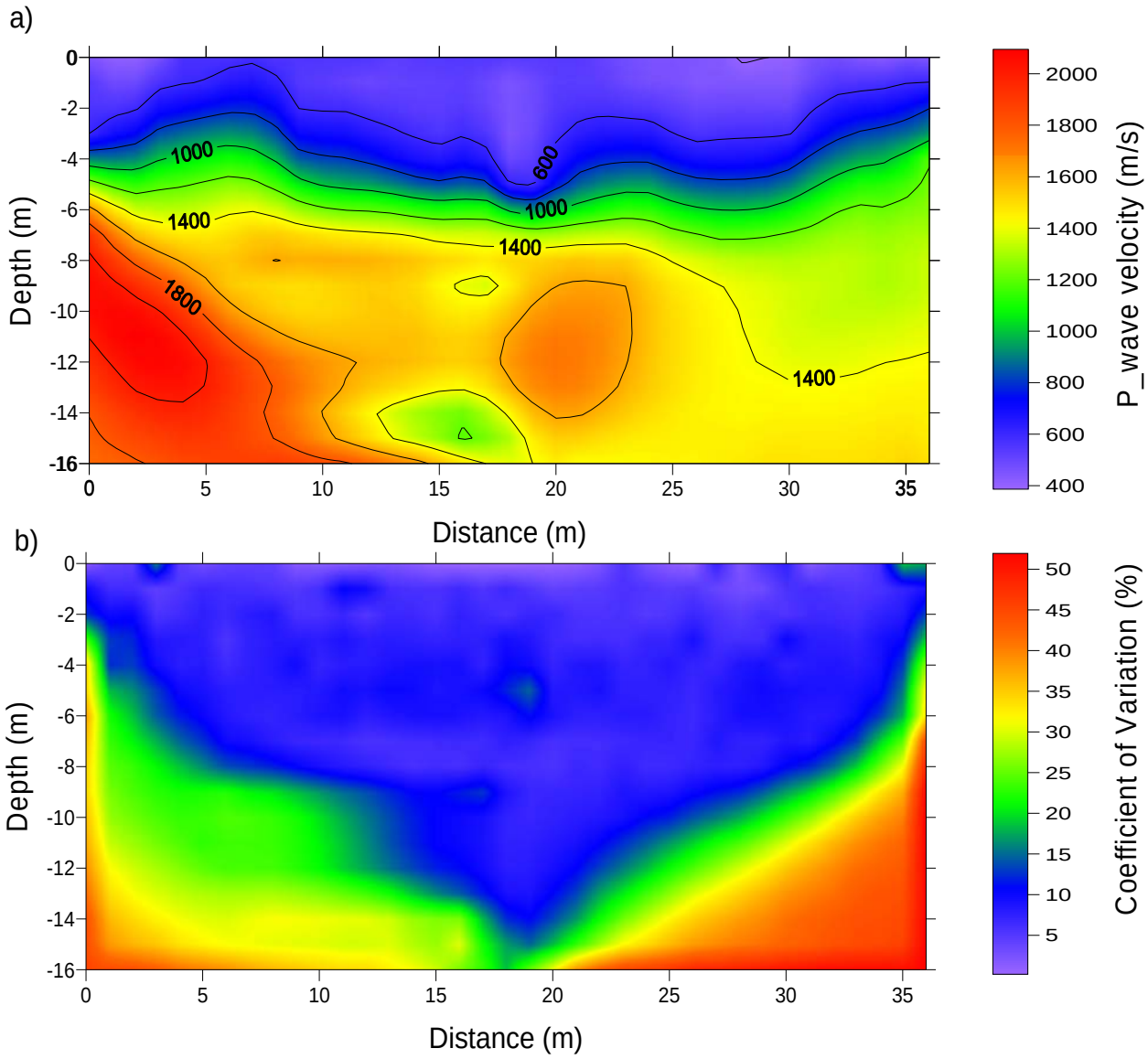

Figure 4-7. Newberry combined data: a) inverted model, and b) uncertainty

using a borehole. Thus, for deep foundation design, the inversion results of the combined data provide credible information of material at the socket, and also partially detect anomalies embedded near the socket. This is very important because the material at and near the socket will carry a majority of load from foundations.

4.3.2 Ft. McCoy Test Site

The second test site is located near Ft. McCoy, Florida. The site is documented to consist of soil over rock, with the top of bedrock at 12-m depth. The test was conducted to measure both surface and borehole data. The surface data were measured with vertical geophones equally spaced at every 1 m from 0 m to 30 m, for a total of 31 measurements. The borehole data were measured in a borehole installed at station 15 m with borehole geophones equally placed at every 1 m from 4 m to 18 m depth, for a total of 15 measurements. Seismic energy was generated by vertically striking a metal ground plate with a sledgehammer, thus producing compression wave (P-wave) first arrivals. Shot locations were placed from 1 m to 3 m spacing along 30 m on the surface and starting from 0 m, for a total of 20 shots. The shot spacing was 1 m for shots close to the borehole, 2 m for shots farther, and 3 m for shots at both ends.

In a fashion similar to the Newberry data, two inversions were run for the surface data and the combined data. For both runs, the depth of medium was selected as 18 m, equal to the depth of the deepest borehole geophone, and the minimum and maximum velocities were 200 m/s and 3000 m/s, respectively. The inversions converged when the estimated first-arrival times from the final accepted model were very close to the observed travel times (Figures 4-8 and 4-9).

Figures 4-10a and 4-10b present the two-dimensional P-wave refraction tomogram determined from test data collected along the surface and the associated uncertainty. Here, it is determined that the depth of investigation is about 10 m, and the surface data provide no

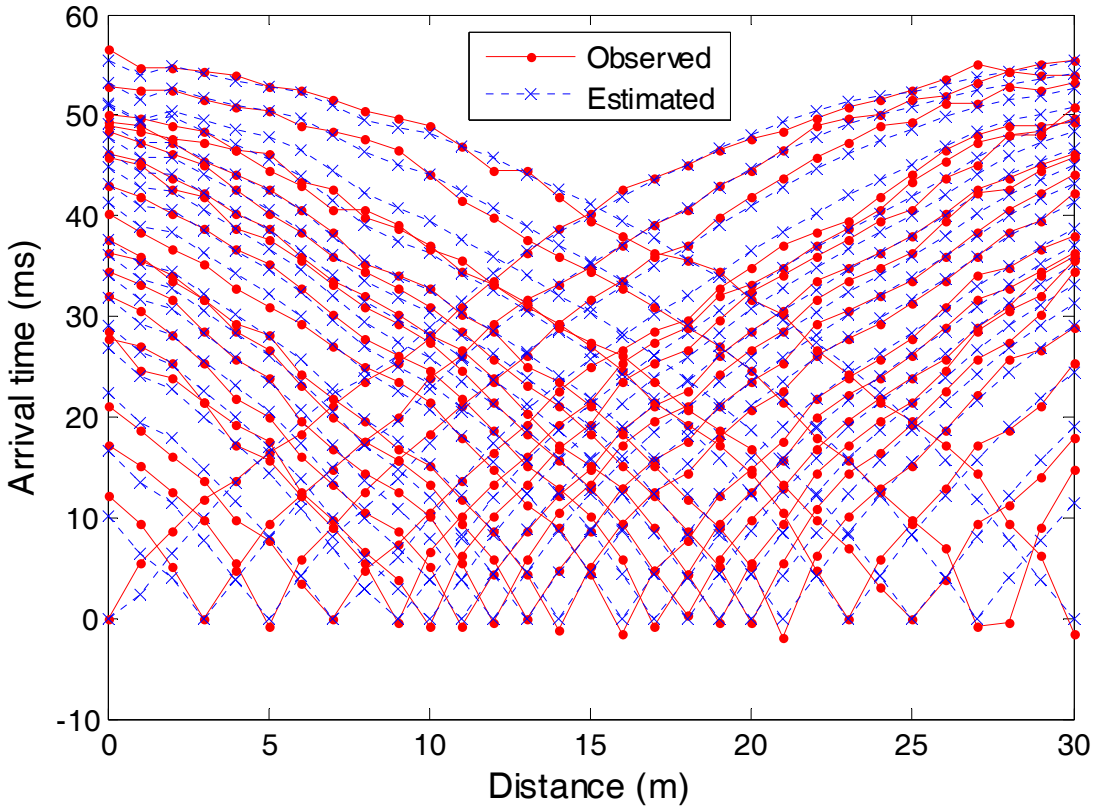

Figure 4-8. Comparison between the observed and estimated first-arrival time for Ft. McCoy surface data

a)

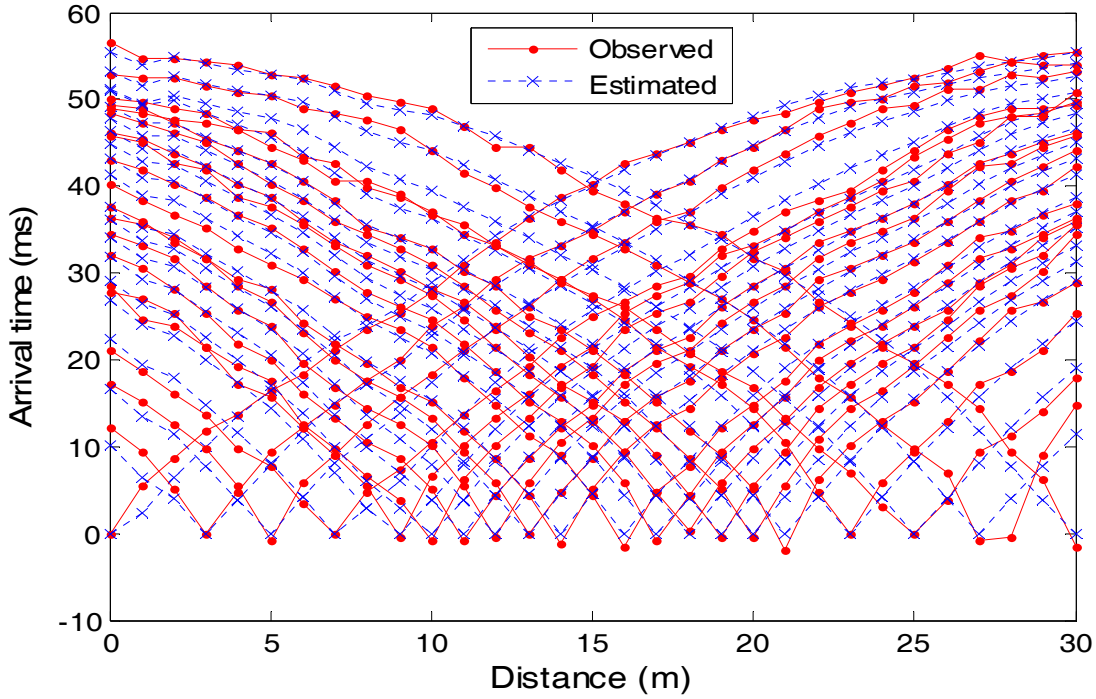

b)

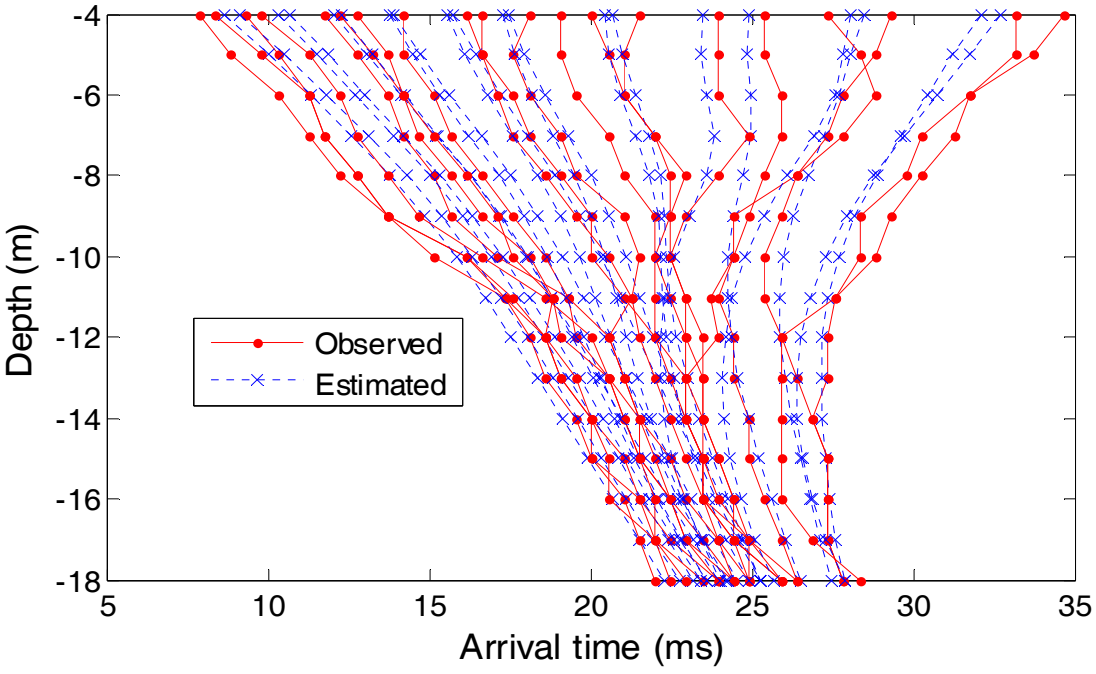

Figure 4-9. Comparison between the observed and estimated first-arrival time for Ft. McCoy combined data: a) surface data, and b) borehole data

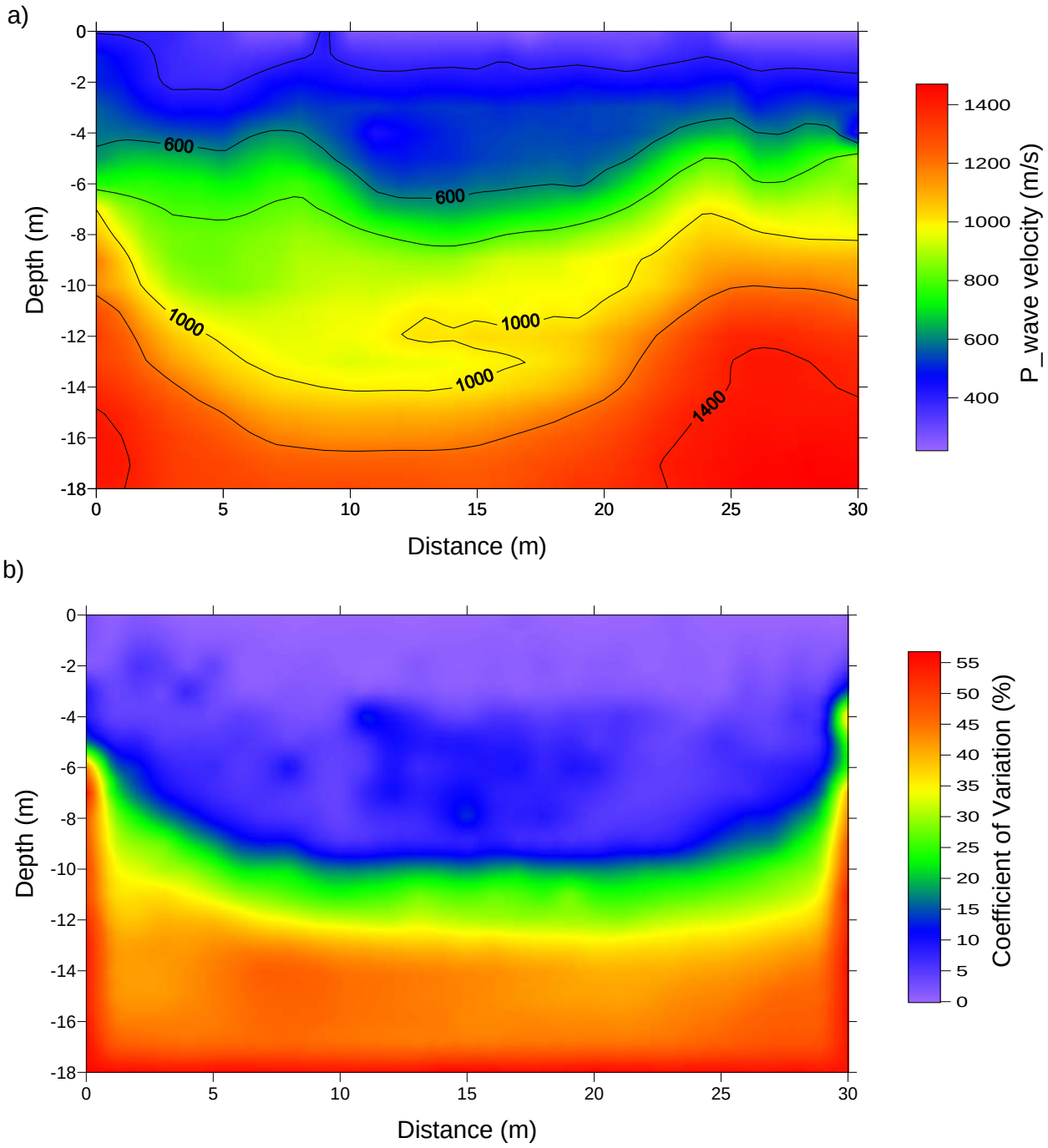

Figure 4-10. Ft. McCoy surface data: a) inverted model, and b) uncertainty

information about the bedrock. Figures 4-11a and 4-11b show the P-wave tomogram and the associated uncertainty determined from combined test data collected along the surface and in the borehole. Consistent with test site 1, the top of bedrock at 12-m depth is again associated with a P-wave velocity contour of 1200 m/s (Fig. 4-11a). It is also observed that the addition of a borehole significantly improves the resolution of the inverted profile, reduces the associated uncertainty, and increases the depth of investigation. Credible characterization of the bedrock is only obtained from the inversion of the combined data.

4.3.3 Dunedin Test Site

The third test site is located in Dunedin, Florida. The site is documented to consist of soil over rock, with the top of bedrock at 20-m depth. In more detail, the profile is sand from the ground surface to 7-m depth, clay to 9.5 m, alternating layers of dense clay and limestone to 20 m, and finally limestone below 20 m. The test was conducted to measure both surface and borehole data. The surface data were measured with vertical geophones equally spaced at every 1 m from 0 m to 30 m, for a total of 31 measurements. The borehole data were measured in a borehole installed at station 13 m with borehole geophones equally placed at every 1 m from 6-m to 25-m depth, for a total of 20 measurements. Seismic energy was generated by vertically striking a metal ground plate with a sledgehammer, thus producing compression wave (P-wave) first arrivals. Shot locations were placed at either 1 m or 2 m spacing along 30 m on the surface, and starting from 0 m, for a total of 20 shots. The shot spacing was 1 m for shots close to the borehole, and 2 m for the farther shots.

In a fashion similar to the Newberry and Ft. McCoy sites, two inversions were run for the surface data and the combined data. For both runs, the depth of medium was selected as 25 m, equal to the depth of the deepest borehole geophone, and the minimum and maximum velocities

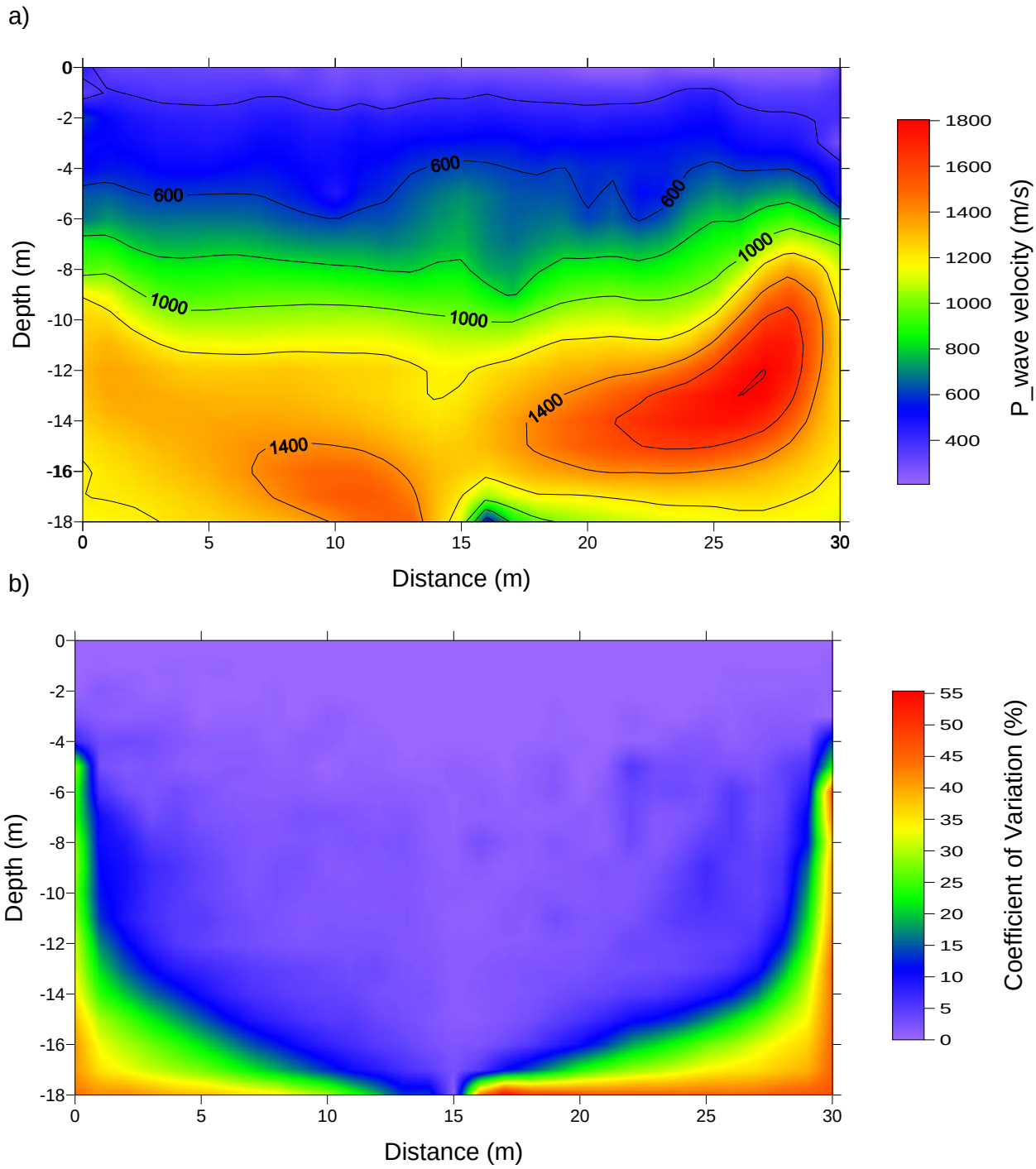

Figure 4-11. Ft. McCoy combined data: a) inverted model, and b) uncertainty

were 200 m/s and 3000 m/s, respectively. Like Newberry and Ft. McCoy, the inversions converged when the estimated first-arrival times from the final accepted model were very close to the observed travel times (shown in Figures 4-12 and 4-13).

Figures 4-14a and 4-14b present the two-dimensional P-wave refraction tomogram determined from test data collected along the surface and the associated uncertainty. Similarly, Figures 4-15a and 4-15b show the P-wave tomogram and the associated uncertainty determined from combined test data collected along the surface and in the borehole. Unlike Newberry and Ft. McCoy, some unusual features are noted in the figures for Dunedin. First, the uncertainty plot for the surface array (Figure 4-14b) suggests that the maximum credible depth of investigation is only about 6 m, compared to 10 m for both Newberry and Ft. McCoy, and despite the fact that the surface arrays were about the same length at all three sites. At Dunedin, it is noted that the P-wave velocity from the surface array at 6-m depth is about 1500 m/s (Figure 4-14a). This is equivalent to the P-wave velocity of water, and suggests that the water table at the site was about 6 m below the ground surface. Thus, all the refracted arrivals measured with the surface array are from the water table, and no information about the soil or rock is obtained from the surface array below 6 m. At the time of testing, water was observed in the borehole at about this depth of 6 m. Water was also observed at shallow depths in the boreholes at Newberry and Ft. McCoy. However, refracted arrivals from a shallow water table were not observed at these two sites. Why the difference? The water observed in the hole at Dunedin is from a high groundwater table located about 6 m below the ground surface. On the other hand, the water observed in the holes at Newberry and Ft. McCoy is due to a deeper water table located somewhere below the rock surface, and under artesian pressure. The water at Dunedin interferes

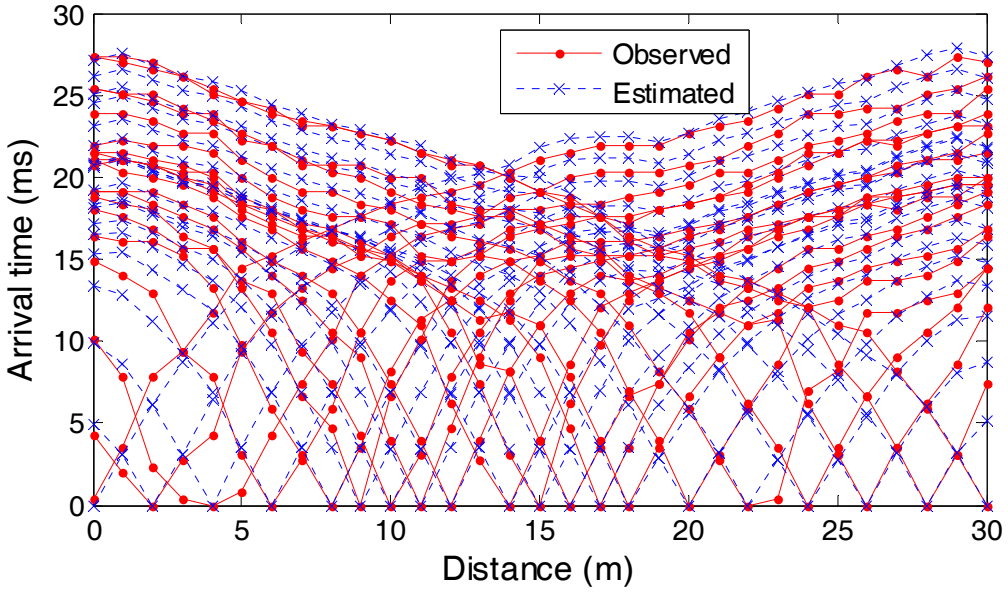

Figure 4-12. Comparison between the observed and estimated first-arrival time for Dunedin surface data

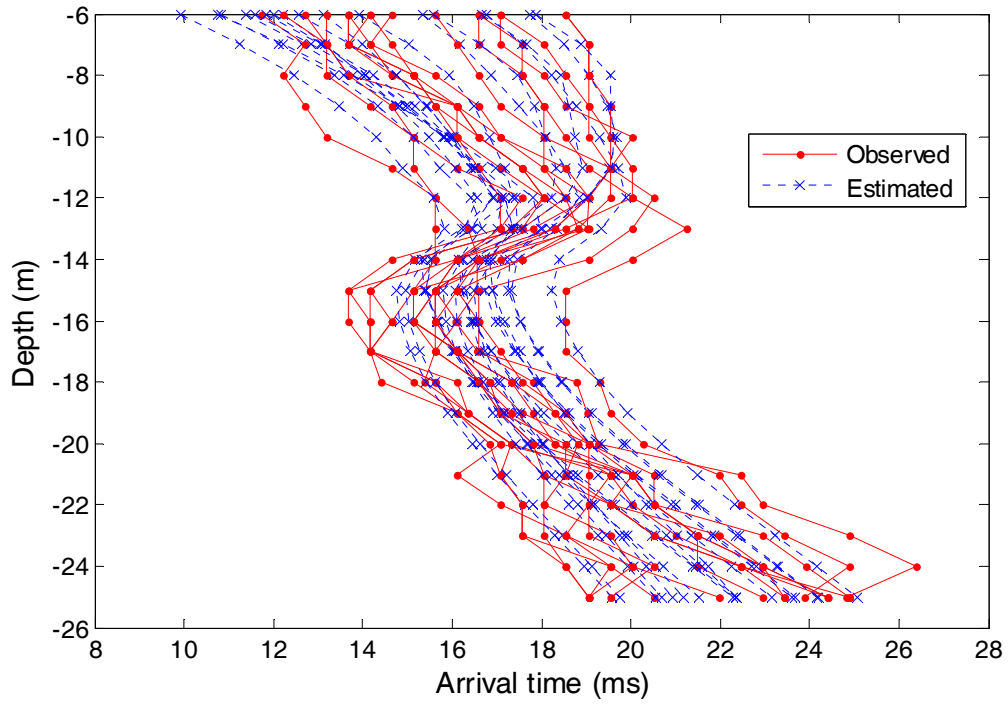

Figure 4-13. Comparison between the observed and estimated first-arrival time for Dunedin borehole data

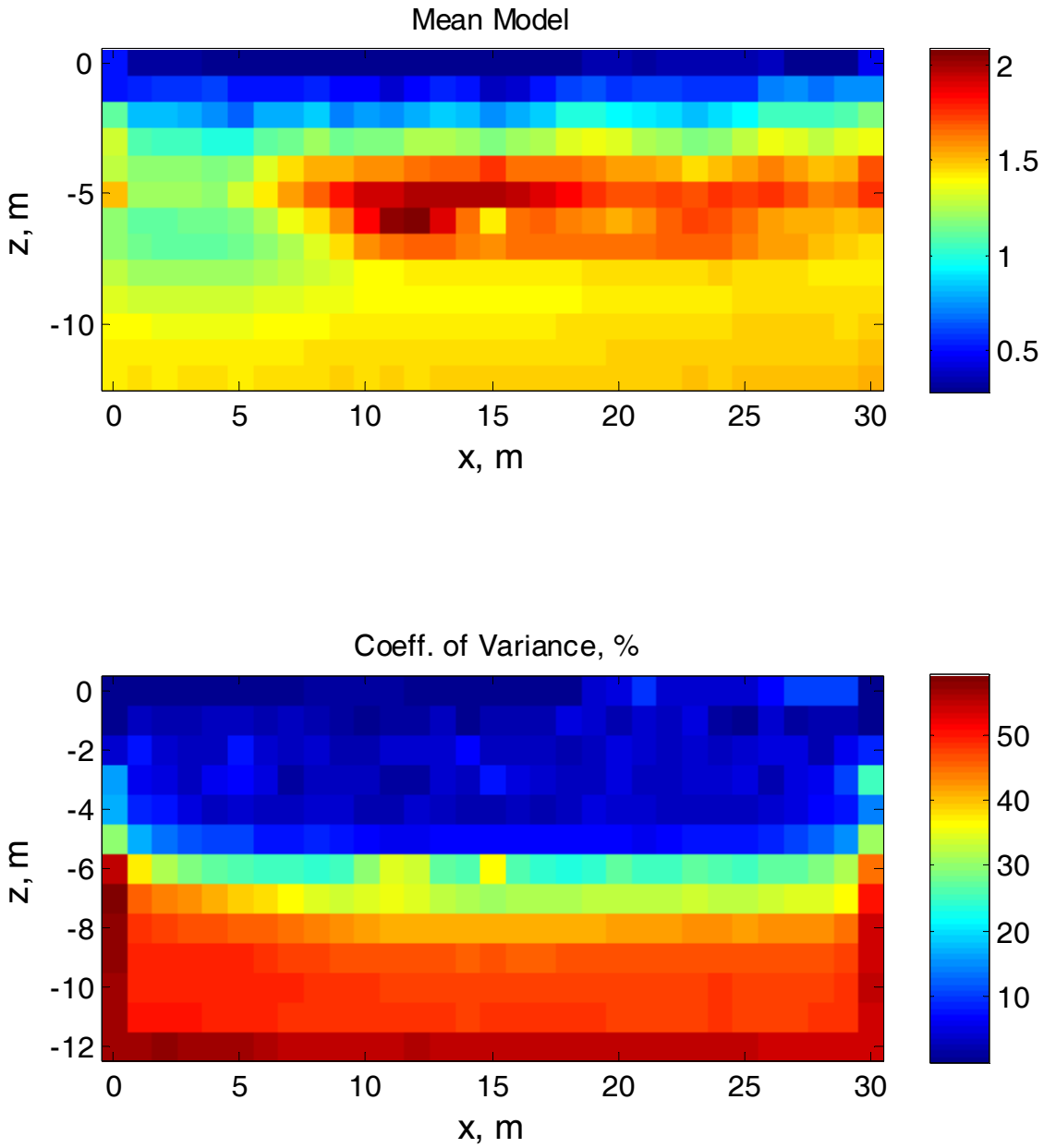

Figure 4-14. Dunedin surface data: a) inverted model, and b) uncertainty

with the P-wave tomogram, while characterization of the soil and soft rock via P-waves is possible at Newberry and Ft. McCoy.

The effects of the high groundwater table at Dunedin are also evident in the data from the borehole array, most notably Figure 4-13. Here, the pattern of borehole arrivals with depth is much different than in the comparable figures for Newberry and Ft. McCoy. The different pattern is caused by the first-arrival data from depths of 6 to 13 m. Unlike Newberry and Ft. McCoy, the first-arrival data in this zone is governed by the P-wave velocity of water, and not the lower-velocity soil. The tomogram (Figure 4-15b) likewise in this zone reflects the characterization of the water and not the soil and/or soft rock. Below 13 m the travel time data (Figure 4-13) transition to more typical behavior because the P-wave first-arrivals return to the soil and/or rock, since at these depths the P-wave velocities now begin to be larger than that of water. Thus, in reality, no characterization of the soil and/or rock is obtained from the surface or borehole arrays between about 6 and 13 m due to the high water table.

As a partial remedy for the high water table problem, a third inversion was conducted based upon a revised interpretation of the borehole array data, and these results are shown in Figures 4-16 and 4-17. First, note that the borehole travel times in Figure 4-16 now look more like those from Newberry and Ft. McCoy. These revised times were obtained by picking a second strong and consistent arrival observed in the records for depths between 6 and 13 m. This second arrival is due to the P-wave in the soil and/or rock that follows the first arrival due to the water. These revised travel times were then used to invert for the P-wave tomogram in Figure 4-17a with associated uncertainty in Figure 4-17b. It is noted from the uncertainty plot and the fit of observed and estimated travel times, that this inversion is not as high in quality as for previous cases. First, the observed travel times estimated for depths 6 to 13 m are more erratic, since it is

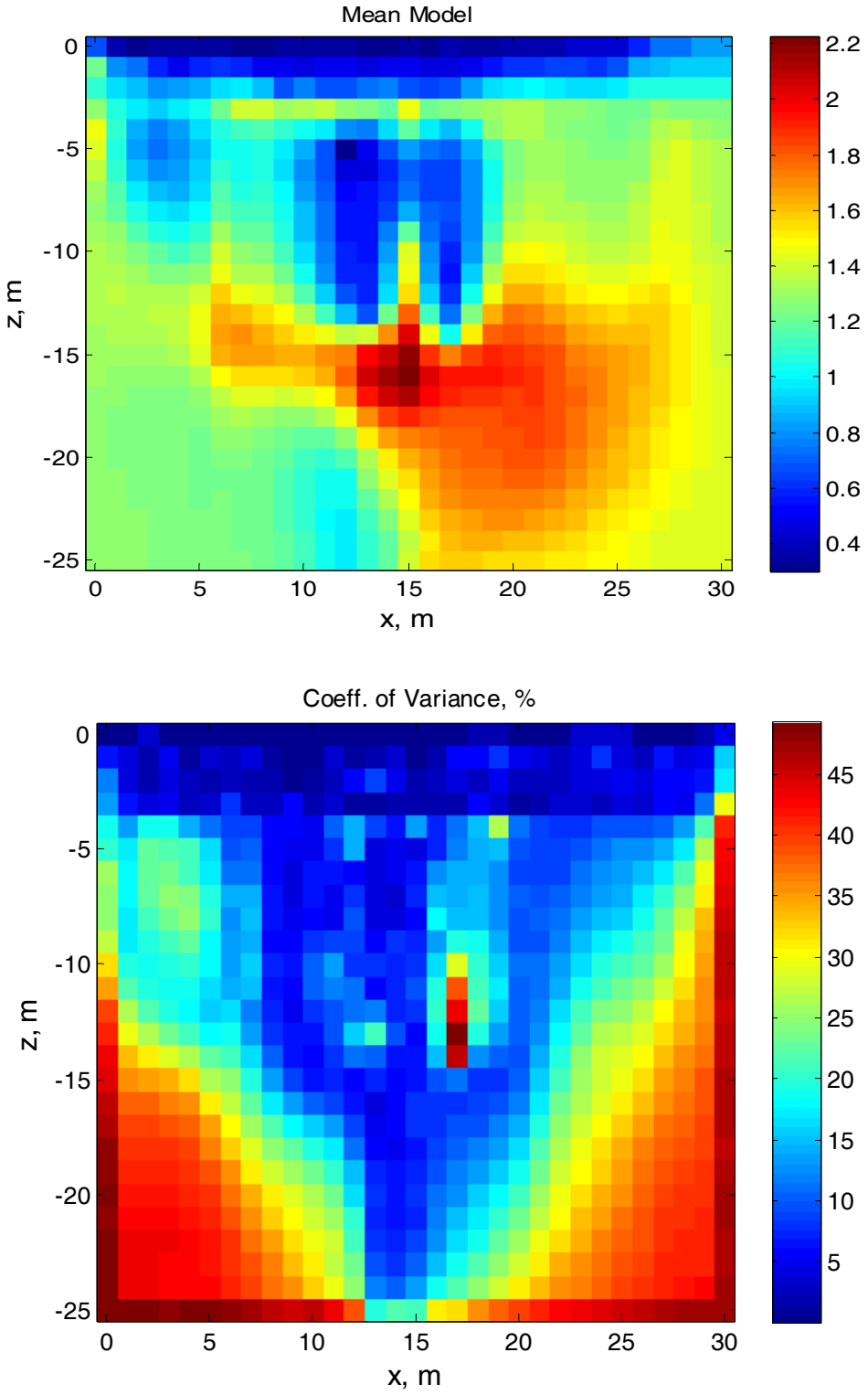

Figure 4-15. Dunedin combined data: a) inverted model, and b) uncertainty

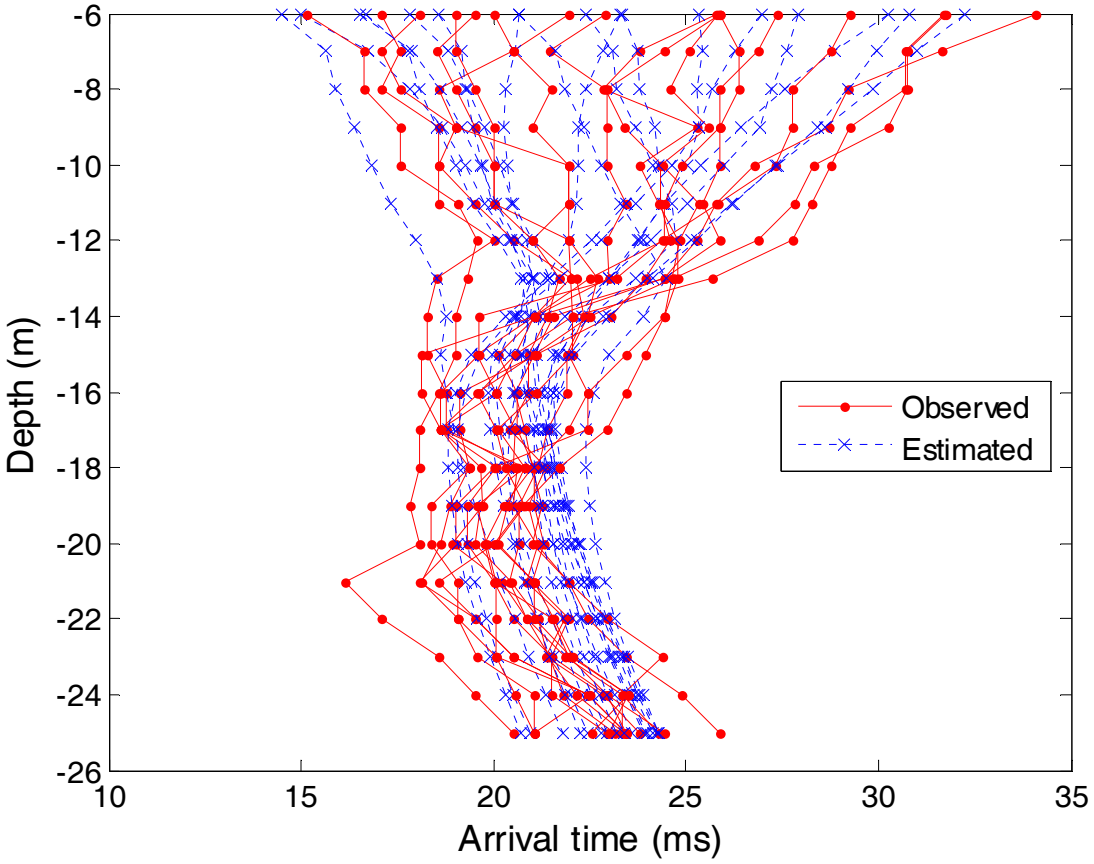

Figure 4-16. Comparison between the observed and estimated revised arrival times for Dunedin borehole data

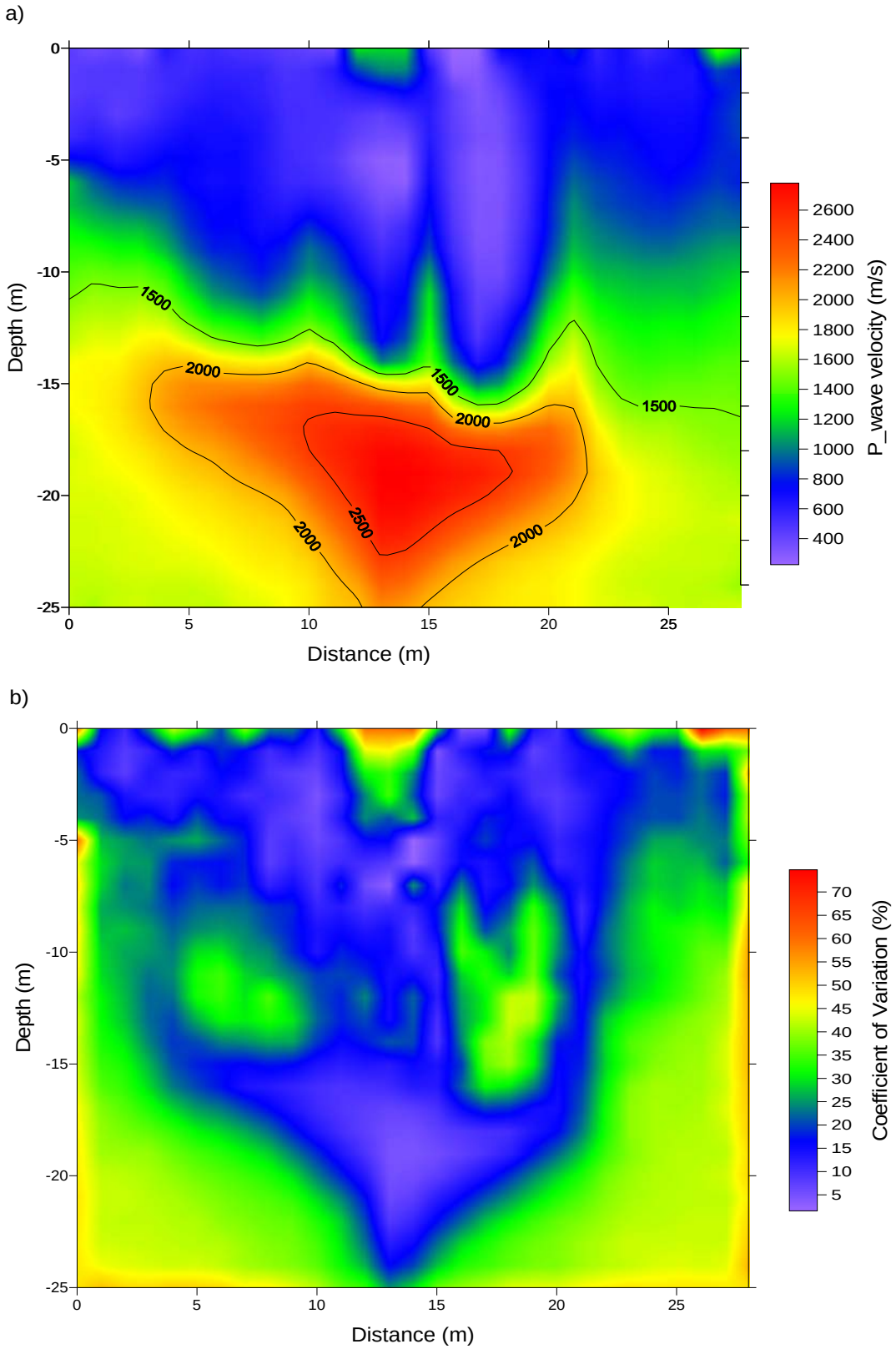

Figure 4-17. Dunedin revised borehole data: a) inverted model, and b) uncertainty

much more difficult to pick credible and consistent arrival times after the first arrival. Second, there are considerably less raypaths available in this model since no raypaths are available from the surface array below a depth of 6 m (all the first arrivals are due to refractions off of the water table). Nevertheless, the tomogram does appear credible, as it reflects P-wave velocities consistent with soil in the upper portion, and the dense clay/limestone layers followed by limestone bedrock below 15 m. Clearly, in this case, it is also observed that the addition of a borehole significantly improves the resolution of the inverted profile, and increases the depth of investigation. Credible characterization of the bedrock is only obtained from the inversion of the borehole data; nothing is learned about the soil and/or rock below 6 m from the surface array.

4.4 Chapter Summary

The global inversion scheme presented in chapter 3 was used on many synthetic and real test data sets. This inversion provides a suite of final models clustering around the global solution, and having comparable least-squared error. This provides an inverted model by averaging all of these models to mitigate the influence of noise and the non-uniqueness of the inversion solutions, and also determining the uncertainty associated with the inverted model. A comparison of inversion results utilizing the combined borehole and surface data against inversion results developed using just the surface data, suggests that significant additional resolution of inverted profiles at depth are obtained, and uncertainties are significantly reduced with the addition of a borehole. This is particularly attractive for characterizing a rock mass underlying a surface soil layer.

Employed for site characterization of deep foundation design, refraction tomography using combined surface and borehole data provides credible information of material at the socket, and has potential to detect anomalies near the socket. This becomes very important, because the material at and near the socket often carries a majority of load from a deep foundation. The

inversion results of the combined data, including inverted profiles and associated uncertainties, enable characterization of spatial variability in geotechnical engineering physical parameters of subsurface formations useful in the design of deep foundations. This could be particularly useful in implementing the new LRFD design methodology that can explicitly account for spatial variability and uncertainty in design parameters.

CHAPTER 5
INVERSION OF FULL WAVEFORMS USING SIMULATED ANNEALING

5.1 Introduction

The technique using combined travel times presented in chapter 4 demonstrates a great capability of characterizing anomalies in subsurface profiles. However, the method requires borehole data that is not always available. This chapter suggests a possible solution by using an inversion of full waveforms to solve problems of 2-D reverse models with only surface data.

The presented technique is based on a finite-difference solution of the 2-D elastic wave equation in the time-distance domain. The strength of this approach is the ability to generate all possible wave types (body waves and surface waves), and to simulate and accurately model complex seismic wave fields that are then compared with observed data to deduce complex subsurface properties. The technique uses the full information of elastic wave fields to increase resolution of inversion results, especially dealing with reverse models. It also employs a global inversion technique, simulated annealing, to invert the full wave fields for near-surface velocity profiles.

The most important advantage of simulated annealing is it avoids being trapped in local minima, and thus to allow final inversion results to be independent of the initial model. However, this technique can require significant computer time, especially if the model contains a large number of model parameters. This disadvantage is reduced herein by using a fast forwarding model solution, and by assuming that interfaces within a medium are multilinear in order to limit the number of model parameters.

The technique is first tested on many different synthetic data sets created from challenging reverse models with high-velocity and low-velocity layers at different depths that are hardly inverted by traditional inversion methods using only the dispersion property of Rayleigh waves.

It is then applied to real experimental data sets, and the inversion results are compared to invasive test results, including those of crosshole, SPT N-value, and material log, or compared to results of independent refraction tests. Inversion results from both synthetic and experimental data show superiority of this technique over traditional methods.

5.2 Methodology

5.2.1 Forward Modeling

Virieux (1986) presented a finite-difference scheme to solve the first-order linear partial differential equation describing elastic wave propagation on a staggered grid. For the 2-D case, the following two sets of equations are solved:

Equations governing particle velocity:

$$\begin{cases} \dfrac{\partial v_x}{\partial t} = \dfrac{1}{\rho}\left(\dfrac{\partial \sigma_{xx}}{\partial x} + \dfrac{\partial \sigma_{xz}}{\partial z}\right) \\ \dfrac{\partial v_z}{\partial t} = \dfrac{1}{\rho}\left(\dfrac{\partial \sigma_{xz}}{\partial x} + \dfrac{\partial \sigma_{zz}}{\partial z}\right) \end{cases} \tag{5.1}$$

Equations governing stress tensor:

$$\begin{cases} \dfrac{\partial \sigma_{xx}}{\partial t} = (\lambda + 2\mu)\dfrac{\partial v_x}{\partial x} + \lambda \dfrac{\partial v_z}{\partial z} \\ \dfrac{\partial \sigma_{zz}}{\partial t} = (\lambda + 2\mu)\dfrac{\partial v_z}{\partial z} + \lambda \dfrac{\partial v_x}{\partial x} \\ \dfrac{\partial \sigma_{xz}}{\partial t} = \mu\left(\dfrac{\partial v_x}{\partial z} + \dfrac{\partial v_z}{\partial x}\right) \end{cases} \tag{5.2}$$

In these equations, (v_x, v_z) is the particle velocity vector, $(\sigma_{xx}, \sigma_{zz}, \sigma_{xz})$ is the stress tensor, ρ is mass density and μ, λ are Lame's coefficients.

Because of the need of a fast forwarding model solution for the global optimization method, some special boundary conditions are employed in this study to allow limiting the medium to the smallest possible size. These boundary conditions are as follows:

Free-surface condition on top:

$$\begin{cases} \sigma_{xz} = 0 \\ \sigma_{zz} = 0 \end{cases} \tag{5.3}$$

or equivalently from equation (5.2) and (5.3):

$$\begin{cases} \dfrac{\partial v_x}{\partial z} = -\dfrac{\partial v_z}{\partial x} \\ \dfrac{\partial v_z}{\partial z} = -\dfrac{\lambda}{\lambda + 2\mu}\dfrac{\partial v_x}{\partial x} \end{cases} \tag{5.4}$$

Symmetrical condition at left-hand side (load line):

$$\begin{cases} \sigma_{xz} = 0 \\ v_x = 0 \end{cases} \tag{5.5}$$

Absorbing condition A1 (Clayton and Engquist, 1977) at bottom:

$$\begin{cases} \dfrac{\partial v_x}{\partial t} + Vs\dfrac{\partial v_x}{\partial z} = 0 \\ \dfrac{\partial v_z}{\partial t} + Vp\dfrac{\partial v_z}{\partial z} = 0 \end{cases} \tag{5.6}$$

and at right-hand side:

$$\begin{cases} \dfrac{\partial v_x}{\partial t} + Vs\dfrac{\partial v_x}{\partial x} = 0 \\ \dfrac{\partial v_z}{\partial t} + Vp\dfrac{\partial v_z}{\partial x} = 0 \end{cases} \tag{5.7}$$

where V_s, V_p are shear and P-wave velocities.

Derivatives are discretized by using center finite-differences. Assuming equations are verified at nodes, discretization leads to a unique staggered grid, as shown at Figure 5.1. The explicit numerical scheme (Virieux, 1986), equivalent to the systems (5.1) and (5.2), is:

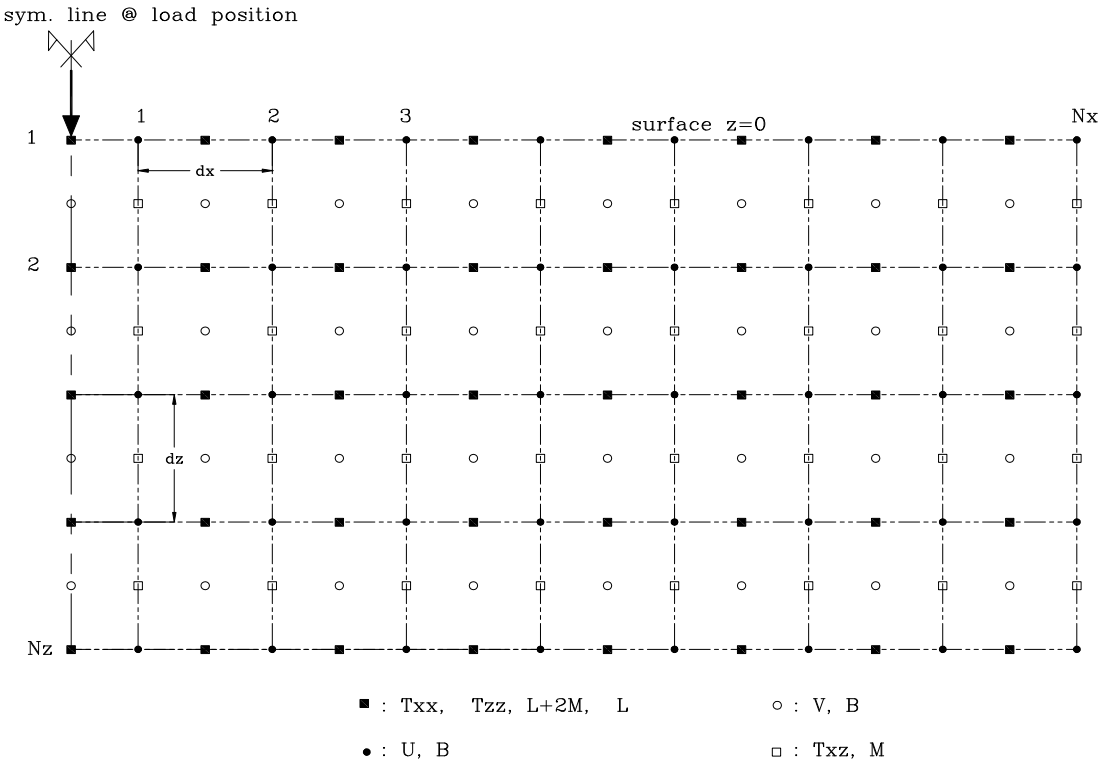

Figure 5-1. Discretization of the medium on a staggered grid

$$U_{i,j}^{k+1/2} = U_{i,j}^{k-1/2} + B_{i,j}\frac{\Delta t}{\Delta x}\left(Txx_{i+1/2,j}^{k} - Txx_{i-1/2,j}^{k}\right) + B_{i,j}\frac{\Delta t}{\Delta z}\left(Txz_{i,j+1/2}^{k} - Txz_{i,j-1/2}^{k}\right)$$

$$V_{i+1/2,j+1/2}^{k+1/2} = V_{i+1/2,j+1/2}^{k-1/2} + B_{i+1/2,j+1/2}\frac{\Delta t}{\Delta x}\left(Txz_{i+1,j+1/2}^{k} - Txz_{i,j+1/2}^{k}\right)$$
$$+ B_{i+1/2,j+1/2}\frac{\Delta t}{\Delta z}\left(Tzz_{i+1/2,j+1}^{k} - Txz_{i+1/2,j}^{k}\right)$$

$$Txx_{i+1/2,j}^{k+1} = Txx_{i+1/2,j}^{k} + \left(L+2M\right)_{i+1/2,j}\frac{\Delta t}{\Delta x}\left(U_{i+1,j}^{k+1/2} - U_{i,j}^{k+1/2}\right)$$
$$+ L_{i+1/2,j}\frac{\Delta t}{\Delta z}\left(V_{i+1/2,j+1/2}^{k+1/2} - U_{i+1/2,j-1/2}^{k+1/2}\right) \tag{5.8}$$

$$Tzz_{i+1/2,j}^{k+1} = Tzz_{i+1/2,j}^{k} + \left(L+2M\right)_{i+1/2,j}\frac{\Delta t}{\Delta z}\left(V_{i+1/2,j+1/2}^{k+1/2} - V_{i+1/2,j-1/2}^{k+1/2}\right)$$
$$+ L_{i+1/2,j}\frac{\Delta t}{\Delta x}\left(U_{i+1,j}^{k+1/2} - U_{i,j}^{k+1/2}\right)$$

$$Txz_{i,j+1/2}^{k+1} = Txz_{i,j+1/2}^{k} + M_{i,j+1/2}\frac{\Delta t}{\Delta z}\left(U_{i,j+1}^{k+1/2} - U_{i,j}^{k+1/2}\right) + M_{i,j+1/2}\frac{\Delta t}{\Delta x}\left(V_{i+1/2,j+1/2}^{k+1/2} - V_{i-1/2,j+1/2}^{k+1/2}\right)$$

In these equations, k, i, and j are the indices for time, x-axis, and z-axis discretization, respectively, and Δt, Δx, and Δz are grid steps for time, x-axis and z-axis, respectively. Numerical velocity (U,V)=(v_x,v_z) at time (k+1/2) Δt, and numerical stress (Txx, Tzz, Txz)= (σ_{xx}, σ_{zz}, σ_{xz}) at time (k+1) Δt, are computed explicitly from velocity at time (k-1/2) Δt and stress at time k Δt. B is $1/\rho$ and M, L are Lame's coefficients (μ, λ).

For free-surface condition, the geometry is chosen so that the free surface is located exactly through the upper part of the staggered grid-points at z=0, that is, σ_{xx}, σ_{zz}, and v_x are located on the free surface. To update the wave field in the proximity of the free surface, both vertical velocity v_z and shear stress σ_{xz} of one row above the surface are required. By imaging σ_{xz} as an odd function around the free surface, it is assured that σ_{xz} =0 there. From equation (5.4), the v_z above the free surface can be obtained as:

$$V_{i+1/2,1/2}^{k+1/2} = V_{i+1/2,3/2}^{k+1/2} + \frac{L_{i+1/2,1}}{(L+2M)_{i+1/2,1}} \frac{\Delta z}{\Delta x} \left(U_{i+1,1}^{k+1/2} - U_{i,1}^{k+1/2} \right) . \qquad (5.9)$$

Similarly, σ_{xz} and v_x are assumed odd functions around the symmetrical line to update the wave field in the proximity of left-hand side boundary. For absorbing boundary conditions (5.6) and (5.7), a backward finite-difference scheme is used in both the spatial and time directions to update velocity components v_x, v_z at vertical gridlines Nx, Nx-1/2 for the right-hand side boundary, and at horizontal gridlines Nz, Nz-1/2 for the bottom boundary.

The initial conditions are set to satisfy equilibrium at time t=0, i.e., stress and velocity are zero everywhere in the medium. Then, the medium is perturbed by changing the vertical stress σ_{zz} at the source that is modeled as a triangle wavelet (Figure 5-4a), or a Ricker wavelet R(t) (Figure 5-4b):

$$R(t) = \left(1 - 2\pi^2 f_c^2 (t - t_0)^2\right) \cdot \exp\left(-\pi^2 f_c^2 (t - t_0)^2\right) , \qquad (5.10)$$

where f_c is the center of the frequency band and t_0 is time shift.

For homogeneous media, the numerical stability condition for this explicit scheme is:

$$V_p \Delta t \sqrt{\frac{1}{\Delta x^2 + \Delta z^2}} \leq 1, \tag{5.11}$$

and for heterogeneous cases, the V_p value in the equation (5.11) should be the maximum P-wave velocity in the media. Δx and Δz are selected to satisfy at least ten points per minimum expected wavelength to avoid numerical dispersion, and then Δt is selected from the stability condition. In the inversion process, Δt is expected to change due to different input V_p values, thus, the wave fields are interpolated to a fixed time interval for comparing to measured wave fields.

The code was developed in Matlab in which all stresses and particle velocities are calculated in matrix forms at each time step, and then advanced along the time direction. The accuracy of this finite-difference method (FDM) was checked by comparing its wave field to that generated by a finite element method (FEM) that is available in commercial software Plaxis2D. Figure 5.2 shows that results from the two methods are almost identical. By using FDM, significant computer time can be saved. On the same standard computer, FDM required less than 1 second, while FEM required a few minutes to generate the wave field shown in Figure 5.2. The fast finite difference solution makes it possible to apply simulated annealing as a global optimization method for inversion, as presented in the next section.

5.2.2 Optimization Method

Rather than discussing the analogy of simulated annealing that has been well described by Sen and Stoffa (1995), a brief description of the process used herein is as follows:

1. Select an initial model P so that each component P_i satisfies $P_i^{\min} \leq P_i \leq P_i^{\max}$, and then calculate the least-squared error E as:

$$E = \frac{1}{N} \sum_{k=1}^{N} \left[d_k - g_k(P) \right]^2 , \tag{5.12}$$

where d_k and g_k are the *kth* observed and computed responses, respectively, and N is the number of observations, equal to the number of receivers times the number of time steps.

a) b)

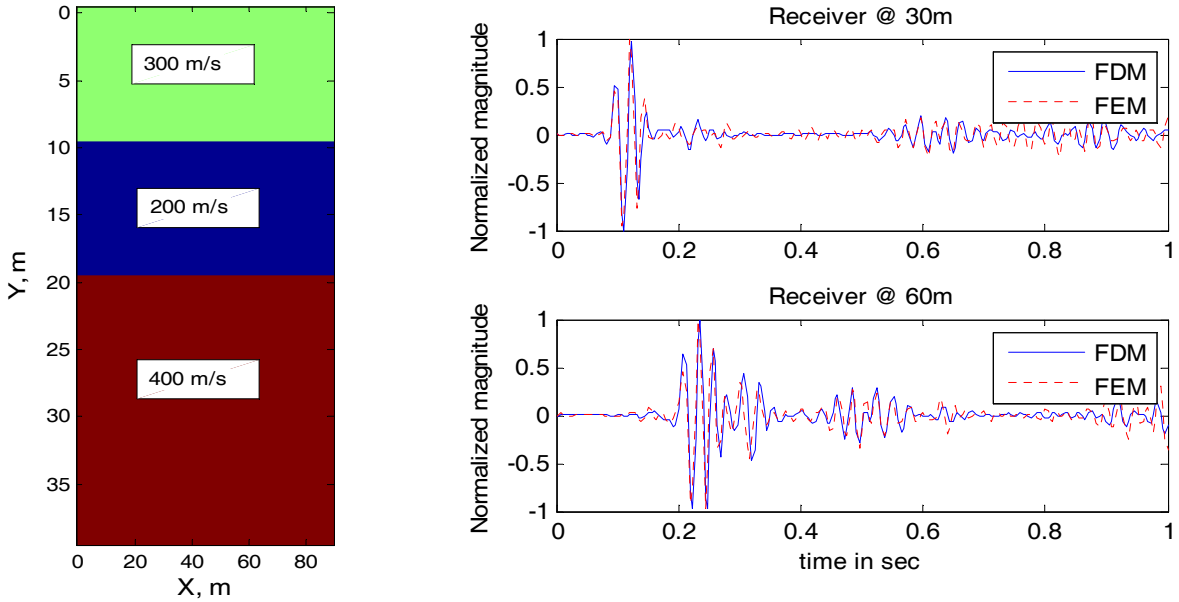

Figure 5-2. Comparison between wave fields generated by FDM and FEM: a) input model shear velocity V_s, and b) wave fields at 2 points x=30m and x=60m on the surface

2. Following the idea of Ingber (1989, 1993), randomly select one parameter (say *ith* parameter) and perturb it according to the Cauchy probability distribution. The updating factor y_i for the *ith* parameter is computed from the equation:

$$y_i = \mathrm{sgn}(u_i - 0.5)\frac{T}{T_0}\left[\left(1+\frac{T_0}{T}\right)^{|2u_i-1|} - 1\right]. \qquad (5.13)$$

In the above equation, y_i varies between -1 and +1, u_i is a random number between 0 and 1, T is the current temperature, and T_0 is the initial temperature. Thus, the parameter P_i is updated to P_i^{j+1} from its previous value P_i^j by:

$$P_i^{j+1} = P_i^j + y_i(P_i^{\max} - P_i^{\min}). \qquad (5.14)$$

The random number u_i sometimes needs to be reselected to guarantee that the value P_i^{j+1} from equation (5.14) satisfies the constraint $P_i^{\min} \le P_i^{j+1} \le P_i^{\max}$. Following the process described, the new model is now obtained and then the least-squared error corresponding to this new model is calculated.

3. The new model is unconditionally accepted if its least-squared error is smaller than that from the previous model, and conditionally accepted if its least-squared error is larger with the following probability:

$$p = \exp\left(-\frac{\Delta E}{T}\right), \tag{5.15}$$

where ΔE is the positive difference between the least-squared errors of the two models.

4. Repeat steps 2 and 3 until a desired number of accepted models is completed, then reduce the temperature to the next level according to a schedule:

$$T(k) = \frac{T(k-1)}{2}\ , \tag{5.16}$$

where *T(k)* is the temperature at the *kth* level.

The criterion for convergence requires that the relative difference between the maximum and minimum least-squared errors from all accepted models at a particular temperature to become very small (empirically say between 0.5% and 1%). If the criterion for convergence is not satisfied, the temperature is reduced to the next level. At a sufficiently low temperature, the accepted models are in the vicinity of the global minimum, and the optimization converges.

The selection of an initial temperature is important. Selecting a high value leads to unnecessary computations, whereas a low value leads to a local solution. In this study, the initial temperature is taken as the nearest lower power of ten to the least-squared error, e.g., if the least-squared error is 0.35 then the initial value is 0.1. In this way, the initial temperature is usually higher than the critical temperature, and any bias in the initial model will be destroyed.

The cooling schedule is another important parameter in the global optimization using simulated annealing. Many schedules have been tested for inversion problems with the number of model parameters up to 40, and it was found that the number of accepted models at each temperature level should be at least 200 times the number of model parameters, and the temperature needs to reach a very low value to obtain the global solution. In this study, the final temperature is about 10^{-4} to 10^{-5} when the initial temperature is 0.1. When the number of model parameters increases, the procedure needs a slower schedule, and the time of computation

increases in order to get the global solution. Therefore, the cooling schedule should be selected with care, particularly when dealing with a large number of model parameters.

5.3 Applications

5.3.1 Applications on Synthetic Data

Synthetic models refer to earth models whose velocity profile is assumed or known a priori. Using a known velocity structure, wave field data is calculated for an assumed test layout. This wave field data is then input to the inversion program as if it were data collected from a field test ("observed" data), and velocity structure (inverted model) is calculated from the observed data. By comparison of the inverted model against the true model, the capability of the inversion technique is appraised.

5.3.1.1 One-dimensional synthetic models

Two challenging 1-D models (1 and 2), that include high- and low-velocity layers are presented in this section. The models are from Tokimatsu et al. (1992), and were previously used by O'Neill (2003) for studies of inversion using surface wave dispersion.

Synthetic model 1

Model 1 consists of a buried low-velocity layer (second layer) between two high-velocity layers, followed by a half-space (Figure 5-3a). The observed wave field was generated in Plaxis2D using 10 receivers at 4-m spacing on the surface, and an active source placed 4 m away from the first receiver. The active source was modeled as a triangle impulsive load (Figure 5-4a), and the source produced a wave field with dominant components between 10 Hz and 30 Hz. The observed wave field (at 10 points from A to J) is presented in Figure 5-5. The figure shows that the magnitude of the wave field decays significantly from point A (closest to the source), to point J (farthest from the source) due to damping. In order to increase the contribution of the far-field signals, the receivers were treated equally by normalizing the maximum magnitude of measured

signals at each receiver to unity before being used for inversion, thus, removing all kinds of damping (material and radiation) in wave propagation.

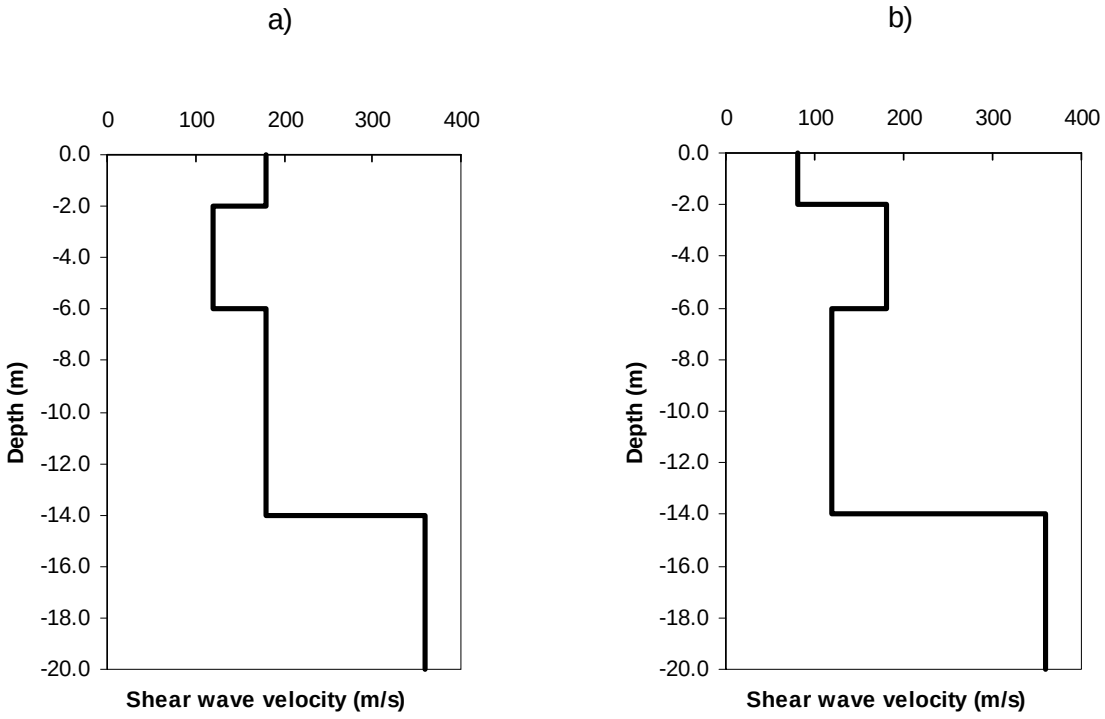

Figure 5-3. Shear wave velocity of 1-D models of Tokimatsu et. al. (1992): a) model 1 and b) model 2

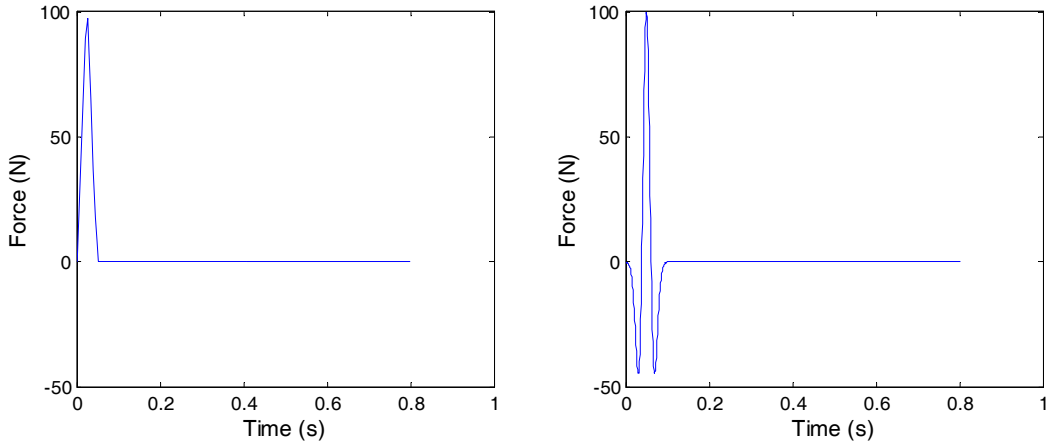

Figure 5-4. Impulsive load: a) triangle wavelet and b) Ricker wavelet

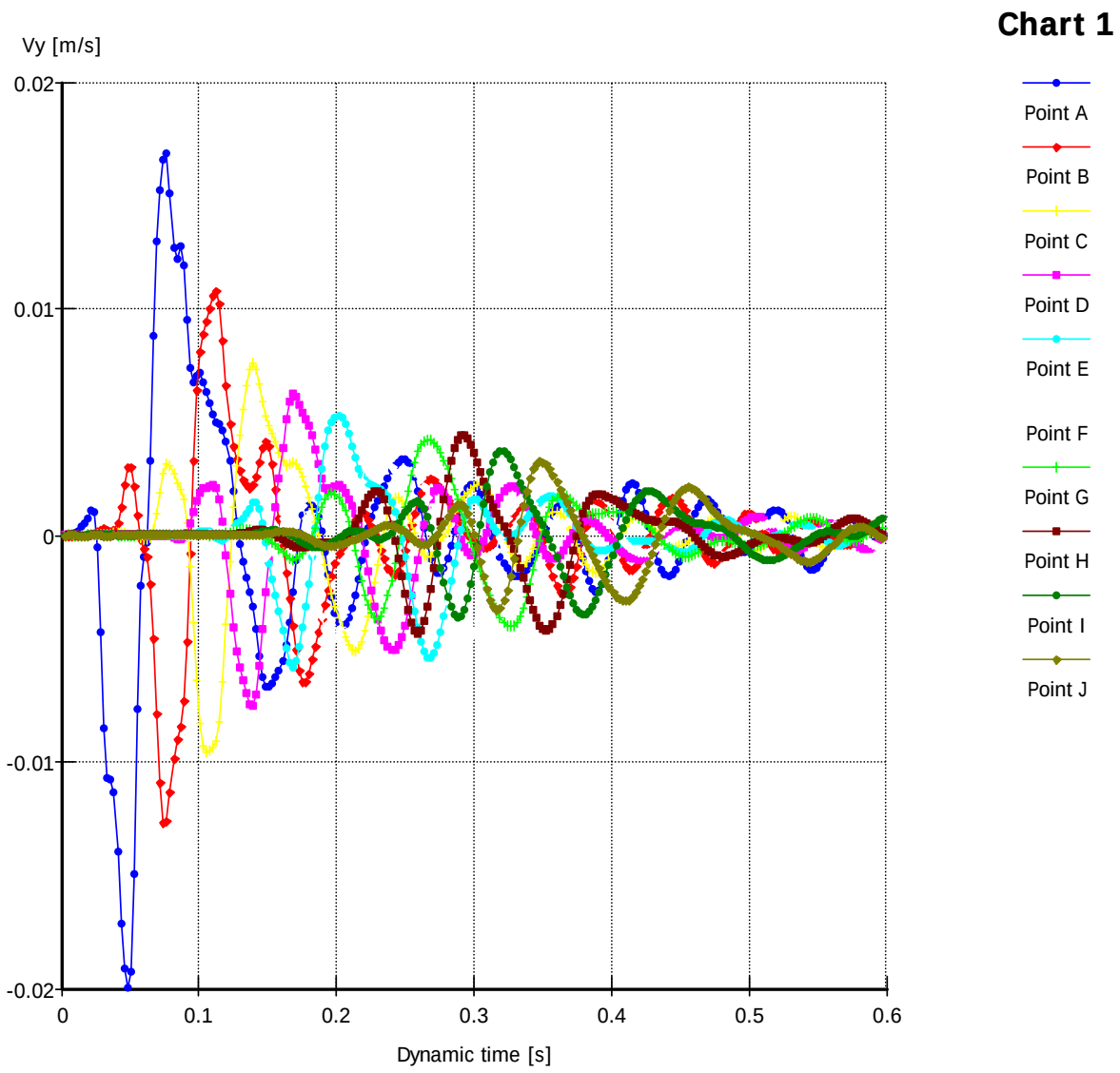

Figure 5-5. Synthetic model 1: particle velocity data from Plaxis2D observed at 10 points (A to J) spaced equally at 4 m on the surface

Before running the inversion, constraints, medium sizes, and the grid size need to be specified. For velocity constraints, S-wave velocities were allowed to vary between 50 m/s and 300 m/s for the 3 layers, and between 200 m/s and 500 m/s for the half-space. For thickness constraints, thicknesses were allowed to vary between 1 m and 5 m for layers 1 and 2, and between 5 m and 10 m for layer 3. For the medium sizes, the medium was selected as 20-m in depth and 60 m wide. The width was extended 20 m horizontally from the last receiver to limit the boundary affect during forward modeling. Finally, based on the receiver spacing and the minimum true S-wave velocity, the grid size was specified as 0.5 m, which can accurately model the maximum frequency of about 30 Hz, at which the criterion of 10 mesh points per wavelength is satisfied.

During inversion, Poisson's ratio and the mass density were kept the same as those used to generate the observed data to limit the number of model parameters to 7 (3 thicknesses and 4 velocities). The inversion began with an initial model of a constant S-wave velocity of 200 m/s, and all thicknesses of 5 m, model parameters were perturbed within the constraints, models were updated, and the temperature was reduced after every 1400 (200 times the number of model parameters) accepted models until the criterion of convergence was satisfied. Convergence was reached when the estimated data was very close to the observed (Figure 5-6), and the least-squared error was reduced from the initial value of 0.2087 to the final value of 0.0240.

Figure 5-6 presents a comparison between the observed and the estimated data. A good match is achieved at every location. Figure 5-7 presents velocity histograms of all accepted models at all temperature levels. At high temperatures, the accepted models are located over a large model space, and accepted velocities are any random value between the constraints. At low

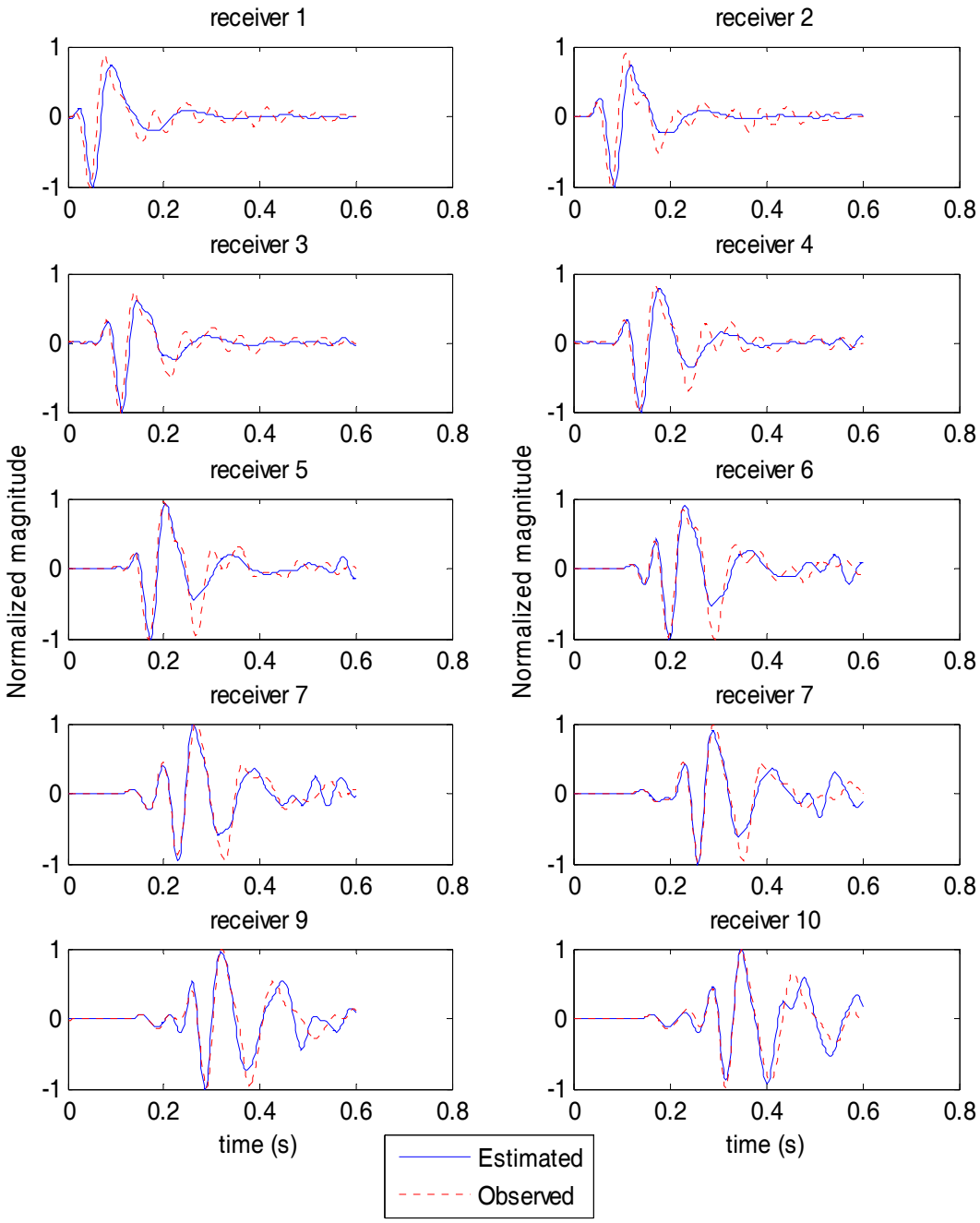

Figure 5-6. Synthetic model 1: comparison between estimated and observed wave fields

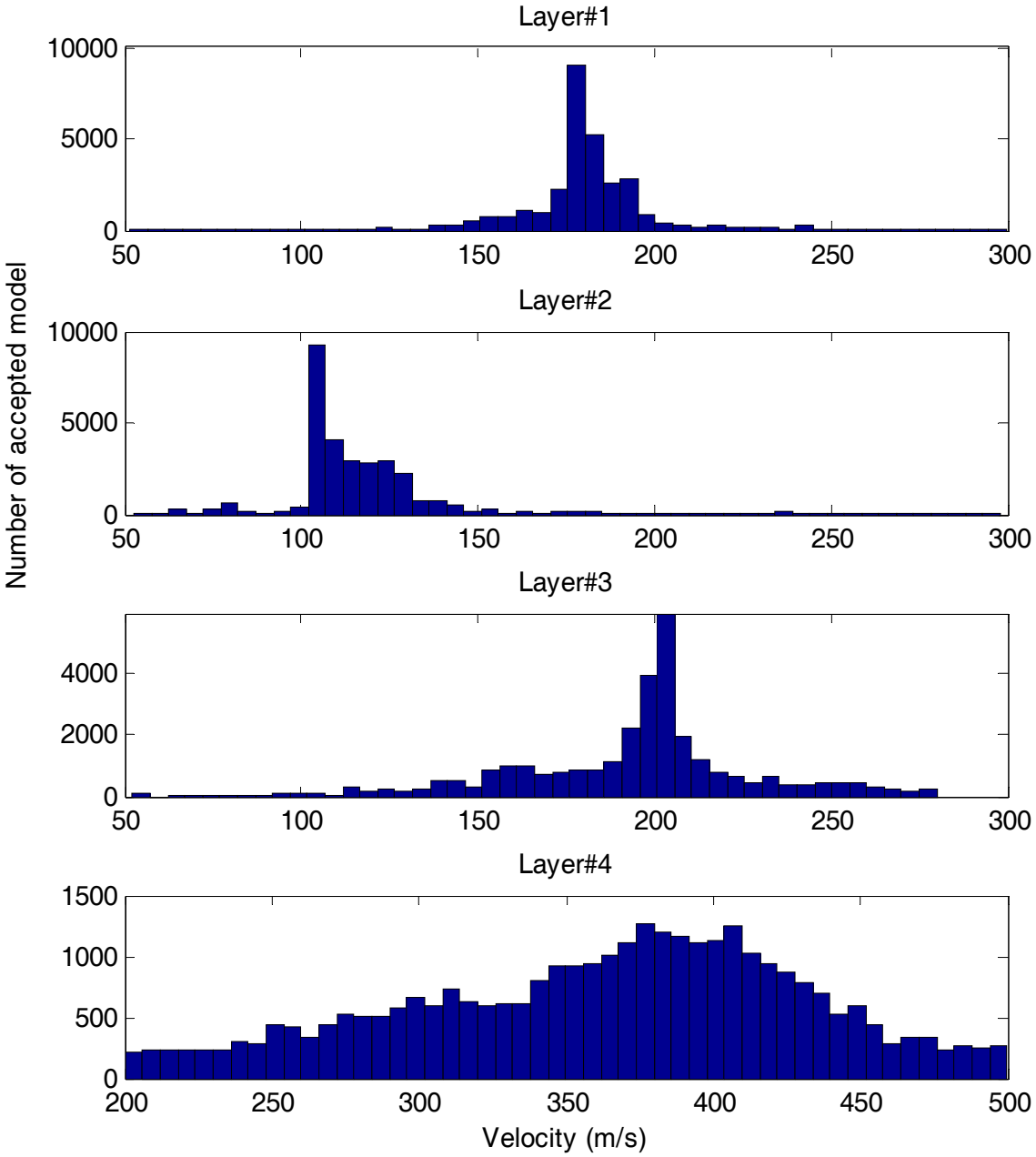

Figure 5-7. Synthetic model 1: velocity histograms from all accepted models

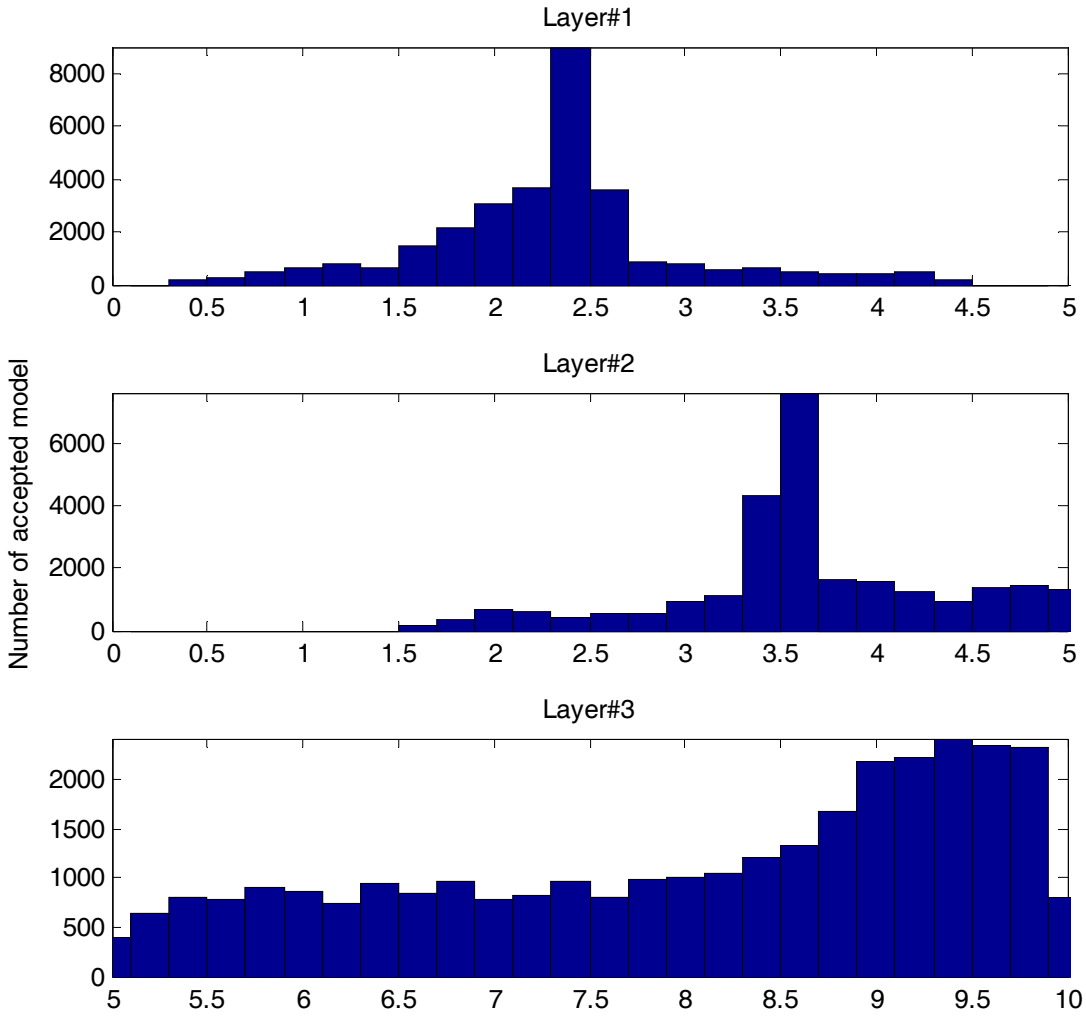

Figure 5-8. Synthetic model 1: thickness histograms from all accepted models

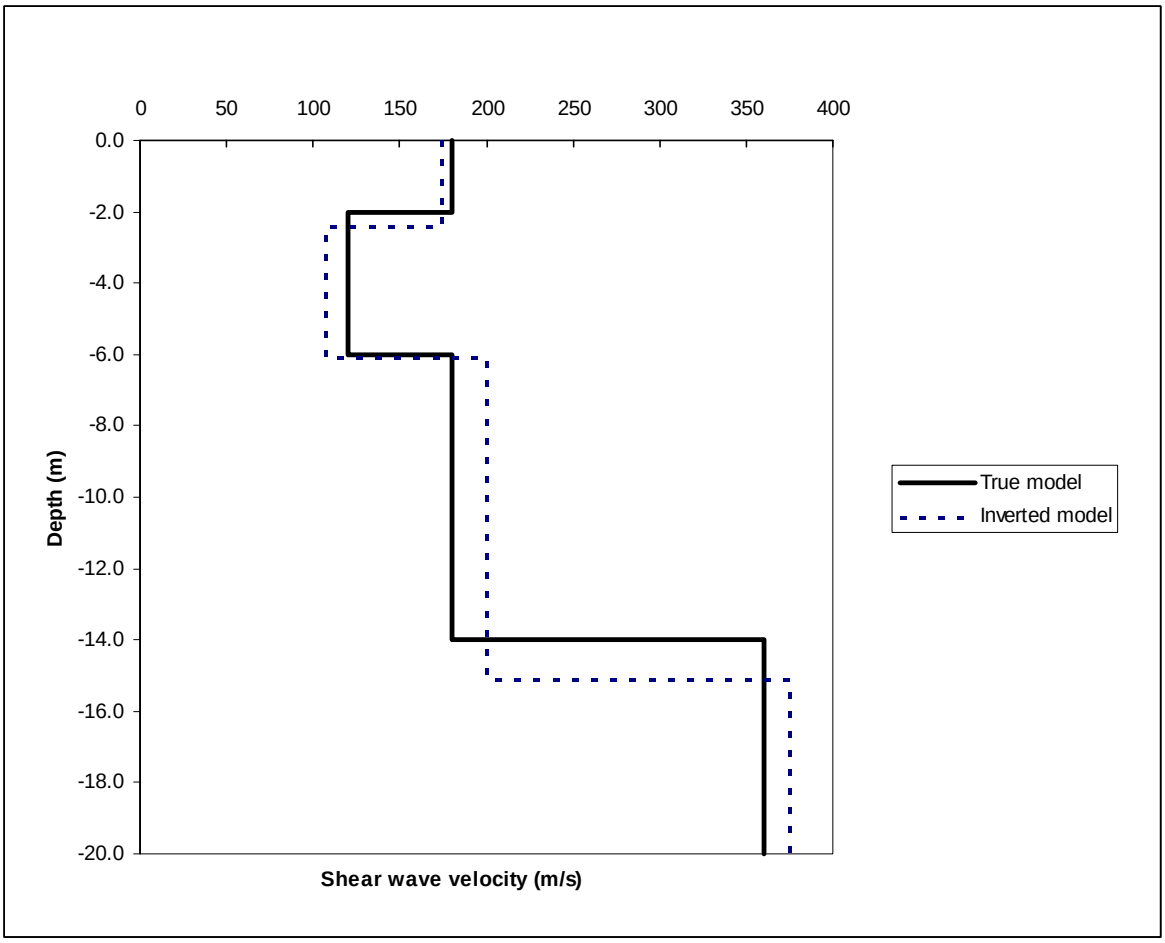

Figure 5-9. Synthetic model 1: comparison between the true and inverted models

temperatures, the accepted models cluster around the global minimum, and the mode values of the histograms are close to those of the true model. Similarly, Figure 5-8 presents thickness histograms of all accepted models, and, again, the mode values are observed to be close to those of the true model.

Figure 5-9 compares the inverted S-wave profile against the true model, and it is observed that the true model is well recovered. The differences of velocities and thicknesses between the true and the inverted models are less than 15%. These differences may be due to the incomparability of the numerical methods used to generate the observed data (FEM) and the estimated data (FDM).

O'Neill (2003) did inversion studies on this same model using dispersion data and a local inversion scheme. Even though the same synthetic modeling methods were used for the observed and estimated dispersion data, he found that the true model was hardly recovered. It could only be recovered if the true depth of the half-space was fixed during the inversion, and the initial model was close to the true model, such as the initial model having the true depth interfaces, and a reasonable shear wave velocity.

Thus, it is clear that the technique presented here requires much less a priori information to invert the true model. The superiority of the technique is attributed to the full waveform data used for inversion that is more sensitive to a low-velocity layer (LVL) than the dispersion data, and the advantage of a global inversion scheme that is independent of the initial model.

Synthetic model 2

Model 2 consists of a buried high-velocity layer (second layer) between two low-velocity layers, followed by a half-space (Figure 5-3b). Similar to model 1, the observed wave field

(Figure 5-10) was generated in Plaxis2D using 10 receivers at 4-m spacing on the surface, and an impulsive source (Figure 5-4a) placed 4 m away from the first receiver.

In the same manner as model 1, an inversion was conducted using the observed data of model 2. During the inversion, the least-squared error decreased from 0.2025 for an initial model of a constant velocity of 200 m/s, to 0.0378 for the final accepted model. Again, the final inverted model (Figure 5-14) is a good recovery of the true model, correctly inverting both interfaces and velocities. The good recovery of the velocity model leads to a good match between the observed and estimated wave fields (Figure 5-11). The velocity and thickness histograms of all accepted models are also shown in Figures 5-12 and 5-13, whose mode values are close to the true model. Similar to model 1, O'Neill (2003) found that this true model could only be recovered if the true depth of the half-space was fixed during the inversion, and the initial model had the true depth interfaces and a reasonable shear wave velocity.

5.3.1.2 Two-dimensional synthetic models

Three 2-D synthetic models (models 3, 4, and 5) are presented here. The first two models consist of linear interfaces, and they can be inverted by data from a few receivers on the surface. The two synthetic data sets from these simple configurations were generated by the commercial software Plaxis2D. The last model consists of multilinear interfaces that require data from many receivers along the surface. For convenience, the synthetic data set from this more complicated configuration was generated by the finite-difference solution.

Synthetic model 3

Model 3 consists of a buried high-velocity layer (second layer) between two low-velocity layers, followed by a half-space (Figure 5-15a). The medium is extended 20 m from the last receiver to limit the boundary affect.

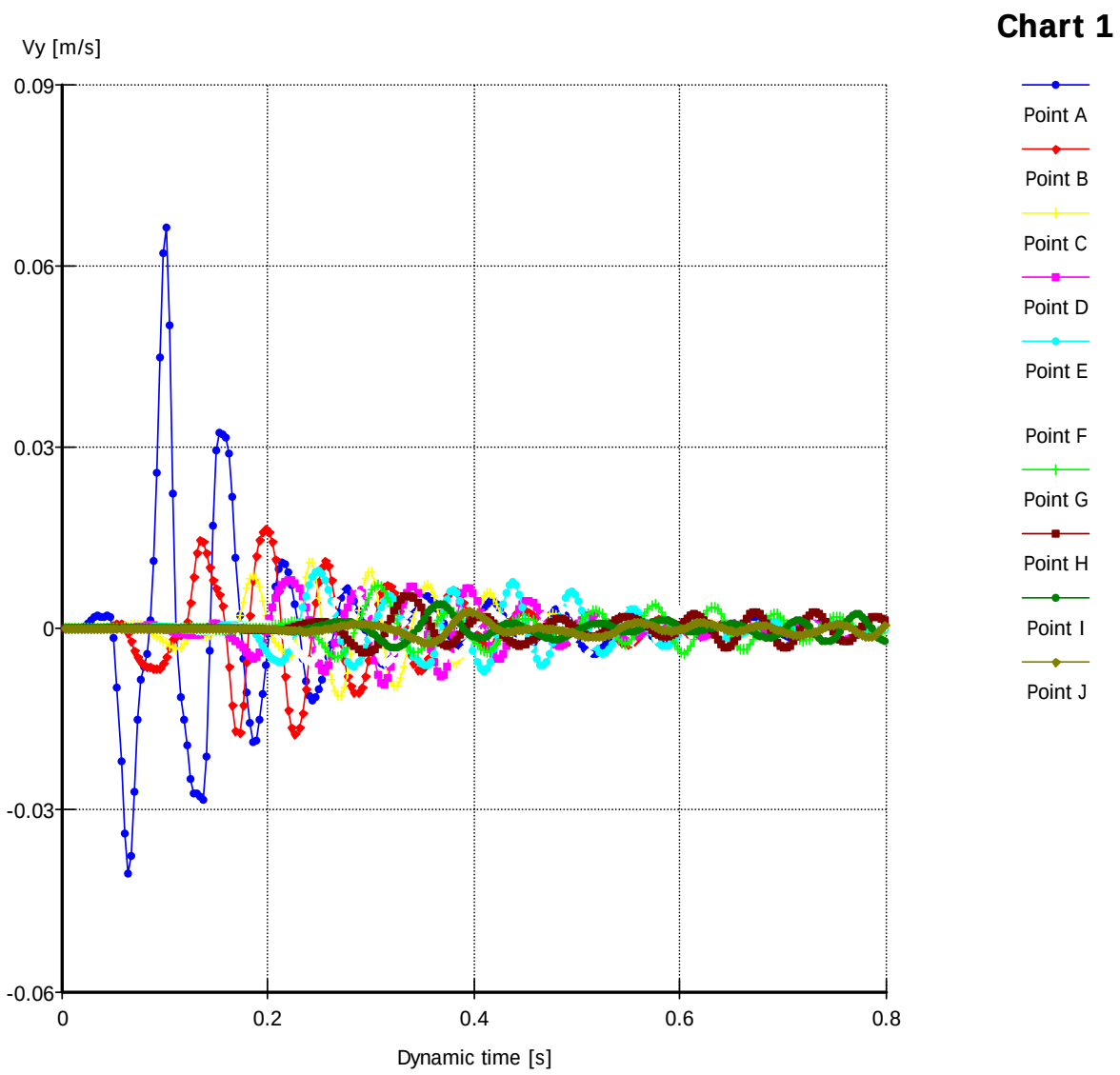

Figure 5-10. Synthetic model 2: particle velocity data from Plaxis2D observed at 10 points (A to J) spaced equally at 4 m on the surface

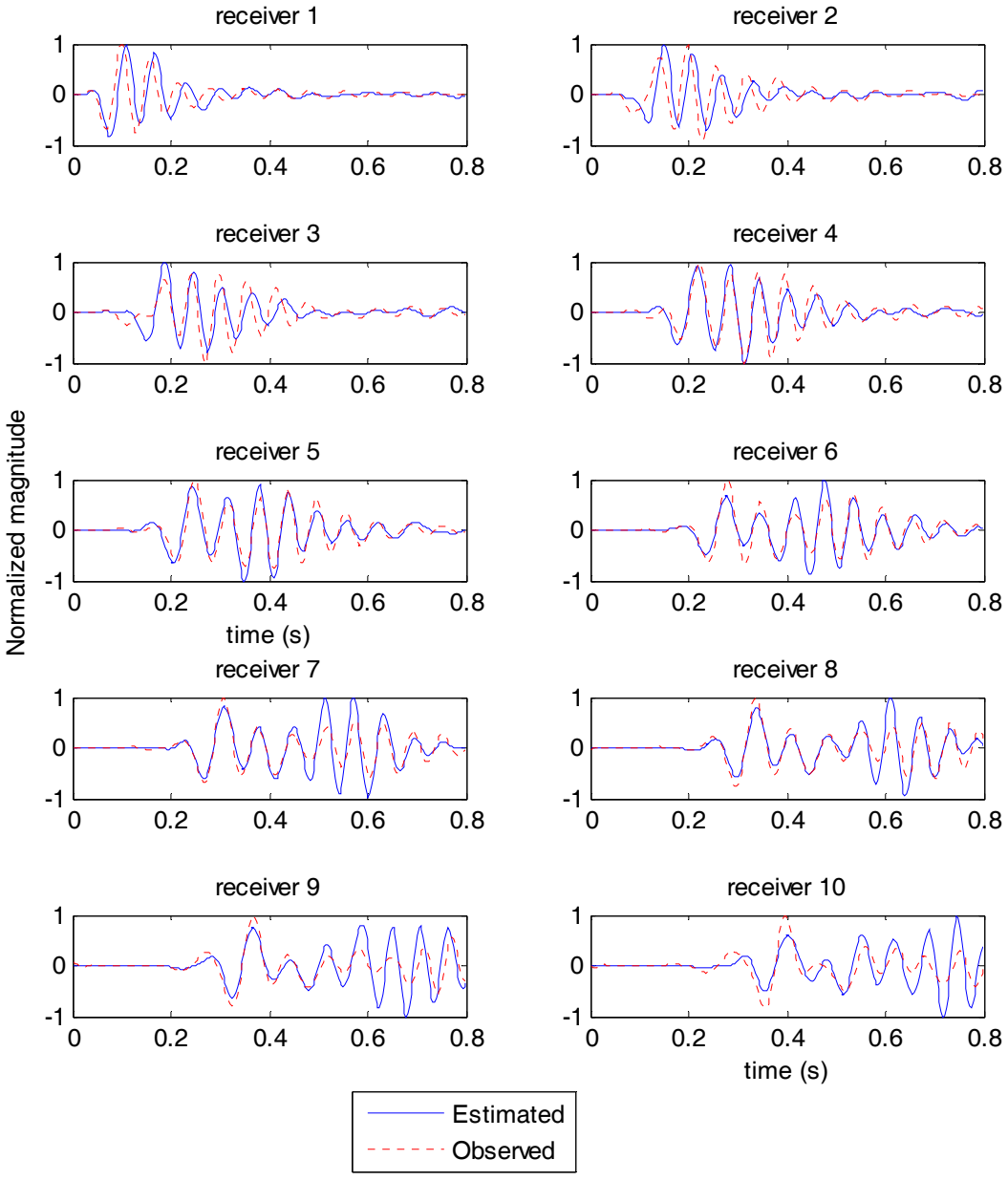

Figure 5-11. Synthetic model 2: comparison between estimated and observed wave fields

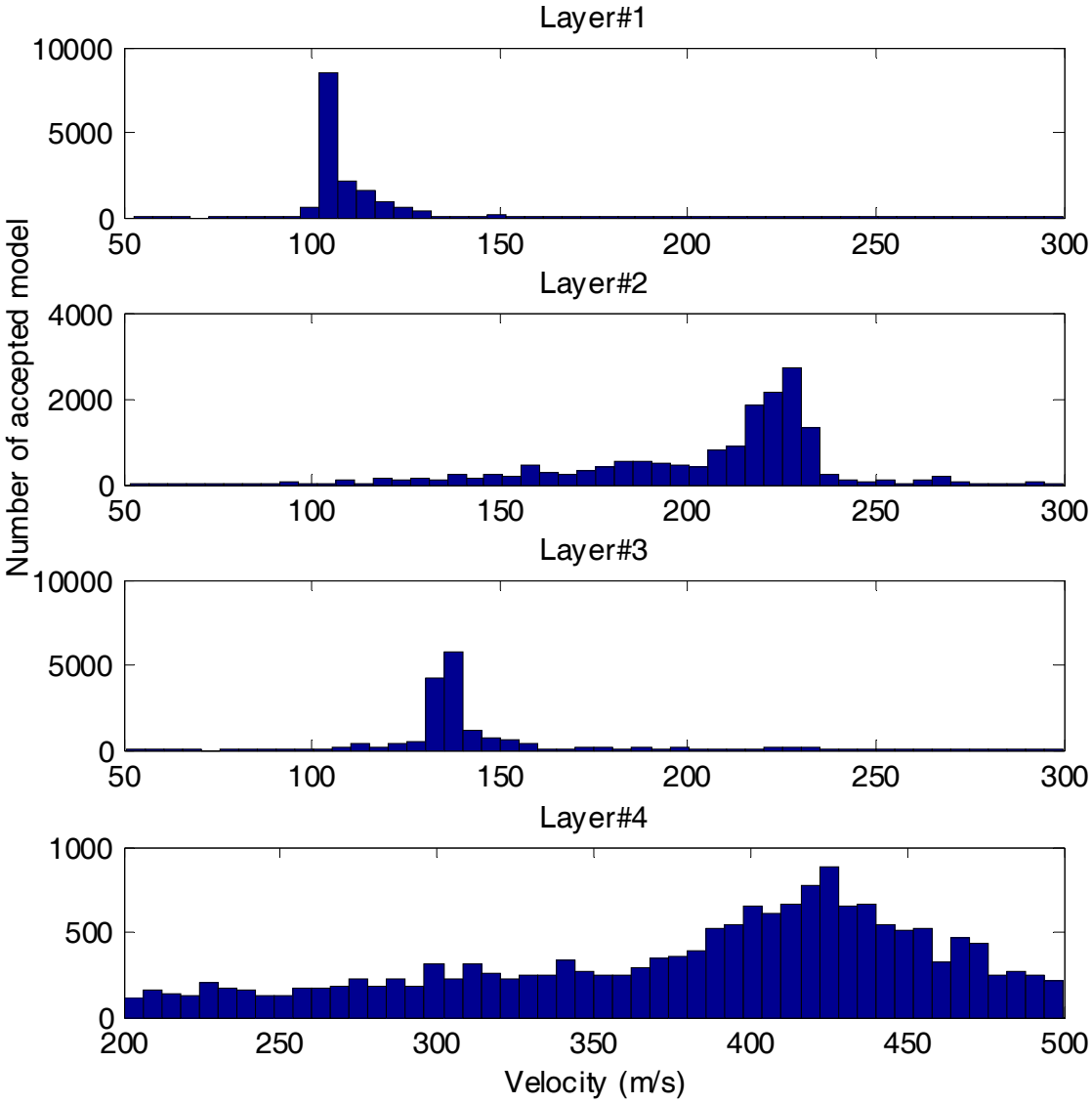

Figure 5-12. Synthetic model 2: velocity histograms from all accepted models

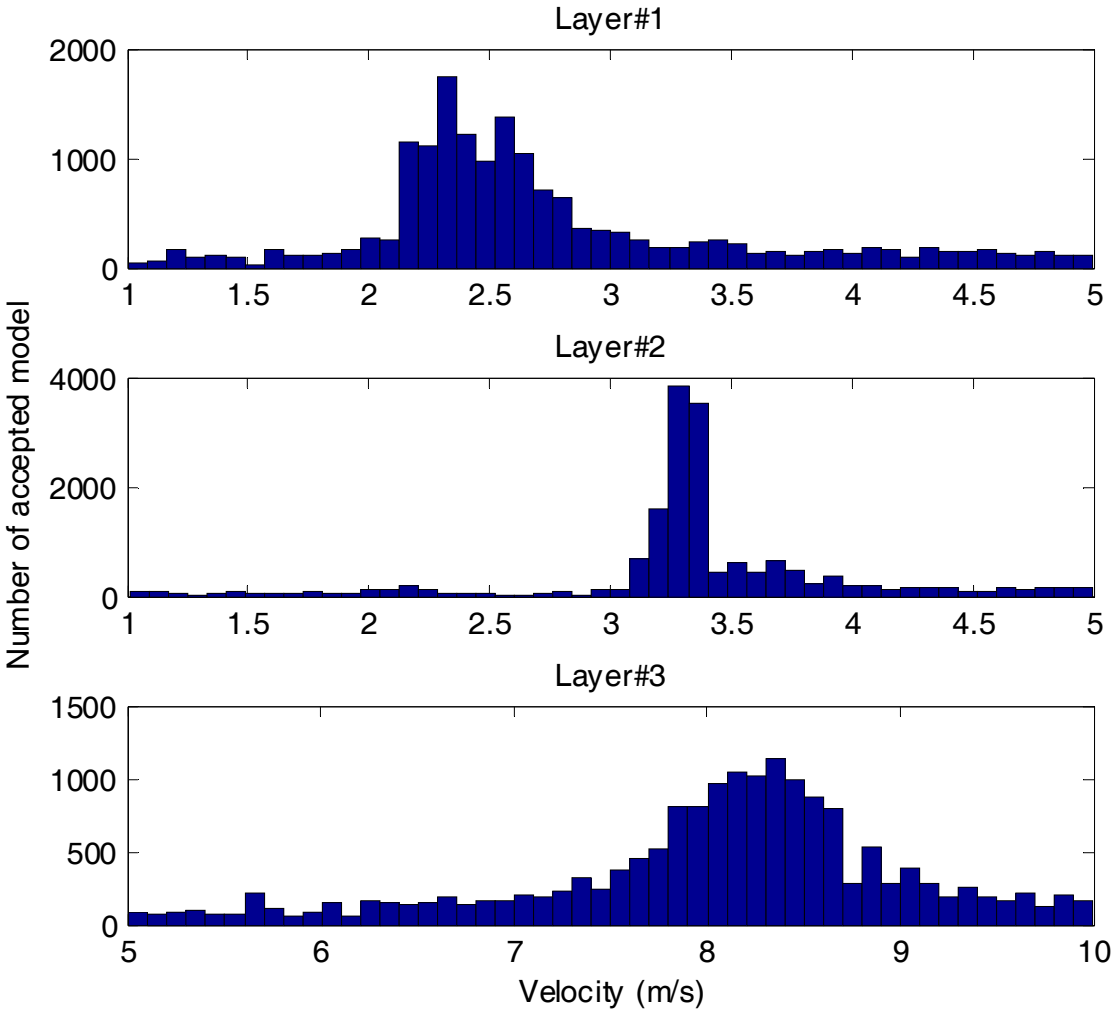

Figure 5-13. Synthetic model 2: thickness histograms from all accepted models

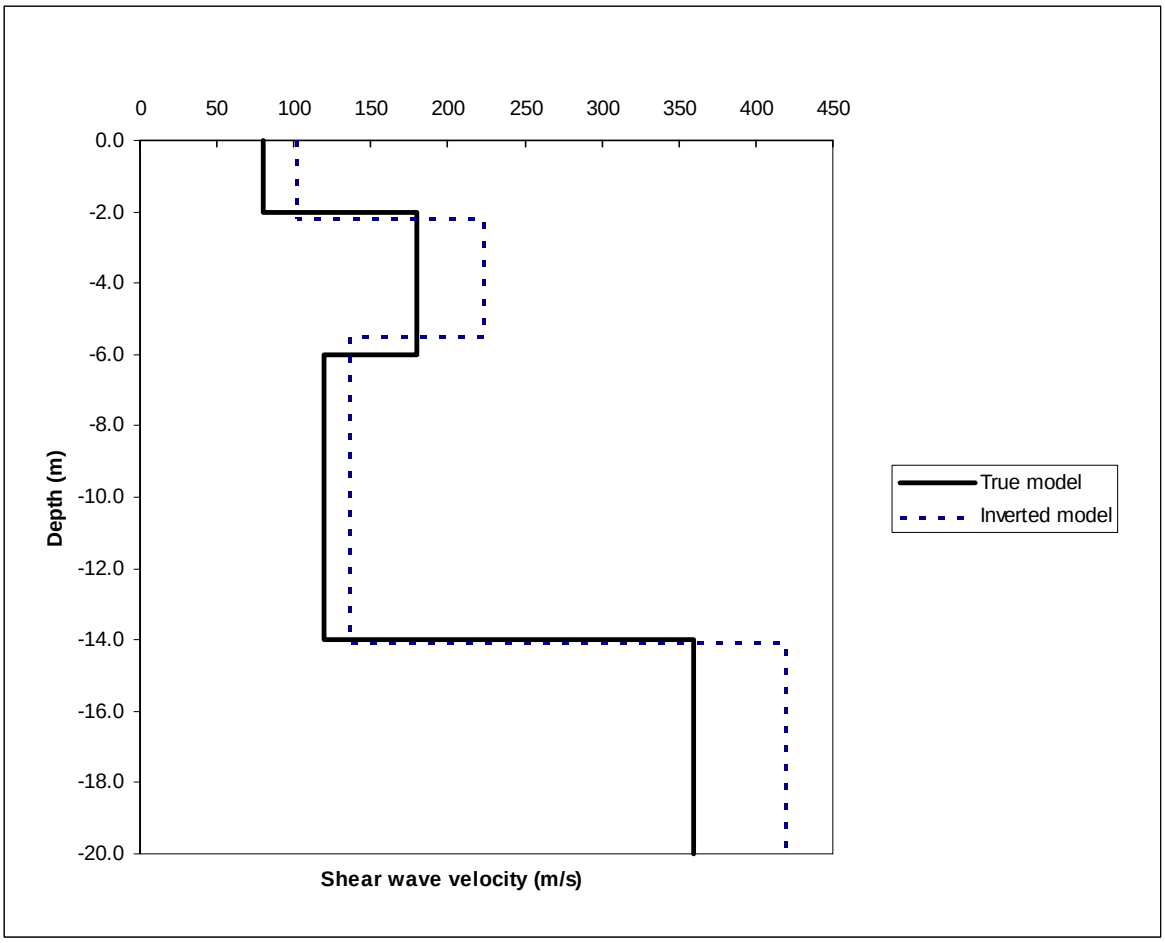

Figure 5-14. Synthetic model 2: comparison between the true and inverted models

a)

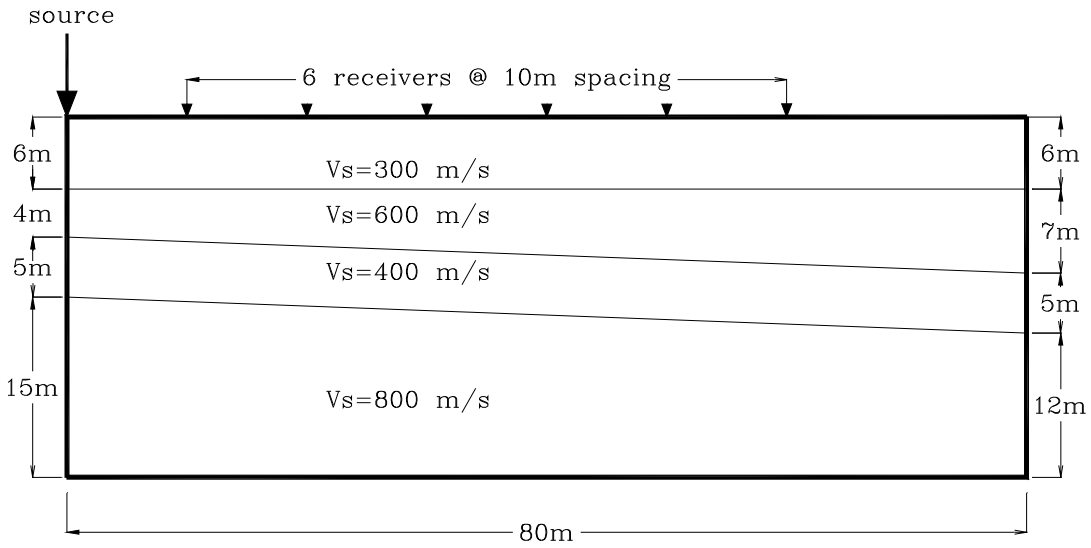

b)

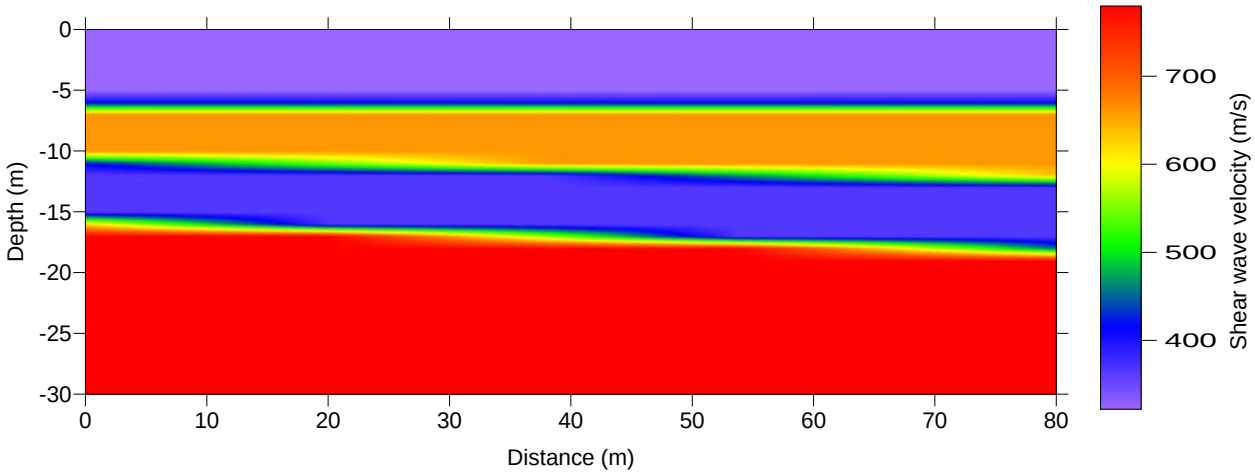

Figure 5-15. Synthetic model 3: a) true model, and b) inverted model

The observed wave field was generated in Plaxis2D using 6 receivers at 10 m spacing on the surface, and an active source placed 10 m away from the first receiver. The active source was modeled as a triangle impulsive load (Figure 5-4a), and the source produced a wave field with dominant components between 10 Hz and 30 Hz.

To run the inversion, the medium sizes were kept the same as those used in Plaxis2D. Poisson's ratio and mass density were also kept the same as values used to generate the observed wave field, thus the number of model parameters was 10 (4 shear velocities, 3 left thicknesses, 3 right thicknesses). The velocities of all layers were allowed to vary between 200 m/s and 1000 m/s, and the thickness was allowed to vary between 2 m and 10 m. The medium was discretized with a grid size of 1 m, and the material property at each node was assigned based on its tributary area, i.e., the material property was interpolated when interfaces lied between grid lines. Based on the grid size and the minimum true velocity, the maximum frequency that could be modeled accurately in forward modeling was 30 Hz, thus, both observed and predicted wave fields were low-pass filtered to remove all signals above 30 Hz before comparing.

The inversion began with an initial model having a constant shear velocity of 500 m/s, and left and right thicknesses of 7.5 m. With this initial model, the least–squared error was 0.1480, and the initial temperature was taken as 0.1. During inversion, velocities and thicknesses were perturbed, models were updated, and the temperature was reduced after every 2000 accepted models until the criterion of convergence was satisfied, at which the final error was 0.0048. The criterion of convergence was satisfied when the difference between the observed and predicted wave fields became very small. As shown in Figure 5-16, an excellent match of the wave fields is observed.

Figure 5-17 presents histograms of velocities from all accepted models for all temperature levels. It demonstrates that, at high temperatures, the accepted models are located over a large model space, and, at low temperatures, the accepted models cluster around the true model. Therefore, the inversion result should be derived from a suite of models that have similar least-squared error near the global minimum. The last 2000 accepted models at the final temperature

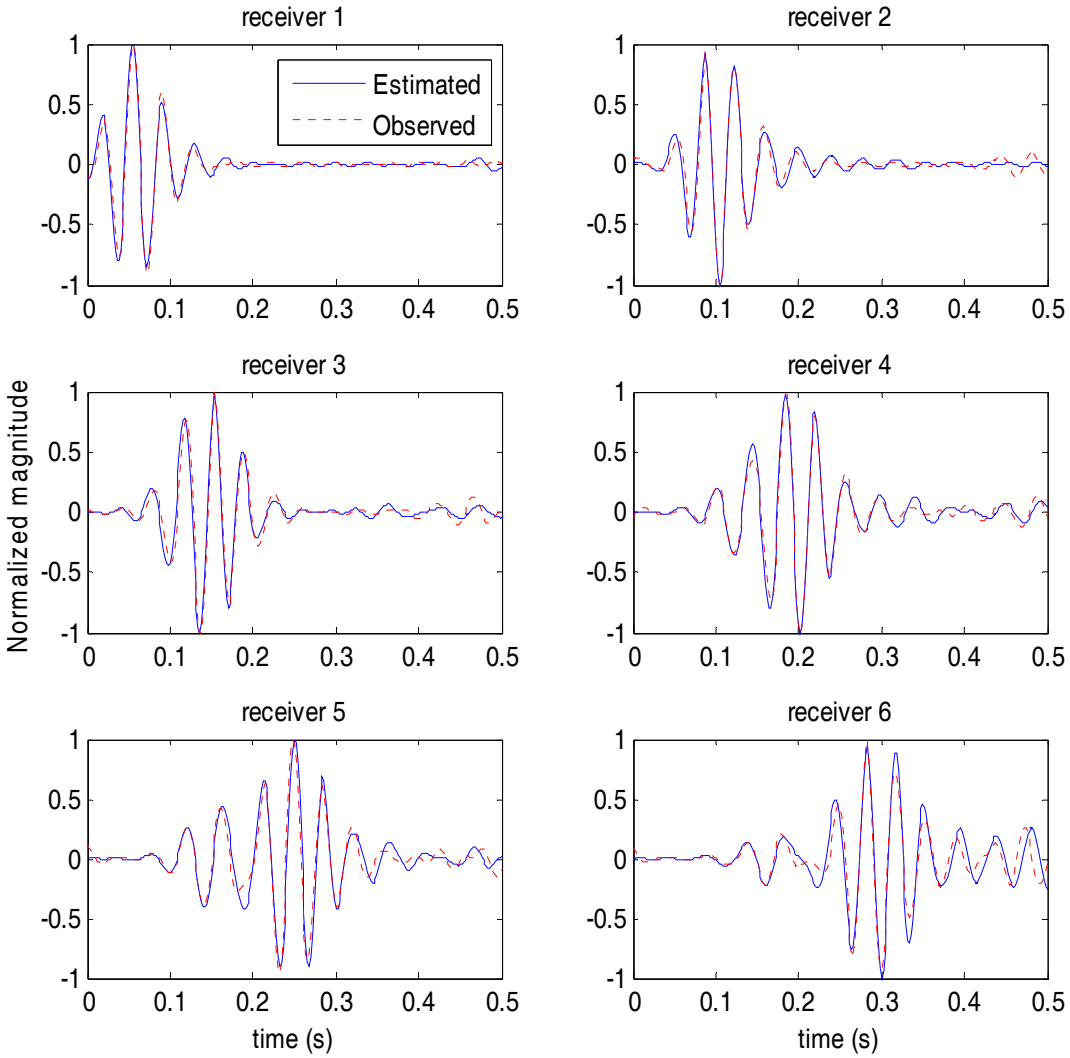

Figure 5-16. Synthetic model 3: comparison between estimated and observed wave fields

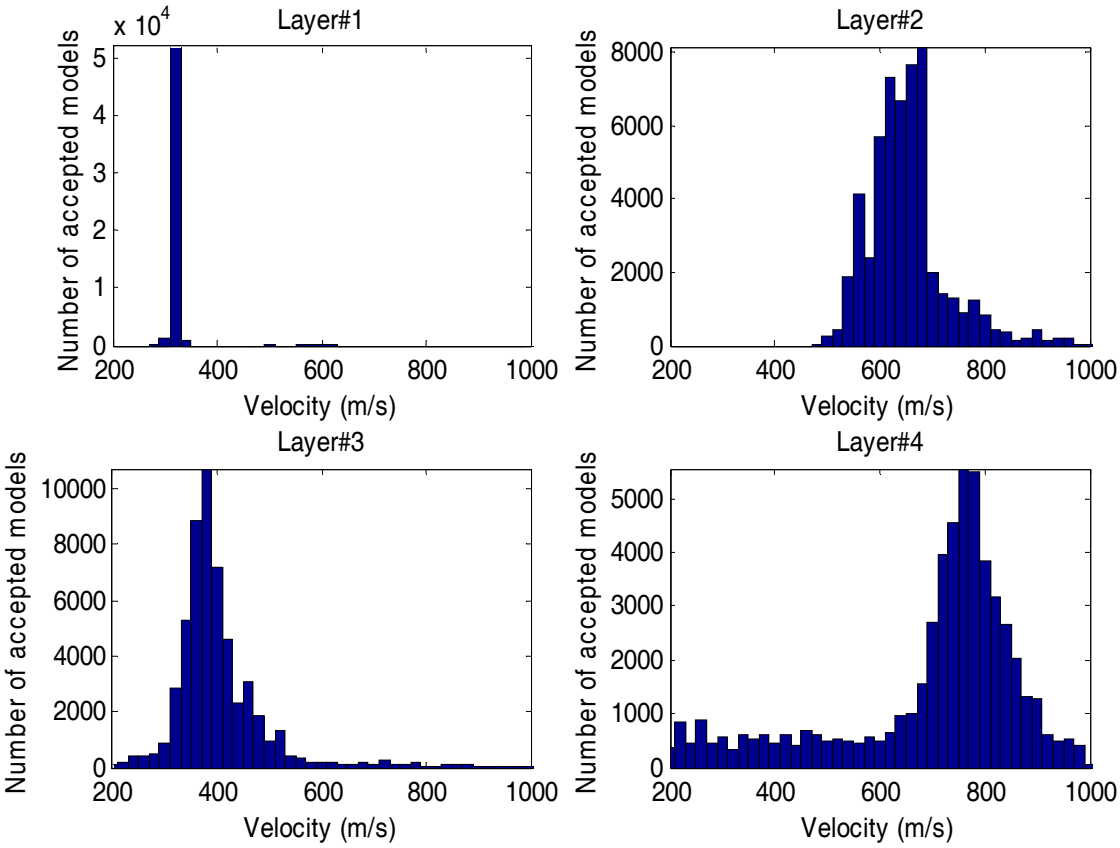

Figure 5-17. Synthetic model 3: velocity histograms from all accepted models

were used to get an average model for the inversion result (Figure 5-15b), and it is observed that the true model is excellently recovered.

Synthetic model 4

Synthetic model 4 (Figure 5-18a) consists of a buried low-velocity layer (second layer) between two high-velocity layers, followed by a half-space. Synthetic data was generated in Plaxis2D in a fashion similar to model 3.

During inversion, the least-squared error decreased from 0.1088 for an initial model of a constant velocity of 500 m/s, to 0.0066 for the final accepted model. Again, the final inversion result (Figure 5-18b) is an excellent recovery of the true model, correctly inverting both interfaces and velocities. The excellent recovery of the velocity model leads to an excellent match between the observed and estimated wave fields (Figure 5-19). The histogram of all accepted models is also shown in Figure 5-20. Here, the mode values are close to the velocities of the true model.

Synthetic model 5

Model 5 consists of three low- and high-velocity layers followed by a half-space, with six linear segments in each interface (Figure 5-21a). The observed wave field was generated by the finite-difference solution using 51 receivers at 1 m spacing on the surface, and an active source placed 10 m away from the first receiver. The active source was modeled as a Ricker wavelet (Figure 5-4b) having a central frequency of 15 Hz. The Ricker wavelet is typically better than the triangle wavelet for modeling an impulsive load, because a wave field generated by the Ricker wavelet has less numerical noise, and less filtering is required.

To run the inversion, the source, Poisson's ratio, mass density, and the number of linear segments in each interface were kept the same as values used to generate the observed wave

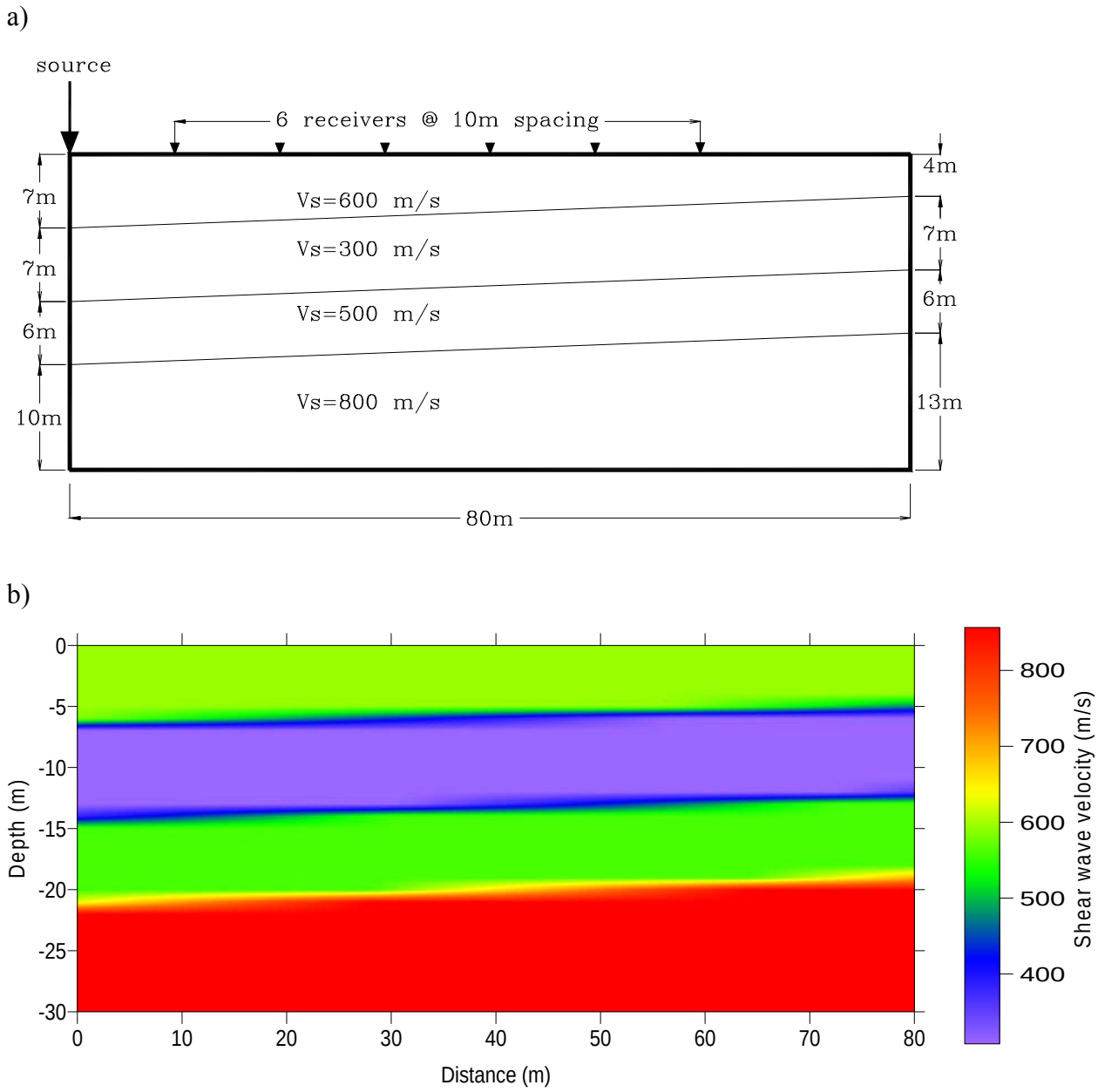

Figure 5-18. Synthetic model 4: a) true model, and b) inverted model

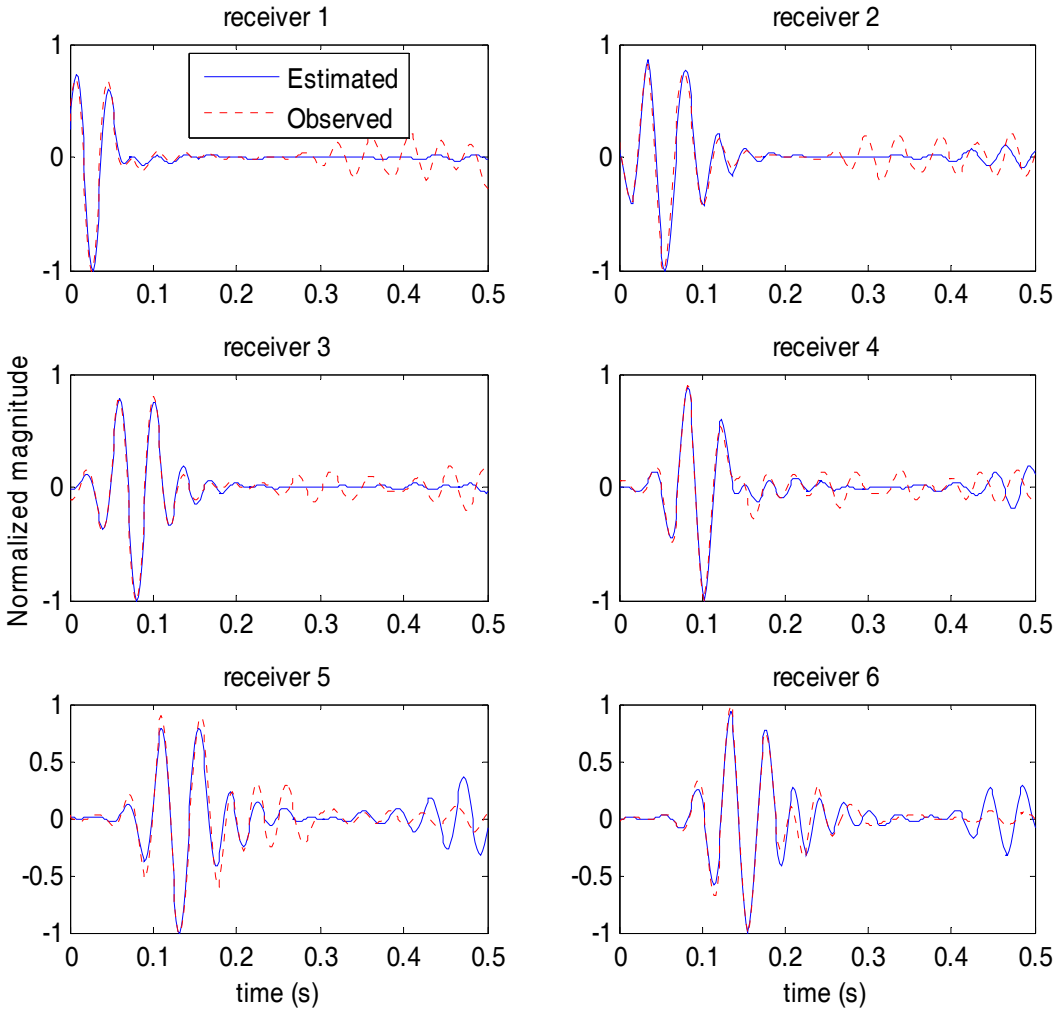

Figure 5-19. Synthetic model 4: comparison between estimated and observed wave fields

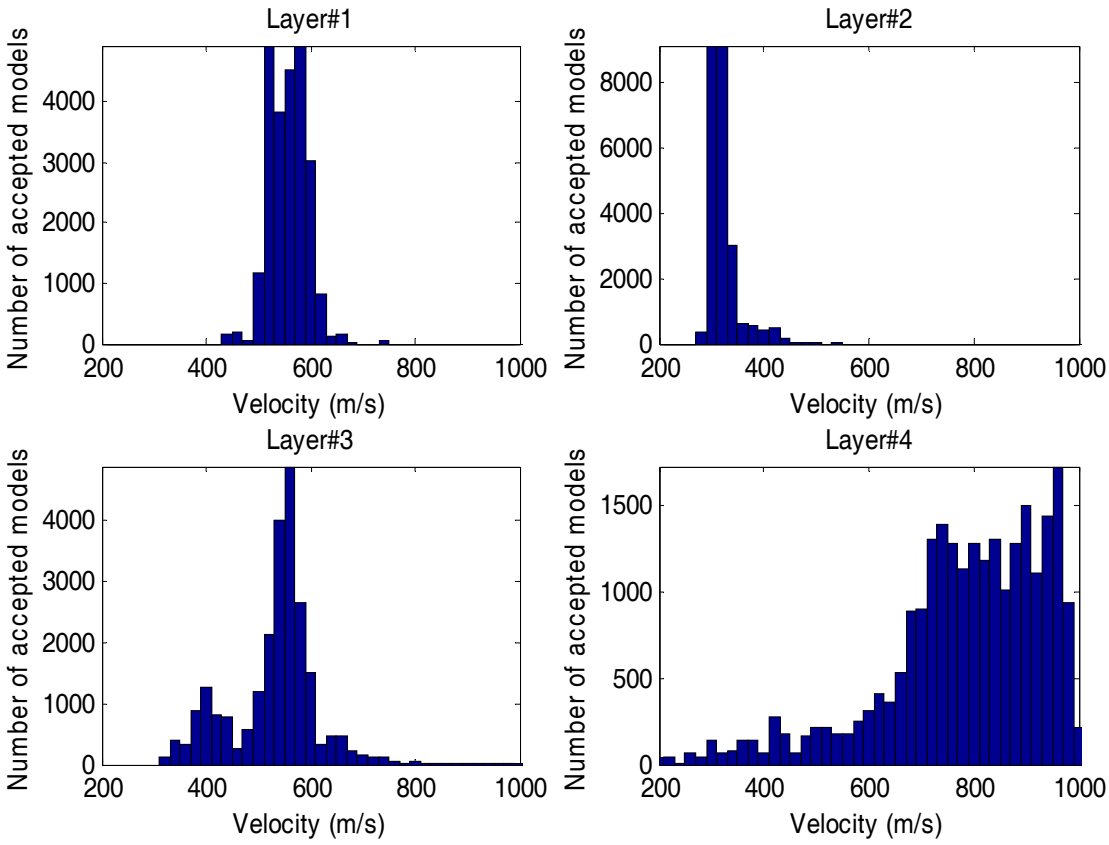

Figure 5-20. Synthetic model 4: velocity histograms from all accepted models

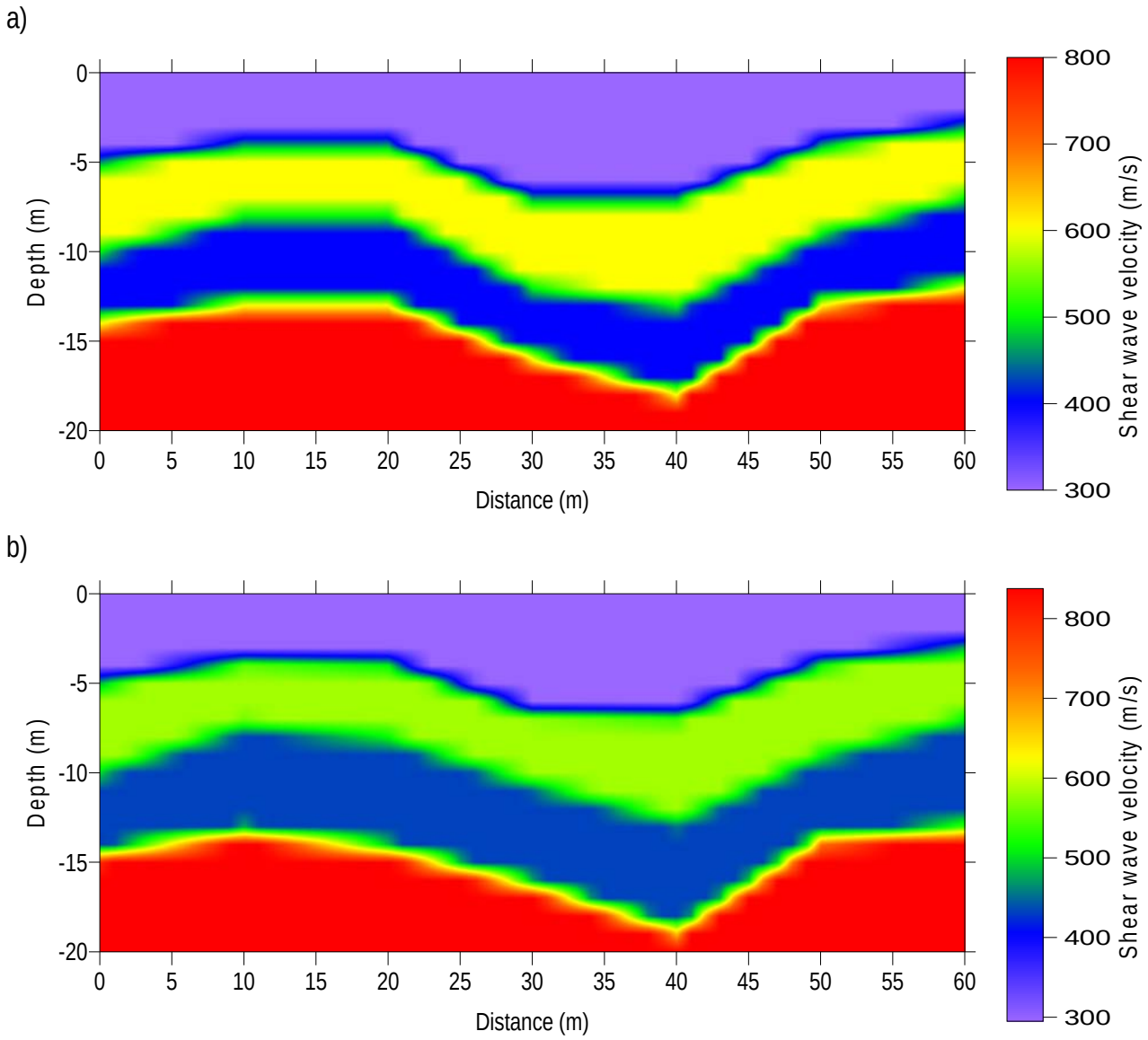

Figure 5-21. Synthetic model 5: a) true model, and b) inverted model

field, thus, the number of model parameters was 25 (7 thicknesses in each layer of the 3 layers, and 4 velocities). The velocity was allowed to vary between 200 m/s and 900 m/s, and the thickness was allowed to vary between 2 m and 10 m. The inversion began with an initial model of a constant velocity of 400 m/s, parameters were perturbed, and the temperature was reduced after 5000 accepted models until convergence. The run tested more than 150,000 trial models in about half a day on a standard laptop computer.

Figure 5-21b presents the inverted model, which is taken as the average model from the last 5000 accepted models at the final temperature. One more time, excellent recovery of the true model is found. Both layer velocities and interfaces are accurately inverted, with differences less than 10% from those of the true model.

The observed wave field, the estimated wave field associated with the last accepted model, and the residuals are shown side-by-side in Figure 5-22. It is observed that the data has been well fit across the entire range of offsets, and the two wave fields are almost identical. The histogram of all accepted models is also shown in Figure 5-23. Again, the mode values are close to those of the true model.

The inversion result of model 5 demonstrates that it is possible using a full wave field from only one shot to characterize 2-D profiles with interfaces of linear segments of a few meters. However, one should not expect too much from just one shot. Dividing the medium into many layers with interfaces of multiple small segments, or dividing the medium into many small cells, would likely require full wave fields from multiple shots for an accurate characterization.

5.3.2 Applications on Real Test Data

The results from the synthetic models have shown the capability of the presented technique in dealing with reverse and high variation profiles. In the end, to gain acceptance and wide-

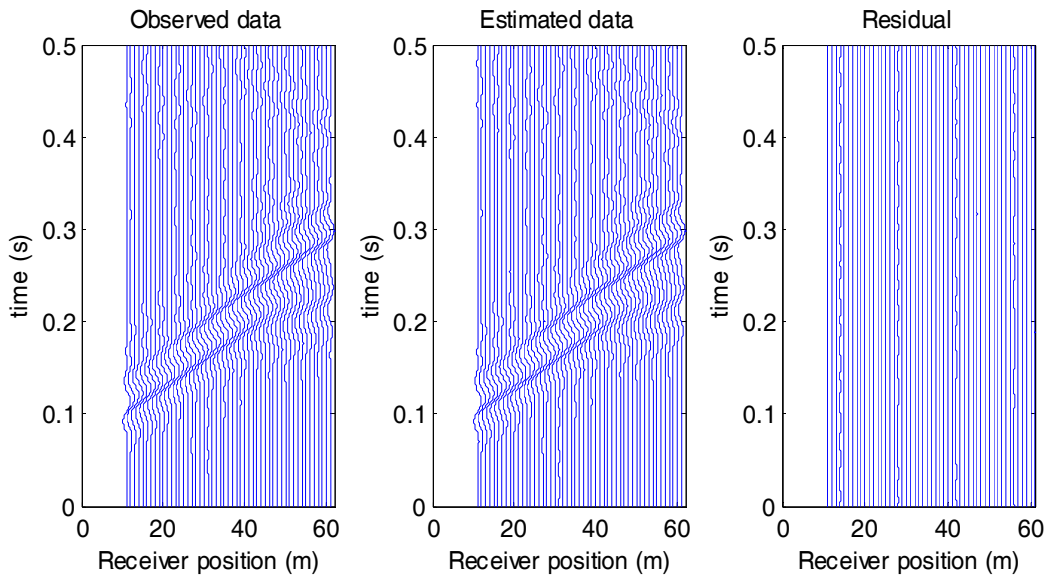

Figure 5-22. Synthetic model 5: comparison between observed and estimated wave fields

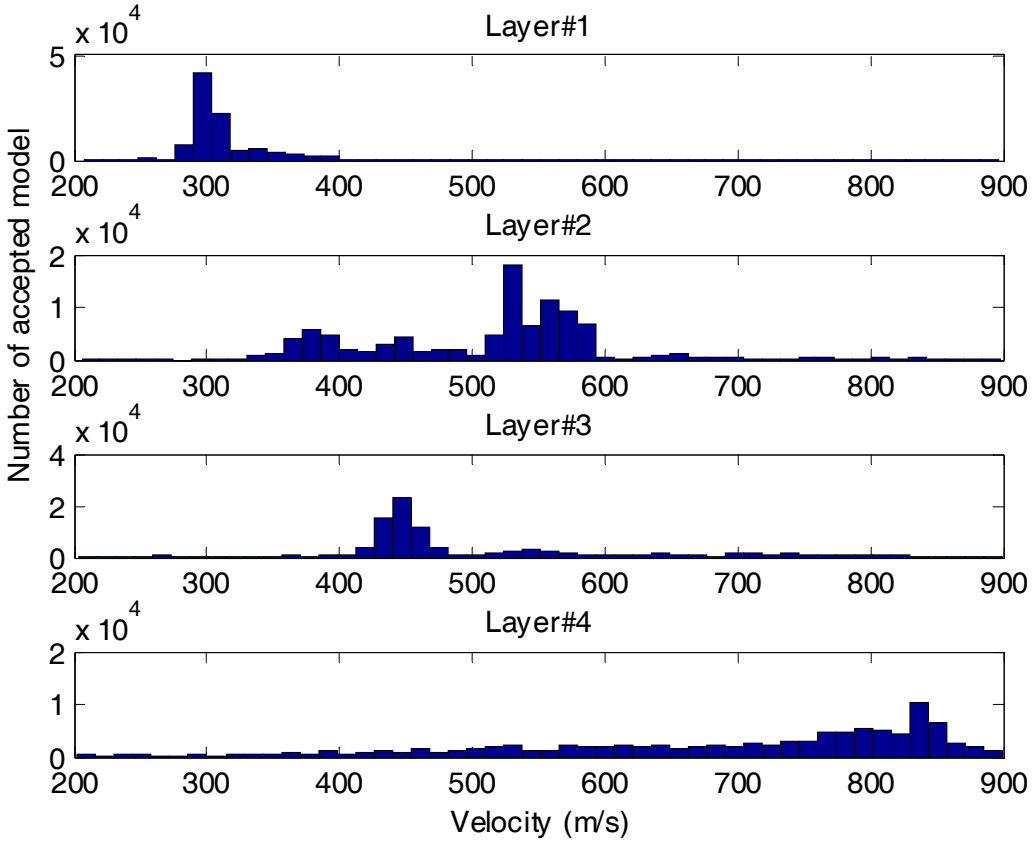

Figure 5-23. Synthetic model 5: velocity histograms from all accepted models

spread application, it must be demonstrated that tomography results compare well with ground truth information obtained from real test sites.

5.3.2.1 TAMU test site

Data were collected at the National Geotechnical Experiment site (NGES) on the campus of Texas A & M University (TAMU). The TAMU site is well documented, and consists of an upper layer of approximately 10 m of medium dense, fine, silty sand followed by hard clay. The multi-channel tests were conducted using 31 receivers at a spacing of 1.22 m, giving a total receiver spread of 36.6 m, and an active source 6 m away from the first receiver. In addition, a crosshole test was conducted at a set of nearby cased boreholes spaced approximately 3 m apart.

Before running inversion, the velocity constraints and the medium depth need to be established. Although the technique does not require strict constraints for convergence, the computer time can be reduced significantly if they are available. To save computer time, estimated velocity constraints and medium sizes must be established. For an estimate of velocity constraints, a spectral analysis was employed. By applying the spectral analysis to the measured data set, the measured wave field was decomposed into components of different frequencies, and the velocity of each component was determined. Figure 5-24 presents the normalized spectrum obtained using the cylindrical beamformer technique. It is observed that most energy of the measured wave field concentrates in a narrow band, and Rayleigh wave velocities are determined to vary from 120 to 500 m/s. Thus, the constraint of shear wave velocity, which is slightly larger than Rayleigh wave velocity, was taken as a range of 100 to 600 m/s. For the estimate of medium size, the depth of investigation was assumed as one half of the geophone spread.

Based on the geophone spacing and the dispersion property from the spectral analysis, the grid size was selected as 0.61 m. To satisfy the criterion of 10 mesh points per wavelength, the

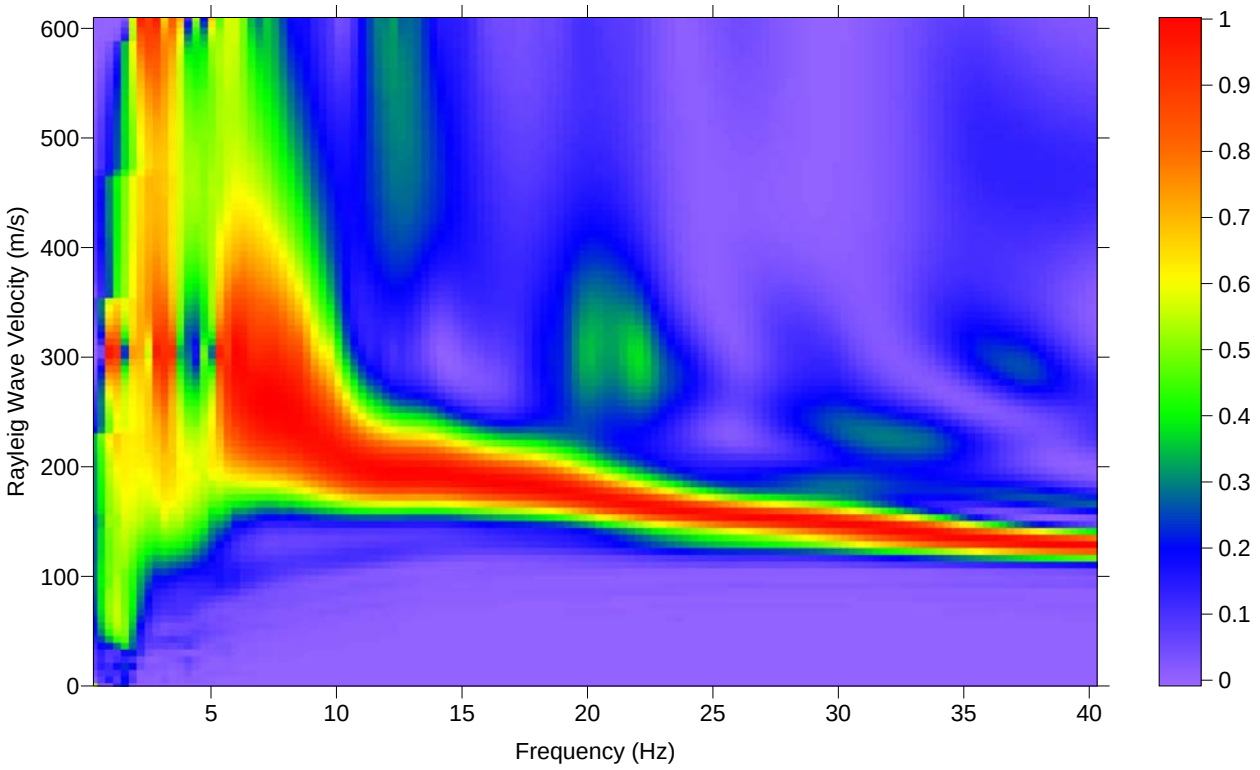

Figure 5-24. Normalized spectral of the measured data at TAMU

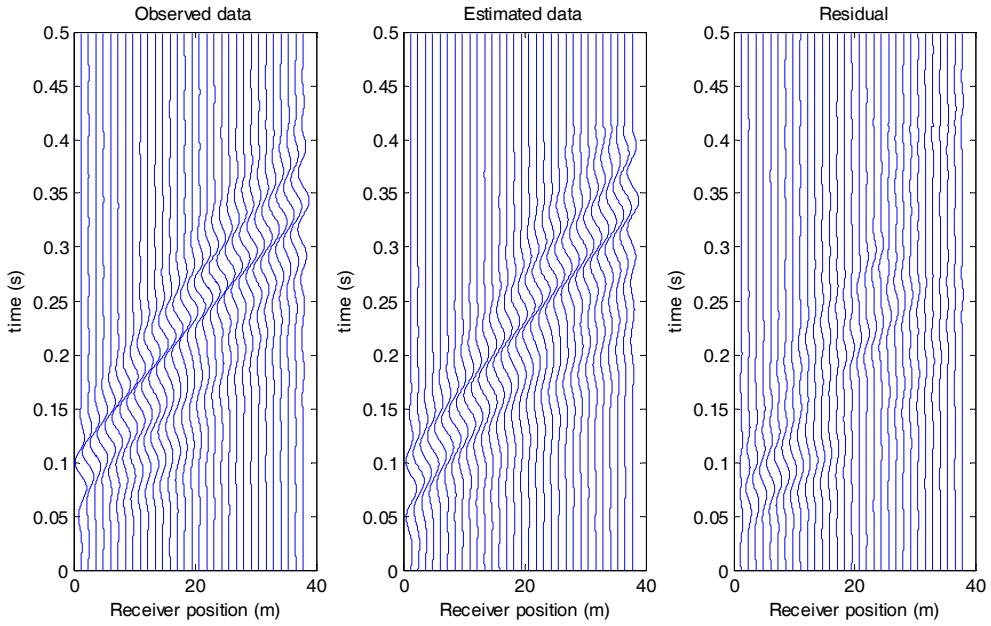

Figure 5-25. Comparison between observed wave field and estimated wave field for the real data set at TAMU

frequency was limited to a maximum of 30 Hz. Therefore, the measured data was low-pass filtered for frequencies below 30 Hz to remove high frequency signals and background noise before using for inversion. In addition, the filtered data from every receiver was treated equally by normalizing the maximum magnitude to unity, thus removing all geometric damping. The central frequency of the filtered data was about 15 Hz, and it was selected to be the central frequency of a Ricker wavelet for an active source in forward modeling.

Because most of the signals in the full wave field measured on the surface are Rayleigh waves, which are not very sensitive to Poisson's ratio and mass density, and because the number of model parameters needs to be limited to reduce computer time, the Poisson's ratio and the mass density were kept constant as 0.3 and 1800 kg/m^3, respectively, for the entire medium during inversion. It was assumed that the medium consists of 3 layers and a half-space, and each interface was divided into five horizontally equal linear segments. Thus, six thicknesses for each layer, and 4 velocities were searched; the number of model parameters was 22.

To run inversion, the shear velocity was allowed to vary between the constraints, the thickness was allowed to vary between 2 m and 8 m, and the temperature was reduced after every 4400 accepted models until the criterion of convergence was satisfied. The least-squared error decreased from 0.1560 for the initial model of constant velocity of 400 m/s, to 0.0160 for the final accepted model after searching over 120,000 trial models in about a half day on a standard laptop computer. The criterion of convergence was only satisfied when the estimated full wave field from the final accepted model was very close to the observed wave field. As shown in Figure 5-25, a good match was achieved.

Because of noise and non-uniqueness of inversion solutions, there is no guarantee that the model corresponding to the smallest error is closest to the true model. Therefore, the inversion

results should be derived from many accepted models clustering around the global minimum, and having similar errors, instead of from only one model that has the smallest error. Similar to the synthetic data sets, the last 4400 accepted models at the final temperature were averaged for the inversion result.

Figure 5-26 presents the velocity histograms from all accepted models. It is observed that the first three layers are characterized better than the half-space below. Figure 5-27 presents the two-dimensional shear wave velocity within the geophone spread (0 - 36.6 m) from the full wave field inversion. The tomogram indicates that the shear wave velocity structure at the test site is a lightly reverse profile with a buried low-velocity layer (layer 3).

For comparison, the V_s profile from the inversion result at distance 10 m, and that is near to the boreholes used for the crosshole test, is plotted together with crosshole measurements, SPT N-values, and material logs, in Figure 5-28. It is observed that the full wave field inverted shear wave profile compares well with the crosshole results, and the presented technique successfully detects the thin low-velocity layer that is hardly detected by traditional surface wave methods that use only the dispersion property of Rayleigh waves. There also appears to be reasonable consistency between the shear wave velocity results and the SPT N-values and material log.

5.3.2.2 Newberry test site

The description of the Newberry test site is provided in section 3.3.2. For the case presented here, the full wave field measurement was conducted at line F from station 36.6 m to 73.2 m, using 31 vertical geophones at a spacing of 1.22 m, giving a total geophone spread of 36.6 m, and the wave field was generated by an active source 6 m away from the first geophone.

To run the inversion of the measured full wave field, the velocity constraints and the medium depth were established. For the velocity constraints, the cylindrical beamformer technique was again employed for spectral analysis of the measured data, and the minimum and

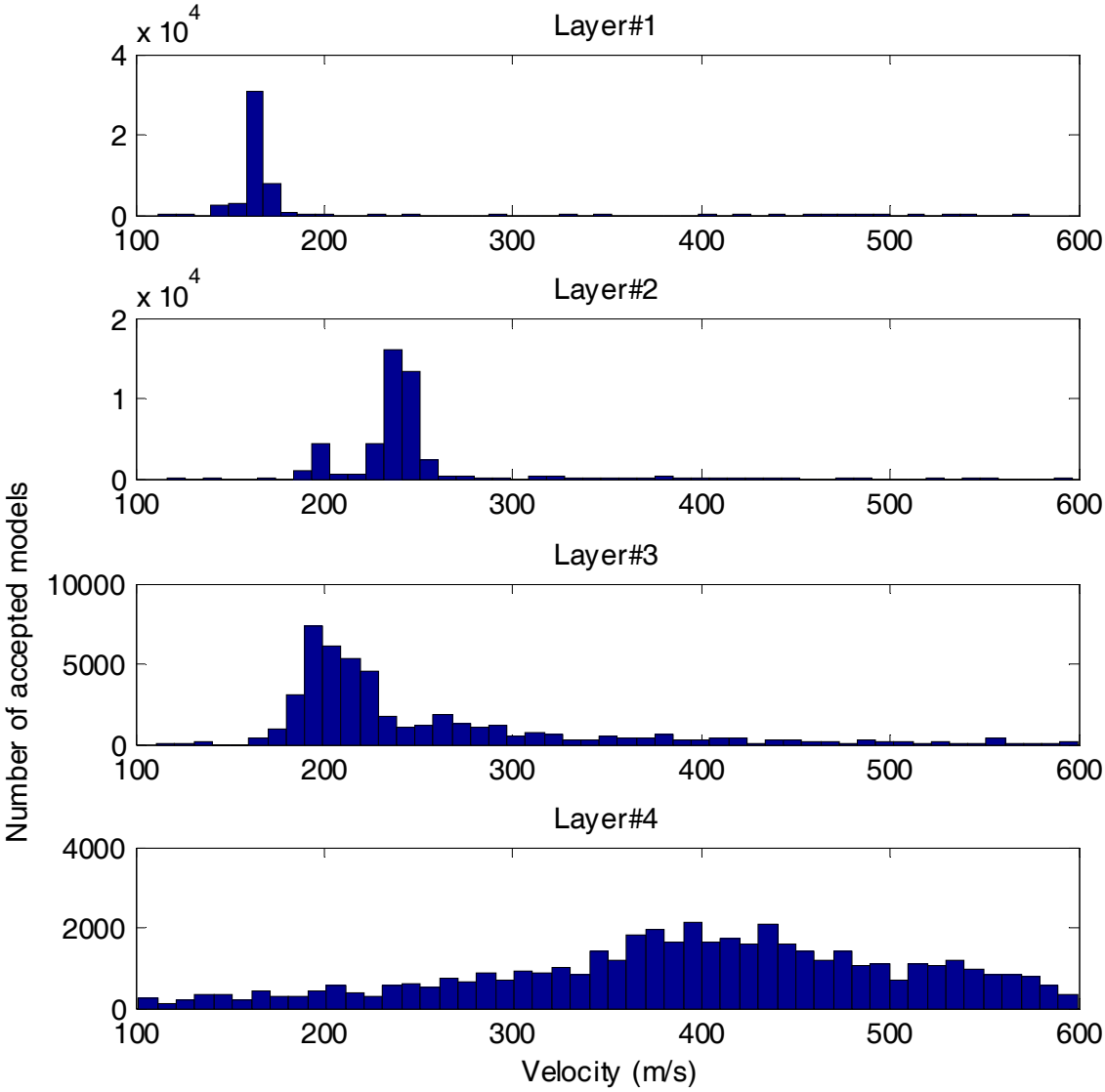

Figure 5-26. Velocity histograms from all accepted models for the real data set at TAMU

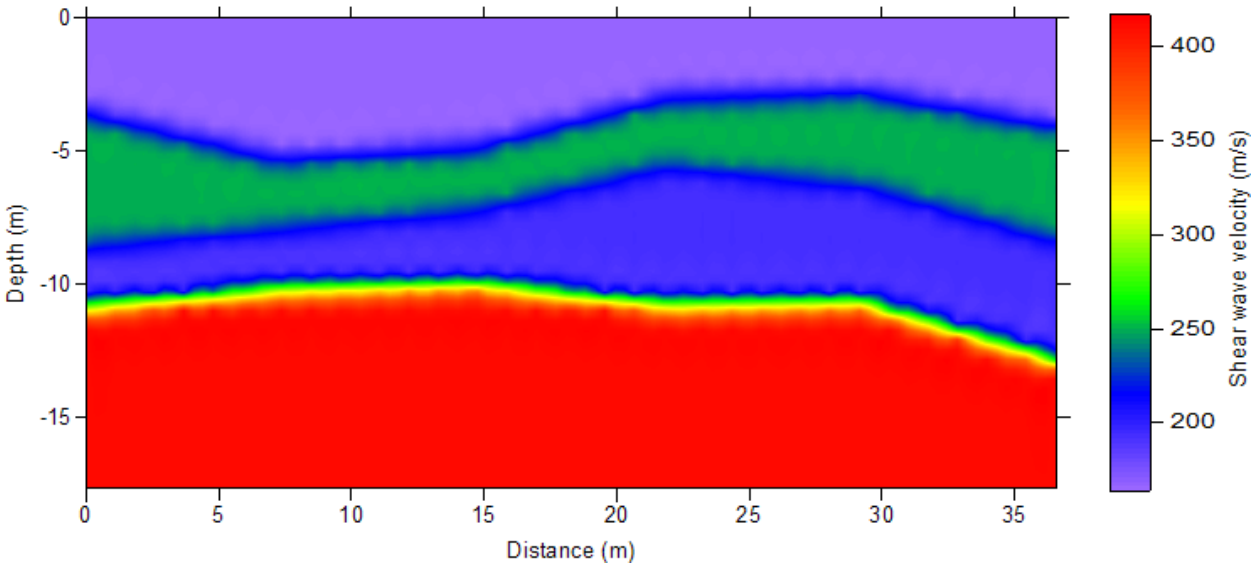

Figure 5-27. Inversion result of shear wave velocity (m/s) profile for the real data set at TAMU

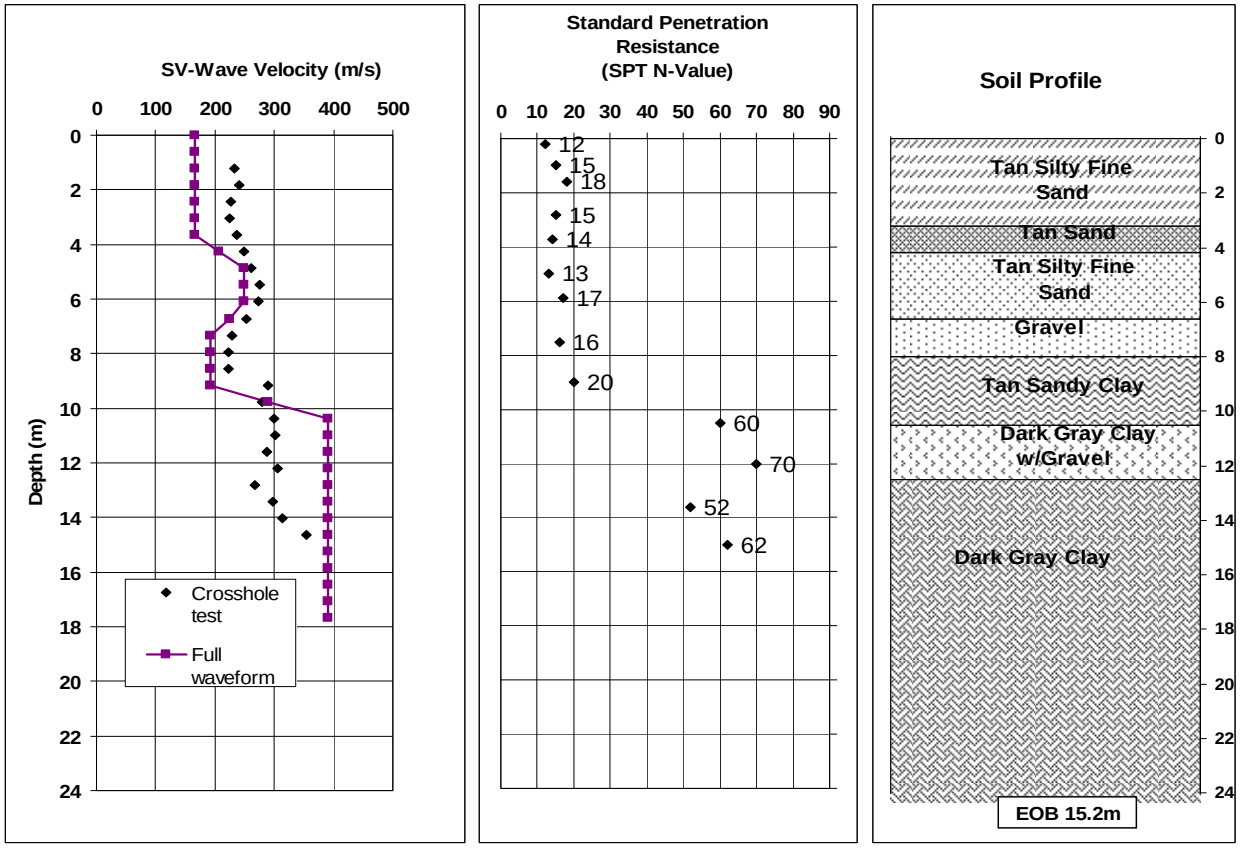

Figure 5-28. Composite soil profile of TAMU

maximum shear velocity constraints were determined as 100 m/s and 1200 m/s, respectively. The medium depth was simply taken as 1/3 of the geophone spread.

The medium was discretized with a grid size of 0.61 m, which can accurately model the maximum frequency of 40 Hz, and the measured data was low-pass filtered to remove all components above 40 Hz before using for inversion. The center frequency at 18 Hz of the filtered data was selected to be the central frequency of a Ricker wavelet for the active source in forward modeling.

Similar to TAMU, during inversion, the Poisson's ratio and the mass density were kept constant as 0.3 and 1800 kg/m^3, respectively, for the entire medium. It was assumed that the medium consists of 3 layers and a half-space, and each interface was divided into five horizontally equal linear segments. Six thicknesses for each of three layers, and four velocities were searched, and the total number of model parameters was 22.

The inversion began with an initial model of a constant velocity of 500 m/s, which led to an initial least-squared error of 0.225. The model was then perturbed and updated by allowing the shear velocity to vary between the constraints, the thickness to vary between 1 m and 6 m, and the temperature was reduced after every 4400 accepted models, until the criterion of convergence was satisfied. The convergence was found at a final least-squared error of 0.0360 after searching over 120,000 trial models in about a half day on a standard laptop computer.

The observed wave field, the estimated wave field associated with the last accepted model, and the residuals are shown side-by-side in Figure 5-29. It is observed that the data has been fit relatively well, except for the last few channels at both ends of the geophone array. The misfit at these channels may be explained that the laterally variable subsurface velocity structure cannot be completely modeled by a 2-D multilinear interface profile. To find a better wave field fit, a

more complex velocity profile is required, such as a medium consisting of small cells with different velocities.

Figure 5-30 presents velocity histograms of all accepted models during the inversion. Again, it demonstrates that, at high temperatures, the accepted models are located over a large model space, and the velocities randomly vary between the constraints. Otherwise, at low temperatures, the accepted models cluster around the global minimum model, whose layer velocities are the mode values in these histograms.

Figure 5-31a presents the two-dimensional shear wave (S-wave) velocity within the geophone spread (36.6-m length) from the full wave field inversion, which is the average model from last 4400 accepted models. The tomogram indicates that the shear wave velocity structure at the test site increases with depth. It is noted that this increasing-velocity-with-depth profile could be well characterized by seismic refraction tomography.

For comparison, the result of the seismic refraction tomography (SRT) developed by Quigley (2006) using commercial software Rayfract is also presented in Figure 5-31b. The refraction test data was measured at the same location as the full wave field test by vertical geophones spaced equally at 0.61 m, for a total of 61 measurements, and shot locations were spaced at 3.0-m intervals along the 36.6-m line, for a total of 13 shots.

The comparison of the S-wave velocity profile (Figure 5-31a) generated from the full wave field, against the P-wave velocity profile (Figure 5-31b) generated from the refraction travel times, is as follows:

- As expected, the P-wave velocity is about twice the S-wave velocity over the medium.
- There is good agreement in the depth to bedrock, which is about 9 m in both tomograms.
- The interface between layer 2 and layer 3 in Figure 5-31a is similar to the interface (contour of 1500 m/s) in Figure 5-31b.

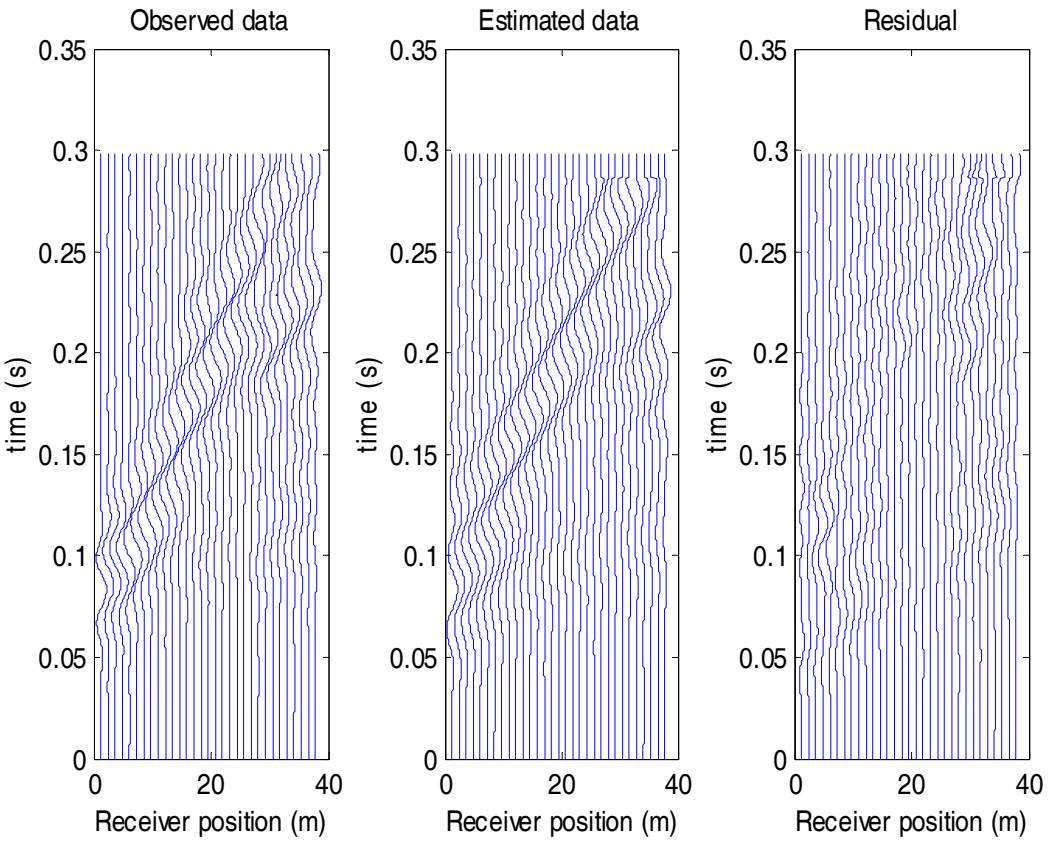

Figure 5-29. Comparison between observed wave field and estimated wave field for the real data set at Newberry

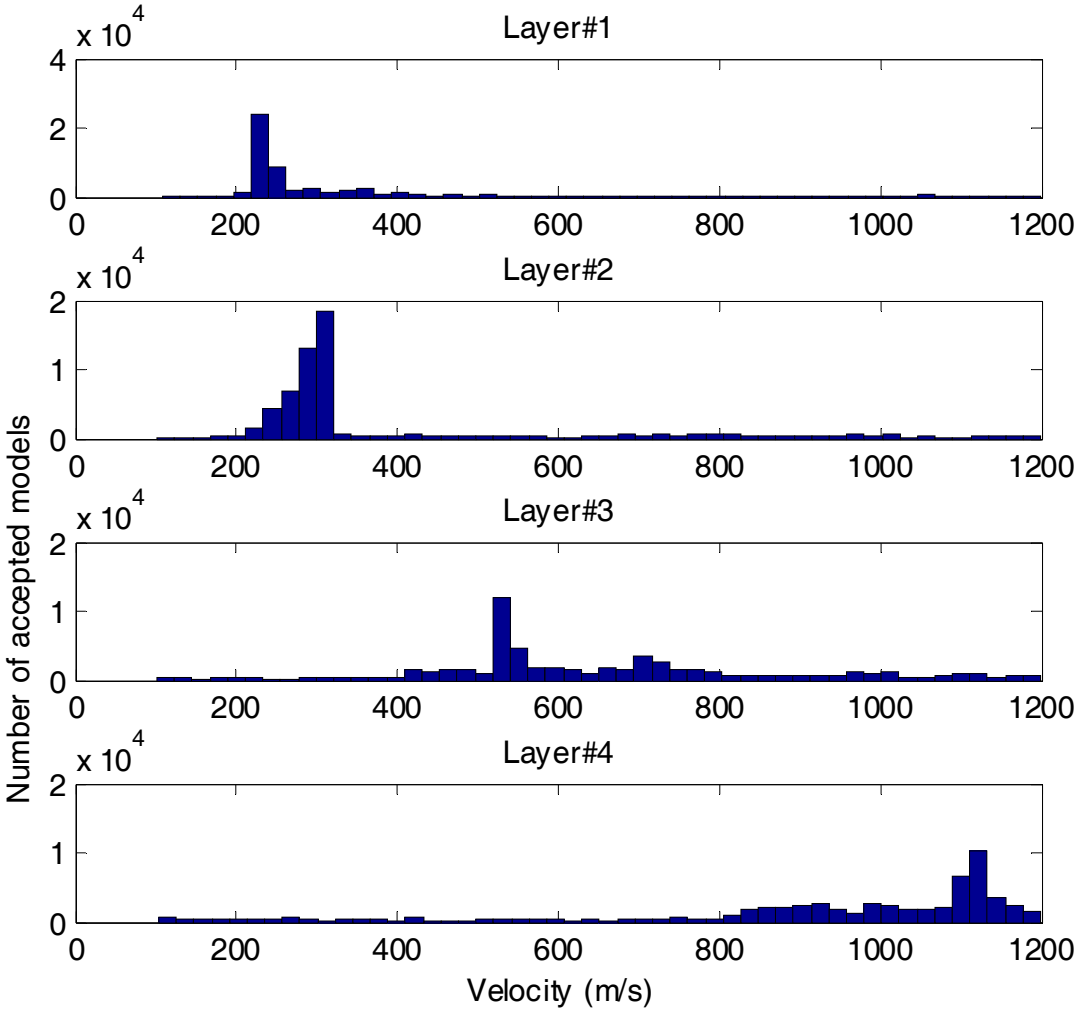

Figure 5-30. Velocity histograms from all accepted models for the real data set at Newberry

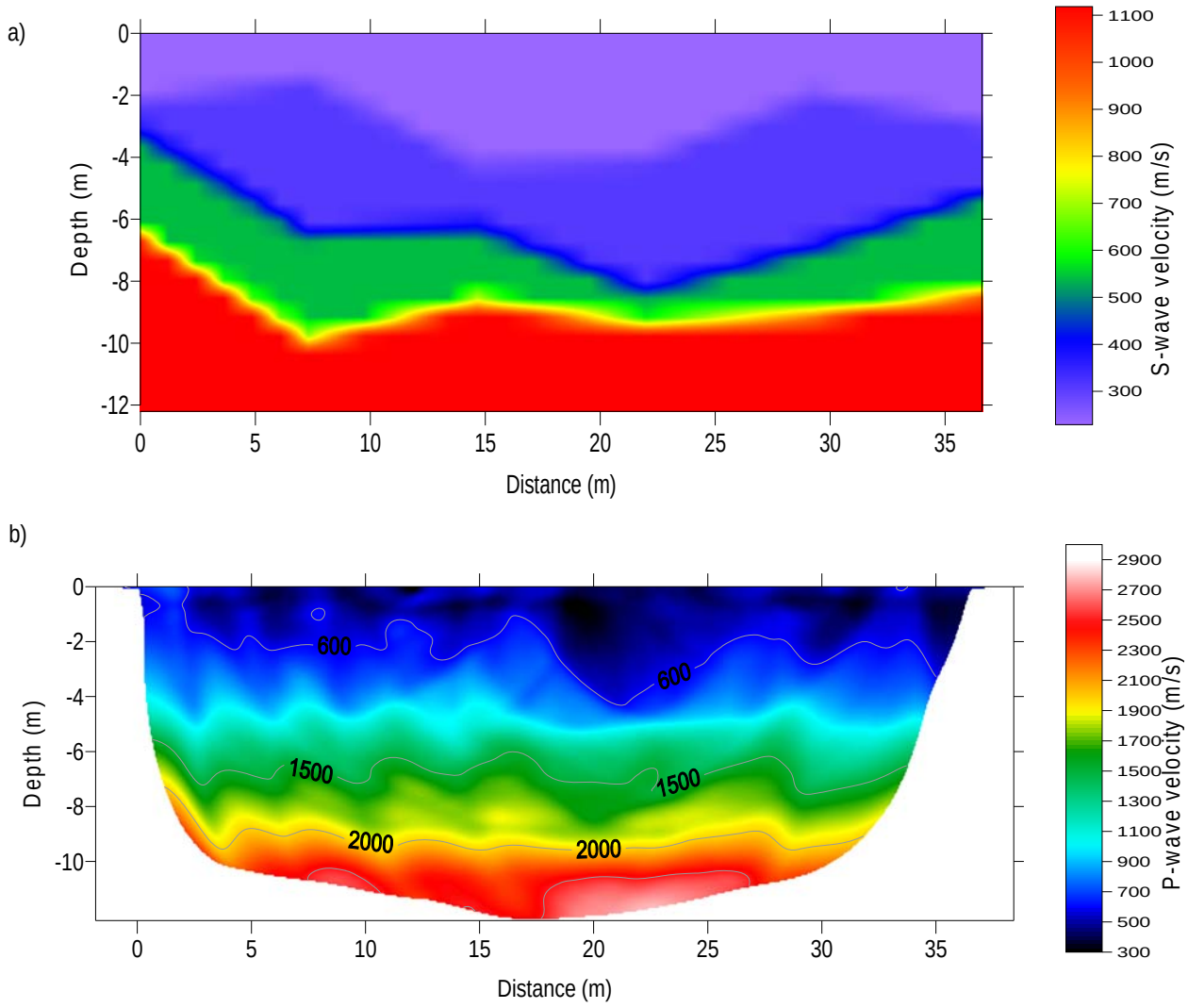

Figure 5-31. Newberry test site: a) S-wave tomogram from the full wave field, and b) P-wave tomogram from refraction travel times

- Slopes in interfaces at the left of the medium are found in both tomograms.
- There are some differences in velocity at shallow depth because the full wave field inversion assumes the medium consists of layers, not cells, and the velocity of each layer is an average value of many cells.

The relatively good agreement between the inversion results of the full wave field and travel times suggests that the full waveform technique could be applied even to normal profiles that can be well characterized by the SRT for two reasons. First, the full waveform technique can characterize sharp contrasts in velocity, which SRT always models by a gradient in velocity. Second, the full waveform technique requires much less effort in both field testing and manual data processing than that of SRT. The SRT usually requires many shots in data measurement, and days for data processing, e.g., manually picking the first-arrival signals.

5.4 Chapter Summary

An optimization scheme based on simulated annealing is presented to obtain near-surface velocity profiles from full wave fields. This technique does not depend on the initial model, and becomes important in regions where a priori information about subsurface profiles is not available. Simulated annealing provides a suite of final models clustering around the global solution, and having comparable least-squared error. This provides a result by averaging all of these models to mitigate the influence of noise and the non-uniqueness of the inversion solutions. The inversion of full waveform can well characterize challenging models with high- and low-velocity at different depths, without requirement of a priori information. Even though the technique requires significant computer time, its capability of accurately inverting the 2-D reverse models demonstrates superiority over 1-D traditional methods that use only the dispersion property of Rayleigh waves. In addition, the technique could possibly replace seismic refraction tomography to characterize normal profiles (increasing velocity with depth), because it requires much less effort in both site testing and manual data processing.

CHAPTER 6
GEOTECHNICAL ENGINEERING PARAMETER RELATIONSHIPS

6.1 Literature Review

6.1.1 Weathering of Limestone

The Florida peninsula is underlain by a series of carbonate-evaporite limestone sequences. These sequences were formed from marine deposits in warm shallow basins with abundant marine life surrounding the peninsula (Schmidt, 1997). The nature of the formation of the limestone units often incorporates both horizontal and vertical discontinuities within the rock mass. Horizontal discontinuities include unconformities and bedding planes. Vertical discontinuities include fractures, joints, and fissures. Over time these discontinuities become pathways to water that subject the rock to weathering processes that drastically affect the composition, texture, and engineering properties.

Weathering can be defined as processes that change rock at or near the earth's surface (Plummer and McGeary, 2007). There are two weathering processes that can be identified: physical and chemical weathering. Physical weathering is the mechanical breakdown of a rock mass into smaller and smaller pieces without changes to chemical composition. Examples of physical weathering include erosion, freeze-thaw cycles, and bio-intrusion. Chemical weathering changes the rock mass on an atomic level, where various chemical reactions occur to change the properties of the rock mass (Plummer and McGeary, 2007). Examples of chemical weathering include carbonation, hydrolysis, oxidation, and dissolution.

In the carbonate-evaporite limestone units that underlie Florida, a dissolution process transpires where slightly acidic rainwater infiltrates into the subsurface, and preferentially flows along discontinuities and dissolves the limestone. As the slightly acidic rainwater travels preferentially along discontinuities and through pore space within the limestone, it acts as a

solvent that contributes to the dissolution process. The acidity is derived from dissociation of carbonic acid. The dissolution process results in significant changes to rock fabric, and development of various types of pore spaces within the limestone (Randazzo and Jones, 1997). This reaction of acidic soil water with calcite forms karst features (Randazzo and Jones, 1997). When limestone ($CaCO_3$) encounters acidic soil water (H_2CO_3), the carbonate constituent (CO_3) of limestone is separated, and dissolved calcium (Ca^{2+}) and bicarbonate ($2HCO_3^{-2}$) are produced. These weathering processes are responsible for the karst in Florida. Karst is a topography formed in unconsolidated soil sediments that overlie soluble carbonate rock. The soluble rock surface is often undulating and erratic with respect to depth. The term "karstic limestone" is often used to describe a limestone lithology that has undergone significant chemical weathering (Hudyma et al., 2007). It should be emphasized that dissolution of near-surface limestone from infiltration of slightly acidic rainwater is an ongoing process.

6.1.2 Classification of Weathering

From an engineering perspective, it is important to systematically describe weathering because of its pronounced effect on engineering properties. Weathering is described using published weathering classification systems. One of the most common weathering classification systems for rock masses is described in the Basic Geotechnical Description of Rock Masses published by the International Society for Rock Mechanics (ISRM, 1981). Within this classification system, weathering states vary between W_1 (fresh unweathered rock) to W_5 (completely weathered rock or soil). The ISRM weathering classification system is shown in Table 6-1. Table 6-1 serves as a general visual guide to qualitatively distinguish weathering zones within rock masses, or the weathering state of individual specimens. It should be noted that, within this classification system, there is no clear distinction between weathering states, but a gradual transition between weathering states, and that the descriptions are somewhat broad.

The broad nature of weathering descriptions is most apparent within the interim descriptions (W_2-W_4). The W_1 and W_5 descriptions are more conclusive, and they tend to be easier to designate. The use of any weathering classification system and subsequent weathering state designation is subjective, and is dependent upon professional judgment and experience.

Table 6-1. Description of weathering states of rock (after ISRM, 1981)

Weathering State	Descriptor	Qualitative Description
W_1	Fresh	No visible sign of rock material weathering. Slight discoloration may be present on major discontinuity surfaces
W_2	Slightly weathered	Weathering indicated by discoloration of rock material and discontinuity surfaces. Rock may be weaker than W_1.
W_3	Moderately weathered	Less than half of the rock material is weathered into a soil. Fresh or discolored rock is present as a discontinuous framework or as corestones.
W_4	Highly weathered	More than half of the rock material is weathered into a soil. Fresh or discolored rock is present as a discontinuous framework or as corestones.
W_5	Completely weathered	All rock material is weathered into soil. The original mass structure is still largely intact.

The dependence of judgment and experience on weathering classification was investigated by Pinho et al. (2006). The authors asked a group of twenty-one qualified engineers to designate weathering classifications using the ISRM system to a set of twenty-five rock specimens. The authors found that significant evaluation errors (a difference in opinion by two weathering states) occurred for 72% of the specimens. It was also found that weathering classifications were more consistent for slightly weathered rock than highly weathered rock.

The process of designating a weathering state is subjective. It is important to use objective and consistent criteria to designate states throughout a project. If at a later time a weathering state is misinterpreted, consistent changes can be made to rectify the misinterpretation.

6.1.3 The Effect of Weathering on Geotechnical Properties

It is well established that weathering negatively influences the geotechnical properties of rock. A review of relevant work in laboratory rock characterization that investigated the effects of weathering on various geotechnical properties are described below.

Tugrul and Gurpinar (1997) presented a study that proposed a weathering classification for basalts and their engineering properties. Essentially, the weathering states of the basalt specimens were qualitatively described based on color, surface texture, and rock to soil ratios. Basic engineering properties such as, density, porosity, coefficient of permeability, uniaxial compressive strength, tensile strength, and Young's modulus were calculated to determine interrelationships. It was concluded that there was a substantial degradation in the engineering properties of the rock beyond a specific degree of weathering.

The strength and dynamic properties of weathered granite, basalt, and quartzite were investigated by Gupta and Rao (1998). The authors attribute that an increase in porosity is due to an increase in weathering. As such, the work focused on the relationship of strength and dynamic properties with porosity. Their results showed that unconfined compressive strength was negatively related to porosity, which means that weathering decreases strength. Furthermore, the relationship between P-wave velocity and unconfined compressive strength were studied. The P-wave velocity decreased as the unconfined compressive strength decreased in a non-linear fashion. This demonstrates that P-wave velocity decreases with an increase in weathering.

The effects of weathering on the physical and mechanical properties of limestone from Istanbul, Turkey were investigated by Tugrul and Zarif (2000). The specimens that were taken from different limestone units within a quarry had different weathering states. Weathering was assessed through the specimen's textural, chemical, and mineralogical composition. Their research suggested that unit weight and porosity are good indicators of weathering. It was

established that, as weathering state increased, the unit weight decreased and porosity increased. The relationships provided linear correlations between unit weight, P-wave velocity, and unconfined compressive strength. The P-wave velocity and unconfined compressive strength increased as unit weight increased. In addition, the modulus of elasticity decreased with decreasing unit weight. The presence of oriented features in the limestone, such as cracks and pores within the intact specimens, lowered the compressive strength (Tugrul and Zarif, 2000).

Arikan et al. (2007) explored the use of porosity and P-wave velocity as a quantitative estimation of weathering grades in weathered volcanic rocks. The authors attributed an increase in porosity was due to an increase in weathering. Results showed that as weathering increased P-wave velocity decreased. The results showed some degree of overlap between various properties within each weathering grade. Furthermore, there was a correlation between weathering grades and engineering properties.

An investigation of the inter-relationship between mechanical properties of nineteen different rock types collected from southern Anatolia was performed by Kilic and Teymen (2008). Of the rock types tested, seven were fresh (W_1) limestone specimens that were free of cracks, fissures or any other flaws that would act as planes of weakness. The behavior of these limestone specimens correlated well with the other rock types investigated in the study. Specifically, unconfined compressive strength was correlated to P-wave velocity and porosity. All relationships were determined to have high correlation.

In a study by Sarno et al. (2009a), 175 Ocala limestone specimens were tested to relate index and physical properties to ISRM weathering state. The specimens were determined to have weathering states ranging from W_2 through W_5. The index tests conducted for the study included point load, indirect tension, and Schmidt hammer tests. Results indicated that the

standard deviation of the unit weight values increased as the weathering state increased, and that overlapping occurred in unit weight values over all weathering states. Furthermore, the results from destructive testing proved to be highly scattered, with poor to moderate correlations for specimens weathered as W_3 through W_5. However, results from specimens classified as W_2 provided good correlations between index and physical properties.

A further investigation of 22 Ocala limestone specimens was conducted in a study by Sarno et al. (2010). Ocala limestone specimens were tested to relate P-wave velocity and unconfined compressive strength (UCS) to weathering and surface texture. It was found that weathering state appears to be a good indicator of strength in terms of unit weight, and, generally, as the weathering state increases, the UCS and P-wave were observed to decrease. However, a high degree of scatter was observed in higher weathering states. In terms of surface texture, it was found that there was a clear influence on UCS and less of an influence on P-wave velocity.

All of these studies show that weathering negatively affects geotechnical properties. A number of studies indicated that, within each designated weathering state, there was overlap with geotechnical properties. For example, Sarno et al. (2009a) showed that specimens with different weathering state had common unit weight values. In addition, it was shown that the presence of discontinuities within specimens lowered both strength and stiffness.

6.2 Laboratory Testing

This section presents a description of the specimens, specimen preparation techniques, testing methods, and summarized test results. The main focus of this section is the process used to assess the weathering states of the specimens. Specimens were classified using the International Society for Rock Mechanics (ISRM) weathering designations, when applicable. A unique group of limestone specimens termed differentially weathered limestone were identified.

Specimens were tested using free-free-resonant-column (FFRC) to determine dynamic properties. The dynamic properties of interest for this study were the resonant frequency (f_n), damping (D), dynamic Young's modulus (E_d), dynamic Poisson's ratio (ν_d), and compression wave velocity (or P-wave velocity) (V_p). Unconfined compression tests were conducted to obtain unconfined compressive strengths and static elastic modulus. Details of the testing and summarized results are presented in this section.

6.2.1 Limestone Specimens

The limestone specimens tested in this research were from cores obtained from the UNF-UF-FDOT geophysical test site located adjacent to State Road 26 outside of Newberry in Alachua County, Florida. The cores were PQ sized (3.4 inch diameter), and were obtained using double-barrel wireline drilling. A total of eight borings were conducted within a 72,800 ft^2 area.

The limestone specimens were from the Ocala limestone unit. Ocala limestone is of Upper Eocene age (56-34 million years ago), and is generally described as soft and porous. Deposits of Ocala limestone are nearly entirely composed of calcium carbonate. Portions of the limestone are hard and dense due to cementation of particles by crystalline calcite (Campbell and Scott, 1991).

The Upper Eocene Ocala limestone is overlaid by undifferentiated siliciclastic sediments and the Hawthorn Group. The siliciclastics are dominantly comprised of quartz sands that contain variable mixtures of clay. This unit virtually blankets Alachua County, ranging in depth from a few feet to greater than 20 feet (Campbell and Scott, 1991). The Hawthorn Group consists of intermingled carbonate and siliciclastics containing varying percentages of phosphate grains. The siliciclastic sediments and the Hawthorn Group lie unconformably on the Ocala limestone. The top of the limestone is extremely variable due to karstification and erosion (Scott, 2001).

6.2.2 Specimens

Core runs were displayed and potential specimens were identified. Ideally, specimens should be 2:1 (length:diameter) right cylinders. The depth interval for all of the identified specimens was recorded, and the specimens were then cut from the core using a diamond blade wet saw. To ensure uniform loading, the specimens were secured in a V-block, and surfaces were ground preceding testing. The specimens were ground flat to within $1/1000^{th}$ of an inch, using a Harig *SUPER 618* surface grinder. Specimen lengths ranged from 5.24 to 7.36 in.

6.2.3 Weathering Classification

Once cut and ground, the specimens were separated into their specific weathering states in accordance with the ISRM weathering classification system. The implementation of a weathering classification system for the specimens consisted of attempting to apply the ISRM weathering designations to all specimens.

The designation of weathering states is not a straightforward procedure. To ensure consistency, the following procedure was followed:

- Initially, the specimens were grouped by consistent appearance that was based on color and surface texture. This resulted in four groups of specimens.
- Next, the ISRM weathering classification table was applied to the four groups. The five descriptors in the ISRM weathering table were closely scrutinized, and a weathering state was assigned to three of the groups. The weathering states that applied were W_1 (fresh), W_3 (moderately weathered), and W_4 (highly weathered).

For one group of specimens, the ISRM weathering descriptors were not applicable, and a weathering state could not be established. The weathering state and appearance of the specimens in this group were unique. They consisted of both highly weathered and slightly weathered zones within the same specimen, indicating multiple weathering states within the same specimen. The specimens exhibited a mottled appearance, and the variation of color was found to be associated with the different weathering states present within each specimen. The lighter color

corresponded to the less weathered zones, whereas the darker color corresponded to the more weathered zones. These specimens were classified as Differentially Weathered Limestone (DWL). The distinguishing characteristics of the specimens classified as DWL were very apparent when viewed adjacent to specimens classified using the ISRM designations. Figure 6-1 contains representative photographs of specimens from each weathering classification, including the Differentially Weathered Limestone. The specimens designated by an ISRM weathering state exhibit consistent appearance throughout the specimen. The differentially weathered limestone specimens exhibit a consistent mottled appearance.

The effect of weathering is most noticeable when comparing specimens from each weathering state. Weathering state increases from left to right. As the weathering state increases, the surface textures become more prominent. W_1 specimens have a smooth texture and very few surface voids. The W_3 specimens have a rough texture and some surface voids. The W_4 specimens have a chalky crater-like surface texture with a more disintegrated appearance. This is expected because, as the weathering increases, the rock transitions to soil.

Features such as surface voids and cracks were observed to be present to some degree within all specimens; however, the weathering state was designated irrespective of the amount of surface voids and cracks observed. Rather, weathering was designated based on the state of the material and how best the ISRM designations could be applied.

The image of the differentially weathered limestone in Figure 6-1 is mottled and has segments of smooth surface textures intermixed with segments of rough surface textures. The smooth portions represent the zones of the specimen that are hard and slightly weathered, and the rougher portions represent the zones of the specimen that are softer and moderately to highly weathered. To confirm that the smooth portions were harder than the surrounding soft portions,

a pocket knife was used to scratch the surface. In all cases, the smooth portions were impenetrable, while the knife penetrated up to an eighth of an inch in the softer portions.

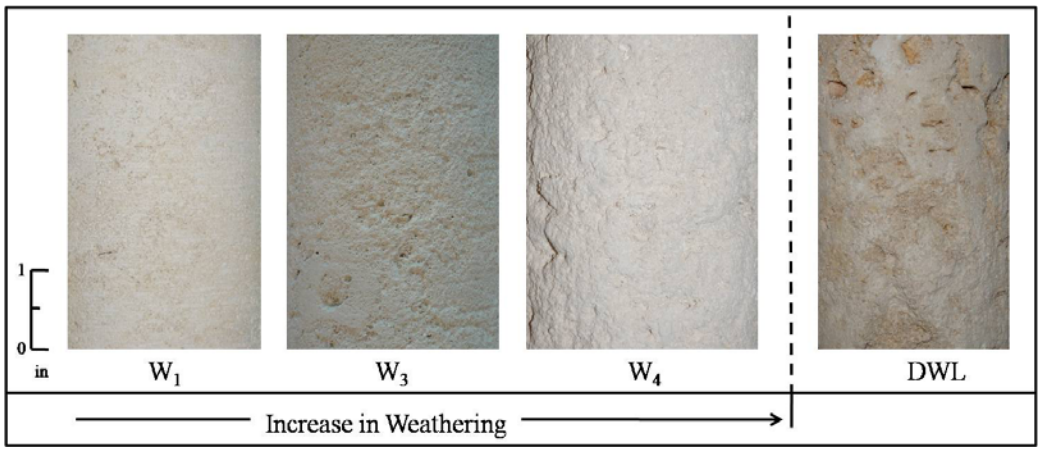

Figure 6-1. Images of representative specimens from each classification

6.2.3.1 W_1 Specimens

Nine specimens were classified as W_1. For these W_1 specimens, there were no visible signs of weathering; however, some of the specimens classified as W_1 displayed oriented surface features, such as small voids and minor cracks. Even though all W_1 specimens are classified the same, there is a large disparity between the amounts of surface features contained within each of the W_1 specimens. Figure 6-2 is an example of three specimens classified as W_1, showing increasing surface features from left to right.

Figure 6-2a shows a W_1 specimen absent of surface features such as cracks or voids. Figure 6-2b is a W_1 specimen observed to have a few small voids and some small cracks. Figure 6-2c is a W_1 specimen that has approximately 30% of its surface area covered in small voids. By visually assessing the specimens in Figure 6-2, it can be discerned that, regardless of the amount of surface features such as cracks or voids, the overall rock matrix appears the same and the weathering state is consistent in each image.

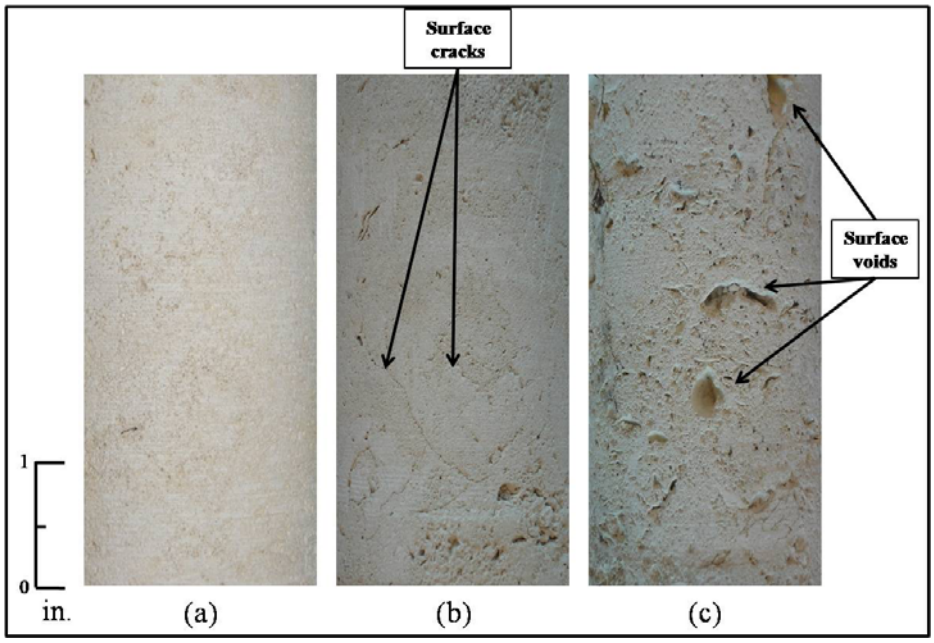

Figure 6-2. Specimens classified as W_1 with depreciating surface features (left to right). Figure (a) no discernable surface features, Figure (b) surface cracks, Figure (c) surface voids

6.2.3.2 W_3 Specimens

For the seventeen specimens classified as W_3, moderate weathering was observed. The predominant surface features were once again surface voids and cracks. Figure 6-3 shows three specimens classified as W_3 with their associated surface features.

Figure 6-3a is a W_3 specimen generally absent of surface features such as cracks or voids. Figure 6-3b is a W_3 specimen observed to have some cracks. The cracks observed in Figure 6-3b are slightly open. In Figure 6-3c the W_3 specimen contains some (approximately 20% to 25% by surface area) small voids. By visually assessing the specimens in Figure 6-3, it can be discerned that, regardless of the amount of surface features such as cracks or voids, the overall rock matrix appears the same and the weathering state is consistent in each image.

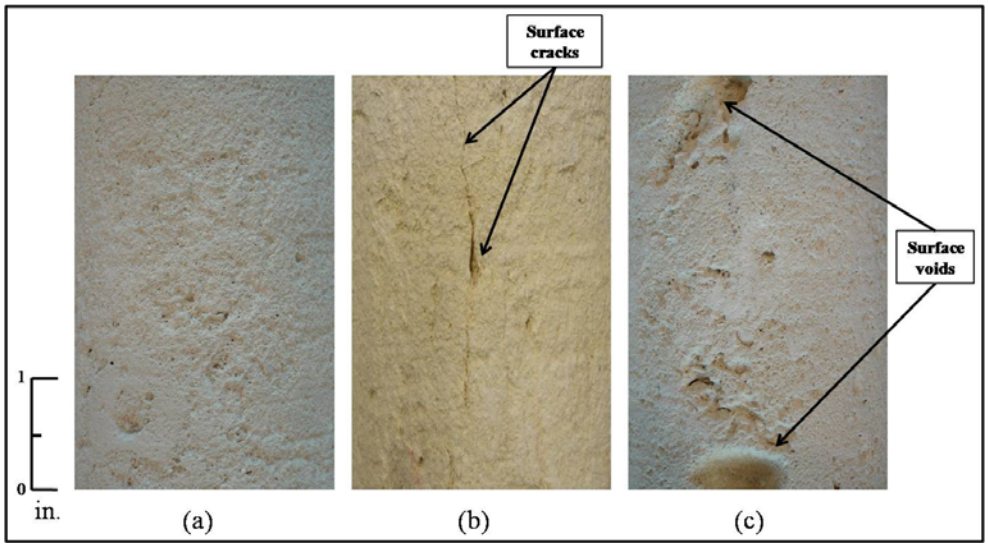

Figure 6-3. Specimens classified as W_3 depicting surface cracks

6.2.3.3 W_4 Specimens

Two specimens were classified as W_4, and an appreciable amount of weathering was observed for these specimens. Due to their high degree of weathering, the specimens were significantly friable. Surface features, such as voids were observed; however, the voids were filled with completely weathered material, giving the texture a crater-like appearance. Figure 6-4 shows a specimen classified as W_4. The image presented in Figure 6-4 accentuates the highly weathered nature of the W_4 specimens. The crater like texture is seen pointed out by the arrows.

6.2.3.4 Differentially Weathered Limestone

Twenty specimens were classified as differentially weathered limestone. These specimens consisted of both slightly weathered zones and highly weathered zones, which together form a matrix that is differentially weathered within the specimen. The differential weathering caused a mottled appearance. This unique variation of weathering made it impossible to classify these specimens in accordance with ISRM weathering states. The predominant surface features for the differentially weathered limestone specimens were segments of smooth surface textures

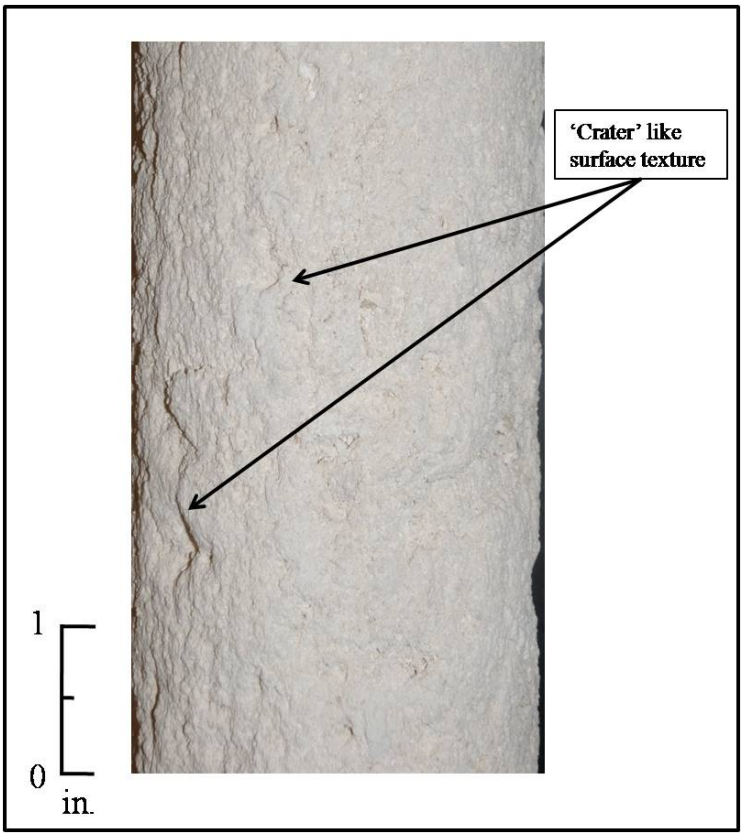

Figure 6-4. Specimen classified as W_4 depicting surface texture

intermixed with segments of rough surface textures. The smooth portions represent the portions of the specimen that are hard and slightly weathered, and the rougher portions represent the portions of the specimen that are softer and moderately to highly weathered. Figure 6-5 contains two images of specimens classified as differentially weathered limestone. These specimens are typical of specimens classified as differentially weathered limestone.

The images presented in Figure 6-5 display two specimens with slightly weathered zones accompanied by highly weathered zones. The slightly weathered zones are distinguished by a lighter color and a smoother surface. The color and surface texture reflects that of specimens classified as W_1. The highly weathered zones are slightly darker, and the surface texture is rough

and chalky, similar to that of specimens classified as W_3 and W_4. A closer inspection of a differentially weathered limestone specimen is presented in Figure 6-6.

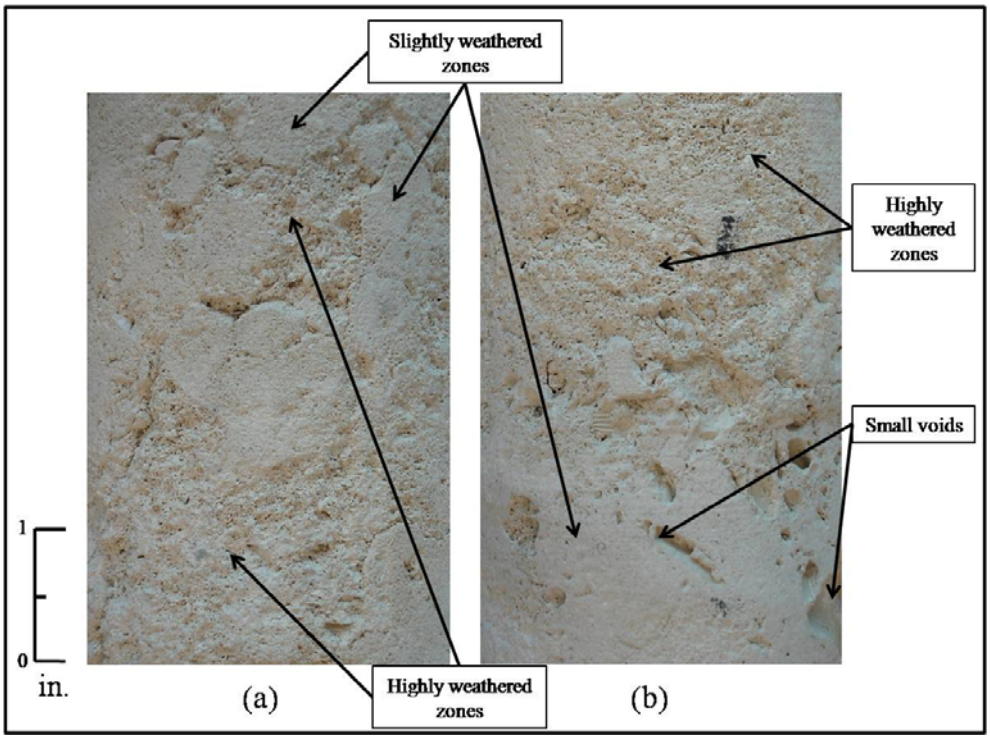

Figure 6-5. Typical specimens classified as a differentially weathered limestone. Figures (a) and (b) specimens indicate slightly weathered zones accompanied by highly weathered zones

The close-up images in Figure 6-6 are useful in differentiating between the two differentially weathered zones. Figure 6-6a is from the highly weathered zone, and Figure 6-6b is from the slightly weathered zone. A comparison of these images confirms that the surface texture of Figure 6-6a is rough like that of a W_3 or W_4 specimen, compared to the smooth surface texture of Figure 6-6b, which resembles a W_1 surface texture.

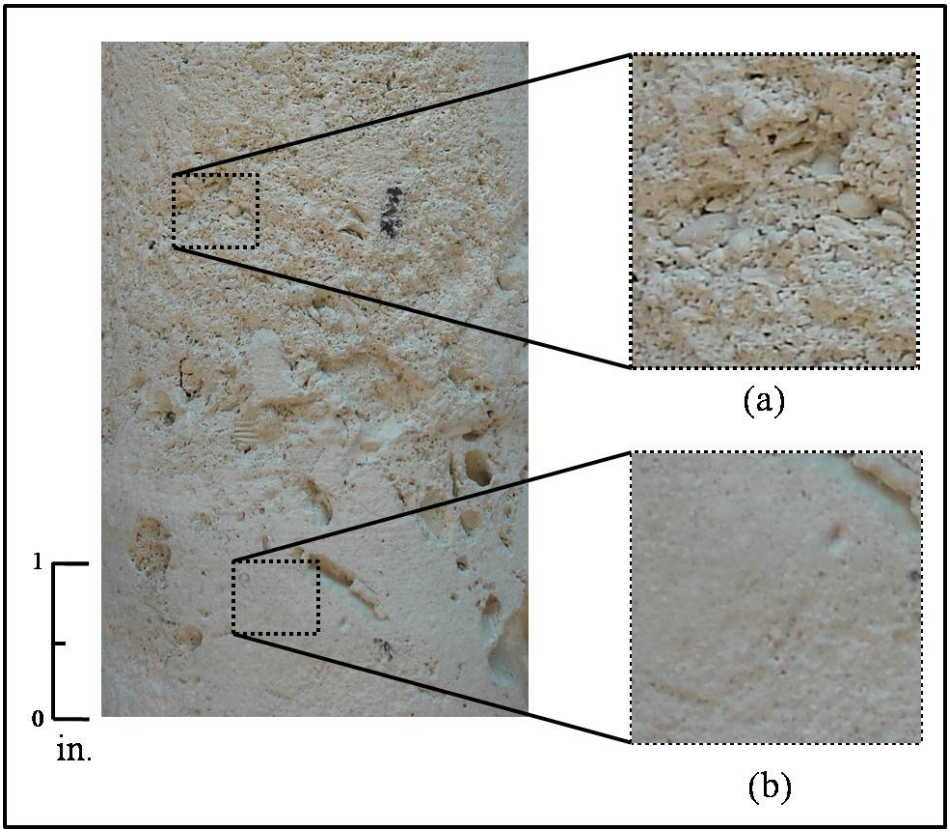

Figure 6-6. Close-up images of a differentially weathered limestone specimen

In addition to an intermixing of slightly weathered zones with highly weathered zones, there were instances where specimens contained a single interface separating two distinct segments. A segment represents a significant portion of a specimen. For example, Figure 6-7 shows a specimen classified as a differentially weathered limestone that was observed to have an upper segment consistent with the differentially weathered limestone appearance, and a lower segment consisting of a highly weathered limestone.

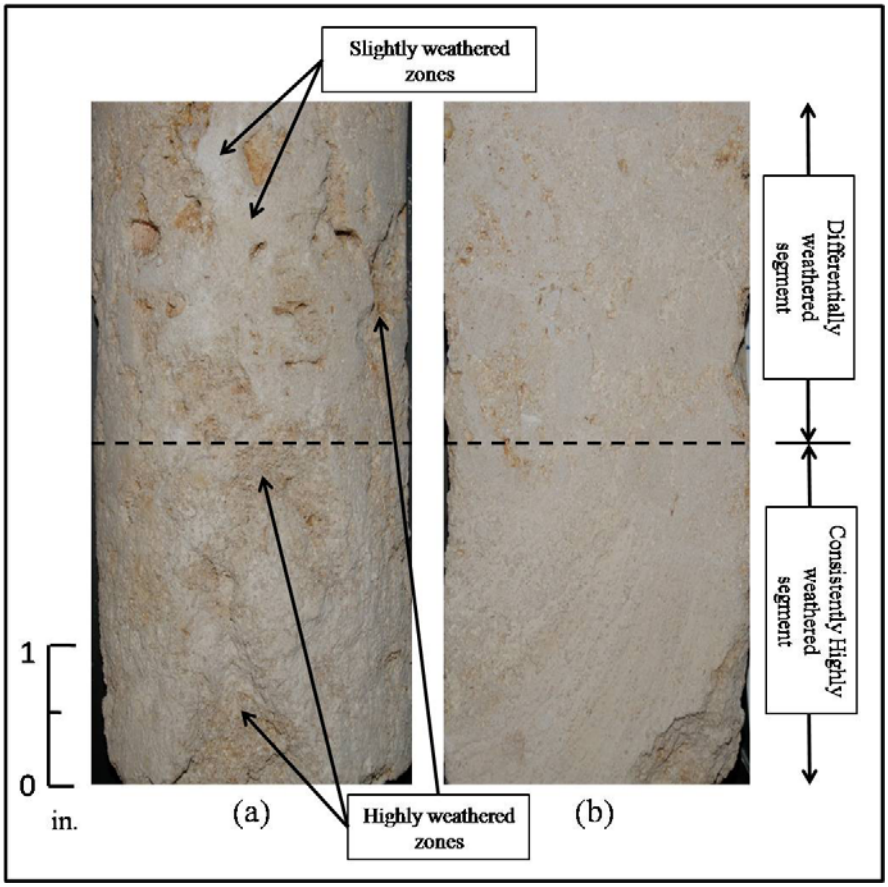

Figure 6-7. Segmented specimen classified as a differentially weathered limestone. Figure (a) shows the surface features and Figure (b) is an image of the interior of the same specimen

Figure 6-7a is the specimen surface and Figure 6-7b is the interior of the same specimen. The upper segment of Figure 6-7a shows the both slightly weathered zones intermixed with highly weathered zones. The lower segment of Figure 6-7a shows a highly weathered zone that is similar to the highly weathered zone in the upper segment, however, the lower segment is consistently weathered.

The same features present on the surface can be observed inside the specimen. Within the upper segment of Figure 6-7b, the slightly weathered portions are intermixed with highly weathered portions. The dashed line represents the distinct interface between the two segments. The lower segment clearly shows the scarring effects from the saw during slab preparation. This

scarring is absent in the less weathered upper segment. Figure 6-8 shows a close up of the scarring effects in the open slab of Figure 6-7b.

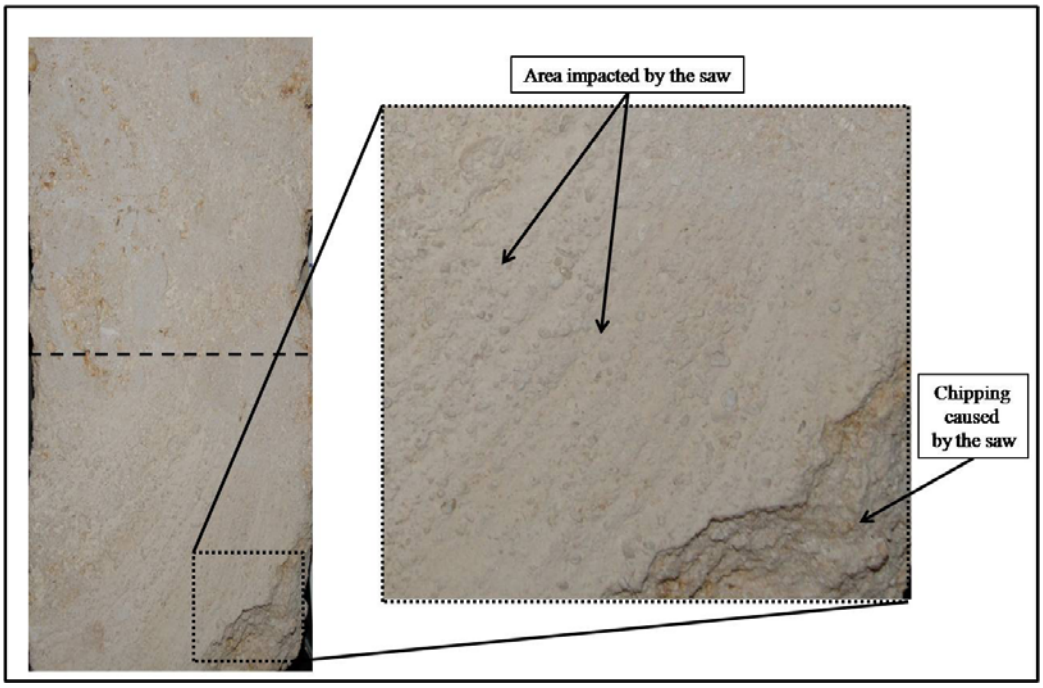

Figure 6-8. Close up image of the scarring effects in the highly weathered segment of a differentially weathered limestone specimen

The most pronounced effects are the circular indentions caused by the motion of the saw and ease of chipping. These effects were not observed in the upper segment, as this segment consisted of predominantly zones of slightly weathered material. This slightly weathered segment was resistant from the effects of the saw.

6.2.4 Unit Weight Measurements

After weathering classification was conducted, the unit weight of the specimens was determined. Three length measurements and six diameter measurements were taken, and the average measurements were recorded to compute the specimen volume. The specimens were

weighed in an air-dried condition. From the volume and weight measurements a unit weight was determined. Table 6-2 shows the range of unit weight values for each weathering group.

Table 6-2. Approximate unit weight values for each weathering group

Weathering State	γ (lb/ft^3)
ISRM W_1	96 - 134
ISRM W_3	84 - 100
ISRM W_4	82 - 82.93
Differentially Weathered Limestone	84.44 - 112.33

For the specimens classified in accordance with ISRM weathering states, the unit weight values were observed to decrease as weathering increased. Also, unit weight values were observed to overlap within W_1 and W_3 weathering states. No overlap was noticed for W_4 specimens; however, only two specimens were associated with this group.

It is possible that with a larger group of W_4 specimens, a larger range of unit weight values would have produced an overlap of unit weight values with the other weathering states. The specimens grouped as differentially weathered limestone were observed to have a range of unit weight values that encompassed all unit weight values within each of the specimens classified in accordance with ISRM weathering states.

6.2.5 Dynamic Testing

The dynamic testing consisted of performing free-free-resonant-column (FFRC) based on ASTM C215 (1997). Dynamic testing was conducted on all forty-eight specimens, representing each identified weathering state (W_1, W_3, and W_4), and the differentially weathered limestone specimens. The specimens were suspended from a rigid frame using a series of nylon strings. A miniature accelerometer was attached to one end, and an impact hammer instrumented with a load cell was used to impact the other end. Given that the test specimens were suspended, the

ends of the specimens were not constrained and the free-free boundary conditions were satisfied. A schematic of the FFRC testing station is displayed in Figure 6-9.

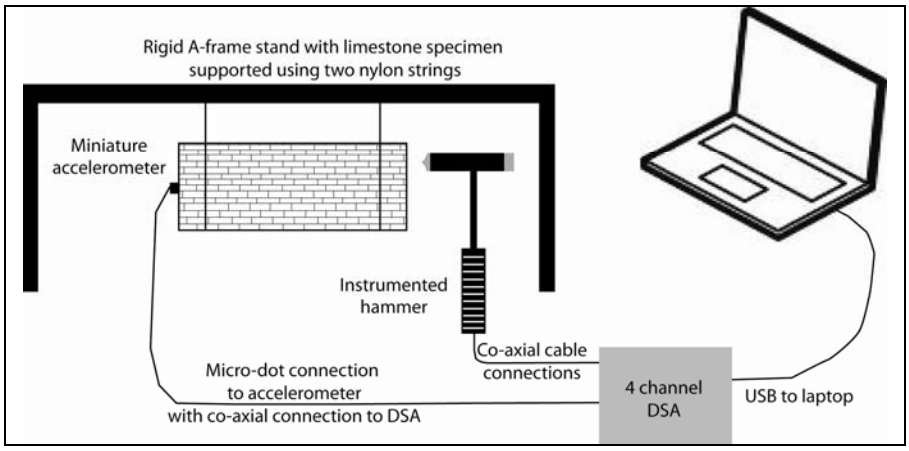

Figure 6-9. Schematic drawing of the FFRC test setup (from Sarno et al., 2009b)

Special consideration was given to the type of hammer tip. The type of tip will influence the range of potentially observable frequencies. Typically for measurements in a low-frequency range, a soft rubber tip is used, and for measurements in a high-frequency range, a hard metal tip is used (Richardson, 1999). A plastic-Teflon tip was used to ensure that all potential frequencies were excited without damaging the specimens. The response data was recorded by a dynamic signal analyzer (DSA).

A dynamic signal analyzer (DSA) is a high-speed data acquisition system that is capable of recording an analog signal in the time domain and converting the signal into its digital frequency domain components to produce a frequency response function (FRF). In order to gain an accurate digital representation of the analog signal, the settings in the analyzer were configured to accept frequency characteristics specific to the limestone specimens. The DSA settings that control the amount of data and the data collection rate are analysis frequency, spectral lines, and Nyquist factor.

The analysis frequency is used to set the maximum frequency range for testing. Increasing the analysis frequency increases the time required to collect the data captured by the DSA (EZ-Analyst, 2006). The analysis frequency must be set high enough to capture all of the frequencies of interest. The number of spectral lines multiplied by the Nyquist factor is the amount of data points collected within the specified analysis frequency. The Nyquist factor is a default multiplier that ensures that enough data points are collected. The DSA must be capable of collecting data at a sufficient rate so the digitized signal adequately represents the impulse signal.

The analysis settings used to record time response data were the highest and fastest that could be selected to ensure the first arrivals could be accurately determined. Employing these settings resulted in very large quantities of data to be collected. The calculation of accurate P-wave velocities was dependent on accurate first-arrival times.

In order to verify the value of the calculated P-wave velocities, a check was conducted using dynamic Poisson's ratio. Dynamic Poisson's ratio ranges between 0 and 0.5 (Gercek, 2006). From free-free-resonant-column (FFRC) testing the resonant frequency was confidently determined from the FRF, and used to calculate the constrained rod velocity (V_r). Next, a Δt was measured from the time response data, and a P-wave velocity was calculated. Then, dynamic Poisson's ratio, which is a function of V_P and V_r, is calculated. If the calculated dynamic Poisson's ratio was within an acceptable range, the P-wave velocity was presumed to be valid. If the dynamic Poisson's ratio fell beyond an unacceptable range, the P-wave velocity value was recalculated using another possible Δt until a valid dynamic Poisson's ratio was reached. This iterative process eliminated the ambiguity associated with the difference in first arrivals, and an accurate measure of P-wave velocity was measured. A similar procedure was followed by Slavova et al. (2010).

The ranges of dynamic properties are shown in Table 6-3. The ranges of dynamic properties generally correlate with their weathering states. For example, the W_1 specimens tend to have higher dynamic properties than W_3 specimens, and W_3 specimens tend to have higher dynamic properties than W_4 specimens. There is a small overlap observed between dynamic properties from each weathering state. As expected, the dynamic properties from the differentially weathered limestone encompass the dynamic properties from all weathering states.

Table 6-3. Approximate range of dynamic properties for each weathering state and differentially weathered limestone

Weathering State	f_n (kHz)	D (Hz)	V_r (ft/s)	V_P (ft/s)	E_d (ksi)	ν_d
ISRM W_1	3.8-10	0.676- 13.67	3543 - 11346	6092 - 11504	291 - 3740	0.11- 0.42
ISRM W_3	1.6-6.2	1.32- 67.5	1713- 6524	2403 - 8470	56 - 916	0.081- 0.42
ISRM W_4	2.5- 2.3	8.65- 52.0	2059- 2172	2143 - 2303	76 - 85	0.18- 0.21
DWL	2.24- 8.85	4.28- 207	2245 - 10553	2808 - 12210	109 - 2431	0.21- 0.43

6.2.6 Static Testing

After dynamic testing, the 48 specimens were tested in unconfined compression. A 200-kip capacity SATEC universal testing apparatus was used to perform unconfined compressive strength (UCS) testing. Compressive strengths and static elastic modulus (large strain modulus) were computed in accordance with ASTM D2938 (1995). The load frame applied a servo-controlled axial strain rate of 45.0×10^{-5} in/in/sec, and force and displacement was monitored at a rate of 60.0×10^{-5} samples/min until the peak force was accurately defined.

A stress-strain curve was created using the data collected. For each curve, the linear-elastic region was isolated, and the elastic modulus was computed from the slope of the linear elastic region. The UCS value was determined as the peak stress sustained by the specimen. Figure 6-10 shows a typical stress-strain diagram with its associated linear-elastic region.

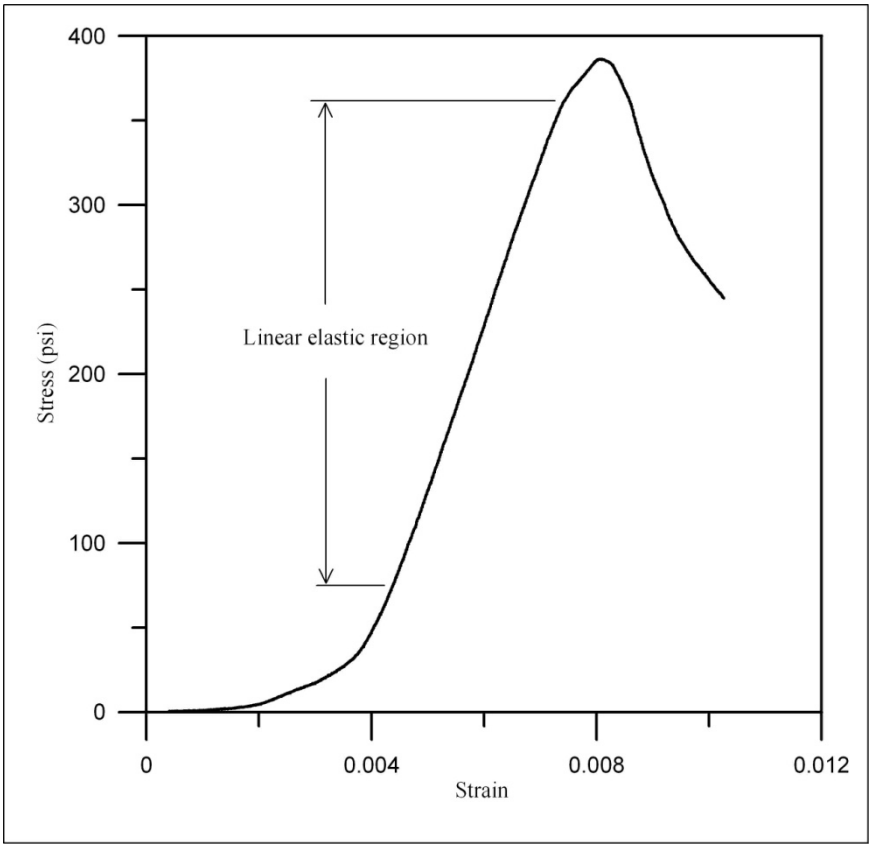

Figure 6-10. Typical stress-strain curve from static testing

UCS and elastic Young's modulus properties obtained from UCS testing are shown for each weathering group in Table 6-4. The results indicate that static properties decrease as weathering increases. Generally, there is a large degree of overlap of static properties between weathering states. The highest values of UCS and dynamic elastic modulus were observed within the specimens designated as W_1. The lowest values of UCS and dynamic elastic modulus

were observed within specimens designated as W_4. The UCS and dynamic elastic modulus values for the specimens classified as differentially weathered limestone were observed to overlap with the UCS and dynamic elastic modulus values measured within all weathering states.

Table 6-4. Approximate range of static properties measured from USC testing

Weathering State	UCS (psi)	E_s (ksi)
ISRM W_1	174.32- 2000	31.65- 746.41
ISRM W_3	91.81- 597.81	16.24- 181.67
ISRM W_4	67.93- 78.69	13.99- 36.53
DWL	77.35- 416.92	11.73- 146.54

6.3 Results

It is widely accepted that highly weathered rock specimens will have reduced engineering properties in reference to fresh rock specimens (Gupta and Rao, 1998; Tugrul and Zarif, 2000; Kilic and Teymen, 2008). Herein, relationships between physical, static, and dynamic properties in terms of weathering state are assessed.

6.3.1 Coefficient of Determination Measurements

The coefficient of determination (R^2) value was obtained for each relationship. The R^2 value was used to determine how well each trend-line fit its data set. Trend-lines for each relationship were modeled by computing the least-squared fit regressions. The least-squared fit is computed by summing the square of the residuals. The residual is the difference between the distance of the actual data point and the predicted value. The regression with the lowest sum is considered the best fit to the data. R^2 can range from 0 to 1.0. An R^2 of 1.0 indicates that all points lie on the regression line, indicating that all of the variability is accounted for. As R^2 values decrease from 1.0, less of the variability is accounted for in the relationship.

Considering that the limestone specimens are a natural material, they are inherently variable in composition. Therefore, the R^2 values for their relationships are unpredictable. Past research that related properties of limestone, indicates a range of R^2 values of 0.4-0.9, depending on the relationship. For this study, an R^2 below 0.4 was considered a poor relationship, a R^2 value between 0.4-0.7 was good, and a R^2 value higher than 0.7 was excellent.

6.3.2 Introduction to the Developed Relationships

The classification of weathering yielded two groups of specimens: specimens that were designated using ISRM weathering states, and specimens that were differentially weathered. Relationships were developed for just the ISRM weathering state specimens, for just the differentially weathered limestone specimens, and for both groups combined.

6.3.2.1 Specimens Classified Using ISRM Weathering States and Relationships

The specimens classified using ISRM weathering states were observed to contain consistent weathering states within each specimen. These specimens were classified as W1, W_3, or W_4. Multiple relationships between physical, static, and dynamic properties in terms of weathering state were developed. It was found that these relationships were good to excellent based on high coefficient of determination (R^2) values. The relationships developed for these specimens are the major focus of this chapter.

6.3.2.2 Differentially Weathered Limestone and Relationships

The differentially weathered limestone specimens were observed to contain both slightly weathered zones and highly weathered zones within each specimen. This intermixing of weathering states is unique to the specimens classified as differentially weathered limestone. Furthermore, this intermixing of weathering states distinctly separates these specimens physically, in terms of appearance and surface texture, from the specimens classified using the

ISRM weathering designations. However, this separation is not only apparent physically, but is equally evident in the relationships between physical, static, and dynamic properties.

The majority of the relationships for the differentially weathered limestone specimens contained a high degree of scatter. This scatter produced poor correlations between physical, static, and dynamic properties, as indicated by a low coefficient of determination (R^2). Due to the high scatter in the data, and resulting poor correlations between physical, static, and dynamic properties, these relationships are not discussed.

6.3.2.3 All Limestone Specimens and Relationships

Data from all of the limestone specimens were combined to produce relationships in only three cases. The first case evaluated unit weight as a function of weathering state. The other two cases incorporated dynamic properties of all the specimens.

6.3.3 Unit Weight and Weathering

Figure 6-11 illustrates the relationship between unit weight and weathering state for all specimens. The specimens classified according to their ISRM weathering state are plotted adjacent to the specimens classified as differentially weathered limestone (DWL).

The specimens classified according to their ISRM weathering states were observed to exhibit decreasing values of unit weight as weathering increases. For example, specimens classified as W_1 were the least weathered, and exhibited the highest unit weights (average unit weight was approximately 97 lb/ft^3). Conversely, specimens classified as W_4 had the highest degree of weathering and had the lowest unit weights (average unit weight was approximately 83 lb/ft^3).

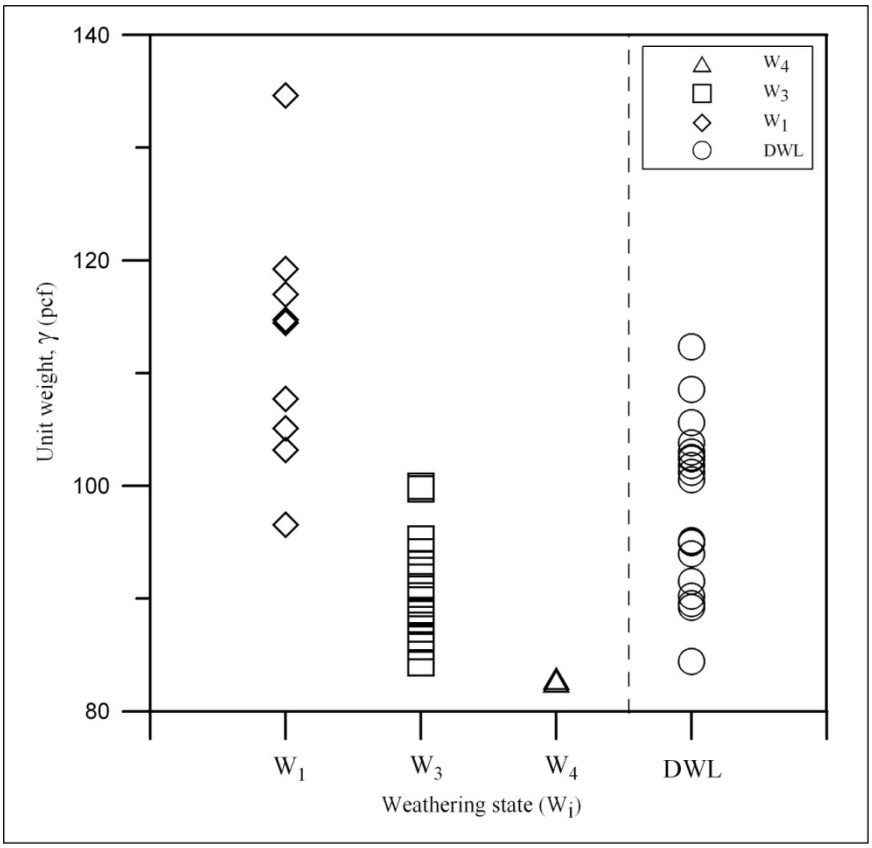

Figure 6-11. Unit weight versus ISRM weathering state and DWL

The specimens classified as W_3, which were slightly to moderately weathered, had an intermediate range of unit weight values (average unit weight was approximately 90 lb/ft^3). Each weathering state had some degree of overlap. This phenomenon was found in similar studies that investigated weathering and unit weight (Arikan et al. (2007); Marques and Vargas (1998); Bynes et al., 1978).

The differentially weathered limestone specimens essentially were observed to encompass the entire range of measured unit weight values found in each weathering state. The range of unit weights ranged from approximately 84 lb/ft^3 to 113 lb/ft^3.

6.3.4 Comparison of Static Elastic Modulus and Unconfined Compressive Strength

Figure 6-12 presents the unconfined compressive strength (UCS) verses static elastic modulus (E_s) data for each weathering classification. The graph in Figure 6-12 shows a global trend line with a good linear relationship (R^2=0.851). As the UCS increases the static elastic modulus also increases. Furthermore, the region of the graph in which the specimens have the highest degree of weathering correspond to the lowest values for both UCS and static elastic modulus; similarly, the region of the graph in which the specimens have the lowest degree of weathering corresponds to the highest values for both UCS and elastic modulus. Hence, it can be concluded that as weathering increases static properties decrease.

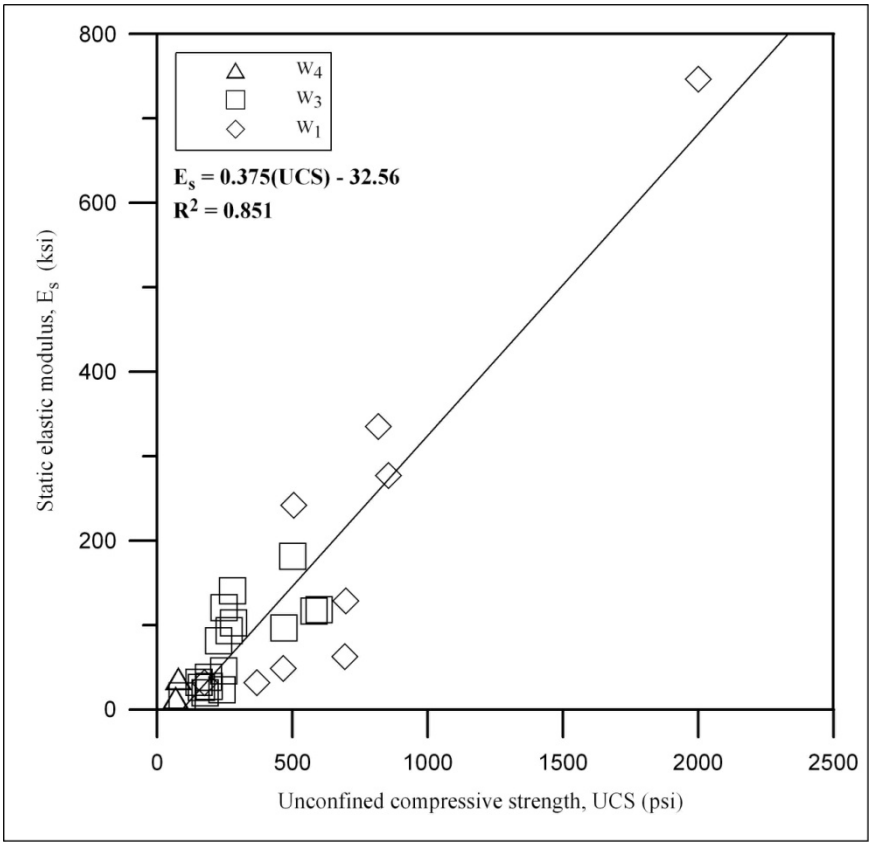

Figure 6-12. Static elastic modulus versus UCS

Overlapping of W_1 and W_3 weathering states for both UCS and static elastic modulus was observed. For the W_1 specimens observed in this overlapping region, the lower values can be attributed to features such as discontinuities and surface voids. The presence of discontinuities and voids contributes to the texture and composition of the rock, and is a controlling factor of the static elastic modulus and compressive strength (Tugrul and Zarif, 2000).

6.3.5 Static Properties and Unit Weight

In this section static properties are presented as a function of unit weight. The static properties of interest are unconfined compressive strength (UCS) and static elastic modulus (E_s).

6.3.5.1 Comparison of Unconfined Compression Strength (UCS) and Unit Weight

Figure 6-13 presents the unconfined compressive strength (UCS) verses unit weight for each weathering state. The best-fit regression of the data corresponds to a linear relationship (R^2=0.662). As the unit weight increases the UCS also increases. Furthermore, the region of the graph in which the specimens with the highest degree of weathering corresponds to the lowest values for both unit weight and UCS; similarly, the region of the graph in which the specimens have the highest degree of weathering corresponds to the highest values for both unit weight and UCS. It can be concluded that an increase in weathering decreases the UCS.

In terms of UCS, overlapping of specimens classified as W_1 with those specimens classified as W_3 is apparent, and contributed to the variance in composition and surface features. Overlapping of data as a result of varying composition and surface features was noted in previous works (for example, Tugrul and Zarif, 2000). Only one specimen classified as W_1 overlaps into a different weathering classification (W_3) in terms of unit weight.

An overlap of data in terms of unit weight is expected, as a specimen classified as a W_1 that has the same unit weight as a specimen classified as a W_2 should have a higher UCS value. The

W_1 specimen seen to have an abnormally high UCS and unit weight was noted to be free of surface features or discontinuities that were slightly more common amongst other W_1 specimens.

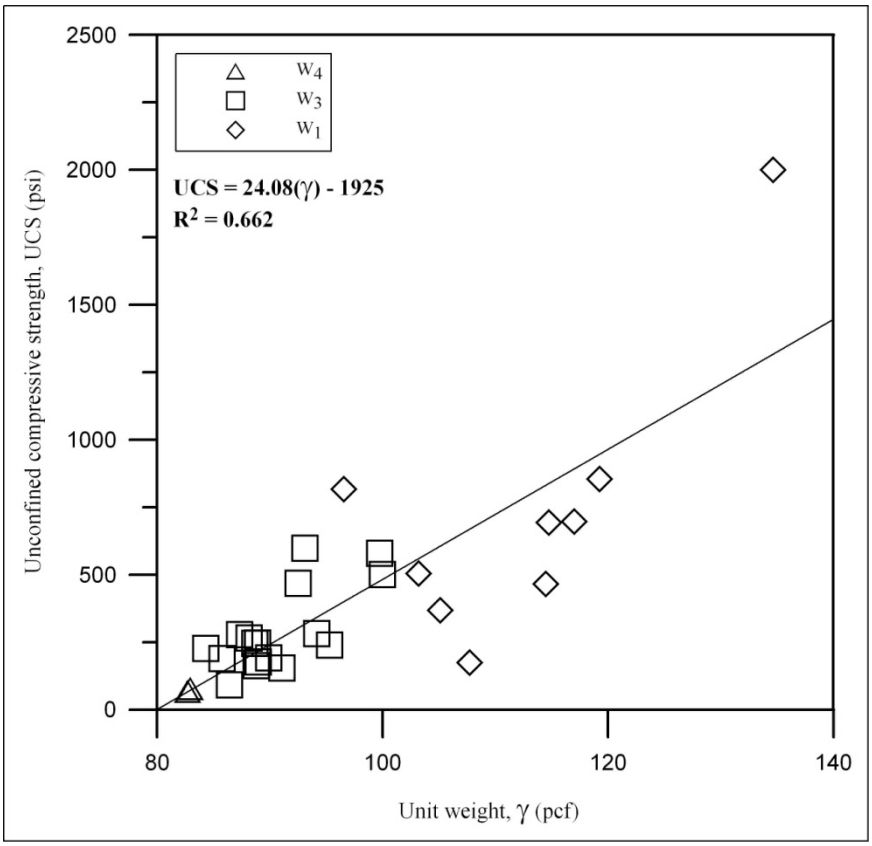

Figure 6-13. UCS verses unit weight

6.3.5.2 Comparison of Static Elastic Modulus and Unit Weight

Figure 6-14 presents the static elastic modulus verses unit weight data for each weathering state. The graph in Figure 6-14 shows a poor linear relationship (R^2=0.406), and the data exhibits a relatively high amount of scatter. The scatter is most present for specimens having a static elastic modulus below 20,000 ksf. Generally, as the unit weight increases the static elastic modulus also increases. Furthermore, the region of the graph in which the specimens have the highest degree of weathering corresponds to the lowest values for both unit weight and static elastic modulus; similarly, the region of the graph in which the specimens have the highest

degree of weathering corresponds to the highest values for both unit weight and static elastic modulus.

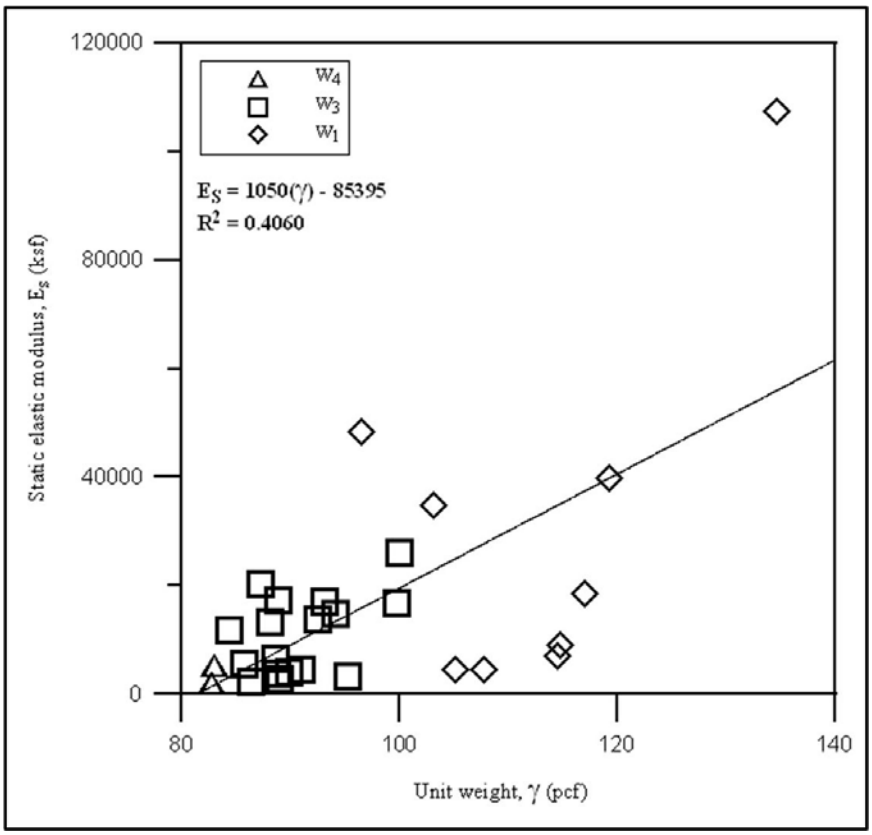

Figure 6-14. Static elastic modulus verses unit weight

In terms of static elastic modulus, overlapping of specimens with different weathering states is extensive below 20,000 ksf. The W_1 specimens should have a higher stiffness than specimens with a higher weathering state. However, those W_1 specimens that contain surface features (small voids and cracks) have stiffnesses comparable to specimens of a higher weathering state (for example, W_3). This effect has been noted in previous works such as Tugrul and Zarif (2000).

6.3.6 Dynamic and Physical Properties

In this section dynamic properties are presented as a function of unit weight. The dynamic properties of interest are P-wave velocity (V_p), resonant frequency (f_n), and dynamic elastic modulus (E_d).

6.3.6.1 Comparison of P-Wave Velocity and Unit Weight

Figure 6-15 presents the P-wave velocity verses unit weight for each weathering state. P-wave velocities are known to be dependent upon unit weight (Goodman, 1989). The weathered limestone specimens show a positive logarithmic relationship between P-wave velocity and unit weight (R^2=0.593). As the unit weight increases the P-wave velocity also increases. The region of the graph where the specimens have the lowest degree of weathering corresponds to the highest values for both P-wave velocity and unit weight; similarly, the region of the graph for which the specimens have the highest degree of weathering, corresponds to the highest values for both P-wave velocity and unit weight.

In terms of P-wave velocity, data overlap occurs between specimens classified as W_1 and W_3 in the region where P-wave velocity ranges from approximately 6,000 ft/s to 8,500 ft/s. In this region the unit weight increases, but the P-wave velocity is relatively constant. This zone represents the upper bound of W_3 and lower bound of W_1 with regards to weathering state. This trend has been shown to exist in previous studies on different rock types (for example, Arikan et al., 2007; Marques and Vargas, 1998; Bynes et al., 1978).

6.3.6.2 Comparison of Resonant Frequency and Unit Weight

Figure 6-16 presents the resonant frequency verses unit weight data for each weathering state. There is a linear relationship; however, there is more variability with resonant frequency in the highly weathered specimens. The variability is reduced for the unweathered specimens.

There is a region between 4000 Hz and 6500 Hz which corresponds to the overlap of the weathering classifications.

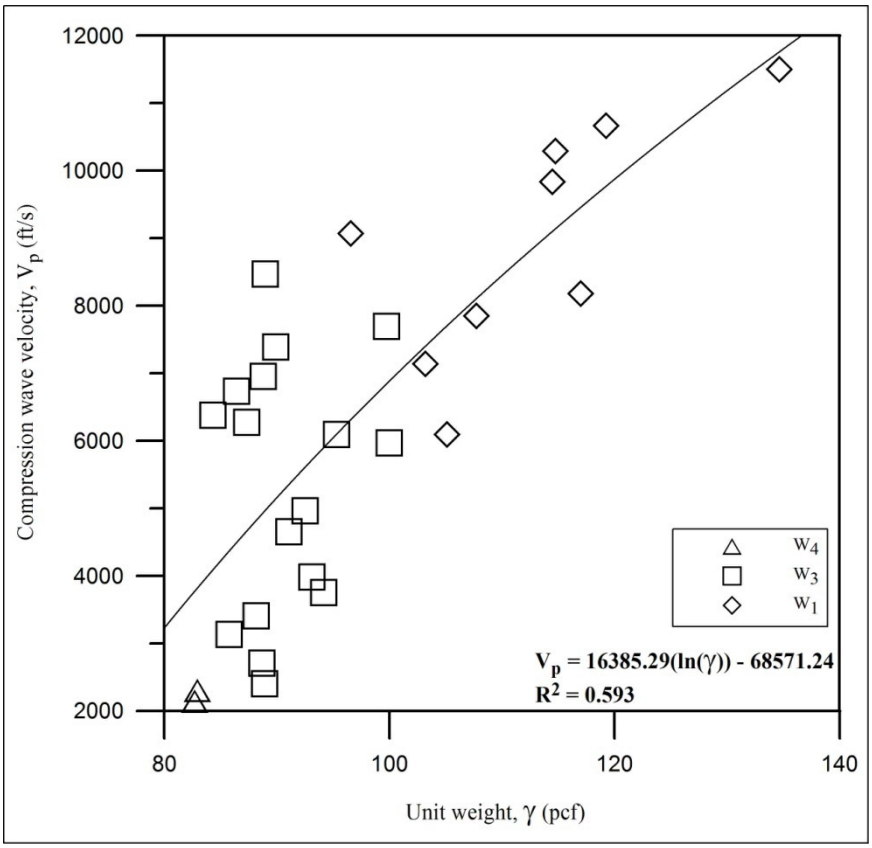

Figure 6-15. P-wave velocity verses unit weight

If weathering is thought to be an indicator of damage, Figure 6-16 shows that highly weathered (damaged) rock has higher variability in resonant frequency than slightly weathered (undamaged) rock. Previous studies have documented changes in resonant frequency of rock (Sun and Hardy, 1990) and plaster of Paris specimens (Sarno et al., 2009b) due to induced damage from laboratory testing. Both studies revealed reductions in resonant frequency due to damage. In Sarno et al. (2009b), resonant frequency was measured before and after unconfined compression testing. The change in resonant frequency ranged between approximately 100 Hz to

1000 Hz depending upon porosity. In general, the specimens with higher porosity had higher changes in resonant frequency. This analogy may provide insight to why the more weathered (damaged) specimens have a wide range of resonant frequencies, whereas the slightly weathered (undamaged) specimens have a more consistent range of resonant frequencies.

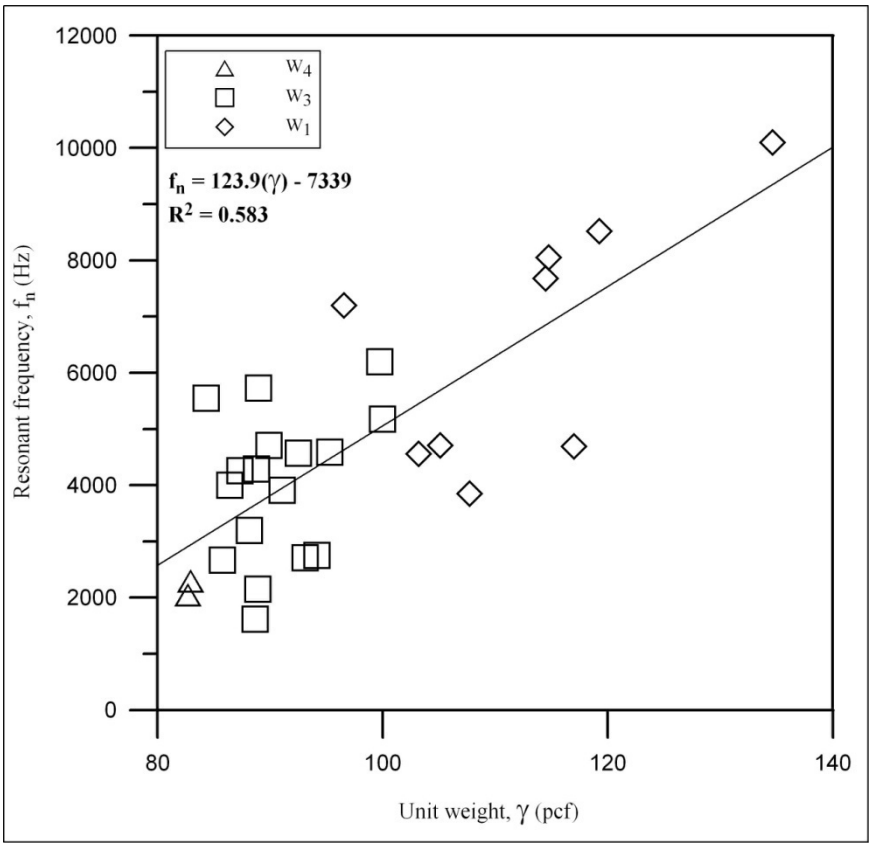

Figure 6-16. Resonant frequency verses unit weight

6.3.6.3 Comparison of Dynamic Elastic Modulus and Unit Weight

Figure 6-17 presents the dynamic elastic modulus verses unit weight data for each weathering state. This figure is very similar to Figure 6-16 because the dynamic elastic modulus is proportional to the square of the natural frequency. The slightly weathered specimens have dynamic elastic modulus values that increase with unit weight. The highly weathered specimens have variable values of dynamic modulus with increasing unit weight. The best-fit regression

line for dynamic elastic modulus and unit weight has a high coefficient of determination (R^2=0.695).

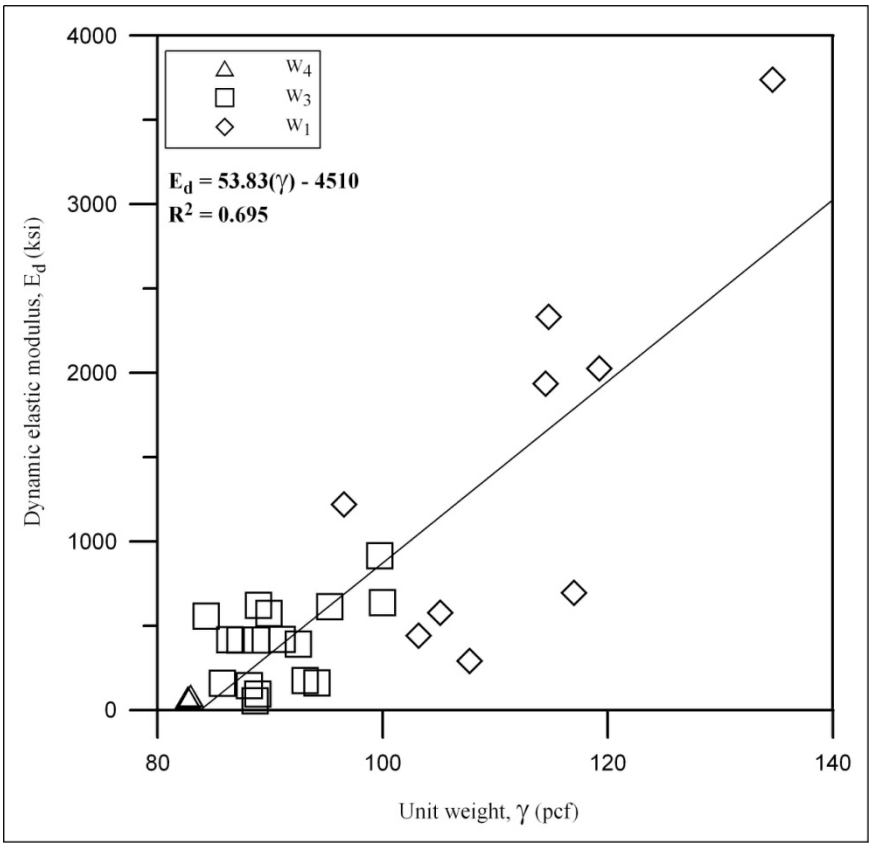

Figure 6-17. Dynamic elastic modulus verses unit weight

In terms of dynamic elastic modulus, overlapping occurs between specimens classified as W_1 and W_3 in the region where the unit weight ranges from approximately 100 pcf to 120 pcf. This overlap is largely influenced by W_1 specimens that have low unit weight values relative to their weathering state.

6.3.7 Dynamic and Static Properties

In this section correlations between dynamic properties and static properties are presented. The dynamic properties of interest are P-wave velocity (V_p), resonant frequency (f_n), and

dynamic elastic modulus (E_d). The static properties of interest are the unconfined compressive strength (UCS) and static elastic modulus (E_s).

6.3.7.1 Comparison of P-Wave Velocity and Unconfined Compression Strength (UCS)

The correlation of P-wave velocity with strength parameters of rock has been established in numerous studies (Judd and Hubber, 1962; D'Andrea et al., 1965; Irfan and Dearman, 1978; Tugrul and Zarif, 2000). Figure 6-18 shows unconfined compressive strength as a function of P-wave velocity. A general increase in P-wave velocity is observed as UCS increases.

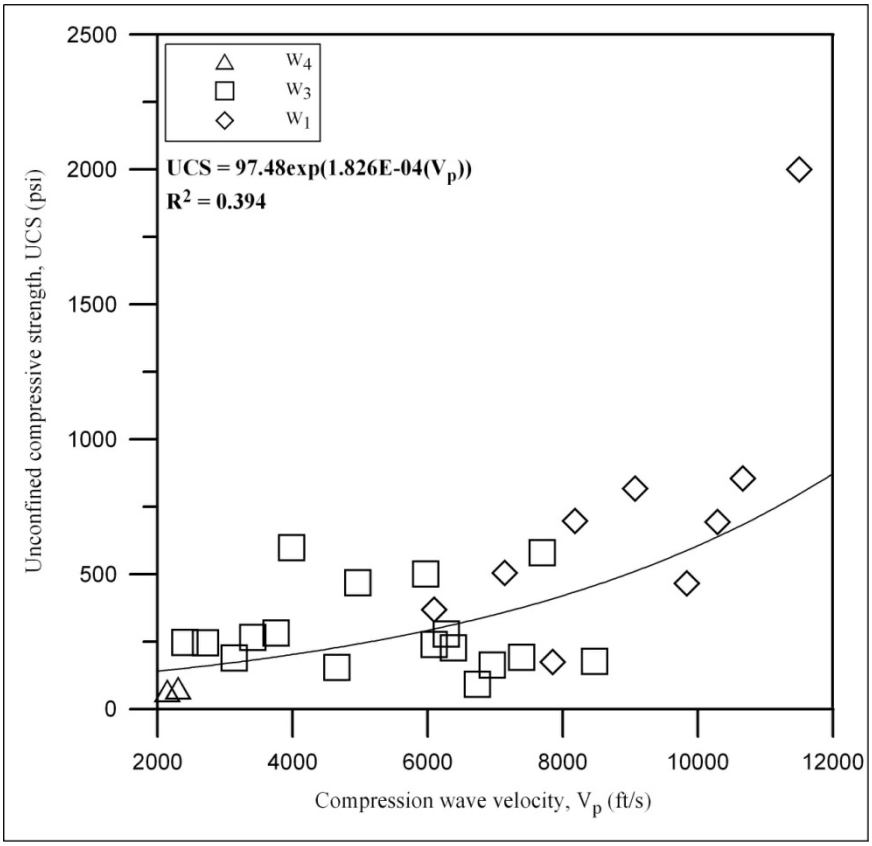

Figure 6-18. P-wave velocity verses UCS

The specimens with the highest degree of weathering have the lowest values and the specimens with the lowest degree of weathering have the highest values. A large degree of scatter is present and the trend line is represented by a poor coefficient of determination

(R^2=0.395). Generally, in the cases of the limestone specimens classified as W_3, the UCS values are constant and a broad range of P-wave velocities are exhibited. Both low and high UCS values pair up with approximately the same P-wave velocity.

6.3.7.2 Comparison of P-Wave Velocity and Static Elastic Modulus

Figure 6-19 shows the graph of P-wave velocity versus static elastic modulus. The data in the graph is highly scattered with a low coefficient of determination (R^2=0.3236). Figure 6-19 indicates that moderately weathered specimens with the same values of static elastic modulus have different values of P-wave velocity. This observation occurs for specimens with low values of static elastic modulus. However, as the static elastic modulus increase, there is a general increase in P-wave velocity for each weathering state.

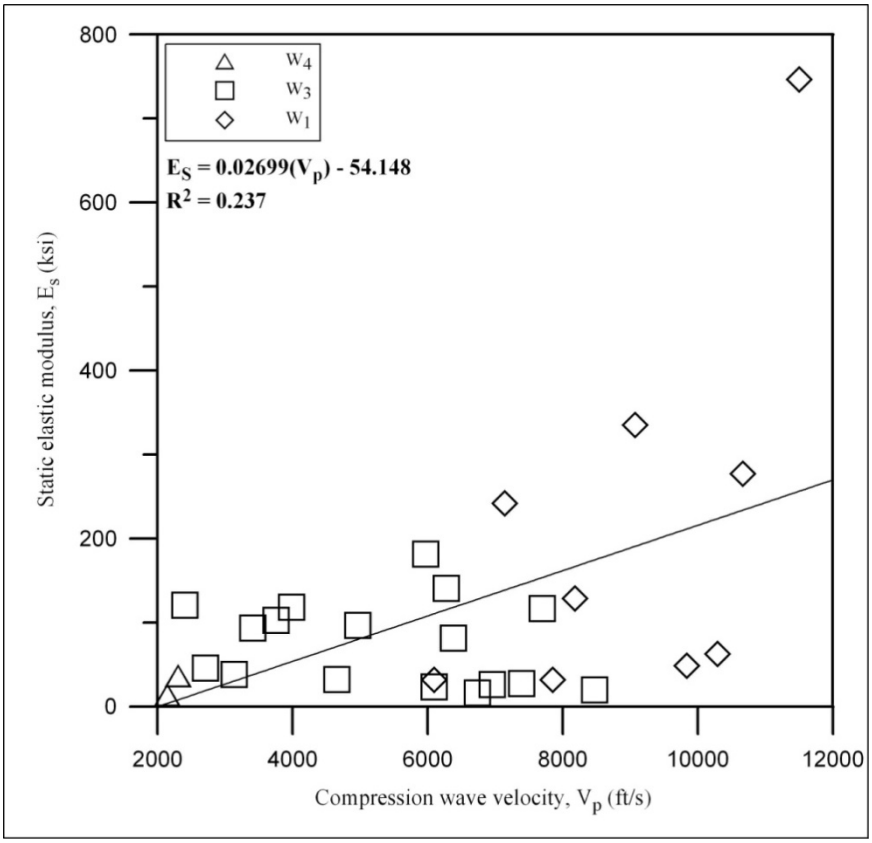

Figure 6-19. Static elastic modulus verses P-wave velocity

6.3.7.3 Comparison of Resonant Frequency and Unconfined Compression Strength (UCS)

Figure 6-20 shows the resonant frequency versus unconfined compressive strength (UCS). There is a general increase in the UCS as the resonant frequency increases. A large degree of scatter is present and the coefficient of determination (R^2=0.5567) is moderate. For the most part, in the cases of the limestone specimens classified as W_1 and W_3, UCS values have a broad range of resonant frequencies and both low and high UCS values pair up with approximately the same resonant frequency. It is seen that for some specimens classified as W_3, the UCS remains relatively constant as the natural frequency increases. This consistency with UCS is plausible as the disparity between the degrees of weathering within the W_3 weathering state is small.

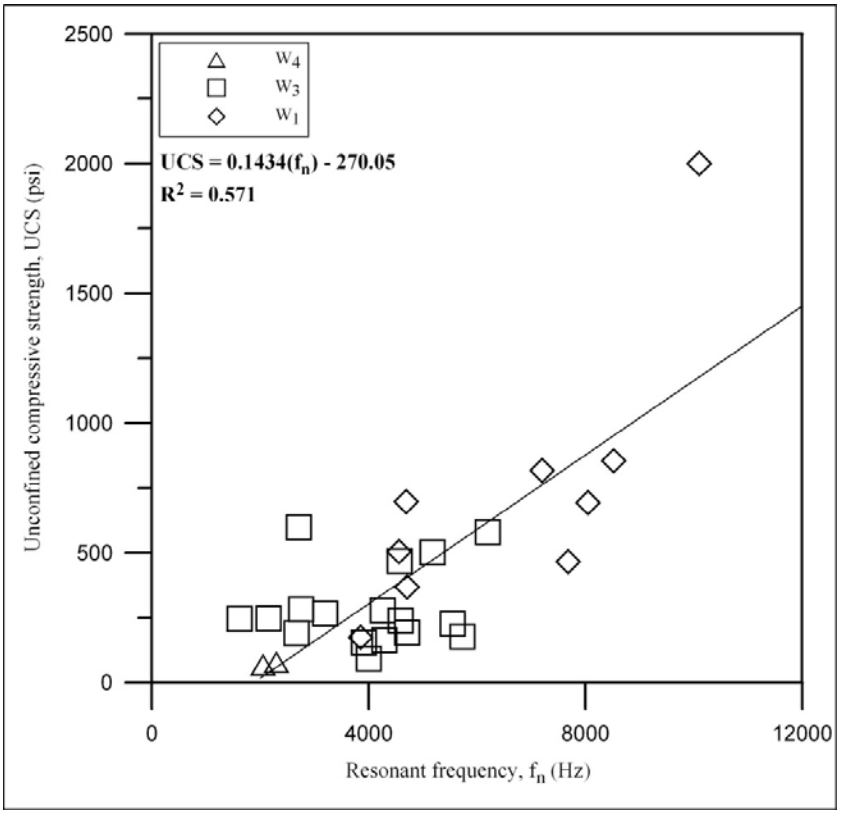

Figure 6-20. UCS versus resonant frequency

The graph of UCS versus resonant frequency is very similar to the preceding graph of P-wave velocity versus UCS shown in Figure 6-19. The data for the specimens as grouped by their

respective weathering classifications are stationed in the same region of the graphs in each figure. This similarity between P-wave velocity and natural frequency shared with UCS is expected because P-wave velocity and natural frequency are related.

6.3.7.4 Unconfined Compression Strength (UCS) Versus Dynamic Elastic Modulus

Figure 6-21 is a display of the UCS verses dynamic elastic modulus. Some overlapping between specimens classified as W_1 and W_3 in the region where UCS values range from 0.1 ksi to 0.6 ksi is observed. A positive trend line with a good coefficient of determination (R^2=0.728) is shown. Even though overlapping of engineering properties within weathering classifications is expected (Arikan et al., 2007), the W_1 specimens that overlap with the W_3 specimens generally have low dynamic elastic modulus and UCS values relative to their classification.

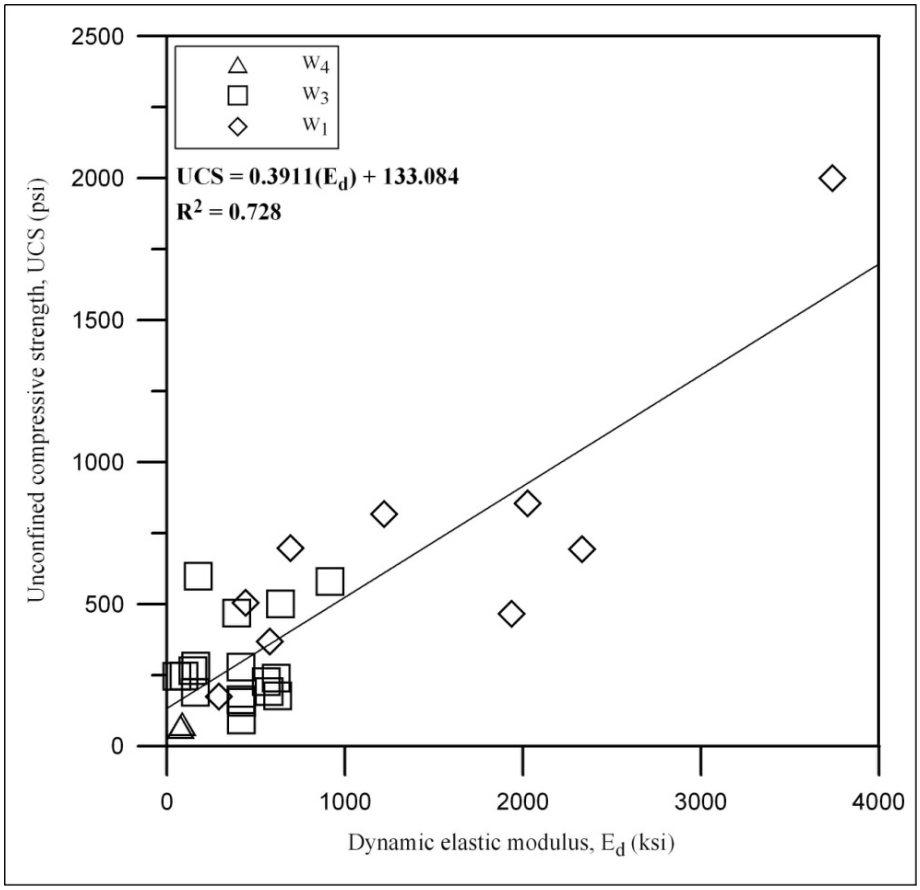

Figure 6-21. UCS verses dynamic elastic modulus

Generally, as the UCS increases the dynamic elastic modulus also increases. Furthermore, the region of the graph in which the samples have the lowest degree of weathering corresponds to the highest values for both dynamic elastic modulus and UCS; similarly, the region of the graph in which the specimens have the highest degree of weathering corresponds to the highest values for both dynamic elastic modulus and UCS.

6.3.7.5 Comparison of Dynamic Elastic Modulus and Static Elastic Modulus

The dynamic elastic modulus versus static elastic modulus plotted with a shaded region between 1:1 and 10:1 lines is shown in Figure 6-22. The 1:1 line is representative of data points that have equal values of dynamic and static moduli. The shaded region represents the expected range of dynamic elastic modulus with respect to static elastic modulus (Ed≈10Es). The lower bound of the shaded region represents moduli that are equal (Ed = Es). The higher bound of the shaded region represents the dynamic elastic modulus is up to 10 times the static elastic modulus.

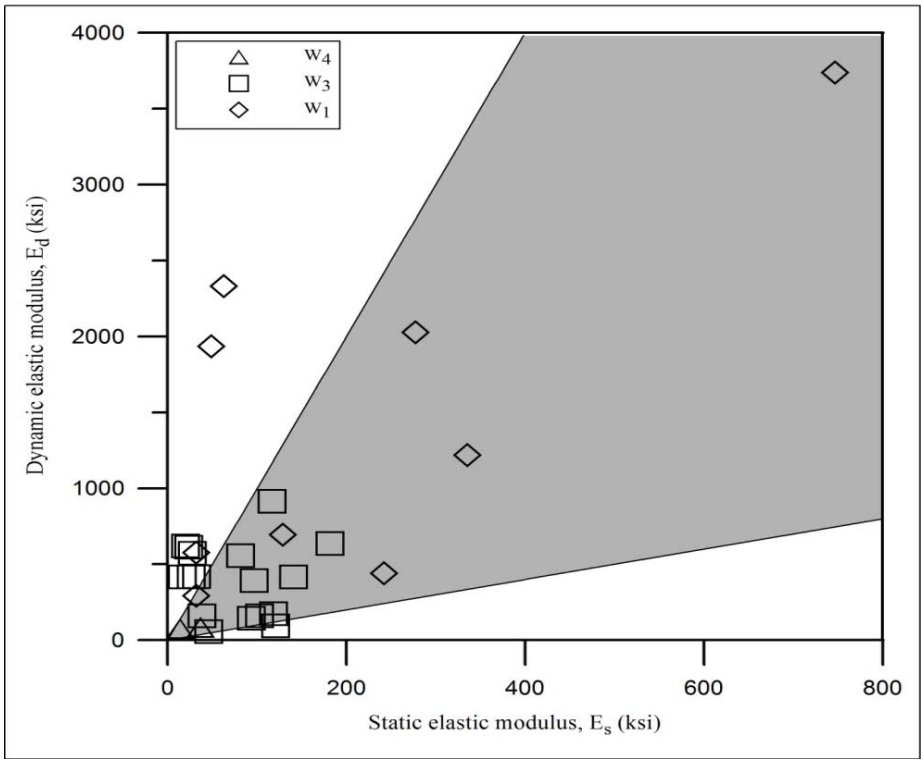

Figure 6-22. Dynamic elastic modulus verses static elastic modulus

Studies conducted by King (1969), Martinez et al. (2008), and Ciccotti and Mulargia (2004) that compare dynamic and static elastic modulus, have concluded that variation between these two parameters can be extensive. Research conducted on variably fissured carbonate rocks indicate that the presence of large fissures relates to low values of dynamic elastic modulus, however, not necessarily a low value of static elastic modulus, which depends on the relative position and orientation of these fissures (Martinez et al., 2008)). Eissa and Kazi (1988) suggested that static moduli are 5 to 10 percent lower than that of dynamic moduli and scatter can be large; static measurements can be as much as an order of magnitude smaller than dynamic measurements. Ciccotti and Mulargia (2004) confirmed the results of Eissa and Kazi (1988).

The data shown is highly scattered with one data point on the 1:1 line and one data point below the 1:1 line. However, the majority of the data points are within 10 per cent or slightly greater, which is in accordance with the previous studies.

6.3.7.6 Comparison of P-Wave Velocity and Resonant Frequency

Figure 6-23 presents the graph of P-wave velocity versus resonant frequency for the specimens classified using the ISRM weathering states and the differentially weathered limestone specimens. The graph exhibits a trend line with an excellent coefficient of determination (R^2=0.862). The trend indicates that as the P-wave velocity increases the resonant frequency increases. Above all, the data indicates P-wave velocity is proportional to resonant frequency, which implies that any defects or discontinuities present in each specimen influence the P-wave velocity and resonant frequency approximately equally.

This proportionality was also observed in a study by Sarno et al. (2009a) of plaster of Paris specimens with varying degrees of known porosity. The specimens were tested to obtain P-wave velocity and resonant frequency. It was observed that approximately the same percent difference in P-wave velocities was observed in the resonant frequency.

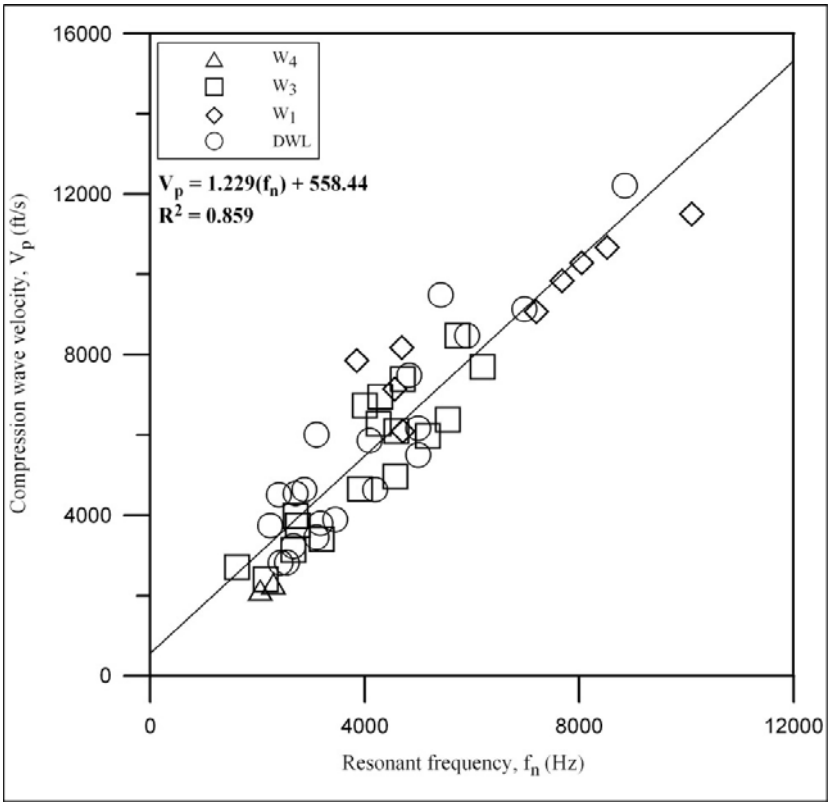

Figure 6-23. P-wave velocity verses resonant frequency

In Figure 6-23, the region of the graph in which the specimens have the highest degree of weathering corresponds to the lowest values for P-wave velocity. The region of the graph in which the specimens have the lowest degree of weathering corresponds to the highest values for both P-wave velocity and resonant frequency. For the case of the differentially weathered limestone specimens, the dynamic properties are spread throughout the range of the trend line. Moreover, although no correlation in terms of weathering between all of the specimens exists, the data measured from the differentially weathered specimens contribute very little scatter.

6.3.7.7 Comparison of P-Wave Velocity and Dynamic Elastic Modulus

Figure 6-24 presents the graph of P-wave velocity versus dynamic elastic modulus for all specimens. Essentially, this figure is a logarithmic representation of the previous figure (Figure 6-23), as the dynamic elastic modulus is based on the square of the resonant frequency. The

graph exhibits a trend line with generally low scatter, and with an excellent coefficient of determination (R^2=0.893). The trend indicates that as the P-wave velocity increases the dynamic elastic modulus increases.

The graph also indicates that the P-wave velocity is exponentially related to the dynamic elastic modulus, which implies that any defects or discontinuities present in each specimen do not influence the P-wave velocity and dynamic elastic modulus equally. This representation results in a higher regression value, and may be more suitable for the correlation of weathering with P-wave velocities.

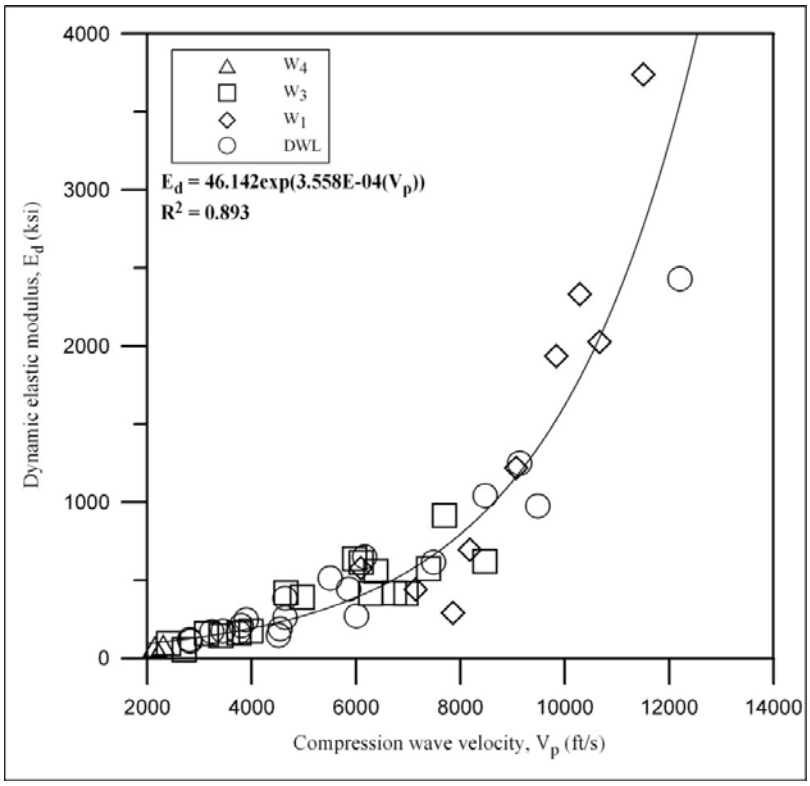

Figure 6-24. Dynamic elastic modulus verses P-wave velocity

The region of the graph in which the samples have the lowest degree of weathering correspond to the highest values for both P-wave velocity and dynamic elastic modulus; similarly, the region of the graph in which the specimens have the highest degree of weathering

corresponds to the lowest values for both P-wave velocity and dynamic elastic modulus., This was not the case regarding the specimens classified as W_4 in Figure 6-24, but in the case of the differentially weathered limestone specimens, the dynamic properties are spread throughout the range of the trend line. Moreover, although no correlation, in terms of weathering, between all specimens exists, the data measured from the differentially weathered limestone specimens contribute very little scatter.

6.4 Chapter Summary

Forty-eight specimens were collected from drilling activities at the UNF-UF-FLDOT geophysical test site in Alachua County, Florida. The specimens were from the Ocala limestone unit, which is the uppermost limestone unit in the area. The specimens were classified into ISRM weathering states. Specimens were either designated as W_1, W_3, W_4, or assigned a designation of differentially weathered limestone (DWL). W_1 specimens were fresh and relatively unweathered with a smooth surface texture. W_3 specimens were moderately weathered with a rough surface texture. W_4 specimens are highly weathered with a chalky and crater-like surface texture. Surface features such as cracks and voids were observed in all specimens. The weathering state was assigned regardless of the amount or type of surface features.

The differentially weathered limestone specimens have a unique appearance and texture. There appeared to be two distinct weathering zones within the specimens. One zone was fresh and relatively unweathered with a smooth surface texture. This zone was identical to the appearance of the W_1 specimens. The other zone was moderately to highly weathered with a rough to chalky crater-like texture. This zone was identical to the appearance of the W_3 and W_4 specimens. The variation of textures within the specimens caused a mottled appearance. For these reasons, these specimens were given the special designation of differentially weathered limestone (DWL).

For all the specimens, the unit weight, dynamic properties, and static properties were obtained. The dynamic properties were resonant frequency (f_n), dynamic Young's modulus (E_d), dynamic Poisson's ratio (ν_d), and compression wave velocity (or P-wave velocity) (V_p). The static properties of interest were unconfined compressive strength (UCS) and static elastic modulus (E_s). For the specimens with designated weathering states, there was minor overlap of all properties between the weathering states. For the differentially weathered limestone there was significant overlap of all properties between all weathering states.

Relationships between physical, static, and dynamic properties were developed for the weathered limestone, differentially weathered limestone, and all limestone specimens combined. The physical property of interest was unit weight. The static properties of interest were unconfined compressive strength (UCS) and static elastic modulus (E_s). The dynamic properties of interest were P-wave velocity (V_p), resonant frequency (f_n), and dynamic elastic modulus (E_d).

The relationships between physical, static, and dynamic properties for the weathered limestone were displayed in terms of weathering. These relationships provided good to excellent correlations as indicated by a high coefficient of determination (R^2) value. The majority of the relationships for the differentially weathered limestone specimens contained a high degree of scatter, and poor correlations between physical, static, and dynamic properties as indicated by a low R^2 value. Due to the high scatter in the data, and resulting poor correlations between all properties, these relationships were not discussed. Data from all of the limestone specimens were combined to produce relationships in only three cases. The first case evaluated unit weight as a function of weathering state. The other two cases incorporated P-wave velocity as a function of resonant frequency and P-wave velocity as a function of dynamic elastic modulus. In the two cases where dynamic properties were incorporated, excellent R^2 values were achieved.

CHAPTER 7
CLOSURE

7.1 Summary of Findings

Two inversion techniques using simulated annealing have been developed to invert travel times and full waveforms for wave velocity profiles. They are first tested on synthetic data and then applied to real test data. The inverted profiles from the real test data are compared to other independent test results such as those of CPT, SPT, geotechnical borings, and crosshole test to assess the capabilities of the techniques for geotechnical engineering applications. A laboratory testing program was conducted on rock cores that assess the relationships between geophysical measurement results and geotechnical engineering design parameters.

7.1.1 Inversion Technique Using Travel Times

The technique using travel times is based on an extremely fast finite-difference solution of the Eikonal equation to compute first-arrival times through the velocity models by the multistencils fast marching method. The core of the simulated annealing, the Metropolis sampler, is applied in cascade with respect to shots to significantly reduce computer time. This technique has been applied to surface data, and to combined surface and borehole data.

For the cases of only surface data, the following findings have been derived:

- Tested on synthetic data, the presented technique produces inverted results consistent with those from commercial codes, including GeoCT-II, SeisImager, and Rayfract, and it performs better than those codes in cases of sharp contrasts in velocity.
- Applied to real test data, the presented technique produces inverted results that appear consistent to those from invasive tests, including CPT, SPT, and geotechnical borings. Using surface travel times, the technique can well characterize normal profiles that increase in velocity with depth.
- Although the presented technique requires more computer time than the three mentioned commercial packages, it has several advantages. First, this inversion technique does not depend on the initial model, and becomes important in regions where a priori information about subsurface profiles is not available. Second, simulated annealing provides a suite of final models clustering around the global solution and having comparable least-squared

error. This provides an inversion result by averaging all of these models to mitigate the influence of noise and the non-uniqueness of the inversion solutions. Last, the technique provides uncertainty estimates associated with inverted results.

- As a typical limitation of surface-based refraction methods, the presented technique fails to detect anomalies such as low-velocity zones and embedded cavities. It also fails to characterize velocity structure below a few meters from the top of the half-space (bottom layer), because the fastest rays only travel within these few meters at the top of the half-space, regardless of how large a geophone spread is used.

For the combined surface and borehole data, the following findings have been derived:

- Tested on synthetic combined data, the presented technique well characterizes velocity structures at depth near the borehole. The presence, location, general shape, and true velocity of embedded low-velocity zones can also be characterized.

- Also tested on synthetic combined data, the presented technique requires just a few shot locations on the ground surface within a few meters around a borehole, surface geophones within this few meters, and a string of borehole geophones, to reliably assess the subsurface properties at depth near the borehole.

- Applied to real combined test data, the presented technique produces credible inverted velocity profiles. A comparison of tomograms utilizing the combined data against tomograms developed using just the surface data suggests that significant additional resolution of inverted profiles at depth are obtained with the addition of a borehole. It is also found that the quantitative uncertainties associated with the inverted profiles are significantly reduced when adding a borehole.

- Employed for site characterization of deep foundation design, refraction tomography using combined surface and borehole data provides credible information of material at the socket, and can detect anomalies near the socket. This becomes important because the material at and near the socket often carries a majority of load from foundations. The inversion results of the combined data, including inverted profiles and associated uncertainties, provide characterization of spatial variability in geotechnical engineering physical parameters of subsurface formations useful in the design of deep foundations. This will be particularly useful in implementing the new LRFD design methodology that can explicitly account for spatial variability and uncertainty in design parameters.

7.1.2 Inversion Technique Using Full Waveforms

The technique using full waveforms is based on a finite-difference solution of the 2-D elastic wave equation in the time-distance domain. It uses the full information of elastic wave fields to increase resolution of inversion results, especially dealing with reverse models. It also employs a global inversion technique, simulated annealing, to invert the full wave fields for near-

surface velocity profiles. The technique is first tested on many different synthetic data sets created from challenging reverse models with high-velocity and low-velocity layers at different depths. Then, it is applied to experimental data sets, and the inversion results are compared to invasive test results including crosshole, SPT N-value, and material log, or compared to results of independent refraction tests. The following findings about the technique have been derived:

- Tested on 1-D synthetic models, the presented technique performs well on reverse models, and shows superiority over traditional techniques using Rayleigh wave velocity dispersion.
- Tested on 2-D synthetic models, the presented technique shows that 2-D profiles with multilinear interfaces of a few-meter segments can be characterized using a full wave field from only one source.
- Applied to real full waveform data, the presented technique produces inverted results that appear consistent to those from invasive tests, including SPT, crosshole, and geotechnical borings. The inverted results from the full waveform data also appear consistent to the inverted results from refraction travel times.
- Besides its superiority over the traditional methods in dealing with reverse profiles, the presented technique can possibly replace seismic refraction tomography to characterize normal profiles (increasing velocity with depth), because it requires much less effort in both site testing and manual data processing.
- The presented technique does not depend on the initial model, and becomes important in regions where a priori information about subsurface profiles is not available. Simulated annealing provides a suite of final models clustering around the global solution, and having comparable least-squared error. This provides an inversion result by averaging all of these models to mitigate the influence of noise and the non-uniqueness of the inversion solutions.

7.1.3 Rock Parameter Relationships

It is well established that weathering has a negative effect on engineering properties of rock. In this study, the relationships between physical, static, and dynamic properties of limestone in terms of weathering were assessed. Ocala limestone specimens were classified according to weathering state and tested. Classification was conducted using ISRM weathering designations, dynamic testing was conducted using free-free resonant column testing, and static testing was conducted using unconfined compression. The following findings have been derived:

- From the classification process, it was found that two distinct groups of limestone specimens exist: specimens that can be classified using ISRM weathering designations, and specimens that are differentially weathered and cannot be classified using ISRM methods. These specimens are termed differentially weathered limestone.

- For both groups of specimens, physical, static, and dynamic properties were obtained. For the specimens classified using ISRM weathering states, the physical, static, and dynamic properties were related to weathering. Good to excellent correlations between physical, static, and dynamic properties were obtained for these specimens.

- For the differentially weathered limestone specimens, a high degree of scatter was observed in the correlations between physical, static, and dynamic properties.

7.2 Conclusions

Based on the findings outlined above, the following conclusions are made. First, the technique using travel times can well characterize normal profiles (increasing in velocity with depth) using only surface data and it also can characterize profiles with embedded anomalies using combined surface and borehole data. The inverted results from travel times appear consistent to those from invasive tests, including CPT, SPT, and geotechnical borings. Second, the technique using full waveforms can characterize challenging reverse models, including high- and low-velocity layers with only surface data. The inverted results from full waveforms are consistent with those from invasive tests, including SPT, crosshole, and geotechnical borings. The inverted results also appear consistent with inverted results from refraction travel times. Third, both inversion techniques do not depend on an initial model, and become important in regions where a priori information about subsurface profiles is not available. Simulated annealing provides a suite of final models clustering around the global solution, and having comparable least-squared error. This provides an inversion result by averaging all of these models to mitigate the influence of noise and the non-uniqueness of the inversion solutions. Lastly, based upon the laboratory testing program, it does appear that relationships between geophysical measurements and geotechnical engineering design parameters are credible, though

significant scatter does exist in the data. It could be postulated that geophysical measurements should be capable of indentifying large zones of poor quality rock.

7.3 Recommendations

Based upon the work report herein, the following recommendations are suggested:

- The combined surface/borehole array concept described herein should be implemented following the procedures utilized at the three field test sites.
    - For equipment, the FDOT currently has data acquisition and surface array geophones available, thus, a string of borehole geophones must be acquired.
    - For field implementation, it is recommended that the test configuration utilized at the Ft. McCoy and Dunedin sites be followed. While this configuration does not take full advantage of the optimized test configurations suggested by the synthetic model studies, it would be better during the learning stage to collect a full array while equipment is deployed in the field, since the time required to collect the additional shots is relatively small (approximately one hour).
    - For data analysis, the software developed and described herein should be utilized to produce inversion images. Here, the optimized configuration concepts could be utilized when processing the test data by simply analyzing only a portion of the shots to produce a preliminary inversion image. Picking arrival times for development of travel time curves is time consuming. Thus, significant savings may be achieved in data processing by following the optimized configurations (e.g., 4 to 6 surface shots). The data for the remaining shots archived during field testing could be analyzed at a later time if the preliminary image suggested an anomaly.
- Development of the combined surface/borehole array concept and the full waveform techniques should be continued and enhanced. For example:
    - Further develop the full waveform surface-based array for shallow site characterization applications. For example, using data from multiple shots to increase the resolution of inverted profiles, the medium can be divided into many small cells and velocity of each cell determined independently. In addition, guidelines for array design and depth of investigation of the full waveform technique are needed. To save computer time, the global inversion techniques could be followed by a local inversion technique.
    - Develop a full-waveform-based model to analyze the data from a combined borehole/surface array. This methodology could significantly improve resolution in the case of a high water table, for example, where the first-arrival time technique could not perform as well at the Dunedin site. In geotechnical applications, shear waves are a common remedy to characterize the stiffness properties of saturated soil. However, it is problematic to reliably produce shear wave first arrivals when there is a strong velocity

contrast in the profile, e.g., soil/rock interface, since the velocity boundary can produce reflected and refracted P-waves that travel faster than shear waves. Thus, even though one may generate a shear wave at the source, the first arrival at the sensor could easily be a reflected or refracted P-wave. A simple first-arrival model will not account for this reality. Thus, it is recommended that a full waveform based analysis technique be developed. Herein, a full waveform model has been demonstrated for a surface array, but further work is required for the combined surface/borehole configuration.

- Develop a new inhole characterization tool that implements full waveform analysis of an instrument array deployed vertically along a borehole. The full waveform analysis could resolve the 2-D variation within a vertical/radial plane, and then the tool could be rotated circumferentially to possibly obtain 3-D variation. The array could eventually be implemented within other borehole-based probes such as CPT or rock shear. This was an early vision for the research reported herein, and it now seems like this could possibly be realized following more research effort.

- It seems possible that significant information about the weathering state of rock could be gained by an in situ surface texture imaging technique. Surface texture measurements could be coupled with the geophysical measurements now available or proposed for additional development as discussed above.

- The geophysical imaging techniques discussed above should all be further corroborated via application at test sites where geophysics is combined with traditional site characterization, sample extraction and testing, and actual construction of real infrastructure elements.

LIST OF REFERENCES

Arikan, F., R. Ulusay and N. Aydin (2007), "Characterization of Weathered Acidic Volcanic Rocks and a Weathering Classification Based on a Rating System," Bull Eng Geol Environ, Vol. 66, February, pp. 415-430.

ASTM D2938 (1995), "Standard Test Method for Unconfined Compressive Strength of Intact Rock Specimens," Annual Book of ASTM Standards, 04-08.

ASTM C215 (1997), "Standard Test Method for Fundamental Transverse, Longitudinal, and Torsional Frequencies of Concrete Specimens," Annual Book of ASTM Standards, 04-02.

Burger, H. R. (1992), "Exploration Geophysics of the Shallow Subsurface," Prentice-Hall, Inc., Englewood Cliffs, New Jersey.

Bynes, F. J., W. R. Dearman, and T. Y. Irfan (1978), "Practical Assessment of Grade in a Weathered Granite," Bull Int Assoc Eng Geol, Vol. 18, pp. 101-110.

Campbell, K. M. and T. M. Scott (1991), "Radon Potential Study, Alachua County Florida: Near-Surface Stratigraphy and Results of Drilling," Florida Geological Survey, Open File Report Number 41, Tallahassee, FL, pp. 41.

Carpenter, P. J., Higuera-Diaz, I. C., Thompson, M. D., Atre, S., and Mandell, W. (2003), "Accuracy of Seismic Refraction Tomography Codes at Karst Sites," Geophysical Site Characterization: Seeing Beneath the Surface, Proceedings of a Symposium on the Application of Geophysics to Engineering and Environmental Problems, San Antonio, Texas, April 6-10, pp. 832-840.

Chopp, D.L. (2001), "Some Improvements on Fast Marching Method," SIAM J. Scientific Computing, Vol. 23, No. 1, pp. 230-244.

Ciccotti, M. and F. Mulargia (2004), "Differences Between Static and Dynamic Elastic Moduli of a Typical Seismogenic Rock," Geophys. J. Int. Abstr., Vol. 157, November, pp. 474-477.

Clayton, R. and Engquist, B. (1977), "Absorbing Boundary Condition for Acoustic and Elastic Waves," Bull. Seimol. Soc. Am., Vol. 67, No. 6, pp. 1529-1540.

D'Andrea, D. V., R. L. Fischer, and D. E. Fogelson (1965), "Prediction of Compressive Strength of Rock from Other Properties," US Bureau of Mines Report, Investigation 6702.

Dijkstra, E.W. (1959), "A Note on Two Problems in Connection with Graphs," Numer. Math. J., Vol. 1, pp. 269-271.

Doyle H. (1995), "Seismology," J. Wiley & Sons, Chichester.

Eissa, E. A. and A. Kazi (1988), "Relation Between Static and Dynamic Young's Modului for Rocks," Int. J. Rock. Mech. Min. Sci & Geomech. Abstr., Vol. 25, September, pp. 479-482.

EZ-Analyst (2008), "EZ-Analyst Users Manual for IOtech Software," IOtech, Cleveland, OH.

Foti S. (2000), "Multistation Methods for Geotechnical Characterization Using Surface Waves," Ph.D. Dissertation, Politecnico di Torino.

Gercek, H. (2006), "Poisson's Ratio Values for Rocks," International Journal of Rock Mechanics and Mining Sciences, Vol. 44, April, pp. 1-13.

Goodman, R. E. (1989), "Introduction to Rock Mechanics," John Wiley, New York.

Gupta, A. S. and K. S. Rao (1998), "Index Properties of Weathered Rocks: Inter-Relationships and Applicability," Bull Eng Env, Vol. 57, No. 2, pp. 161-172.

Hassouna, M.S. and Farag, A.A. (2007), "Multistencils Fast Marching Methods: A Highly Accurate Solution to the Eikonal Equation on Cartesian Domains," IEEE Trans. Patt. Anal. Mach. Int., Vol. 29, No. 9, pp. 1-12.

Hiltunen, D. R. and Cramer, B. J. (2008), "Application of Seismic Refraction Tomography in Karst Terrane," Journal of Geotechnical and Geoenvironmental Engineering, Vol. 134, No. 7, pp. 938-948.

Hudyma, N., D. Hiltunen, and C. Samakur (2007), "Variability of Karstic Limestone Quantified Through Compressional Wave Velocity Measurements," Proceedings of Geo-Denver 2007, Problematic Soils and Rocks and In Situ Characterization, Geotechnical Special Publication 162, CD-ROM.

Ingber, L. (1989), "Very Fast Simulated Reannealing," Math. Comput. Modeling, Vol. 12, No. 8, pp. 967-993.

Ingber, L. (1993), "Simulated Annealing: Practice versus Theory," Math. Comput. Modeling, Vol. 18, No. 11, pp. 29-57.

Inman, D. J. (2007), "Engineering Vibration," Prentice Hall, Upper Saddle River.

International Society for Rock Mechanics (ISRM) (1981), International Journal of Rock Mechanics. Min. Sci. Geomech. Abstr.,Vol. 18, No. 1, pp. 85–110.

Irfan, Y. and W. R. Dearman (1978), "The Engineering Petrography of a Weathered Granite in Cornwall, England," Q J Engineering Geology, Vol. 11, pp. 233-244.

Jin, X., Luke B., and Calderon-Macias C. (2009), "Role of Forward Model in Surface-Wave Studies to Delineate a Buried High-Velocity Layer," Journal of Environmental and Engineering Geophysics, Vol. 14, No. 1, pp. 1-14.

Judd, W. R. and C. Huber (1962), "Correlation of Rock Properties by Statistical Methods," Proc International Symposium of Mining Resources, pp. 621-648.

Kilic, A. and A. Teymen (2008), "Determination of Mechanical Properties of Rocks Using Simple Methods," Bull Eng Geol Environ, Vol. 67, No. 2, pp. 237-244.

Kim, S. (1999), "ENO-DNO-PS: A Stable, Second-Order Accuracy Eikonal Solver," Soc. Exploration Geophysicists, pp. 1747-1750.

King, M. S. (1969), "Static and Dynamic Elastic Moduli of Rocks Under Pressure," The 11th U.S. Symposium on Rock Mechanics, June, pp. 330-351.

Li J. (2008), "Study of Surface Wave Methods for Deep Shear Wave Velocity Profiling Applied in the Upper Mississippi Embayment," Ph.D. Dissertation, University of Missouri–Columbia.

Louie, J. N. (2001), "Faster, Better, Shear-Wave Velocity to 100 Meters Depth from Refraction Microtremor Arrays," Bulletin of Seismological Society of America, Vol. 91, No. 2, pp. 347-364.

Marques, E. A. G. and E. A. Vargas (1998), "Geotechnical Characterization of Weathering Profiles in Biotite Gneiss (Kinzigites) from Rio de Janerio City-Minerological Changes and Physical Properties," 8th International IAEG Congress, pp. 1680-2673.

Martinez, J., D. Benavente, and M. Angeles Garcia-del-Cura (2008), "Comparison of Static and Dynamic Modulus in Fractured Building Rocks," The 33rd International Geologic Congress MRC-08, August, pp. 118-125.

Metropolis, N., Rosenbluth A., Rosenbluth M., Teller A., and Teller E., (1953), "Equation of State Calculations by Fast Computing Machines," J. Chem. Phys., Vol. 21, No. 6, pp. 1087-1092.

Montgomery, D. C., G. C. Runger, and N. F. Hubele (2006), "Engineering Statistics," John Wiley & Sons, Danvers.

Moser, T.J. (1991), "Shortest Path Calculation of Seismic Rays," Geophysics, Vol. 56, pp. 59-67.

Nakanishi, J. and Yamaguchi, K. (1986), "A Numerical Experiment on Non-Linear Image Reconstruction from First-Arrival Times for Two-Dimensional Island Structure," J. Phys. Earth, Vol. 34, pp. 195-201.

Nazarian, S. (1984), "In Situ Determination of Elastic Moduli of Soil Deposits and Pavement Systems by Spectral-Analysis-of-Surface-Waves Method," Ph.D. Dissertation, The University of Texas at Austin.

Nichols, D.E. (1996), "Maximum Energy Travel Times Calculated in Seismic Frequency Band," Geophysics, Vol. 61, pp. 253-263.

O'Neill, A. (2003), "Full-Waveform Reflectivity for Modeling, Inversion, and Appraisal of Seismic Surface Wave Dispersion in Shallow Site Investigations," Ph.D. Dissertation, The University of Western Australia.

Park, C. B., Miller, R. D., and Xia, J. (1999), "Multi-Channel Analysis of Surface Wave (MASW)," Geophysics, Vol. 64, No. 3, pp. 800-808.

Pinho, A., J. A. Rodrigues-Carvalho, C. Gomes, and I. M. Duarte (2006), "Overview of the Evaluation of the State of Rock Weathering By Visual Inspection," 7th Congress of the International Association for Engineering Geology and the Environment, pp. 1-8.

Plummer, C. C. and D. McGeary (1985), "Physical Geology," Wm. C. Brown Publishers, Dubuque.

Pratt, R. G. (1998), "Seismic Waveform Inversion in the Frequency Domain, Part 1: Theory and Verification in a Physical Scale Model," Geophysics, Vol. 64, No. 3, pp. 888-901.

Pullammanappallil, S.K. and Louie, J.N. (1994), "A Generalized Simulated Annealing Optimization for Inversion of First-Arrival Time," Bull. Seimol. Soc. Am., Vol. 84, No. 5, pp. 1397-1409.

Quigley, T. P. (2006), "Ground Proving Seismic Refraction Tomography (SRT) in Laterally Variable Karstic Limestone Terrain," Master's Thesis, University of Florida.

Randazzo, A. F. and D. S. Jones (1997), "The Geology of Florida," University Press of Florida Publishers, Tallahassee.

Redpath, B. B. (1973), "Seismic Refraction Exploration for Engineering Site Investigations," Technical Report TR E –73-4, U. S. Army Engineer Waterways Experiment Station Explosive Excavation Research Laboratory, Livermore, California, May.

Richardson, M. H. (1999), "Structural Dynamics Measurements," Technical Report SD2000, Vibrant Technology, Inc., Jamestown.

Sambridge M. and Mosegaard K. (2000), "Monte Carlo Methods in Geophysical Inverse Problems," Reviews of Geophysics, Vol. 40, No. 3.

Sarno, A., R. Farah, N. Hudyma, and D. R. Hiltunen (2009a), "Relationships Between Index and Physical Properties of Weathered Ocala Limestone," 43rd US Rock Mechanics Symposium and 4th U.S.-Canada Rock Mechanics Symposium, pp. 134-143.

Sarno, A., N. Hudyma, D. R. Hiltunen, and M. MacLaughlin (2009b), "Modal Testing: An Innovative Approach to Dynamic Rock Specimen Characterization," The Joint 14th Intermountain Conference on the Environment & 42nd Engineering Geology and Geotechnical Engineering Symposium, November, pp. 77-82.

Sarno, A., R. Farah, N. Hudyma, and D. R. Hiltunen (2010), "Relationships Between Compression Wave Velocity and Unconfined Compression Strength for Weathered Florida Limestone," GeoFlorida 2010, Annual Geo-Congress of the Geo Institute of ASCE, February, pp. 950-959.

Scott, T.M. (2001), "Text to Accompany the Geologic Map of Florida," Florida Geologic Survey Open File Report Number 80, Florida Geological Survey, Tallahassee.

Schmidt, W. (2001), "Geomorphology and Physiolgraphy of Florida," Florida Geologic Survey Open File Report Number 80, Florida Geological Survey, Tallahassee.

Sen, M.K. and Stoffa, P.L. (1991), "Nonlinear One-Dimensional Seismic Waveform Inversion Using Simulated Annealing," Geophysics, Vol. 56, pp. 1624-1638.

Sen, M.K. and Stoffa, P.L. (1995), "Global Optimization Methods in Geophysical Inversion," Adv. Explor. Geophysics, Vol. 4, Elsevier Sci., New York.

Sethian, J.A. (1996), "Fast Marching Set Level Method for Monotonically Advancing Fronts," Pro. Nat. Acad. Sci., Vol. 93.

Sethian, J.A. (1999), "Level Set Methods and Fast Marching Methods," 2nd ed., Cambridge Univ. Press.

Sharma, S.P. and Kaikkonen, P. (1998), "Two-Dimensional Non-Linear Inversion of VLF-R Data Using Simulated Annealing," Geophysics J. Int., Vol. 133, pp. 649-668.

Sheehan, J.R., Doll, W.E., and Mandell, W.A. (2005), "An Evaluation of Methods and Available Software for Seismic Refraction Tomography Analysis," Journal of Environmental and Engineering Geophysics, Vol. 10, pp. 21-34.

Sheen, D. H., Tuncay, K., Baag, C. E., and Ortoleva1, P. J. (2006), "Time Domain Gauss–Newton Seismic Waveform Inversion in Elastic Media," Geophysical Journal International, Vol. 167, pp. 1373-1384.

Shipp, R. M. and Singh, S. C. (2002), "Two-Dimensional Full Wavefield Inversion of Wide-Aperture Marine Seismic Streamer Data," Geophysical Journal International, Vol. 151, pp. 325-344.

Slavova, D. Z., D. M. Weidinger, A. F. Sevi, and L. Ge (2010), "Evaluation of Compacted Silt Characteristics by Ultrasonic Pulse Velocity Testing," GeoFlorida 2010, Annual Geo-Congress of the Geo-Institute of ASCE, February, pp. 1284-1293.

Sun, X. and H. R. Hardy Jr. (1990), "A Feasibility Study of Modal Analysis in Geotechnical Engineering: Laboratory Phase," Rock Mechanics Contributions and Challenges, Proceedings of the 31st U.S. Symposium on Rock Mechanics, Hustrulid and Johnson, eds., pp. 661-668.

Tokimatsu, K., Tamura, S., and Kojima, H. (1992), "Effects of Multiple Modes on Rayleigh Wave Dispersion Characteristics," J. Geotech. Eng., Vol.118, No. 2, pp. 1529–1543.

Thomson W.T. (1950), "Transmission of Elastic Waves Through a Stratified Solid Medium," J. Applied Physics, Vol. 21, No. 1, pp. 89-93.

Tugrul A. and O. Gurpinar (1997), "A Proposed Weathering Classification for Basalts and Their Engineering Properties (Turkey)," Bulletin of the International Association of Engineering Geology, Vol. 55, April, pp. 139-149.

Tugrul, A. and I. H. Zarif (2000), "Engineering Aspects of Limestone Weathering in Istanbul, Turkey," Bull Eng Geol Env, Vol. 58, No. 3, pp. 191-206.

Van Trier, J. and Symes, W. (1991), "Upwind Finite-Difference Calculation of Travel Times," Geophysics, Vol. 56, pp. 812-821.

Vidale, J.E. (1988), "Finite-Difference Travel Time Calculation," Bull. Seis. Soc. Am., Vol. 78, pp. 2062-2076.

Virieux, J. (1986), "P-SV Wave Propagation in Heterogeneous Media: Velocity-Stress Finite-Difference Method," Geophysics, Vol. 51, No. 4, pp. 889-901.

Zhang, J. and Toksoz, M.N. (1998), "Nonlinear Refraction Traveltime Tomography," Geophysics, Vol. 63, No. 5, pp. 1726-1737.